INFORMATION TO USERS

This manuscript has been reproduced from the microfilm master. UMI films the text directly from the original or copy submitted. Thus, some thesis and dissertation copies are in typewriter face, while others may be from any type of computer printer.

The quality of this reproduction is dependent upon the quality of the copy submitted. Broken or indistinct print, colored or poor quality illustrations and photographs, print bleedthrough, substandard margins, and improper alignment can adversely affect reproduction.

In the unlikely event that the author did not send UMI a complete manuscript and there are missing pages, these will be noted. Also, if unauthorized copyright material had to be removed, a note will indicate the deletion.

Oversize materials (e.g., maps, drawings, charts) are reproduced by sectioning the original, beginning at the upper left-hand corner and continuing from left to right in equal sections with small overlaps.

Photographs included in the original manuscript have been reproduced xerographically in this copy. Higher quality 6" x 9" black and white photographic prints are available for any photographs or illustrations appearing in this copy for an additional charge. Contact UMI directly to order.

Bell & Howell Information and Learning
300 North Zeeb Road, Ann Arbor, MI 48106-1346 USA

UMI®
800-521-0600

Reproduced with permission of the copyright owner. Further reproduction prohibited without permission.

Reproduced with permission of the copyright owner. Further reproduction prohibited without permission.

EFFECTS OF CO-DOPANTS ON THE MICROSTRUCTURE AND ELECTROLUMINESCENCE OF ZnS:Mn THIN FILM PHOSPHORS

By

QING ZHAI

A DISSERTATION PRESENTED TO THE GRADUATE SCHOOL OF THE UNIVERSITY OF FLORIDA IN PARTIAL FULFILLMENT OF THE REQUIREMENTS FOR THE DEGREE OF DOCTOR OF PHILOSOPHY

UNIVERSITY OF FLORIDA

1999

Reproduced with permission of the copyright owner. Further reproduction prohibited without permission.

UMI Number: 9956653

Copyright 2000 by
Zhai, Qing

All rights reserved.

UMI®

UMI Microform 9956653
Copyright 2000 by Bell & Howell Information and Learning Company.
All rights reserved. This microform edition is protected against
unauthorized copying under Title 17, United States Code.

Bell & Howell Information and Learning Company
300 North Zeeb Road
P.O. Box 1346
Ann Arbor, MI 48106-1346

Reproduced with permission of the copyright owner. Further reproduction prohibited without permission.

To my parents and grandma.

Reproduced with permission of the copyright owner. Further reproduction prohibited without permission.

ACKNOWLEDGMENTS

I would first like to thank Dr. Paul H. Holloway, my advisor and the chairman of my supervisory committee, who offered me the opportunity to fulfill the research for my degree. Without his guidance, advice and support, which was not limited to research, this dissertation would not have been possible. I would like to thank Dr. Kevin S. Jones, who cochaired my committee, for his constructive discussions and positive attitude during the whole process of this project. I would also like to thank Dr. Michael J. Kaufman, who served in my committee for three years. I benefit a lot from his open door policy, supportive attitude and his approaches to analysis of issues. I am fortunate to have Dr. Robert DeHoff in my committee. I learned a lot from him, not only from our discussions about research or the courses he taught, but also from his approach to doing his job. I also like to thank Dr. Timothy Anderson for serving on my committee.

I would like to thank Dr. Jinghong Li, who invested a lot of enthusiasm and help from the first day of this project. I would also like to thank Dr. Mark Davidson, Barbara Speck, and Jongpyo Kim for supplying the sputter deposited samples. I thank Jay Lewis, Karen Waldrip, and Patrick Keys for showing me how to use the equipment. I would like to thank Ms. Ludie Harmon, who is the best secretary a graduate student can get.

I would like to thank my peers in the groups of both Dr. Holloway and Dr. Jones. I really had a good time with them.

Reproduced with permission of the copyright owner. Further reproduction prohibited without permission.

I would like to thank my family and friends, without whom I would have achieved nothing. First, I would like to thank my husband, Yaowu Hao, for his understanding and support during all those ups and downs and everything between over the past four years. I am grateful to my parents and parents-in-law who are the safety net under me, which makes me feel comfortable and confident to reach higher and go farther. I also like to say "thank you" to my dear brother, who always has tons of jokes and funny stuff that lift my spirit up when things are low. My special thanks go to Ms. Karina Yu-Wang, Charles Caplash, Michael Dearborn, and Andrew Hu for their encouragement and full support at every aspect, both in Beijing and in the United States. I feel lucky to have the friendship of Tong Li, Ding Li, Hao Chen, Lihong Mu, Dr. Bo Wu, and Dr. Xiaoying Zhu; all have been so tolerant and patient with me for so many years, cheering with me when I am joyous and soothing me when I shed tears. I am grateful. I feel indebted to Drs. Jian Hu and Sanjay Shrivastava, who helped me to adapt to this whole new environment when I first arrived. I also like to thank Dr. Lei Wei, who helped me to deal with the stresses that seemed to come from nowhere during the last year of my study.

Lastly, but definitely not leastly, I would like to express my gratitude to my grandma, Shuying Liang, who showed me the best of this world even before I really met it. May God help me to let her know that "everything I do, I do it for you....."

Reproduced with permission of the copyright owner. Further reproduction prohibited without permission.

TABLE OF CONTENTS

Page

ACKNOWLEDGEMENTS iii

ABSTRACT viii

CHAPTERS

1. INTRODUCTION 1

2. BACKGROUND: LITERATURE REVIEW 4

2.1 Electroluminescence Device Physics 4
2.1.1 Electron Tunneling 5
2.1.2 Electron Acceleration 7
2.1.3 Impact Excitation 8
2.1.4 Photon Generation 9
2.1.5 A Model for ACTFEL Devices 10
2.2 Device Characterizations of EL Devices 13
2.2.1 Charge-Voltage (Q-V) Diagram 13
2.2.2 Brightness-Voltage (B-V) Curve 14
2.2.3 CIE Coeffients 15
2.2.4 Luminous Efficiency 16
2.3 Materials Requirement for EL Devices 17
2.3.1 Substrate 17
2.3.2 Electrodes 18
2.3.3 Insulators 19
2.3.4 Phosphor 20
2.3.4.1 Host Material 21
2.3.4.2 Luminescent Centers 21
2.3.4.3 Luminescent Center Host Interaction 22
2.4 ZnS:Mn System 23
2.4.1 Microstructure of ZnS and ZnS:Mn 24
2.4.2 ZnS:Mn ACTFEL Devices 29
2.5 Microstructure Evolution of Thin Films 38
2.5.1 Nucleation and Impingement 41
2.5.2 Grain Growth 42
2.5.3 Texture 46

Reproduced with permission of the copyright owner. Further reproduction prohibited without permission.

3. EXPERIMENTAL PROCEDURE AND SAMPLE PREPARATION..... 48

3.1 Introduction..... 48
3.2 Device Fabrication..... 48
3.3 Rapid Thermal Annealing Conditions..... 51
3.4 Microstructure Characterization 53
3.4.1 X-ray Diffraction (XRD)..... 53
3.4.2 Transmission Electron Microscopy (TEM).....54
3.4.2.1 Introduction 54
3.4.2.2 Sample Preparation 57
3.4.2.2.1 Cross-section Transmission Electron Microscopy (XTEM) Samples 59
3.4.2.2.2 Plan-view Transmission Electron Microscopy (PTEM) Samples 62
3.4.3 Energy Dispersive Spectrometry (EDS)..... 63
3.4.4 Secondary Ion Mass Spectrometry (SIMS)..... 66
3.4.5 Grain Size Measurement 68
3.5 Device Characterization..... 69
3.5.1 Electroluminescence (EL) Properties 69
3.5.2 Photoluminescence (PL) Properties 70

4. ZnS:Mn WITH KCl AS A CO-DOPANT 72

4.1 Introduction..... 72
4.2 Background 72
4.3 Results and Discussion 73
4.3.1 Secondary Ion Mass Spectrometry (SIMS)..... 73
4.3.2 Transmission Electron Microscopy (TEM)..... 79
4.3.3 Compositional Analysis by Energy Dispersive Spectrometry (EDS)..... 91
4.3.4 X-ray Diffractometry (XRD).....95
4.3.5 Electroluminescence (EL) Properties..... 103
4.3.6 Photoluminescence (PL) Properties..... 111
4.4 Summary..... 113

5. ZnS:Mn WITH Ga_2S_3 AS A CO-DOPANT..... 115

5.1 Introduction..... 115
5.2 Results and Discussion 116
5.2.1 Secondary Ion Mass Spectrometry (SIMS)..... 116
5.2.2 X-ray Diffractometry (XRD)..... 118
5.2.3 Transmission Electron Microscopy (TEM)..... 121
5.2.4 Compositional Analysis by Energy Dispersive Spectrometry (EDS)..... 131
5.2.5 Electroluminescence (EL) Properties..... 136
5.3 Summary..... 142

Reproduced with permission of the copyright owner. Further reproduction prohibited without permission.

6. ZnS:Mn WITH KCl AND Ga_2S_3 AS CO-DOPANTS 143

6.1 Introduction..... 143
6.2 Results and Discussion 144
6.2.1 Secondary Ion Mass Spectrometry (SIMS)..... 144
6.2.2 X-ray Diffractometry (XRD)..... 147
6.2.3 Transmission Electron Microscopy (TEM)..... 154
6.2.4 Compositional Analysis by
Energy Dispersive Spectrometry (EDS)..... 164
6.2.5 Electroluminescence (EL) Properties..... 166
6.3 Summary..... 173

7. CONCULSIONS AND FUTURE WORK..... 175

REFERENCES..... 179

BIOGRAPHICAL SKETCH..... 185

Reproduced with permission of the copyright owner. Further reproduction prohibited without permission.

Abstract of Dissertation Presented to the Graduate School
of the University of Florida in Partial Fulfillment of the
Requirements for the Degree of Doctor of Philosophy

EFFECTS OF CO-DOPANTS ON THE MICROSTRUCTURE AND
ELECTROLUMINESCENCE OF ZnS:Mn THIN FILM PHOSPHORS

By

Qing Zhai

December, 1999

Chairman: Paul H. Holloway
Cochairman: Kevin S. Jones
Major Department: Materials Science and Engineering

The objective of this study is to investigate the effects of the co-dopants of KCl and Ga_2S_3 and post-deposition annealing on the microstructure and electroluminescence (EL) properties of ZnS:Mn thin film phosphors. ZnS:Mn thin films are deposited by radio frequency (RF) magnetron sputtering from ZnS and Mn targets onto pre-deposited indium tin oxide (ITO) and aluminum titanium oxide (ATO) layers on Corning 7059 glass. Argon at 20mTorr is the sputtering ambient. The substrates are held at 180°C during deposition. Co-dopants are thermally evaporated after the ZnS:Mn films, and diffused into the ZnS:Mn films by *ex situ* annealing between 600°C and 800°C for 5 minutes in a nitrogen ambient. Secondary ion mass spectrometry (SIMS), x-ray diffractometry (XRD), transmission electron microscopy (TEM), and energy dispersive

Reproduced with permission of the copyright owner. Further reproduction prohibited without permission.

spectrometry (EDS) in the TEM are used to characterize the composition and microstructure of the ZnS:Mn thin films. Brightness versus the applied voltage, luminous efficiency, and photoluminescence (PL) are used to characterize the EL devices. The figures of merit are the threshold voltage V_{th}, at which luminescence is first detected, B_{40} and η_{40}, the brightness and efficiency at 40V above the threshold voltage, respectively.

In the as-deposited ZnS:Mn phosphor, the microstructure is heavily defected with two different grain morphologies: a roughly 100nm layer of equiaxed fine grains at the insulator/phosphor interface and columnar grains with an average diameter of 89nm in the rest of the film. The EL properties of as-deposited films are poor, with a V_{th} of 125V, B_{40} of 48.7nits, and a η_{40} of 0.2275lm/W. Annealing at 700°C for 5 minutes raises B_{40} to 99.6nits and η_{40} to 0.4463lm/W, with little change in V_{th}.

In KCl doped ZnS:Mn samples, after 5 minutes of annealing at 700°C, SIMS indicates a uniform distribution of K and a complete diffusion of Cl throughout the phosphor. It is postulated that K is an interstitial while Cl substitutes a sulfur site, and Zn vacancies exist to compensate the charge. KCl co-doping enhances grain growth by improving dislocation motion, and the columnar grain size increases from 132nm to 187nm. EL properties are improved, with a B_{40} of 252nits and η_{40} of 0.9879lm/W. A slight increase in V_{th} (130V versus 125V) is observed. It is postulated that both interstitial K and substitute Cl act as donors in ZnS:Mn, to increase the hot electrons current which results in luminescence. The improved microstructure also contributes to the improved EL properties, but KCl doped samples show poor PL brightness.

In ZnS:Mn samples with Ga_2S_3, the grain growth is less than that in undoped ZnS:Mn. Energy dispersive spectrometry (EDS) data show Ga segregation to grain

Reproduced with permission of the copyright owner. Further reproduction prohibited without permission.

boundaries and triple points. Decreases of 40V in V_{th} and 10nits in B_{40} are observed from ZnS:Mn,Ga_2S_3 samples annealed at 800°C. It is postulated that Ga_2S_3 creates a range of shallow donor states at the interface close to the conduction band, which causes lower threshold voltages and "leaky" turn-on properties. The low EL brightness is attributed to the low threshold voltage, which is insufficient to accelerate the injected electrons to high energy states to efficiently impact excite the luminescent centers. On the other hand, the lack of reduction of the defects in the microstructure of ZnS:Mn,Ga_2S_3 during anneal is another reason for the poor EL properties. These defects may act as either scattering centers or trap sites for hot electrons. The improved PL brightness in these Ga_2S_3 doped samples verifies from another point of view that the problem is in the excitation process rather than the relaxation process.

When samples are doped with Ga_2S_3 first followed by KCl, much better EL properties are observed than from samples doped with KCl first followed by Ga_2S_3 (B_{40} of 120nits versus 64.2nits). This indicates that KCl can anneal out the Ga_2S_3 induced lattice defects that deteriorate the EL properties.

Reproduced with permission of the copyright owner. Further reproduction prohibited without permission.

CHAPTER 1
INTRODUCTION

The last decade in twentieth century has seen a lot of commercialized products due to breakthroughs and significant improvements in science and technology, among which the flat panel display (FPD) technologies are drawing more and more attention. FPDs are taking the place of the traditional cathode ray tube (CRT) for information display. The driving forces for this trend come from the increasing demand of portable computers, communication equipment, and other consumer electronic products. Current FPD technologies include liquid crystal displays (LCD), plasma displays (PD), field emission displays (FED), and electroluminescent displays (ELD), among which LCD covers the largest percentage of today's market [1].

The FPD technologies can be classified into two categories: non-emissive and emissive displays. In the case of non-emissive displays such as in LCDs, a back light and an array of filters and shutters are used to define a pixel. An electric field is applied to the liquid crystals shutters, which are normally made from organic molecules, to make them open or close. Because of their organic nature, LCDs have many inherent drawbacks, such as limited temperature tolerance, insufficient contrast in daylight conditions, and limited viewing angle. On the other hand, emissive displays including FED, PD and ELD have a much wider viewing angle, higher contrast, larger operation

Reproduced with permission of the copyright owner. Further reproduction prohibited without permission.

temperature range, better ruggedness and longer life span, because they are solid-state instead of liquid-state devices.

Currently, ELDs are the most prevalent display devices in the emissive category [2]. The advantages that ELDs have over the other technologies include a better ability to withstand shock and vibration. The market percentage of ELD increased in the last decade [1]. However, two main drawbacks of ELDs, insufficient color gamut and relatively high production cost, must be overcome to meet the increasing demands of the market. This calls for further research and development.

The specific ELD device that will be investigated in the present study is the thin film electroluminescence display device driven by an alternating current (a.c.) field, which is called the alternating current thin film electroluminescence device (ACTFELD). Two configurations with and without a transparent substrate of an ACTFELD are schematically shown in Figure 1.1. These devices are also called metal-insulator-semiconductor-insulator-metal (MISIM) devices. In order to understand and improve the performance of an ACTFELD, considerations from the following aspects are necessary: device structure, electrical and optical properties of the components, device physics, and the unique materials requirements for each component. These factors cannot be isolated from the others; they all interact.

The literature regarding ACTFEL devices is introduced in Chapter 2. Chapter 3 reports the experimental procedure and sample preparation. The emphasis of the present study lies on the microstructure modifications and accordingly EL performance of the phosphor layer resulting from co-doping KCl and/or Ga_2S_3. The results and discussions are presented in Chapters 4, 5, and 6. Future work is discussed in Chapter 7.

Reproduced with permission of the copyright owner. Further reproduction prohibited without permission.

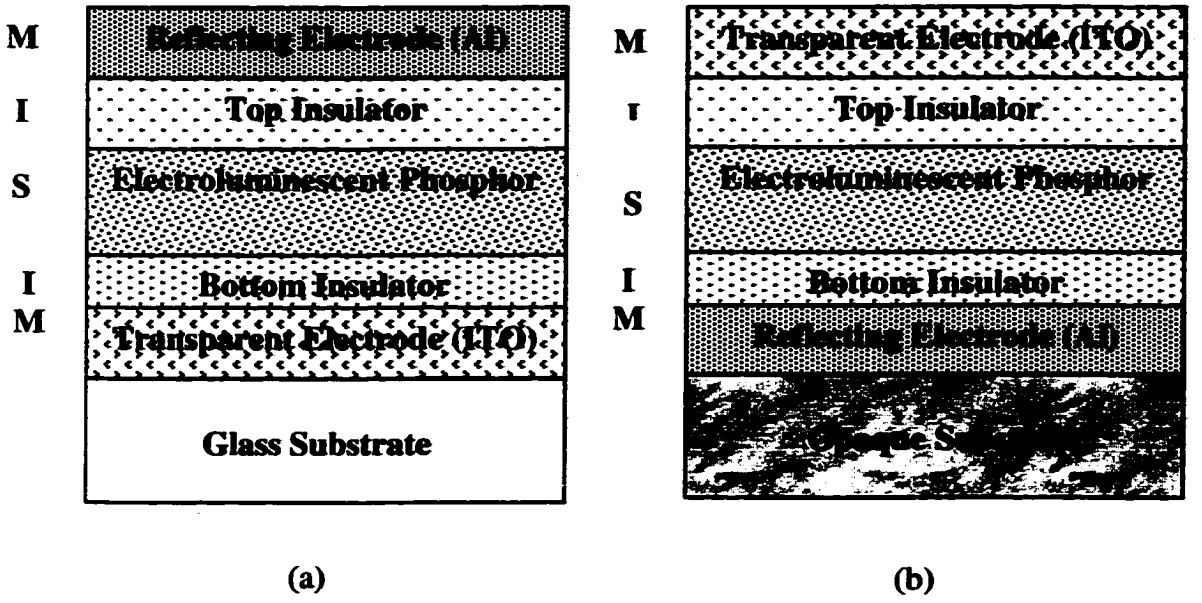

Figure 1.1 Typical structure of ACTFEL device, with (a) standard, and (b) inverted configuration.

Reproduced with permission of the copyright owner. Further reproduction prohibited without permission.

CHAPTER 2
BACKGROUND: LITERATURE REVIEW

2.1 Electroluminescence Device Physics

Electroluminescence (EL) is a phenomenon in which electrical energy is converted to luminescence energy without generating thermal energy. Basically, there are four main steps that complete the EL process [3], as shown in Figure 2.1:

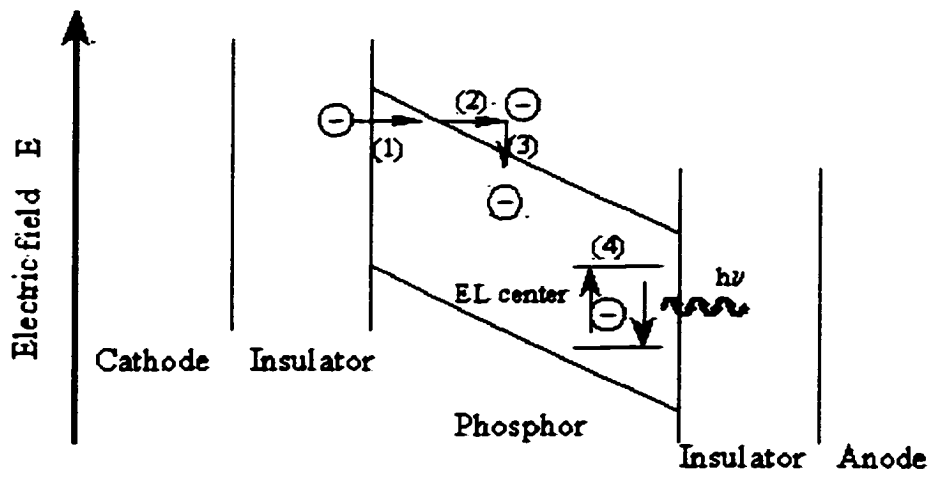

Figure 2.1 Four main steps of emission from a ACTFEL device.

(1) When the applied voltage is above the threshold voltage (the concept will be further described in section 2.1.5), electrons tunnel into the phosphor layer from the insulator/phosphor interface.

Reproduced with permission of the copyright owner. Further reproduction prohibited without permission.

(2) These electrons are accelerated in the phosphor layer by the electric field applied across the device. They are called hot electrons, carrying several electron volts of energy.

(3) The hot electrons impact excite the electrons in the luminescent centers in the phosphor layer to higher energy states.

(4) The excited electrons of the luminescent centers de-excite back to the ground state by radiative recombination, that is, by generating photons. The light is therefore observed.

2.1.1 Electron Tunneling

First, it is necessary to determine the sources of hot electrons. The source may locate at the insulator/phosphor interface or in the phosphor film. Experimental observations have indicated that in an ACTFEL device, the origin of the hot electrons is generally the insulator/phosphor interface. It has been reported that when the top and bottom insulators are from the same material, switching one material to another for both insulators brings different threshold voltages (the concept will be further addressed in section 2.1.5). When the top and bottom insulators are from different materials, the threshold field and device current are generally asymmetric [4].

The two main characteristics of the electrons at the interface are the trap depth and the density of energy states. The trap depth controls how much energy is required to tunnel electrons out of the interface, i.e, how high an external electric field must be applied to the device. A value of 1.0eV to 1.3eV has been reported to be the optimum trap depth for ACTFELD performance [5]. If the trap depth is too low, the electrons will

Reproduced with permission of the copyright owner. Further reproduction prohibited without permission.

be ejected out of the interface at a low field and will be difficult to accelerate to the high energy state necessary to efficiently excite the luminescence centers in the phosphor. If it is too high, it would take a very high electric field to achieve tunneling, which means high cost. The density of energy states is defined as the number of energy states per unit energy. Obviously, a high value of the state density is desired in an ACTFEL device.

The phosphor film may also have donor impurities that can ionize at the operating voltage. These electrons can consequently be accelerated to high energy states by the applied electric field. In this way, these donors supply additional hot electrons to impact excite the luminescent centers [6].

Electrons from the insulator/phosphor interface can be injected into the phosphor film under the applied electrical field by two mechanisms; one is thermionic emission and the other is tunneling. In thermionic emission, electrons overcome the interface energy barrier by absorbing thermal energy, which means a strong temperature dependence would be expected. Tunneling, also called Zener breakdown or field emission, is a quantum mechanical effect. When the potential barrier is not very high and the barrier is relatively narrow, which is the case when the EL device is under a relatively high external electric field, the electron wave "penetrates" the potential barrier [7], as depicted in Figure 2.1. Tunneling is independent of temperature. Since the experimental observations indicate that the ACTFEL device current is slightly temperature dependent, it is concluded that the operating mechanism of electron injection in an ACTFEL device is controlled by a thermally assisted tunneling mechanism [5].

Reproduced with permission of the copyright owner. Further reproduction prohibited without permission.

2.1.2 Electron Acceleration

It is believed that after the electrons tunnel into the phosphor layer, they are accelerated to a high kinetic energy by the applied electric field and transported to the luminescent centers to impact excite them. During the transportation, they may experience scatter and lose energy due to different causes. In an effort to understand the mechanisms, several models have been developed [8, 9, 10, 11, 12]. Basically, there are two approaches: one is based upon numerical Monte Carlo simulation [8, 9, 10], and the other is known as the lucky-drift model [11, 12].

Numerical Monte Carlo computer simulation method is widely used to model the electron transport under an applied electric field. It simulates the trajectories of a certain amount of carriers as they move under the applied electric field, subject to random scattering events caused by different electron-phonon interactions. This is achieved via calculating the electron energy distribution in a device by describing the carrier dynamics and the carrier kinetics as a function of the field. The carrier dynamics is determined by energy dispersion, and carrier kinetics is controlled by all of the possible scatters.

In 1988, Brennan performed a full band structure calculation for the density of states in the first two conduction bands and electron-photon scattering to simulate the steady-state hot electrons transport in bulk ZnS [9]. His simulation indicated that very few carriers are hot enough to sufficiently excite Mn^{2+} luminance centers in ZnS, when the applied electric field is at 10^8V/m. This obviously is not consistent with the high luminance of ZnS:Mn EL devices. Two years later, assuming a simple parabolic conduction band and polar optical phonon scattering being the only electron scattering mechanism, Mach *et al* calculated the electrons in ZnS thin film undergoing ballistic or

Reproduced with permission of the copyright owner. Further reproduction prohibited without permission.

loss-free transport [10]. Contrary to Brennan's results, their simulation indicated that extremely high-energy electrons were resulted. A more realistic ensemble Monte Carlo simulation of both transient and steady state electron transport in ZnS phosphor under high electric field is reported by Bhattacharya *et al* in 1993 [8]. They assumed a non-parabolic multi-valley band and considered polar optical phonons, acoustic phonons, inter-valley scattering, ionized impurities and neutral impurities as possible electron scattering sources.

The lucky-drift model consists of the following two modes [11,12]. The ballistic mode occurs before the electron's first collision, and the drift mode occurs after the electron has suffered one collision. In the ballistic mode, the optical-phonon mean free path λ is the product of group velocity v_g and the time interval between electron-phonon collision τ_m. In the drift mode, the energy relaxation length λ_E is determined by a field-dependent drift velocity v_d and the energy relaxation rate $1/\tau_E$. The energy loss due to electron-photon interaction can also be calculated by this model.

2.1.3 Impact Excitation

Once the hot electrons with high energy interact with the luminescent centers, the electrons of these luminescent centers can be excited out of their ground states either to a higher atomic state (impact excitation) or to the conduction band of the phosphor (impact ionization) [13]. Impact ionization is not desired in an ACTFEL device because it causes avalanche breakdown of the semiconducting phosphor film [14]. The excitation probability of the luminescent centers by hot electrons is a function of the product of the electric field in the phosphor and the mean free path of the hot electron [15].

Reproduced with permission of the copyright owner. Further reproduction prohibited without permission.

2.1.4 Photon Generation

When the luminescent centers' electrons are promoted to higher atomic states, they can de-excite back to the ground state either radiatively by generating photons or non-radiatively by generating phonons. The latter does not contribute to EL performance, since phonons are the vibrations in the phosphor lattice. The existence of a variety of lattice defects, such as interstitials, vacancies, dislocations, stacking faults, and grain boundaries, can cause problems for photon generation.

It should be noted that the radiative recombination process taking place in the phosphor films in ACTFEL devices is an atomic transition, which is localized within the luminescent center ion. An atomic transition can be either an intershell transition (d-f) or an intrashell transition (d-d, f-f), and it is determined by the quantum numbers of the initial and final states of the transition [3].

There are two basic selection rules for determining whether an optical transition is allowed. The first is called the Laporte selection rule, which states that when the change of angular momentum quantum number, Δl, is ± 1, the optical transition is allowed. The second is the spin selection rule, which says when Δs, the change in spin quantum number, is 0, the optical transition is allowed. However, some of the forbidden transitions do occur, in the occasions when asymmetry of the lattice or spin-orbit coupling exists. Taking ZnS:Mn as an example, the electron configuration is $1s^2 2s^2 2p^6 3s^2 3p^6 3d^5 4s^2$, and the transition occurs at 5d orbitals, which is a d-d intrashell transition. This transition is forbidden by the Laporte selection rule. However, since

Reproduced with permission of the copyright owner. Further reproduction prohibited without permission.

Mn^{2+} substitutes Zn^{2+} in the lattice, which does not have a center symmetry. The Laporte selection rule is therefore relaxed.

2.1.5 A Model for ACTFEL Devices

An equivalent circuit diagram for an ACTFEL device is shown in Figure 2.2. A typical a.c. trapezoidal waveform that is usually used to drive an ACTFEL device is shown in Figure 2.3. The typical used frequency is 60Hz. Before the applied voltage reaches the threshold voltage, the device is a circuit with three capacitors in series, two from the two dielectric layers and one from the phosphor layer. Above the threshold, the phosphor layer becomes two Zener diodes back to back. The threshold voltage is defined as the voltage necessary to produce the electric field at which the phosphor layer experiences a Zener breakdown, as introduced in Section 2.1.1. Normally, an ACTFEL device consists of a 1μm phosphor film sandwiched between 0.2μm dielectric layers. When the device is driven by 200 to 250V, the resulted electric field strength is 1-2 MV/cm in the phosphor layer at Zener breakdown. A model that is used to describe the EL performance of the ACTFEL devices is introduced below.

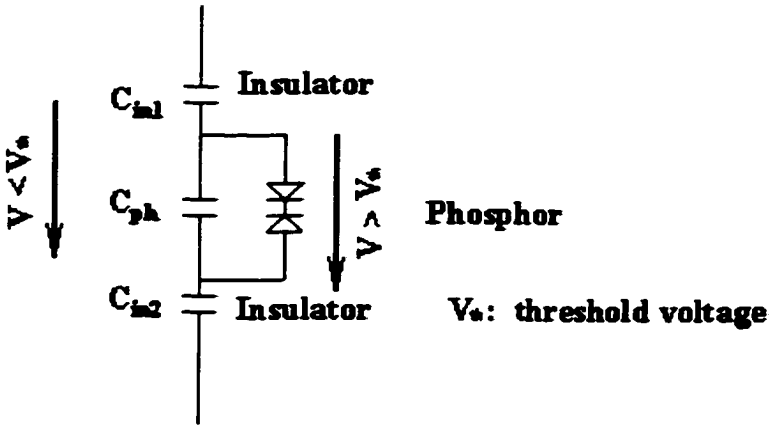

Figure 2.2 An equivalent circuit diagram of an ACTFEL device.

Reproduced with permission of the copyright owner. Further reproduction prohibited without permission.

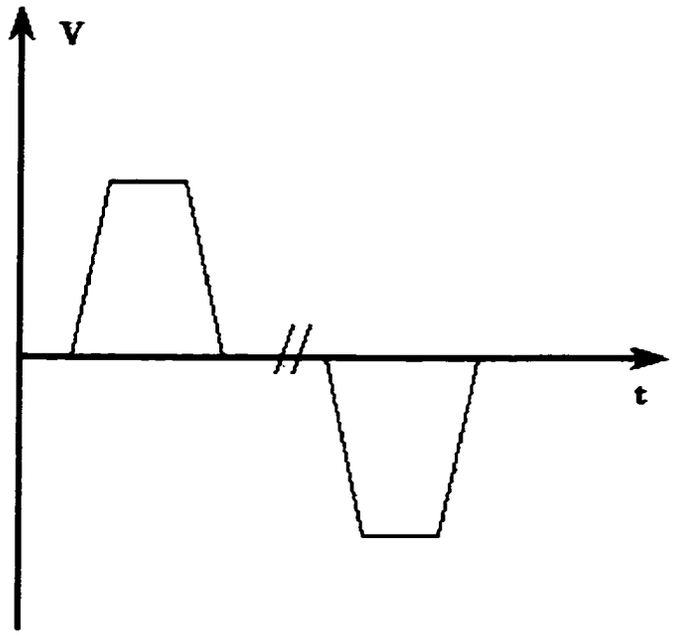

Figure 2.3 A typical a.c. trapezoidal waveform used to drive ACTFEL devices.

Before the voltage reaches the threshold voltage, the EL device is equivalent to three capacitor, C_{in1}, C_{ph}, and C_{in2} in serial. The total capacitance C is given by

$$1/C = 1/C_{in} + 1/C_{ph} = 1/C_{in1} + 1/C_{in2} + 1/C_{ph} \quad (2\text{-}1)$$

The voltage drops from the applied voltage across the EL device on phosphor and insulator layers, V_{ph} and V_{in}, respectively, are given by

$$V_{ph} = C_{in}V_a/(C_{in}+C_{ph}) \quad (2\text{-}2)$$

$$V_{in} = C_{ph}V_a/(C_{in}+C_{ph}) \quad (2\text{-}3)$$

where V_a is the applied voltage.

Above the threshold voltage, the voltages on phosphor layer and insulator layers, $V_{ph,f}$ and $V_{in,f}$, respectively, are given by

$$V_{ph,f} = V_{ph,th} = C_{in}V_{th}/(C_{in}+C_{ph}) \quad (2\text{-}4)$$

Reproduced with permission of the copyright owner. Further reproduction prohibited without permission.

$$V_{in,f} = V_a - V_{ph,f} \tag{2-5}$$

where $V_{ph,th}$ is the threshold voltage of the phosphor layer, and V_{th} is the threshold voltage of the device. It should be pointed out that Equations (2-4) and (2-5) indicate that the electric field in the phosphor layer is kept at a constant value above the threshold voltage, which is known as the clamp effect [15]. This effect has been experimentally observed in several cases. Therefore, the excess voltage is placed on the insulators. After the first pulse, the charge density transferred to the phosphor/insulator interface, ΔQ_1 is expressed as

$$\Delta Q_1 = C_{in}(V_a - V_{th}) = \int^{\infty}_{0} dt\, i_{ph,R} \tag{2-6}$$

where $i_{ph,R}$ is the current supplied by the resistive branch of the phosphor layer, and t is the time. This amount of charge generates an internal electric field in the phosphor layer, whose polarity is opposite to the electric field induced by the applied voltage. When the second pulse of the same amplitude but opposite polarity is applied to the EL device, the real electric field across the phosphor layer is the summation of the electric fields from both the applied voltage and the stored charge at the interface. The voltage across the phosphor layer is the same as given in Equation (2-4), and the transferred charge density to the insulator/phosphor interface, ΔQ_2, is given by

$$\Delta Q_2 = 2C_{in}(V_a - V_{th}) \tag{2-7}$$

Succeeding pulse with an alternating polarity will result in the same amount of transferred charge density. Therefore, in a steady-state pulse excitation, the transferred charge density ΔQ is given by

$$\Delta Q = 2C_{in}(V_a - V_{th}) \tag{2-8}$$

The brightness B is the product of the luminous efficiency η and the input power P_{in}:

Reproduced with permission of the copyright owner. Further reproduction prohibited without permission.

$$B=\eta P_{in}=\eta 2f\Delta Q V_{ph,th}=\eta 2f2C_{in}(V_a-V_{th})V_{ph,th}=4\eta fC_{in}(V_a-V_{th})V_{ph,th} \quad (2\text{-}9)$$

where the factor 2 is because the charge transfer occurs twice a cycle, and f is the frequency.

2.2 Device Characterizations of EL Devices

2.2.1 Charge-Voltage (Q-V) Diagram

A typical charge-voltage (Q-V) diagram is shown in Figure 2.4. The following information can be obtained from this measurement:

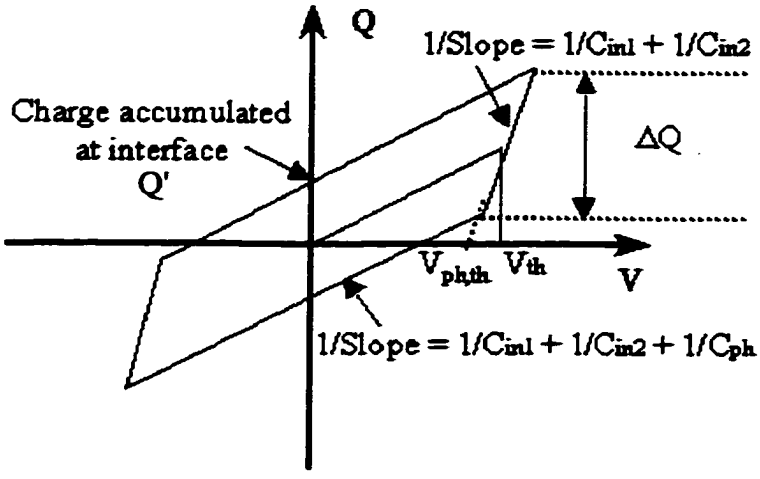

Figure 2.4 A schematic charge-voltage diagram.

(1) The threshold voltage of the device V_{th} and the threshold voltage of the phosphor layer $V_{ph,th}$;

(2) The total capacitance of the three capacitors (two insulators C_{in1} and C_{in2}, and a phosphor C_{ph}) before the voltage reaches the threshold voltage;

Reproduced with permission of the copyright owner. Further reproduction prohibited without permission.

(3) The total capacitance of the two insulator capacitors when the voltage is above the threshold voltage.

(4) The amount of charge that transports across the phosphor ΔQ, and the amount of charge that accumulates at the anode phosphor/insulator interface Q'.

(5) The total power dissipated in the device after a cycle of operation. It is the area encompassed within the Q-V diagram.

2.2.2 Brightness-Voltage (B-V) Curve

Brightness versus voltage (B-V), also called luminance versus voltage (L-V) curves, are the most important characterization methods for ACTFEL devices. The typical a.c. trapezoidal waveform that is utilized to drive the device is shown in Figure 2.3. The corresponding B-V data are schematically plotted in Figures 2.5. A B-V curve contains the following information about an EL device.

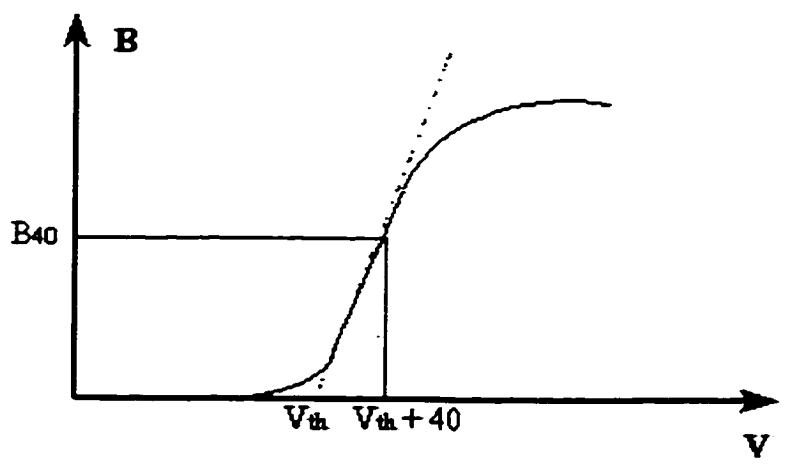

Figure 2.5 A schematic B-V plot.

(1) The threshold voltage of the device, which is the B = 0 intercept of the maximum slope tangent.

Reproduced with permission of the copyright owner. Further reproduction prohibited without permission.

(2) The B_{40} value, which is the brightness corresponding to the threshold voltage plus 40V. It is commonly used to characterize the brightness of a device.

(3) The turn-on properties of the EL device, which is presented by the maximum slope of the curve.

When one reports brightness data of an ACTFEL device, it is necessary to specify the waveform, and the a.c. frequency, since the brightness is dependent on the waveform and is proportional to the frequency. In most of the cases, a frequency of 60Hz is used [17].

2.2.3 CIE Coefficients

The Commission Internationale de l'Eclairage (CIE) coordinates, x, y, and z, are used to characterize the color of the emission [17]. Usually, x and y are obtained from the emission spectra, and z is from the relation of $x + y + z = 1$. The primary colors, blue, red and green, are achieved from a particular set of phosphors in EL displays. The color gamut of ELDs, which is achieved by the combination of the three primary colors, is characterized by plotting the coordinates (x, y) on the CIE diagram. A standard CIE diagram is shown in Figure 2.6. All the visible colors can be represented by a point with coordinates (x, y) in the area enclosed between the saturated colors and the straight line labeled "magenta". In addition, the CIE coefficient can be used to detect whether the luminescent centers and/or the host material have changed after processing stages, such as anneals and doping.

Reproduced with permission of the copyright owner. Further reproduction prohibited without permission.

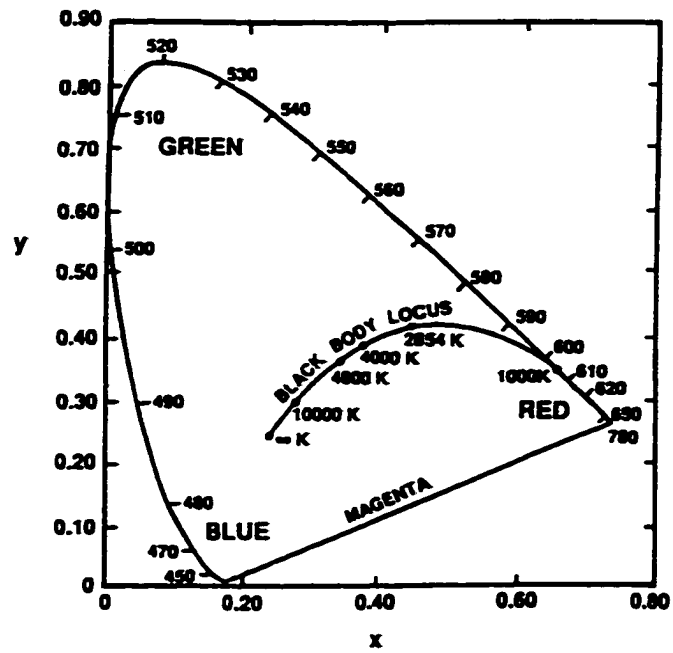

Figure 2.6 A standard CIE chromaticity diagram from reference [15].

2.2.4 Luminous Efficiency

Another important property that is used to characterize the EL performance is the luminous efficiency, η [3]. It is simply calculated by dividing the brightness measured in foot-Lambert (fL), nits (cd/m^2), or watts by power density (W), as given in Equation (2-10):

$$\eta[\mathrm{lm/W}] = L\,[\mathrm{cd/m^2}]/P_{in}\,[\mathrm{W/m^2}] \qquad (2\text{-}10)$$

Luminous efficiency characterizes how much of the applied electric energy has been converted to light.

Reproduced with permission of the copyright owner. Further reproduction prohibited without permission.

2.3 Material Requirements for EL Devices

Realizing how EL devices work, it is the task for material scientists to select proper materials, fabricate the devices and improve their performance. As depicted in Figure 1.1, there are four kinds of materials that make up a complete EL device, which are substrate, insulators, phosphor, and electrodes. Each of them will be discussed in this section.

2.3.1 Substrate

Depending on the viewing direction, the substrate can be either transparent or opaque. Since the substrate is the starting point of the whole device fabrication, and all the layers that will be deposited onto it have relatively small thickness values, a basic requirement is that the substrate should be smooth. Normally, Corning 7059 glass and silicon are used as substrates for standard and inverted ACTFEL devices, respectively.

First of all, Corning 7059 glass is cost effective. Secondly, it has no alkali metals that have high diffusivities. However, one disadvantage is its relatively low glass transition temperature, 598°C [3], which limits the post-deposition anneal conditions of the phosphor layer. Post deposition anneal is important to all ACTFEL devices, because significant improvement in EL performance has been widely reported. Moreover, the higher the annealing temperature, the better the results are. This will be discussed in detail in later sections. Some efforts have been made to use ceramic materials as substrates, because they are much more high temperature tolerant. However, two factors limit their commercialization to date. One is the much higher cost, not only from the

Reproduced with permission of the copyright owner. Further reproduction prohibited without permission.

materials, but also from the inevitable polishing procedure. The other is the bad pixel resolution due to the surface roughness. It is reported that the resolution is only about 100μm [3], while the resolution of a glass substrate device can reach 25μm [2].

2.3.2 Electrodes

There are two electrodes in an ACTFEL device in either configuration; one is transparent and the other is reflective, as illustrated in Figure 1.1. The challenge is the transparent electrode, in terms of material selection. Conductive materials, such as metallic materials, are normally opaque to visible light. It is because the interband transition in them requires a relatively low energy, which causes strong absorption of the light. On the other hand, almost all of the insulators are transparent in the region from infrared to ultraviolet, because they have empty conduction bands and completely filled valence bands. In addition, the band gap in an insulator is very wide, so that the interband transitions are hard to occur. For semiconductors, the transition depends on whether they are intrinsic or extrinsic. Intrinsic semiconductors behave very much the same as the insulators, except that the band gap is normally narrower. In the case of extrinsic semiconductors, because of the existence of either donors or acceptors, some energy states are introduced into the band gap. As a result, optical transitions from or to these states may occur, which causes absorption, especially in the infrared region.

The most commonly used transparent electrode material is indium tin oxide (ITO), whose sheet resistivity is 5Ω/□. The conductivity comes from the large amount of shallow donors located only about 30meV below the conduction band. They can be thermally activated into the conduction band at room temperature. It is believed that

Reproduced with permission of the copyright owner. Further reproduction prohibited without permission.

these donors are the Sn^{+4} ions substituting In^{+3} ions, and O^{-2} vacancies plus intentionally doped F^- ions [3]. Other possible candidates for transparent electrodes can be ZnO and ZnO:(Al,In,Ga).

The most widely used reflective electrode is aluminum, which has good conductivity, high reflectivity, and high electromigration resistance under a high electric field [18]. If a high temperature (above the melting point of aluminum, 660°C) processing step cannot be avoid during packaging, molybdenum and tungsten are the promising candidates.

2.3.3 Insulators

As introduced before, the electric field in an ACTFEL device within the phosphor layer can be as high as 1-2 MV/cm during operation. Therefore, the insulators must have the following properties:

(1) A high dielectric constant is necessary to maximize the voltage drop across the phosphor layer. It is known that the applied voltage can be expressed as

$$V_a = E_{in}d_{in} + E_{ph}d_{ph} \tag{2-11}$$

where E_{in} and E_{ph} are the electric field in insulators and phosphor, respectively, and d_{in} and d_{ph} are the layer thickness of insulators and phosphor, respectively. Knowing that before reaching the threshold voltage, Maxwell's equations are satisfied:

$$\varepsilon_0\varepsilon_{in}E_{in} = \varepsilon_0\varepsilon_{ph}E_{ph} \tag{2-12}$$

where ε_0 and ε_{in} are the dielectric constant of vacuum and the relative dielectric constant of insulating layer material, respectively, and ε_{ph} is the relative dielectric

Reproduced with permission of the copyright owner. Further reproduction prohibited without permission.

constant of the phosphor layer. Therefore, the voltage across the phosphor layer is given by

$$V_{ph} = E_{ph}d_{ph} = \varepsilon_{in}d_{ph}Va/(\varepsilon_{in}d_{ph} + \varepsilon_{ph}d_{in}) \qquad (2\text{-}13)$$

(2) A high electric field strength to avoid dielectric breakdown. As introduced in section 2.1.5, the excessive voltage above the threshold voltage goes to the insulator layer, due to clamp effect.

Besides these, thickness uniformity of the insulators is critical. As indicated by Equation (2-13), the lower the insulator thickness, the higher the voltage drop across the phosphor is resulted. Therefore, insulators normally have very low thickness, about 200 to 300nm. At this thickness, a pinhole or non-uniformity in thickness can be extremely dangerous, because a localized breakdown can be fatal to the device [3].

2.3.4 Phosphor

The phosphor is the material that converts other energy into light. The excitation energy can be in different forms, such as electrical, thermal, or optical. In an ACTFEL device, the phosphor has two components: (1) the host material that dominates the electrical properties, and (2) the luminescent center that determines the optical properties. The radiative recombination occurring in the phosphor layer in an ACTFEL device is an atomic transition. Different from a donor-acceptor recombination, an atomic transition is localized within the luminescent center. To achieve this, the host lattice and the luminescent centers must satisfy certain requirements, as discussed below.

Reproduced with permission of the copyright owner. Further reproduction prohibited without permission.

2.3.4.1 Host material

First of all, the band gap energy of the host material must be larger than the energy for photon generation; otherwise the applied electric field will excite the electrons from valence band to conduction band, leaving holes in the valence band without generating photons. It has been shown that the two main characteristics of the electrons at the insulator/phosphor interface, the density of energy states and the trap depth, are determined by the phosphor host material in most of the cases [15]. In other words, the host material controls the "turn-on" properties. After the electrons are injected into the phosphor, they must be accelerated to sufficiently high energy states to impact excite the luminescent centers. The excitation probability is a function of the product of electron mean free path and the electric field in the phosphor layer. Therefore, the host material must have minimum lattice defects and high dielectric breakdown strength. Any kind of lattice defects, such as vacancies, dislocations, stacking fault, sub-grain boundaries, and grain boundaries, can act as non-radiative emission sites and/or the trap sites to the hot electrons. Post-deposition annealing is widely carried out to decrease the defect density in the host lattice.

2.3.4.2 Luminescent centers

Most of the available luminescent centers are transition and rare earth elements. Depending on the electron structure of the luminescent center, the localized radiative recombination can be either intrashell or intershell transition. One of the most important characteristics of the luminescent centers is the atomic transition energy, which dictates the color of the phosphor. Another property is the impact excitation cross section,

Reproduced with permission of the copyright owner. Further reproduction prohibited without permission.

because the EL efficiency is proportional to it. A good approximation of the impact cross section is the geometric diameter of the luminescent center ion. A larger cross section is desired. Incorporation of a complex instead of a simple ion increases the impact cross section. A good example is in ZnS:TbOF system, where a TbOF complex, instead of a simple Tb^{3+} ion, is introduced as the luminous center.

2.3.4.3 Luminescent center host interaction

Because the concentration of the luminescent centers is always less than 5at% [19], the phosphor is essentially a substitutional solid solution with the host being the solvent and the luminescent center being the solute. It is desirable for the solubility of the luminescent center in the host to be higher than the required concentration. The internal strains resulting from the incorporation of the luminescent center should be minimized, which means the center and the host species should have comparable ionic radii. Charge neutrality is another requirement that needs to be satisfied, which is often achieved by compensating with a co-dopant.

If the luminescent center is a transition metal, the radiative transition will follow the intrashell transition mechanism in the d-orbitals. By checking the electron configurations of these ions, the outer d orbitals are not shielded from the lattice by any other orbitals. Therefore, the local host environment, such as crystal field, will affect the transition. As an example, the electron configuration in manganese is $1s^2 2s^2 2p^6 3s^2 3p^6 3d^5 4s^2$. The radiative transition occurs in 3d-orbitals, which are the outer ones. In this case, an improvement in the host lattice significantly improves the EL performance, as will be discussed later in Chapter 4.

Reproduced with permission of the copyright owner. Further reproduction prohibited without permission.

When the luminescent centers are rare earth ions, sometimes both intershell 5d-4f and intrashell 4f-4f transitions are possible. Since 4f-orbitals are shielded from the host by 5d-orbitals, it is argued that this type of intrashell transition is relatively immune to the host environment. However, a decrease in defect density will also improve the EL properties because there would be fewer trap sites and scatter centers for hot electrons when they are transported from cathode to anode by the applied electric field, i.e., the excitation probability will be increased.

The complexity of the outer energy levels of the ions after they form the ionic compound must be considered, since the nearby ions may affect the energy levels. In addition, the symmetry of the lattice, the symmetry of the orbitals, the ion spacing, and the molecular orbital overlap must be considered carefully as well.

In general, most of the host materials for ACTFEL device are sulfides, among which ZnS is the most widely investigated one. ZnS has a band gap energy of 3.7eV at 300K [20], which is larger than the blue photon energy of 3.1eV. Its dielectric field is about 1MV/cm. Besides, it has a very high density of energy states and the trap depth is around 1.0eV to 1.3eV. Table 2.1 summarizes some of the ACTFEL phosphor materials and device performance [3].

2.4 ZnS:Mn System

ZnS:Mn is the most widely investigated and the most successful yellow phosphor material with the emission peak at 485nm. The optimum concentration of Mn^{2+} is 1 to 2mol%, which is lower than the solubility of Mn in ZnS [19, 21]. In addition, Mn^{2+} ions

Reproduced with permission of the copyright owner. Further reproduction prohibited without permission.

are easy to incorporate into the ZnS lattice by substituting Zn^{2+} ions, because they have similar ionic radii (Zn^{2+} = 0.74Å, and Mn^{2+} = 0.80Å) and the same valence. In general, ZnS:Mn thin film EL devices have high brightness, high luminous efficiency and long life span [2]. The device performance is also briefly summarized in Table 2.1.

Table 2.1 ACTFEL Phosphor Materials and Device Performance [3].

Posphor Material	Color	Luminance L_{40} at 60Hz (cd/m^2)	Efficiency (lm/W)	Peak Wavelength (nm)	CIE coordinates	
					x	y
ZnS:Mn	yellow	300	5	585	0.65	0.35
ZnS:Mn/filter	red	70	0.8	610	0.65	0.35
ZnS:Sm, Cl	red	12	0.08	650	0.64	0.35
CaS:Eu	red	12	0.05	650	0.68	0.31
CaSSe:Eu	red	25	0.25	620	0.66	0.33
ZnS:TbOF	green	100	1.3	545	0.3	0.6
ZnS:Tb	green	90	0.6	545	0.3	0.6
CaS:Ce, Cl	green	10	0.1	505	0.27	0.53
ZnGa2O4:Mn	green	10	0.2	501	0.68	0.08
Zn2SiO4:Mn	green	10	0.2	510	0.68	0.15
SrS:Ce, F	blue-green	16	0.4	478	0.37	0.17
SrS:Ce, Mn,Cl	blue-green	105	1.63	508	0.5	0.3
SrS:Ce	blue-green	100	0.8	515	0.5	0.3
SrS:Ce/filter	blue	10	0.1	480	0.18	0.13
ZnS:Tm,F	blue	0.2	<0.01	450	0.15	0.15
SrGa2S4:Ce	blue	5	0.02	445	0.15	0.1
CaGa2S4:Ce	blue	10	0.04	460	0.15	0.19
SrS:Ce, Eu	white	36	0.2	490	0.37	0.39
ZnS:Mn/SrS:Ce	white	450	1.6	580	0.42	0.48

2.4.1 Microstructure of ZnS and ZnS:Mn

Figure 2.7 shows the Zn-S binary phase diagram. The ZnS compound has two different crystal structures, hexagonal (wurtzite) and cubic (saphalerite or zinc blende),

Reproduced with permission of the copyright owner. Further reproduction prohibited without permission.

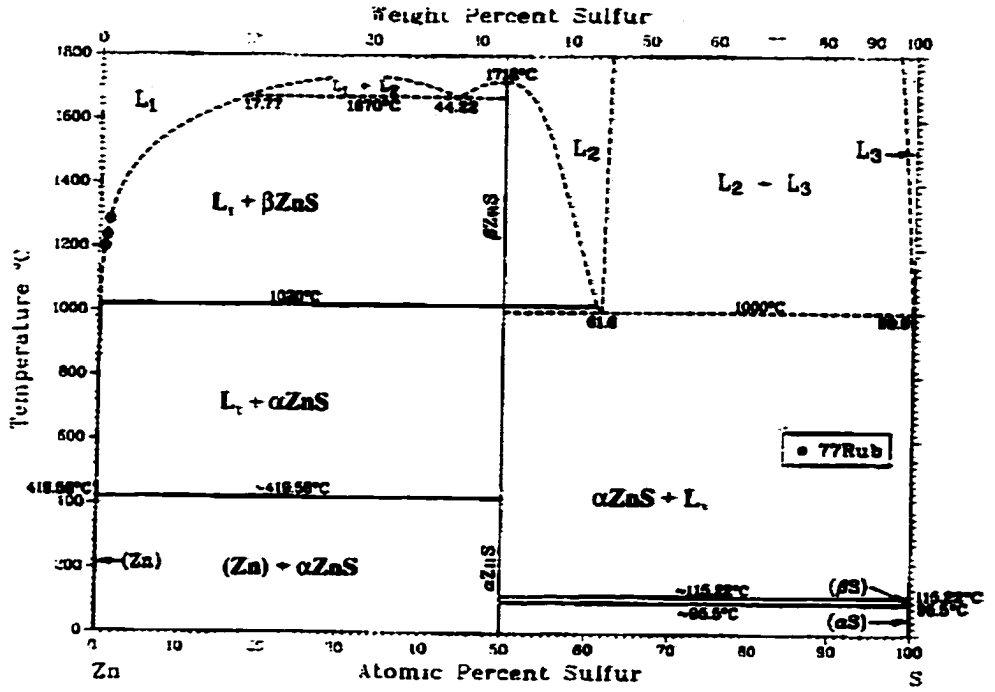

.Figure 2.7 The phase diagram of Zn-S system.

with the former being stable at temperatures above 1024°C [22]. Incorporation of manganese and iron ions in ZnS tends to reduce the temperature of cubic-hexagonal transition [22]. A unit cell of ZnS with zinc blende structure is shown in Figure 2.8. More commonly, people use [110] projection of (111) planes to symbolize the structure, as illustrated in Figure 2.9. From this pattern, it is clear to see the following characteristics of the ZnS compound in it cubic structure:

(1). (-111) planes, which are normal to the paper plane and appear as horizontal lines, are not equally separated, when the pattern is examined along the [-111] direction.

(2). The stacking sequence of the (-111) planes is AaBbCcAaBbCc..... The atoms in A and a, B and b, C and c layers are aligned along the [-111] direction, which means when

Reproduced with permission of the copyright owner. Further reproduction prohibited without permission.

viewed along this direction, atoms project on top of each other. Also, these planes are widely separated, but a and B, b and C, and c and A planes are narrowly separated.

(3). A and a, B and b, and C and c planes contain Zn^{2+} and S^{2-}, respectively, thus {-111} and {1-1-1} planes are nonequivalent.

It is well known that good crystallinity is desired for good EL performance [19]. However, most of the polycrystalline ZnS films contain a lot of lattice defects, such as point defects, dislocations, stacking faults and polytypism. It is generally assumed that these defects can be electronically active, causing poor device performance.

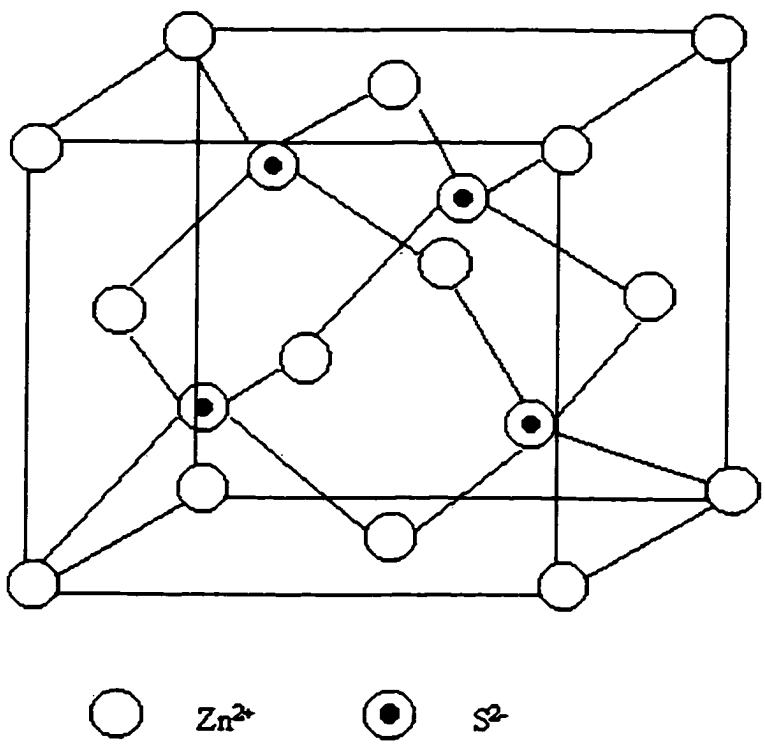

Figure 2.8 A unit cell of cubic ZnS compound.

Reproduced with permission of the copyright owner. Further reproduction prohibited without permission.

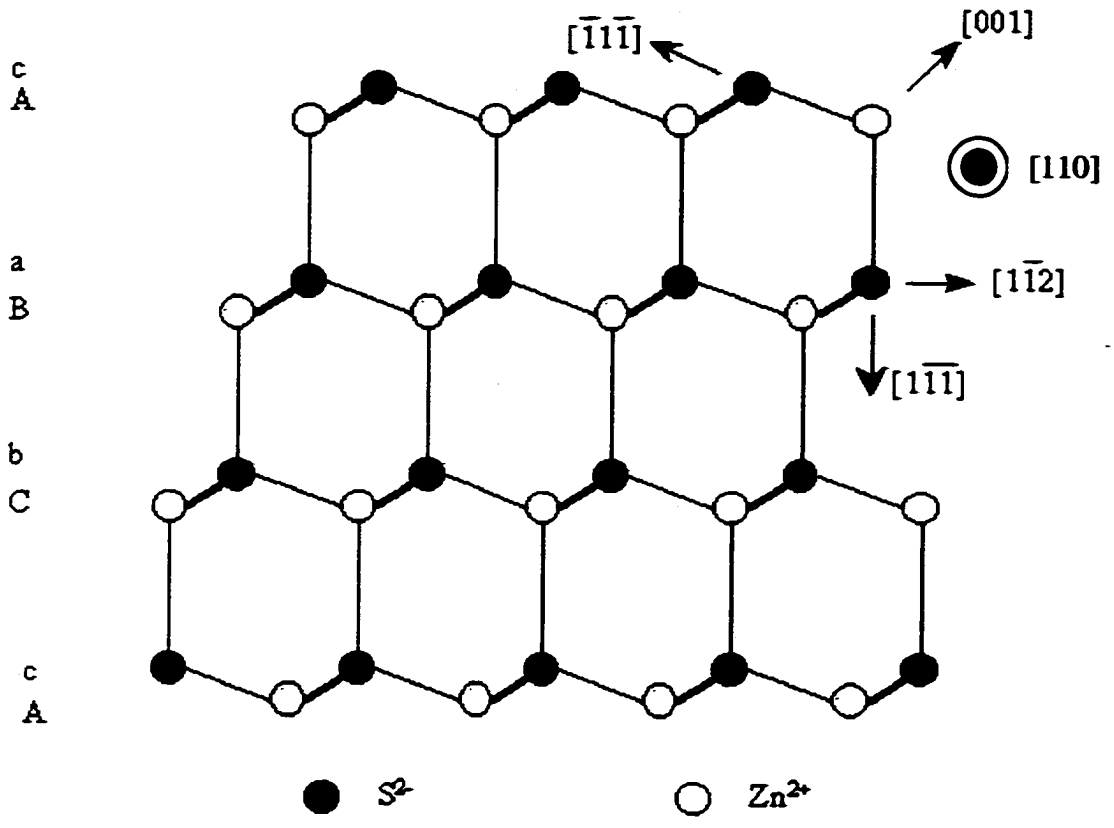

Figure 2.9 Atom locations in the (111) planes looking along the [110] direction in a zinc blende structure.

Point defects can be either vacancies or interstitials. Due to the fact that there are more than one species in the ZnS compound, the point defects can be complex. Vacancies can form on both the sulfur and the zinc lattices. Likewise, both sulfur and zinc interstitials can exist. In addition, anti-site defects, which are unique to compounds, can also form, such as when a sulfur atom takes the position of a zinc atom, resulting in the configuration of a sulfur bonded with other four sulfur atoms. The electronic properties of point defects in compound semiconductors are not fully understood because of the variety [23].

Reproduced with permission of the copyright owner. Further reproduction prohibited without permission.

Dislocations are the two-dimensional defects in atom packing. In cubic structure, perfect dislocations usually have a Burgers vector of a/2[110], and their slip planes are {111} planes. If the slip planes are the narrowly spaced (-111) planes, the dislocations are termed as "glide sets", otherwise they are called "shuffle sets" [24, 25]. Specifically, if the dislocation terminates on a (-111) plane that contains group V or group VI atoms, it is called an α dislocation. If it terminates on a group II or group III atom plane, it is called a β dislocation [26]. Normally, these two types of dislocations do not have the same mobility. Therefore, there are actually four different kinds of perfect dislocations in compounds with zinc blends structure. In the case of ZnS, due to its low stacking fault energy (SFE), perfect glide set dislocations tend to dissociate into two partials with a Burgers vector of a/6[2-1-1]. For example, a/2[1-10] = a/6[2-1-1] + a/6[1-21]. A typical dissociation that has been observed and widely reported is the dissociation of the native 60° dislocations into a 30° and a 90° partials [24, 27, 28]. Attempts have been made to determine experimentally the energy level of the dislocations in compound semiconductors, but the results are not conclusive due to the co-existence of point defects [29, 30]. Calculations of the dislocation energy states in GaAs are presented by Jones *et al* [31], which indicate that the energy level are related to the nature of the dislocation.

Because of the low SFE, it is easy to form stacking faults and twins in ZnS. The faulting planes are always {111}, the most close packed planes in zinc blende and wurtzite structures. Contrary to single element materials, in a binary compound like ZnS, a stacking fault can be considered as a two-layer-thick micro-twin, simply because its {111} planes may be either zinc or sulfur. Unlike dislocations, stacking faults, and point defects, which generate dangling bonds, twins do not, since the faulted and un-faulted

Reproduced with permission of the copyright owner. Further reproduction prohibited without permission.

regions are coherently bonded to each other. Therefore, it is argued that coherent twin boundaries in compound semiconductors are not electrically active.

Another microstructure characteristic of ZnS is a phenomenon called polytypism. It results from the ability of a substance to crystallize in different modifications, in which two dimensions of the unit cell are the same while the third is a variable integral multiple of a common unit [32]. The difference between polytypism and polymorphism is that the latter is used to describe a material having different crystal structures. Obviously, there should be significant density and entropy differences between two polymorphs. In the case of polytypes, the differences in the internal energy are negligible, and the difference in structure of two polytypes is often due to a few stacking faults. The unit of a polytype may range from two layers of {111} to more than one hundred {111} planes [32].

The grain boundaries in polycrystalline ZnS and ZnS:Mn materials can be considered as an array of dislocations. If the dislocation spacing is smaller than the core dimension, it is a high angle grain boundary; otherwise it is a low angle boundary. As a result, the electrical properties of the grain boundaries can be treated in the same way as those of dislocations.

2.4.2 ZnS:Mn ACTFEL Devices

ZnS:Mn thin films have been deposited using various techniques, such as electron beam (e-beam) evaporation [33], co-evaporation [34], thermal evaporation [35], sputtering [36, 37, 38], atomic layer epitaxy (ALE) [39, 40], metal-organic chemical vapor deposition (MOCVD) [41, 42, 43, 44], multi-source deposition [45], and halide-transport chemical vapor deposition (HTCVD) [46]. Physical deposition (PVD) methods

Reproduced with permission of the copyright owner. Further reproduction prohibited without permission.

are good for growth of uniform thin films over a large area at high rates, while chemical vapor deposition (CVD) techniques produce good crystallinity, a lower defect density and a larger grain size.

As introduced earlier, the first step of the ACTFEL device operation is the injection of electrons into the phosphor layer from the insulator/phosphor interface. This process is dominated by the density of the interface states and the trapping depths. These properties are characteristics of the phosphor layer, although the insulators may play a role. Petre *et al* used optical charging spectroscopy and thermally stimulated depolarization measurements on a Au/Al_2O_3/ZnS:Mn/Al_2O_3/ITO/glass device to quantify the interface trapping states [35]. The phosphor film was deposited by thermal evaporation. Two groups of trapping levels were determined at the insulator/phosphor interface, centered at depths of 0.55eV and 0.875eV in the band gap of ZnS:Mn films. The concentration of these states is higher at the bottom interface than at the top, although both top and bottom insulators are the same materials. However, they did not determine whether those trapping states were donor or acceptor type.

Experimental observations also verified that the hot electrons accelerated by the external electric field play an important role in exciting Mn^{2+} centers [43]. Electro-photoluminescence (EPL), which is basically doing PL when the device is under a certain external electric field, was performed on ZnS:Mn MISIM devices. The results were compared with the conventional PL intensity. It is shown that the EPL intensity of the ZnS:Mn MISIM device exceeded the PL intensity of a ZnS:Mn by an order of magnitude.

Poor EL efficiencies can be caused by poor crystal quality, a low number of hot electrons for impact excitation, too low or too high concentration of the luminescence

Reproduced with permission of the copyright owner. Further reproduction prohibited without permission.

centers, and/or a small collision cross section for excitation of the luminescent center [46]. Also, since the 3d-orbitals of Mn^{2+} are not shielded from the host lattice, the defects in ZnS host lattice may also cause non-radiative emission. In fact, improved crystallinity improves every aspect mentioned above. Thus, crystallinity is very important to the EL performance of this system. Crystallinity is a fairly general term, covering defects, defect density, texture, grain size and grain size distribution, etc. Hot electrons can be generated by either ejection from insulator/phosphor interface states or from co-dopants within the phosphor film.

The desired microstructure of polycrystalline ZnS:Mn for an ACTFEL device consists of the largest columnar grains extending the entire film thickness with the grains having the lowest defect density. With this microstructure, electrons injected into the phosphor layer from the cathode insulator/phosphor interface may move at high speed towards the anode insulator/phosphor interface with a low probability of impact on grain boundaries or other defects. The probability of non-radiative recombination will be reduced as well. However, the as-deposited films produced by sputtering, e-beam evaporation, and other PVD methods usually have a layer composed of tiny equiaxed grains close to the substrate interface. This is the so-called "dead layer", because in this region the electrons do not have sufficient mean free path to excite the Mn^{2+} luminescent centers [33]. In other words, the grain size in this layer is smaller than the mean free path of the hot electrons. So, the existence of a “dead layer” causes both low brightness and low luminous efficiency. It is believed that the formation of the "dead layer" occurs during the nucleation stage of the film. However, the "dead layer" does not form in films made by CVD methods [44].

Reproduced with permission of the copyright owner. Further reproduction prohibited without permission.

In all PVD and some CVD depositions, thin film starts from heterogeneous nucleation, which means the substrate or the sub-layer material must be taken into account. Nucleation is closely related to the film/substrate interface energy. Ihanus *et al* presented data on the effects of the substrate on the nucleation of ZnS films [40]. Atomic force microscopy (AFM) was employed to investigate the nucleation of films deposited by ALE. The nucleation density was found to be much higher on glass than on mica, because the cleavage of mica along its basal plane produces a nearly defect-free surface, whereas the glass surface is more heterogeneous. Film crystallinity on mica is much better than on glass based upon XRD analysis. It is suggested that the film growth on mica is more like "layer-by-layer" deposition.

Texture is another issue concerning the crystallinity of phosphor films. Generally, texture in thin film is related to substrate materials, growth temperature and growth rate. There is normally a texture developed during the growth of the film, which is called growth texture. Post-deposition anneals may modify the growth texture. Nakanishi and his coworkers investigated the dependence of texture on film thickness of ZnS:Mn made by e-beam evaporation on a Y_2O_3 sub-layer on film thickness [33]. The polycrystalline Y_2O_3 substrate has a (100) fiber texture. Reflection high-energy electron diffraction (RHEED) indicated that (100) texture was observed in the first stage of the phosphor film growth. When the film thickness was about 50nm, a texture transition from (100) to (111) occurred. Beyond this thickness, (111) fiber texture dominated. It was also argued that the first 50nm of the film actually formed the dead layer. Shift in texture has also been reported [46]. Blackmore and coworker reported that ZnS thin film deposited by sputtering onto glass has a strong (111) preferred orientation and the extent of the

Reproduced with permission of the copyright owner. Further reproduction prohibited without permission.

preferred growth is dependent on the growth atmosphere [37]. Besides the effect of texture on crystallinity, it also influences the electric properties of the host material, since different crystallographic orientations correspond to different local crystal fields. For ZnS:Mn thin films with h(0002) and/or c(111) texture versus films with c(311) texture, the conduction charge, that is, the total charge transported across the phosphor film during a voltage pulse, can be measured from charge-phosphor field strength curves. This conduction charge is proportional to the number of electrons that tunnel out of the trap states located at the insulator/phosphor interface. Thus, it is sensitive to the distribution of interface energy states. The results reported by Chen *et al* indicate that the conduction charge in c(311) textured film is twice as much as that in c(111) and/or h(0002) textured film [46]. Apparently, the less dense growth planes of the c(311) films result in more interface states. The basic difference between c(111) and/or h(0002) texture and c(311) texture is that growth along c(111) and/or h(0002) planes proceeds by alternating layers of one species followed by the other, while growth in the c(311) direction is along atomic planes populated by both Zn and S.

Post-deposition annealing has been proved to improve the crystallinity, such as to reduce the defect density and increase the grain size. However, the diffusion between layers of a multi-layered structure device should be a concern. Blackmoor *et al* pointed out that in ZnS:Mn film deposited on a cadmium stannate (CS) substrate by radio frequency (RF) sputtering, annealing at 450°C caused extensive cadmium penetration into the ZnS:Mn as well as zinc and manganese penetration into the CS [36]. The EL properties of these devices were not satisfactory. To avoid this kind of diffusion, co-dopants are introduced into the film to achieve the grain growth at a lower temperature

Reproduced with permission of the copyright owner. Further reproduction prohibited without permission.

where diffusion does not occur. This is also one of the objectives of this current study. Another factor that contributes to good EL performance is the incorporation of Mn^{2+} ions into the ZnS host lattice. It is widely accepted that there is an optimum concentration of Mn^{2+} ions. If the Mn^{2+} concentration is too low, there are not sufficient luminescent centers to excite. If the Mn^{2+} concentration is too high, a phenomenon called "concentration quenching" will occur [47]. The reason for this phenomenon is the three-dimensional coupling between Mn^{2+} ions and non-radiative defects. It is assumed that an excited Mn^{2+} center can transfer energy to an unexcited one through a resonant, non-radiative transfer process. To avoid concentration quenching, Mn^{2+} ions were δ-doped into ZnS [47, 48 and 49], that is, Mn^{2+} ions were doped in separated atomic layers. It was concluded that a distance of about 10nm between the doping planes was large enough to avoid three-dimensional coupling between the Mn^{2+} ions, which resulted in significant luminescence quenching in ZnS:Mn phosphor films grown by MOCVD.

Crystallinity can be characterized either directly or indirectly. The microscopy techniques, including scanning electron microscopy (SEM), transmission electron microscopy (TEM), and atomic force microscopy (AFM), belong to the direct characterization methods, while any microstructure-related property measurement belongs to the indirect category. SEM and AFM are mostly used to supply the morphology image of a free surface or sometimes the fracture surface. The grain size in plan-view or cross-sectional directions can also be roughly measured [40, 44, 45, and 50] by SEM and AFM. TEM is capable of providing much more information on crystallinity, such as grain size, grain size distribution, texture, sub-grain features, defects, even composition if it has an X-ray energy dispersive spectrometry (EDS) detector connected

Reproduced with permission of the copyright owner. Further reproduction prohibited without permission.

to it [19, 26, 51, 52]. XRD, photoluminescence (PL), and cathodoluminescence (CL) are three of the most commonly used indirect ways to investigate crystallinity.

XRD is a universal method to characterize crystallinity. It provides information on crystal structure, grain orientations, averaged crystallite size and internal strains. CL and PL are more often used for semiconductors. Both of PL and CL can be collected at either room temperature or lower temperature by using cold stages. The CL process is generating luminescence from the recombination of excess electrons with excess holes in a direct-band-gap semiconductor. It is detected by a photo-detector. The radiative recombination occurs within the nearly perfect regions of the crystal, whereas the non-radiative recombination takes place at electrically active defects. By measuring the CL intensity across a surface, it is possible to map the distribution of the defective areas. The lateral resolution depends on the size of the electron beam that is used to excite the luminescence. Therefore, when CL is installed in an electron microscope, such as an SEM [50] or a TEM [51, 52], the resolution can be increased. For instance, CL in TEM can have a resolution as high as 0.4nm. Moreover, the electron beam acceleration voltage can easily go to 100kV. Mitsui *et al.* reported their work on structural defect characterization in MBE made ZnS and ZnSe by CL in TEM [19]. First, the spectrum from all the recombinations occurring during CL was obtained, then a certain wavelength corresponding to a certain peak was chosen to get monochromatic CL image. This wavelength has the characteristics of the energy levels involved in recombination. Combining the defect information from both the TEM image and the monochromatic CL image, the nature of the recombination and its locations was detected. The correlation between microstructural defects and certain recombination was achieved. For example,

Reproduced with permission of the copyright owner. Further reproduction prohibited without permission.

in ZnS thin films, areas with low densities of stacking faults were observed to have neutral acceptor to bond exciton transition, whereas the areas with a high density of stacking faults gave rise to free electron and ionize acceptor transitions.

When a semiconductor is irradiated by light with energy greater than its band gap energy, excess carriers can recombine radiatively and non-radiatively. This phenomenon of light emission is photoluminescence (PL). It differs from CL in that the source that generates excess carriers. Figure 2.10 schematically summarizes the possible electron-hole recombination paths. There can be band-to-band (B-B), donor-to-valence (D-V), conduction donor-to-acceptors (D-A), and conduction band-to-acceptor (C-A) recombinations.

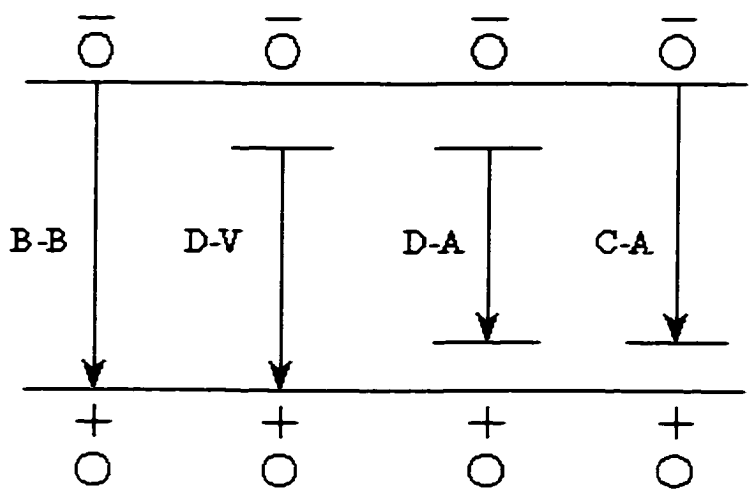

Figure 2.10 The possible electron-hole recombination paths.

The wavelengths corresponding to different recombination paths are recorded during PL measurement. PL can be carried out with or without an external electric field applying to the device [43]. When the light source has higher energy than the band gap energy of the semiconductor, band gap emission becomes possible. By comparison the

Reproduced with permission of the copyright owner. Further reproduction prohibited without permission.

relative intensity of the band gap emission to the self-activated emission intensity, the general crystal quality can be detected [47]. In Kina *et al*'s work, He:Cd laser with a wavelength of 325nm was used to excite PL from both pure ZnS and ZnS:Mn at 11K [44]. The peak at 460nm from both samples was believed to be due to the self-activated (SA) emission, resulted from the combination of Zn vacancy and the co-activator situated at the nearest lattice point from the Zn vacancy. It was reported that the sample with the lowest Zn vacancy density has the weakest SA emission peak. In addition, the peak shift in PL is a mark of charge in crystal field. Reference [44] also pointed out that the PL peak shift corresponded to the difference in texture.

Photoluminescence does not only produce information regarding crystallinity, it can also be used to detect other luminescent center related properties as well. For instance, if the PL brightness is much intenser than the EL brightness, it is suggested that either there are not sufficient hot electrons in the phosphor, or the excitation probability is low. The high PL intensity indicates that there are plenty of luminescent centers that can be excited and de-excited radiatively in the phosphor film. Combined with other electrical characterization techniques, the real reason behind low EL brightness can be determined [53]. Wang *et al* used PL to investigate the aging mechanism of ZnS:Mn ACTFEL devices. The sharp decrease in PL intensity from aged sample compared to fresh sample indicated that the aging process changed the properties of Mn^{2+} luminescent centers [54].

Lastly, with respect to the aging mechanism of ZnS:Mn phosphor with heavier Mn^{2+} doping, lower EL brightness and a shift to higher threshold voltage could be found after 100 hours of performance. It has been reported that aging was due to the water

Reproduced with permission of the copyright owner. Further reproduction prohibited without permission.

absorbed on the film surface [54]. The Mn^{2+} ions reacted with the moisture that diffused from the environment into the EL structure, and formed a deep level trap. This trap behaved like a non-radiative center. In addition, it captured some hot electrons tunneled from the phosphor/insulator interface, resulting a higher threshold voltage.

2.5 Microstructure Evolution of Thin Films

There is a close connection between the microstructure of a polycrystalline material and its properties that affect the intended usage. An understanding of the microstructural evolution allows the achievement of the most desirable microstructure.

Tanaka *et al* reviewed the growth mode of thin film on a solid surface, which is classified as Volmer-Weber (VW - island growth), Frank-van der Merwe (FM - layer-by-layer growth), or Stranski-Krastanov (SK - layer + island growth) [55], as illustrated in Figure 2.11. These growth modes can be explained in terms of free energies of substrates, films and their interfaces, including strain energies, surface or interface energies.

The evolution of polycrystalline films typically begins with the nucleation of individual crystals, which then coarsen into three-dimensional structure or remain as a two-dimensional film until they impinge upon each other and form a continuous film. The final microstructure depends on both the nucleation and the growth conditions. After impingement, grain boundaries between the nucleated structures may migrate, leading to grain growth. Growth texture can develop during nucleation, grain growth and/or post-deposition annealing.

Reproduced with permission of the copyright owner. Further reproduction prohibited without permission.

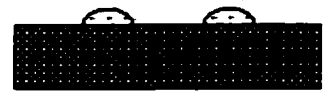

Volmer-Weber (VW) mode

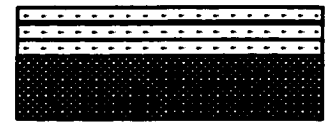

Frank-van der Merwe (FM) mode

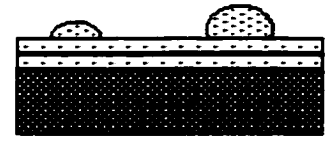

Stranski-Krastanov (SK) mode

Figure 2.11 Three types of thin film growth modes.

Many polycrystalline films are deposited in the form of columnar grains that grow to be much longer than their diameters [55]. The columnar structure is strongly influenced by the deposition conditions such as the substrate temperature and the pressure in sputter deposition. As the film thickens, the diameters of the columnar grains may increase; as a result, columnar grains become wider and crowed out others, as shown in Figure 2.12. Generally, the morphology of the deposited film has been described by a zone model first proposed by Movchan and Demchishin [56] and later modified by Thornton [57, 58]. Figure 2.13 shows a schematic of the regions of film morphology as a function of substrate temperature and incident ion energy. The substrate temperature is normalized to the melting point of the deposited material. Although this model is broadly applicable, the boundaries between region I and II and III may vary from material to material.

Reproduced with permission of the copyright owner. Further reproduction prohibited without permission.

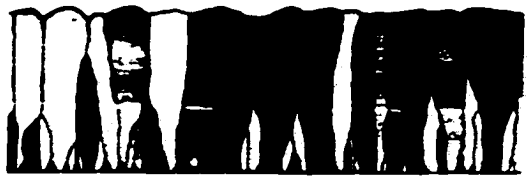

Figure 2.12 The grain growth during deposition.

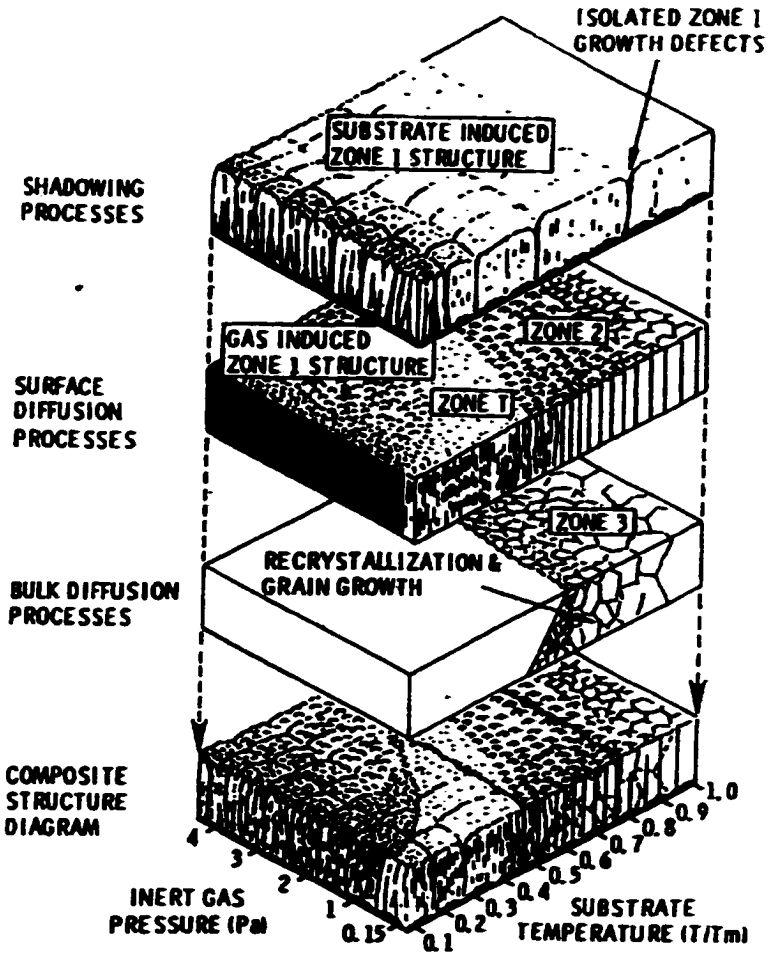

Figure 2.13 The zone model for deposited thin film.

In the first zone with the lowest temperature and the lowest incident ion energy, the deposited film tends to be amorphous and porous with a low density. This is caused

Reproduced with permission of the copyright owner. Further reproduction prohibited without permission.

by the low adatom mobility on and in the growing film. In the "T" zone, the films are highly specular and have very small grains. At large substrate temperatures (zone I), the films will have tall and narrow columnar grains that grow vertically from the surface. In zone 3, the film has large three-dimensional grains due to high atomic mobility. The surfaces of the films in the second and third zones are moderately rough, and the films may appear milky or hazy due to the light reflections from the grain boundaries.

2.5.1 Nucleation and Impingement

Impinging fluxes onto a substrate and leading to the film nucleation and growth have been simulated and modeled. Two extreme cases in nucleation are site saturation, in which all sites nucleate simultaneously, and continuous nucleation, in which the nucleation rate remains constant with time. An intermediate case is that the nucleation rate decreases with time [59]. A preferred crystal orientation is assumed to be prevalent during nucleation [60]. After nucleation, the coarsening rates of different nuclei can be either identical or different, and the resulted grain morphologies are schematically shown in Figure 2.14. One of the main driving forces for island coarsening is the minimization of the surface energy [61, 62].

Reproduced with permission of the copyright owner. Further reproduction prohibited without permission.

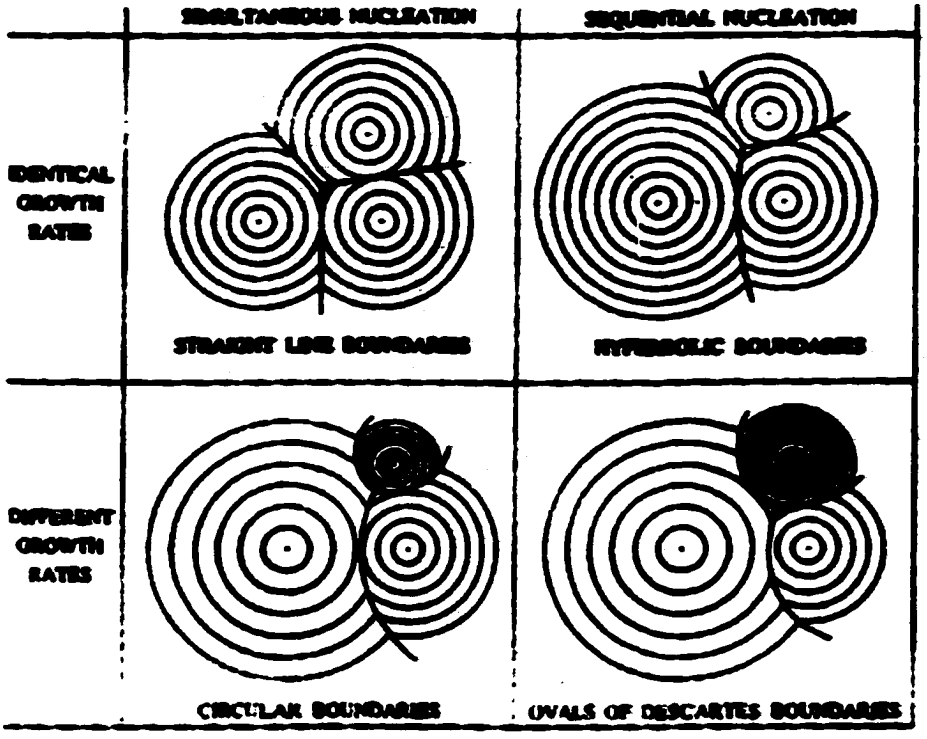

Figure 2.14 Growth to impingement of three neighboring crystals under two different nucleation conditions and two different growth rate conditions [59].

2.5.2 Grain Growth

Grain growth is the process by which the mean grain size of an aggregate of crystals increases with time. The driving force for grain growth is the reduction in system free energy, associated with the reduction of grain boundary area [63], strain energy [64], free surface energy and film-to-substrate interface energy. Grain growth is achieved either by grain boundary migration or by grain "rotation".

When the grain size is much smaller than the film thickness, the growth is a three-dimensional process. When the grain size is comparable to or larger than the film thickness, the grain growth becomes a two-dimensional process [59, 63]. Due to the

Reproduced with permission of the copyright owner. Further reproduction prohibited without permission.

complexity of three-dimensional growth, grain growth models are hard to develop for this situation. On the other hand, there are well-developed models for two-dimensional growth. It was noticed half a century ago that soap froths and polycrystals evolve in similar ways [65]. For two-dimensional grain growth, three elementary topological transformations have been reported [66]. They are called T1, T2, and reverse mitosis, as shown in Figure 2.15. In T1, the vertices at either end of an edge move towards one another so that it shrinks to zero length and a new edge, ideally perpendicular to the old edge, grows out of the intermediate quadruple vertex. In T2, a cell with three edges shrinks down to zero area so that only a triple vertex is left. It has also been reported that three-sided grains vanish by a crystallographic orientation change to match that of its neighbor [59].

Mullins found that grains with five or fewer sides shrink, and those with seven or more sides grow [67]. Frost and Thompson [68, 69] further reported that the grain boundary velocity is determined by the local curvature, the driving force and the local grain boundary mobility. Comparing the various simulations to experimental observations has always been a challenge. Actually, for two-dimensional structure, minimization of total system free energy involves more than just minimization of grain boundary area; the effects of free surfaces must be considered.

It has been observed that normal grain growth in thin films stagnates when the average grain diameter is two or three times the film thickness [70, 71]. This is the so-called specimen thickness effect. Mullins proposed that the stagnation of the normal grain growth in thin films occurred when grain boundary grooved at the triple points where the grain boundaries met the free surface of the film [72].

Reproduced with permission of the copyright owner. Further reproduction prohibited without permission.

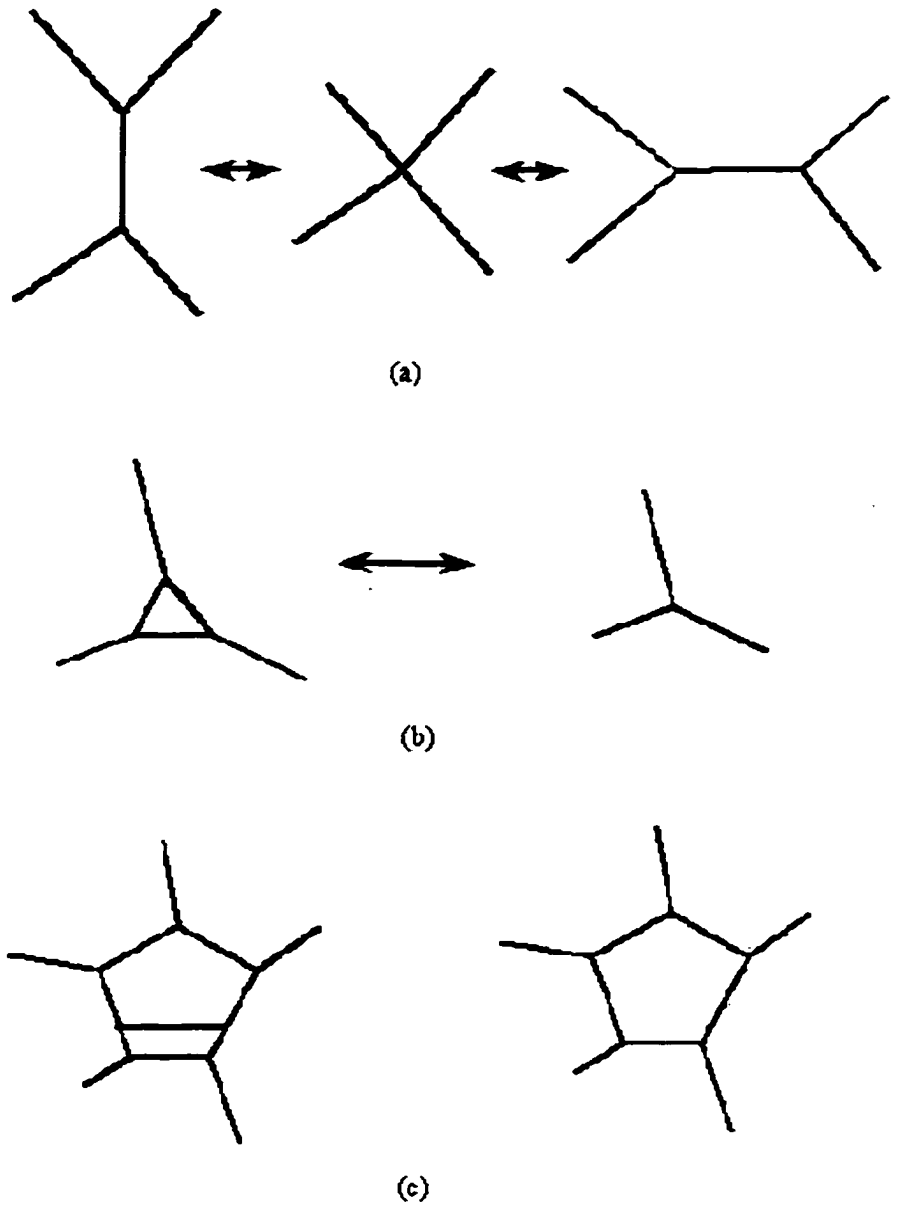

Figure 2.15 Three elementary local rearrangement processes. (a) T1, (b) T2, and (c) reversed mitosis.

Another phenomenon that occurs during grain growth in thin films is abnormal grain growth. This occurs when the boundaries of a few grains move outward rapidly relative to most other boundaries. These abnormally large grains grow much faster than

Reproduced with permission of the copyright owner. Further reproduction prohibited without permission.

the other grains. The process is completed when these grains impinge upon one another and all the normal grains are consumed. It is known that the grain boundary velocity is the product of driving force, local grain boundary curvature and the grain boundary mobility. Among these three terms, the driving force has the most significant effect on abnormal grain growth. For instance, grains with different crystallographic orientations may have different free surface-to-grain boundary energy or film-to-substrate interface energy, allowing some with large energy differences to grow more rapidly.

Grain boundary migration can also be induced by diffusion [73, 74], and it is termed as diffusion induced grain boundary migration (DIGM). When a polycrystalline sample is heated up to diffuse a certain species, and the grain boundaries act as diffusion channels, grain boundary migration occurs. This process may or may not be associated with grain boundary precipitation. Although the mechanisms of this phenomenon are not completely understood yet, some suggestions have been reported. First, it is speculated to be associated with the fact of grain boundary energy being changed by the existence of the diffused species. As a result, the driving force and mobility of grain boundary migration are increased [75]. Second, a vacancy flux may help the diffused species to be substitutionals in grain boundaries. The emission of these vacancies from grain boundary dislocation sources will stimulate the grain boundary migration [76]. If there is a Kirkendall effect, the grain boundary migration is likely to continue throughout the diffusion process.

Besides the grain growth through grain boundary migration, "*in situ*" growth is another path to achieve grain growth [69]. This occurs mainly in grains separated by low angle boundaries. A few degrees of one grain's "rotation" is sufficient to allow two

Reproduced with permission of the copyright owner. Further reproduction prohibited without permission.

adjacent grains to have the same crystallographic orientation. Thus, the grain boundary disappears and the two small grains become one larger grain.

Despite the fact that the real microstructural evolution in bulk materials, or even in thin films, may not be truly represented by what occurs in a 100 to 150nm-thin-TEM foil, *in situ* heating in TEM has been one of the experimental methods used to investigate grain growth [63]. It offers the possibility of visually examining the grain boundary motion at elevated temperatures in real time. Nichols reported the observations of T1 and T2 transformations and other grain growth phenomena of aluminum films using *in situ* heating in TEM [73]. Guillemet, *et al* performed *in situ* TEM to investigate the grain growth rates of silicon films [74].

2.5.3 Texture

Texture is a preferred crystallographic orientation in a material. In the case of thin film, texture development is determined by deposition conditions and post-deposition treatment. Texture lowers the total free energy of the system, considering surface energy, interface energy and strain energy. The final texture depends on which of these factors dominates. Thompson suggested that there is a critical thickness for thin films, below which surface energy minimization controls texture evolution during grain growth [64]. Above this thickness strain energy controls. When the film is not free standing, the difference in thermal expansion coefficients of the film and the substrate or sub-layer may induce strains into the system. In fact, texture can develop during nucleation [60], islands coalesce [69], grain growth [64], and/or post-deposition treatment [59].

Reproduced with permission of the copyright owner. Further reproduction prohibited without permission.

As discussed earlier, the texture of ZnS:Mn thin film may change with film thickness. Similar observations were made in Cr [77, 78] and Mo thin films [79]. This phenomenon was explained using surface energy and strain energy models.

Pole figure and reverse pole figure diagrams are the best ways to represent the texture in a sample [80]. The reverse pole figure can even offer quantitative information. Acquisition of a pole figure using XRD was once tedious, but with breakthroughs in software packages and instrumentation, it is much easier today. If quantitative data are not required, conventional XRD intensities can be used to qualitatively determine the preferred crystallographic orientations in a sample. When a thin film has fiber texture and has no in-plane constraint, results from conventional XRD technique are sufficient to present texture.

Reproduced with permission of the copyright owner. Further reproduction prohibited without permission.

CHAPTER 3
EXPERIMENTAL PROCEDURE AND SAMPLE PREPERTION

3.1 Introduction

In this study, two kinds of co-dopants, KCl and Ga_2S_3, were introduced into the magnetron sputtered ZnS:Mn phosphors by a process of thermal evaporation and diffusion at elevated temperatures. The effects on microstructure and EL performance were investigated. The experimental outline is shown in Figure 3.1.

3.2 Device Fabrication

Corning 7059 glass substrates with transparent conductor indium tin oxide (ITO) and insulator aluminum titanium oxide (ATO) layers were supplied by Planar Systems. The ITO and ATO layers are 300nm and 220nm in thickness, respectively. ZnS:Mn thin films were deposited using a radio frequency magnetron sputter system with a chamber pressure at 20mTorr of argon. ZnS and Mn were deposited from two separated targets, and the concentration of Mn was controlled by the power and duty cycle of the manganese source. The substrates were preheated to and held at 180°C during deposition. Since all the devices investigated in this study are half stacks, no top insulators were deposited. Reflective aluminum electrodes were thermally evaporated on

Reproduced with permission of the copyright owner. Further reproduction prohibited without permission.

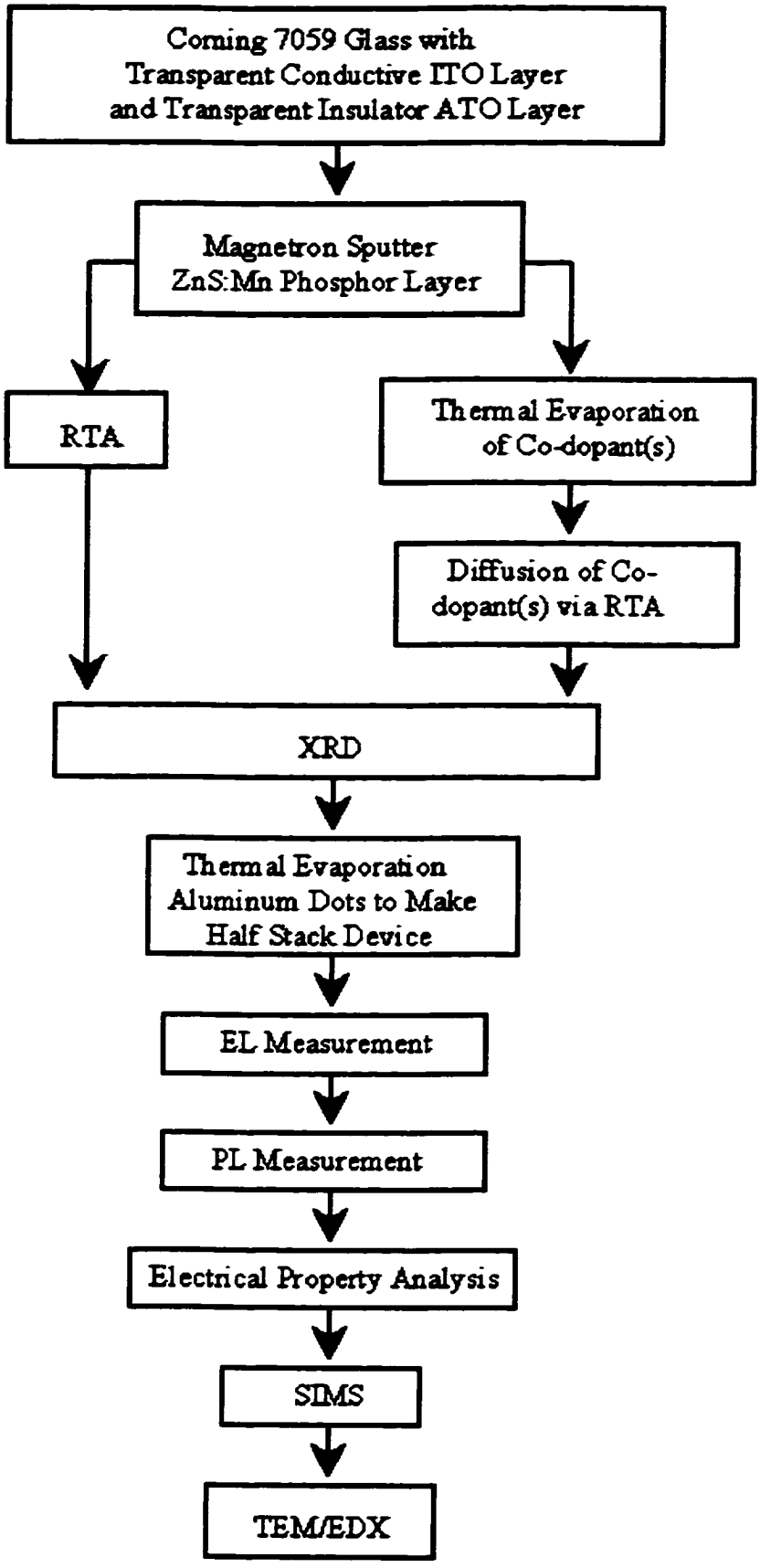

Figure 3.1 Experiment Procedure flow chart.

Reproduced with permission of the copyright owner. Further reproduction prohibited without permission.

top of the phosphor film. The schematics of both half stack and full stack standard devices are shown in Figure 3.2.

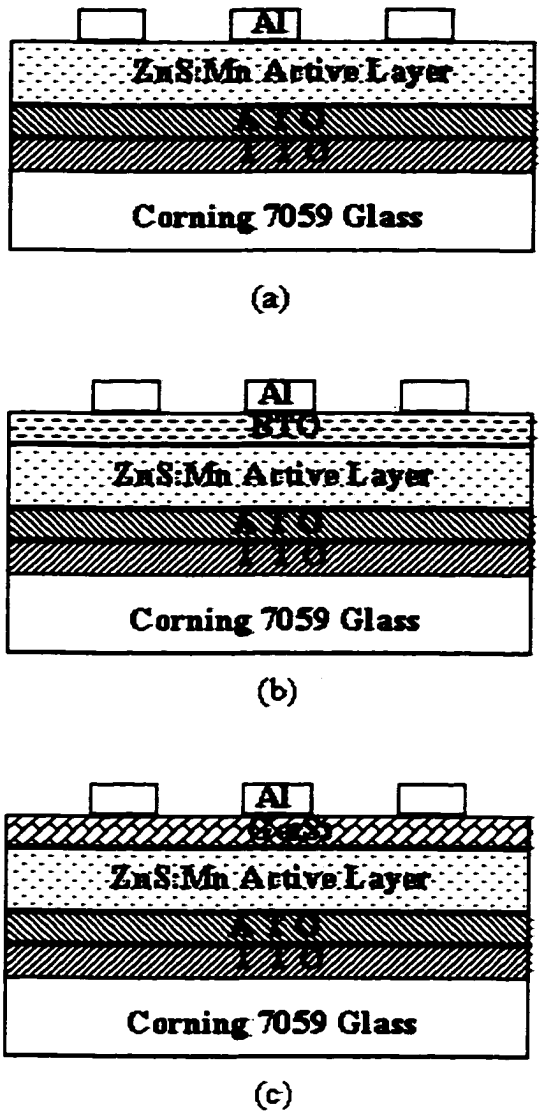

Figure 3.2 Schematics of standard (a) half stack EL device, (b) full stack EL device and (c) half stack EL device with a layer of Ga_2S_3 that did not diffuse into ZnS:Mn.

Co-dopant was deposited onto the phosphor layer by thermal evaporation at pressure lower than 10^{-6} Torr at room temperature. Rapid thermal annealing (RTA) was

Reproduced with permission of the copyright owner. Further reproduction prohibited without permission.

conducted to let the co-dopant diffuse into the phosphor. The amount of KCl was controlled to be 100nm in thickness and the excessive KCl after diffusion was rinsed off by de-ionized water. Since no success was achieved in finding a way to remove the excessive Ga_2S_3 after diffusion without damaging the film, a thin layer of Ga_2S_3 is remained on top of the ZnS:Mn layer, as shown in Figure 3.2c.

3.3 Rapid Thermal Annealing Conditions

Rapid thermal annealing was carried out in ultra high purity nitrogen (99.99999%) at a minimum flow rate of 10psi. The purpose of the RTA is twofold: (1) to optimize the EL performance by annealing out some of the lattice defects, and (2) to diffuse co-dopant(s) into the phosphor layer. As introduced in the previous Chapter, the as-sputtered microstructure has a high density of defects, which are not good for EL performance. These defects may trap, and scatter the hot electrons, as well as act as non-radiative recombination centers.

The heating sources for RTA are two sets of halogen lamps, cooled by both water and air on top and bottom of the quartz tube chamber. The samples were located in a covered graphite susceptor, with a thermocouple about 1mm away from the phosphor film to control the temperature. To avoid contaminations from the graphite, two pieces of un-doped silicon wafers were put on top and bottom of the sample, with the polished surfaces towards the sample. The controlling unit was made by Micristar, which can be programmed to apply a temperature profile to the system. To minimize the deleterious effects of oxygen, nitrogen was purged for 40 minutes before the temperature ramp was

Reproduced with permission of the copyright owner. Further reproduction prohibited without permission.

started, and was kept flowing during the annealing. Figure 3.3 shows the schematic of the RTA setup used in this study. In order to avoid contaminations from different co-dopants, different susceptors were used when the dopant was changed, and the chamber was cleaned before processing different samples.

The time for temperature ramping was set for 2 minutes, and the RTA time was consistently at 5 minutes for the temperature-holding period in this study. When cooling down, zero power input was applied. It normally took 30 minutes to cool down to 50°C. Three groups of samples were investigated. 1) ZnS:Mn phosphor films without any co-dopants for comparison, 2) ZnS:Mn with either KCl or Ga_2S_3 co-dopant, and 3) ZnS:Mn with both KCl and Ga_2S_3. In the last group, co-doping was fulfilled by an evaporation/ RTA/evaporation/RTA procedure, so the total RTA time was 10 minutes for each sample.

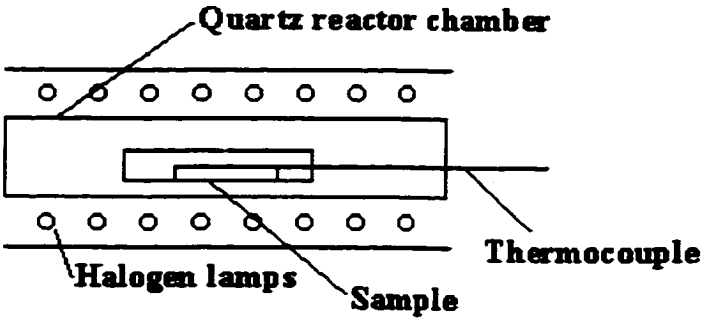

Figure 3.3 A schematic of RTA setup.

Reproduced with permission of the copyright owner. Further reproduction prohibited without permission.

3.4 Microstructure Characterization

3.4.1 X-ray Diffractometry (XRD)

X-ray diffractometry (XRD) is widely used in material characterization [73]. It generates information of both crystallography and chemistry. It is not destructive, and sample preparation is fairly simple.

A collimated beam of X-rays is generated from a copper target bombarded by a high-energy electron beam. The generated X-ray wavelength is 1.54056Å. When this X-ray beam is incident on a specimen, it diffracts by the crystalline phases in a specific crystallographic orientation, following Bragg's law:

$$n\lambda = 2d_{hkl} \sin \theta \qquad (3\text{–}1)$$

where n is an integer, λ is the wavelength of the incident X-ray, d_{hkl} is the hkl interplane spacing of the sample, and θ is the angle between incident or detection direction and the sample's surface normal. The sampling depth is a few micrometers, depending on the X-ray absorption coefficient of the detected material.

By recording the intensity versus the diffraction angle 2θ, the following information can be obtained [80]:

(1) the crystallographic structure(s) in the sample;

(2) the preferred crystallographic orientation, i.e. texture;

(3) internal strains;

(4) Cystallite or domain size;

It should be noticed that all the information from XRD is from the whole sampling volume. XRD does not have depth-profiling capability, and its lateral

Reproduced with permission of the copyright owner. Further reproduction prohibited without permission.

resolution is poor (about 10mm by 10mm). When the sample is a thin film, the XRD intensity is usually low due to the fact that the X-ray penetrates deeper than the film thickness.

In the present study, crystallinity and texture of the phosphor films were analyzed by XRD, conducted on a Phillips APD 3720 X-ray diffractometer. In an effort to get consistent results, all the samples were bigger than the beam size (1cm by 1cm), and extra cautions were taken during sample assembly to avoid the errors from sample height variation. A copper target operated at 40kV and 20mA was utilized to generate K_α and K_β for the analysis. The full width at half maximum (FWHM) was used as an indicator of the crystallinity and the relative intensities of different diffraction peaks were used to measure the texture.

3.4.2 Transmission Electron Microscopy (TEM)

3.4.2.1 Introduction

Transmission electron microscope is an electronic analogue of an optical microscope [81]. In TEM, a high-energy electron beam takes the place of visible light, and it is focused by sets of electromagnetic coils rather than lenses. Thus, TEM has an extremely high resolution. It is extensively used to characterize the microstructure of conductive materials.

The sample for TEM analysis must be thin enough to be transparent to 200keV electrons. Normally this thickness is around 100-200nm, depending on material. To get such a thin area on a sample requires special sample preparation techniques, which will be introduced below. TEM can be operated in two modes, diffraction and image modes.

Reproduced with permission of the copyright owner. Further reproduction prohibited without permission.

Three kinds of images can be achieved, which are bright field (BF) image, dark field (DF) image and high resolution image. The analogous ray diagram of each mode is schematically shown in Figure 3.4 [81]. When an energy dispersive X-ray spectrometry (EDS) is carried out in TEM, a TEM becomes an analytical electron microscope (AEM).

The TEM diffraction pattern (DP) is similar to an X-ray diffraction pattern; one can tell whether the sample is single crystal, polycrystalline or amorphous. If it is a crystalline material, its lattice parameter, symmetry, and other information can be determined by indexing the diffraction pattern. In case of a polycrystalline material, it is also possible to know qualitatively the sample texture, the grain size, etc.

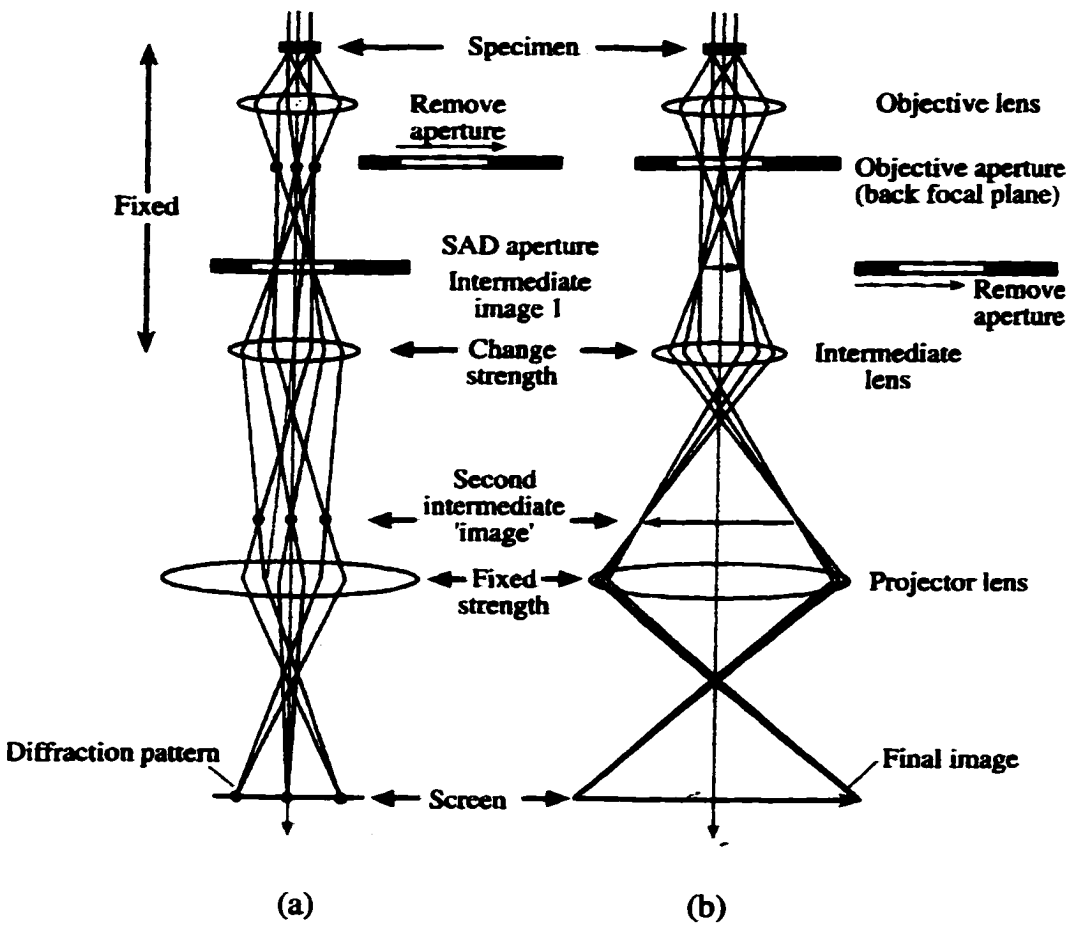

Figure 3.4 Equivalent ray diagram for (a) image and (b) diffraction modes.

Reproduced with permission of the copyright owner. Further reproduction prohibited without permission.

A BF image has the information from the transmitted beam, which is the most "straight forward" of all the TEM images. To interpret a BF image, it is important to remember that TEM provides two-dimensional images of a three-dimensional sample. The information in the third dimension (z direction) must be carefully interpreted. A BF image shows defects, internal strains, grain size, and grain size distribution, if it is a polycrystalline sample. The contrast in BF images is from diffraction, that is, from crystallographic orientation differences.

A DF image carries the information from one or several diffracted beams, i.e., only the parts that have certain crystallographic orientation(s) are bright. Therefore, DF images are useful when defects or phases with a certain crystallographic orientation are of interest. When characterizing defects, a BF/DF pair of images is usually taken, together with a DP to interpret the nature of the defects or crystallite.

If both transmitted and diffracted beams are contributing to the image, we can get an "atomic" image of the sample, the so-called high resolution image. This "atomic"-like image is not the direct image of the crystal, but a result from the interference of the beams. However, it gives lattice spacing information. The contrast in a high resolution (HR) image is from the phase difference among the beams. For HRTEM analysis, it is necessary to use image simulation to assist the interpretation, because the HRTEM image is always obtained at a certain unfocused condition. There are some software packages available for this purpose [81].

In this study, the microstructure of the phosphor films was characterized using TEM on both cross-section (XTEM) and plan-view (PTEM) samples. The microscope used for conventional analysis is JOEL 200CX, operating at 200kV. A JEOL 4000FX

Reproduced with permission of the copyright owner. Further reproduction prohibited without permission.

high resolution TEM, operating at 400kV, was employed to obtain high-resolution images at a certain crystallographic orientation parallel to a specific zone axis.

3.4.2.2 Sample preparation

With TEM applications becoming more and more extensive, new techniques and instruments for sample preparation have been developed. A commonly used procedure for preparing PTEM samples is:

(1) cut a thin slice from the bulk material;

(2) cut the slice into a disk with a diameter of 3mm;

(3) mechanically pre-thin the disk;

(4) further thin the disk to get an electron transparent area.

There are two ways to do the final thinning. One way is using chemical reagents and electropolishing, and the second is a physical removal by ion milling. Fast thinning and no mechanical damage are the merits of electropolishing. But it has some limitations, too. First, it is only useful for conductive materials, like metals. Secondly, it may change the sample surface chemistry. Electropolishing has been called "black magic" for decades. It takes a lot of test-runs to get the proper conditions, such as temperature, solution chemistry, stirring rate, applied voltage/current, hydraulic flow conditions [78].

Contrary to electropolishing, ion milling is a physical thinning process. The sample is bombarded by high-energy plasma beams, so that material is sputtered off the sample until an electron transparent thin area is achieved. Argon is normally used to generate the plasma, because it is heavy and chemically inert. Due to its physical

Reproduced with permission of the copyright owner. Further reproduction prohibited without permission.

removal nature, ion milling can be used for any kind of materials, even composites. However, it does introduce artifacts, such as argon ion implantation, re-deposition and defect generation. If the sample is multiphase, the difference in sputter yield of each phase results in different thinning rates, which causes large variation in electron transparency.

Semiconductor devices are usually multilayered structure with each layer being very thin. Moreover, the materials for each layer vary over a large range, from metal/alloy to semiconductor to oxide to other ceramic materials. In order to fully understand the device microstructure using TEM characterization, a uniform thin area that covers all aspects is highly desired. To meet this demand, new techniques and instrument have been explored in the past ten years, such as tripod polishing [80], and focused ion beam (FIB) [80, 82, 83]. In fact, FIB has been a revolutionary improvement in multi-layered XTEM sample preparation, and is becoming the routine TEM sample preparation method in semiconductor materials research.

Parallel to the development in FIB, research and technique/instrument development on conventional ion milling have also been carried out to deal with multi-layered sample, such as various IC devices. It has been reported that by rocking the sample over a certain range of angle versus the incoming ion beam, the difference in sputter rate from different materials can be minimized. This makes it possible to get a uniform large thin area [84, 85]. It further indicates that a rocking angle of around 40° is good when the multi-layered structure is composed of materials with great sputter yield difference, such as for systems $Pt/Ti/SiO_2/Si$ and $W/TiN/SiO_2/Si$. A rocking angle of 80°

Reproduced with permission of the copyright owner. Further reproduction prohibited without permission.

is good for systems composed of materials with similar sputter rates. The rocking angle is illustrated in Figure 3.5.

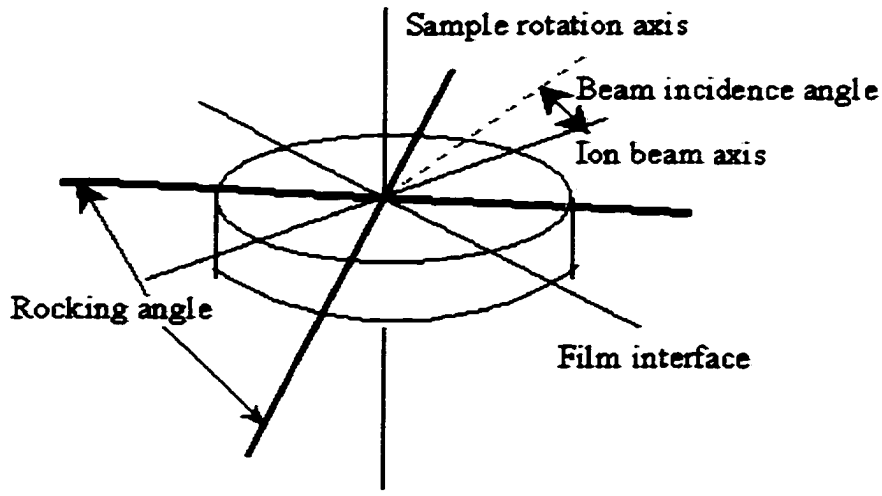

Figure 3.5 Rocking angle and it relationship to the incoming ion beam.

This sputter thinning technique is used for all of the TEM samples in this study. The rocking angle for XTEM is set at ±50° and that for PTEM is set at ±70°. The ion miller used here is a Hungry made Technoordge Linda IV thinning unit. Figure 3.6 shows the main steps of sample preparation. Details are introduced below.

3.4.2.2.1 Cross-section transmission electron microscopy (XTEM) samples

A Sample was first cut into 1.7mm by 5mm strip using a low speed diamond saw, then it was mechanically thinned from the glass side to about 470μm using 240 grit sandpaper with water. The thickness should be less than 500μm for further processing. This strip was then cut into several small pieces with dimensions of 1.7mm by 600μm by 470μm using a low speed diamond saw, as shown in Figure 3.6(ii). These tiny pieces

Reproduced with permission of the copyright owner. Further reproduction prohibited without permission.

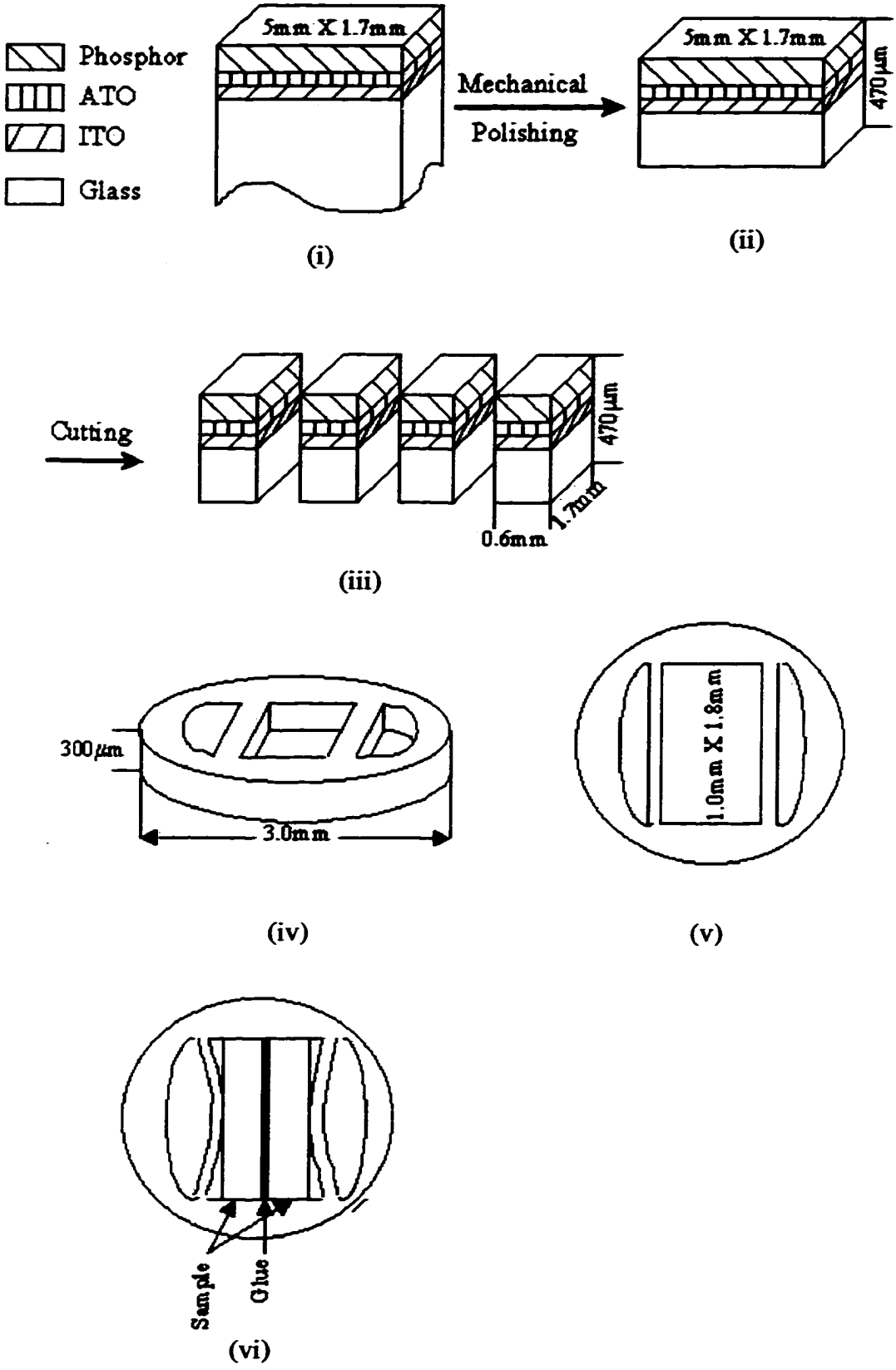

Figure 3.6 Flow chart of XTEM sample preparation.

Reproduced with permission of the copyright owner. Further reproduction prohibited without permission.

were well cleaned by dipping into acetone to get rid of the crystal bond, which was used as an adhesive.

A specially designed titanium ring was used to make XTEM samples in this study. Its shape and dimension are shown in Figure 3.6(v). This titanium ring has two functions: supporting the sample for easy handling and making better electrical and thermal conductivity to the TEM sample holder. Two pieces of tiny strips were placed with the film side facing each other into the rectangular slot of the titanium ring, then the two walls were bent towards the sample using a jewelry screwdriver to make sure that the two pieces of samples were clamped securely. These steps were conducted under an optical microscope. Although the whole device is transparent to light, it is easy to tell the film side from the glass side under an optical microscope, because the glass side was lapped only by 240 grit sandpaper.

A carbon contained conductive epoxy is used to fill up the open space of the titanium ring, again both for supporting and enhancing electrical/heat conductivity. This epoxy took two hours to cure at 150°C on a hot plate in air. After the epoxy was completely cured, the sample was glued onto a jig and mechanically lapped from both sides to the thickness of about 50μm, using a Gatan grinder and sandpaper with water. The last polish step should be finished using 4000 grit sandpaper with water. Cautions must be used to remove the sample from the jig and clean up the crystal bond residue with acetone. This sample then was ready to be ion milled. It is glued onto a one-sided sample holder using carbon paint.

The ion mill used in this study is Technoordge Linda IV sample thinning unit. It has two ion guns that can operate at up to 10kV. The milling procedure is as follows.

Reproduced with permission of the copyright owner. Further reproduction prohibited without permission.

First, two guns were operating at 10kV and 4mA, with the sample rotating continuously, until a valley at the glue line could be observed. Then one gun stopped and only the other gun was used at the same power and current intensity. At this time the sample was rocking at 50° relatively to the beam, as shown in Figure 3.5, to "push" one side of the valley away from the glue line. The sample then was flipped over and these two steps repeated. The sample continually rocked at ±50° until a hole appeared on one half of the sample. Milling stopped when the back of the hole reached the interface, or just a little bit over the interface. The sample should be checked with an optical microscope to see if there are good interference fringes at the film area. For better results, the sample should be carbon coated before placing in the TEM.

3.4.2.2.2 Plan-view transmission electron microscopy (PTEM) samples

A round piece of sample with diameter of 3mm was first cut using an ultrasonic coring drill. It was mechanically lapped down from the glass side to 50μm using sandpaper with water. The last step was a polish with grit 4000 sandpaper. It was then glued onto the one-sided sample holder and put into the chamber for thinning by ion milling. At the beginning, two guns operated at 10kV and 4mA, with the sample rotating continuously. When the thickness of the center was about 10 to 15μm, a piece of copper ring or carbon ring was glued on the film side to mechanically support the sample. This was to support the fragile glass substrate since its thickness was only about 10μm. After gluing the ring, continue to mill the sample using only one gun at 10kV and 4mA with the sample rocking at ±70° relative to the ion beam until a hole was formed. Flip it over and mill for five minutes using one gun to get rid of the re-deposited material on the film

Reproduced with permission of the copyright owner. Further reproduction prohibited without permission.

side. Take out the sample and check it under an optical microscope to see how diffuse the interference fringes were. A good sample should have diffusive interference fringes from the incident visible light. The wider the spacing between the fringes, the more uniform is the thin area. PTEM sample must be carbon coated before analyzing in the TEM.

3.4.3 Energy Disperisve Spectrometry (EDS)

As introduced earlier, TEM is mostly used to characterize microstructure. However, a TEM can become an analytical electron microscope (AEM), if certain X-ray spectrometry detectors are connected to it, such as an energy dispersive spectrometer (EDS). The combination of chemical analysis capability at high lateral resolution with imaging makes AEM very useful in material science research [78].

The three main parts that make up an EDS system are the detector, the processing electronics, and the multi-channel analyzer (MCA). A computer controls all three parts. Figure 3.7 is a flow chart of how an EDS works. First, the detector generates a charge pulse proportional to the X-ray energy. This pulse is then converted to voltage. Next, the signal is amplified through a field effect transistor (FET), and isolated from other pulses, further amplified, then identified electronically as resulting from an X-ray of a specific energy. Finally, a digitized signal is stored in a channel assigned to that energy in the MCA.

Reproduced with permission of the copyright owner. Further reproduction prohibited without permission.

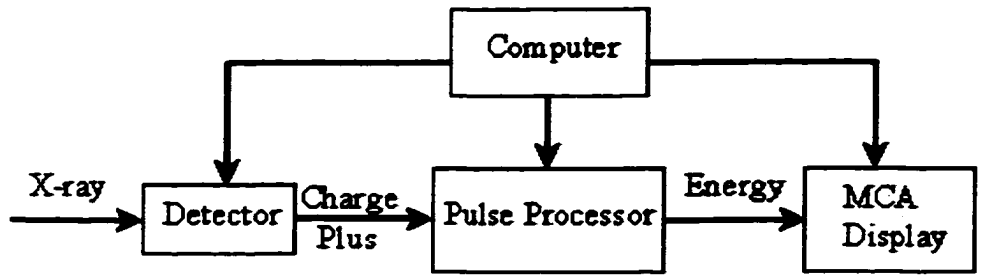

Figure 3.7 A Flow chart of an EDS.

The advantage of EDS in TEM over EDS in SEM or electron microscope probe analysis (EMPA) is the remarkable improvement in spatial resolution. The beam size for the TEM can be as small as 2nm while that for the SEM or EMPA is typically as large as 1μm. In addition, the sampling volume is much smaller in the TEM, since thin foil specimens are used. The electron scatter as the beam traverses the specimen is largely reduced. Secondly, the electron beam in an AEM has much higher energy (100 to 400keV) than that in an EMPA (5 to 30keV), which allows better focusing and further reduced scatter. From another point of view, increase in accelerating voltage decreases the lateral spread of the beam-specimen interaction volume in thin samples, resulting in a more localized X-ray signal source and a higher spatial resolution. In the case of bulk samples, increasing the voltage increases the interaction volume, and spatial resolution rarely improves below about 1.0μm. Because of the high accelerating voltage and the high current of the primary electron beam, EDS is always performed with the specimen in a low-background holder that is capable of being cooled to liquid-N_2 temperature to minimize the degradation and contamination. Be has been the widely used material for this purpose.

Reproduced with permission of the copyright owner. Further reproduction prohibited without permission.

When conducting EDS analysis, the detector should "look" toward the thin region of the specimen rather than toward the thicker region, as illustrated in Figure 3.8a. In this way, the X-ray escaping path through the sample is minimized and thus X-ray absorption is minimized. Getting the proper analysis location is done in the STEM mode. When the chemistry across a certain planar interface is of interest, such as in this study, it is essential to have the specimen orientated so that the interface is parallel to the detector axis and the beam, as shown in Figure 3.8b. This situation is often called "edge-on". In practice, two basic rules are followed to get a grain boundary "edge-on". First, select two adjacent grains that have comparable diffraction contrast. Then a line scanning is carried out across the grain boundary to confirm the edge-on situation. The profile should be symmetrical.

EDS in the TEM was performed at the Oak Ridge National Lab (ORNL), Oak Ridge, Tennessee. The microscope for this purpose was a Phillips CM-200 with a field emission gun. Both line scanning and stationary probe analysis were carried out. The length of the line scanning was 38nm, and it was attempted to have the scanning direction perpendicular to the grain boundary. The sampling time for the stationary probe was 100 seconds for each spot with the dead time is around 20%. The diameter of the beam was 2nm for the probe and the accelerating voltage was 200kV.

Reproduced with permission of the copyright owner. Further reproduction prohibited without permission.

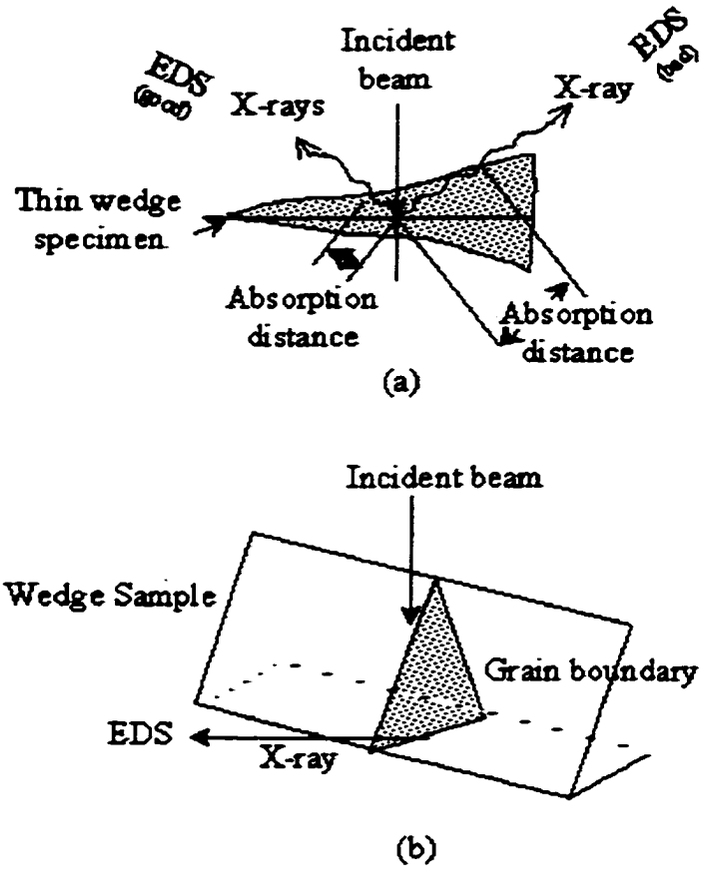

Figure 3.8 (a) Good and bad positions of EDS detector relative to a wedge shaped sample. (b) The grain boundary should parallel to the incident beam.

3.4.4 Secondary Ion Mass Spectrometry (SIMS)

SIMS is a widely used method for chemical characterization in material science, especially for semiconductors [84]. In this technique, secondary ions are sputtered from a sample surface by bombarding it with primary ions, typically, Cs^+, O_2^+, O^-, and Ar^-, in an ultrahigh vacuum chamber. The primary ion beam can be focused to less than 1 μm in diameter. A small fraction of the sputtered atoms are ionized either positively or negatively. These secondary ions are mass analyzed and the count rate is plotted versus

Reproduced with permission of the copyright owner. Further reproduction prohibited without permission.

their mass-to-charge ratio. This information is used to determine the composition of the near surface and throughout a thin film. This procedure is shown in Figure 3.9.

SIMS normally can be used in two modes: static and dynamic modes. In the static mode, a primary ion flow of $<10^{14}cm^{-2}$ is used, which leaves the sample surface relatively undisturbed in the time required to collect a spectrum. In this case, most of the secondary ions are generated from the top one or two mono-layers of the sample. A mass spectrum covering hundreds or thousands of atomic mass units may be obtained. In the dynamic mode, the selected secondary ion intensities are monitored as a function of the sputtering time that is converted to a sputtered depth using a calibration procedure. A concentration vs. depth profile thus results. The depth resolution of this technique is in the 5 to 20nm range. The dynamic mode is widely used for the study of the trace dopant and impurities in semiconductors, because SIMS yields quantitative information by comparing with a standard uniform host material.

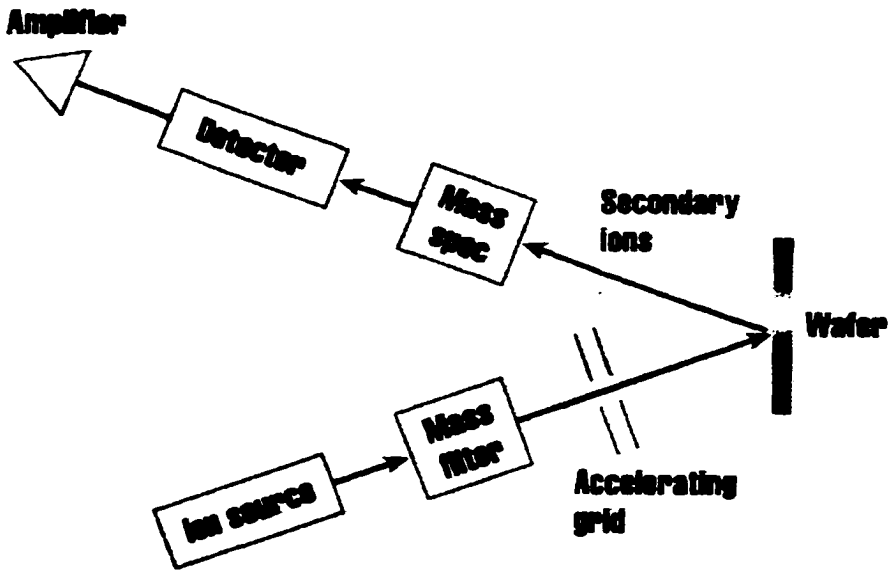

Figure 3.9 A schematic showing the operation procedure of SIMS [80].

Reproduced with permission of the copyright owner. Further reproduction prohibited without permission.

SIMS has very high sensitivity (in the ppb range) to most elements. Three factors may limit its sensitivity: ionization efficiencies, dark counts or dark current, and the introduction of the analyte element from the instrument. To perform quantitative SIMS analysis, standard material from which to measure the relative sensitivity factors (RSF) is required. Ion implantation is a good way to make standards, since it is possible to implant any element into any matrix.

SIMS in the dynamic mode was used to characterize the diffusion of the co-dopant(s). In this study, a PHI 6600 machine with a quadropole mass spectrometer was used. Oxygen primary ions were used to detect the positive ion species because of its high electron affinity, and cesium primary ions were used to detect the negative ion species because they can lower the work function of the solid to increase the negative ion yield.

3.4.5 Grain Size Measurement

The mostly used measure of feature size is the average surface-to-surface distance through the feature. Mean linear intercept $\langle\lambda\rangle$ was used to characterize grain size in this study. The first step was to randomly draw straight lines across the measured feature from border to border, as shown in Figure 3.10. The length of each line was measured, summed and recorded. By dividing the total length of these lines by the number of the lines for each grain, the mean linear intercept $\langle\lambda\rangle$ was obtained. Obviously, it is better to have a population of the features [86].

Reproduced with permission of the copyright owner. Further reproduction prohibited without permission.

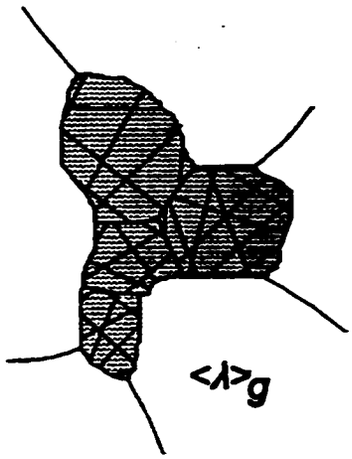

Figure 3.10 A Schematic showing the grain size measurement used in this study [86].

3.5 Device Characterization

3.5.1 Electroluminescence (EL) Properties

The a.c. waveform used to measure the EL brightness of the half stack ACTFEL devices is schematically shown in Figure 2.3. The pulse rise and fall time is 8μs, and its holding time is 40μs. Besides the EL brightness, CIE color coefficients and the emission spectrum were also recorded in the meanwhile.

A PR-650 spectra colorimeter™ was used to measure the EL brightness. It consists of Pritchard-style viewing and measuring optics, a holographic grating, a diode array spectrometer, a CMOS microcomputer, a back-lit super-twist liquid crystal display (LCD) read-out, an integrated circuit memory (ICM) card, and a rechargeable battery. It is designed to perform a variety of measurements, including luminance, illuminance, integrated and peak radiance, chromaticity, color temperature, color difference, and source refresh frequency.

Reproduced with permission of the copyright owner. Further reproduction prohibited without permission.

The circuit used for luminous efficiency measurement is given in Figure 3.11. A known resistor, a known capacitor and the investigated EL device are connected in series. Three coefficients are recorded for luminous efficiency calculation:

(1) the EL brightness from the EL device,

(2) the voltage that is applied on the EL device from terminals 3 and 4, and

(3) the voltage drop on the standard resistor from terminal 1 and 2, from which the current that flows through the EL device is obtained.

By multiplying current and voltage on the EL device, the consumed power is achieved. The luminous efficiency is calculated by dividing the brightness by the consumed power.

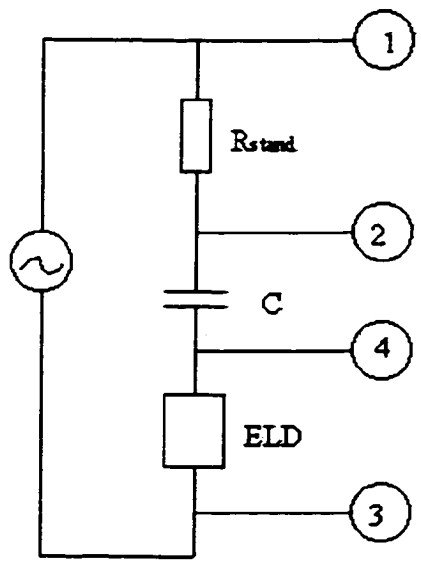

Figure 3.11 The circuit for luminous efficiency measurement.

3.5.2 Photoluminescence (PL) Properties

A He:Cd laser with a wavelength of 325nm was utilized to excite PL from the phosphor layers in this study. PL measurement was carried out at room temperature. The emission spectrum from 330nm to 800nm was recorded. In order to compare the

Reproduced with permission of the copyright owner. Further reproduction prohibited without permission.

intensity from different samples, all samples were glued on one piece of glass to avoid the intensity variation from different samples. In this way, the intensities from the whole set of samples can be compared.

Reproduced with permission of the copyright owner. Further reproduction prohibited without permission.

CHAPTER 4
ZnS:Mn WITH KCl AS A CO-DOPANT

4.1 Introduction

This Chapter presents the results from ACTFEL devices with KCl co-doped phosphor films after different RTA conditions, including EL properties (threshold voltage/field, brightness, EL spectra, and luminous efficiency), PL properties, and microstructure characterization results, form XRD, TEM, EDS and SIMS. For comparison, results from samples without KCl after the same RTA processing are also discussed.

4.2 Background

The microstructure of the as-sputtered films contains many lattice defects. There are two different grain morphologies across the thickness. At the insulator/phosphor interface, there is an equiaxed grains layer. The grain size in this layer is extremely fine. With further growth of the film, the grains become mostly columnar. TEM micrographs that clearly depict these characteristics are presented in the Results and Discussion section. The lattice defects can be either scatter centers, trap sites for hot electrons and/or non-radiative paths for recombination, which are bad to EL performance. To reduce the

Reproduced with permission of the copyright owner. Further reproduction prohibited without permission.

defect density and improve the crystallinity in the equiaxed grain layer and the columnar grain region, post-sputter anneals are necessary. However, since the device is a multi-layered structure and the glass transition temperature of the Corning 7059 glass substrate is only 598°C [3], both annealing time and temperature are limited. To maximize the annealing effects at a limited time and temperature regime, co-dopants are introduced into the systems.

4.3 Results and Discussions

Anneals were conducted from 600°C to 800°C with intervals of 50°C for 5 minutes in nitrogen on both co-doped and blank ZnS:Mn ACTFEL devices.

4.3.1 Secondary Ion Mass Spectrometry (SIMS)

SIMS was carried out on samples to characterize the diffusion of KCl co-dopant. The analyzed secondary ions are Zn^{2+}, Mn^{2+}, K^{+}, Cl^{-} and S^{2-} ions. Since the concentration of the co-dopant in the vicinity of the interface is of interest, aluminum, which exists in the ATO sub-layer, was detected to indicate the insulator/phosphor interface position. The high zinc count rate in the ATO film is an artifact resulted from the mass interference between Zn^{2+} (m/e = 64), and TiO^{+} (m/e = 64) from ATO. Figures 4.1 and 4.2 are the profiles from ZnS:Mn without and with KCl samples, as-deposited (Figure 4.1a), after annealing at 700°C or 800°C (Figures 4.1b and 4.1c), as-deposited with KCl (Figure 4.2a), after annealing at 600°C, 650°C, 700°C, and 800°C (Figures 4.2 b, 4.2c, 4.2d and 4.2e), respectively.

Reproduced with permission of the copyright owner. Further reproduction prohibited without permission.

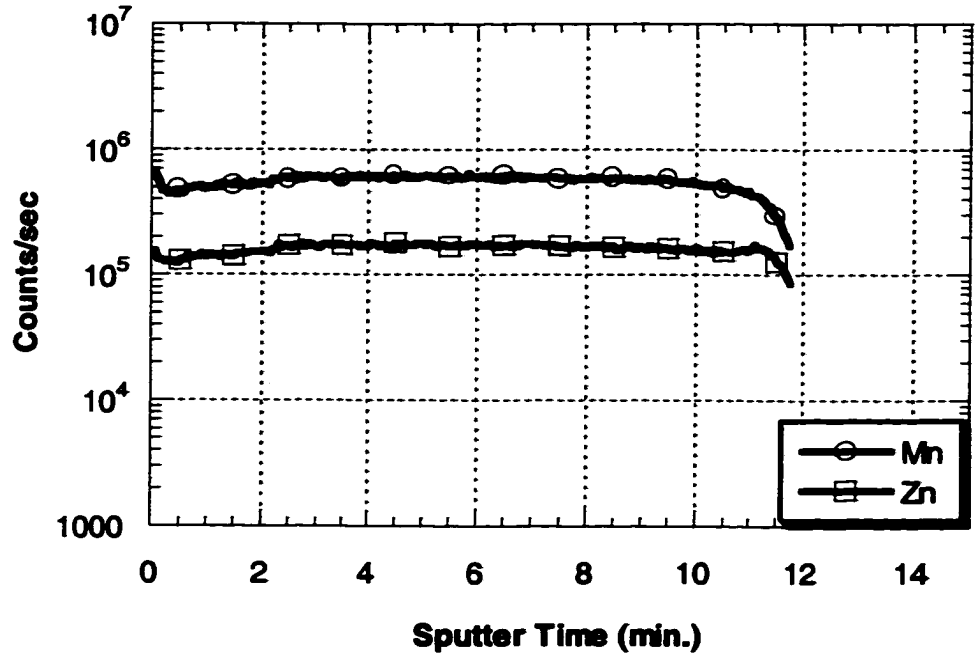

(a)

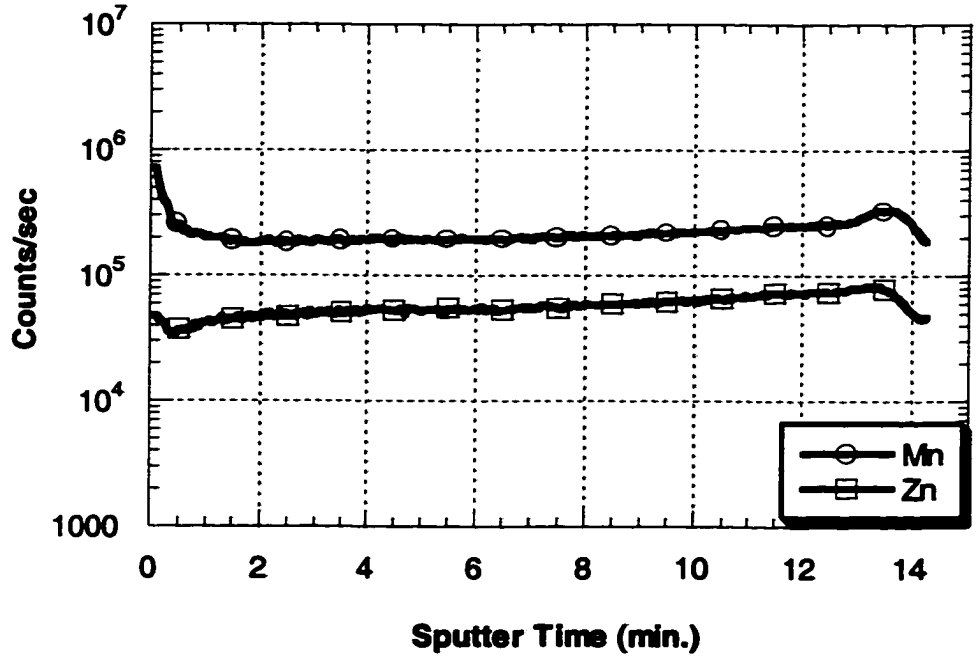

(b)

Figure 4.1 SIMS profiles from ZnS:Mn films (a) as-deposited, (b) after 5 minutes of RTA at 700°C, and (c) 800°C.

Reproduced with permission of the copyright owner. Further reproduction prohibited without permission.

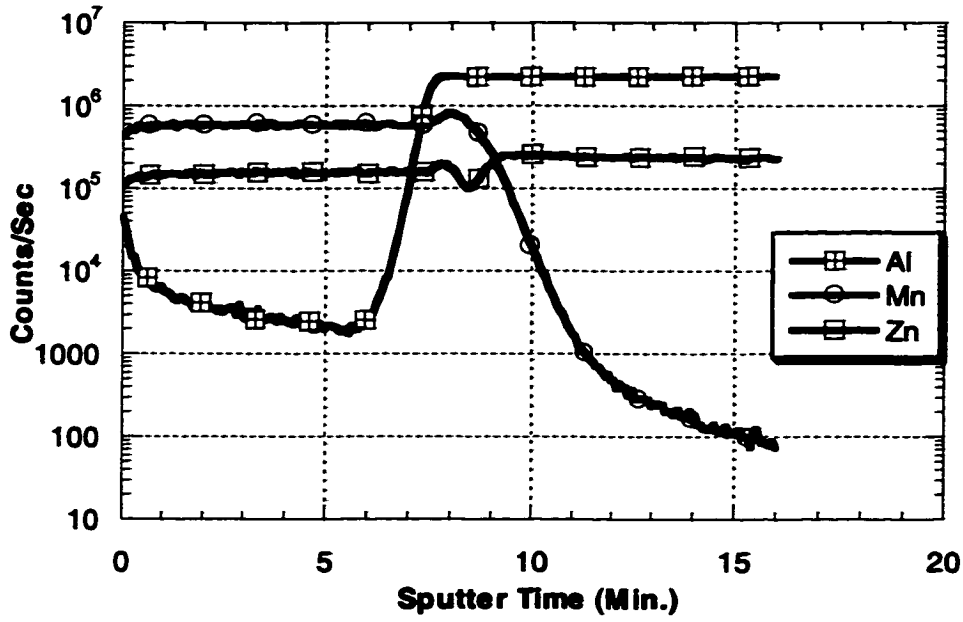

(c)

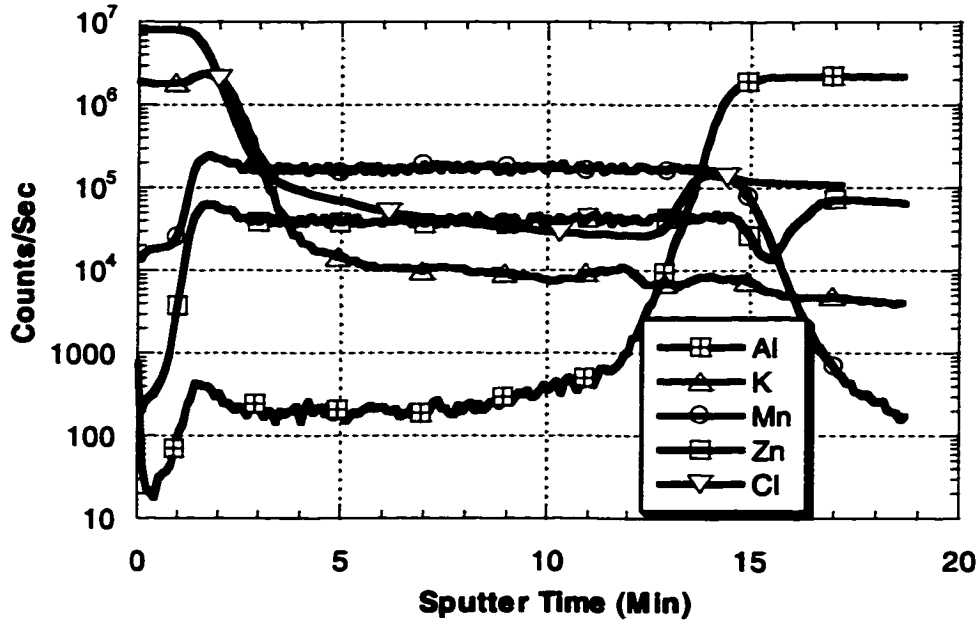

(a)

Figure 4.2 SIMS profile of (a) as-deposited ZnS:Mn films with KCl, after 5 minutes of annealing at (b) 600°C, (c)650°C, (d)700°C, and (e)800°C.

Reproduced with permission of the copyright owner. Further reproduction prohibited without permission.

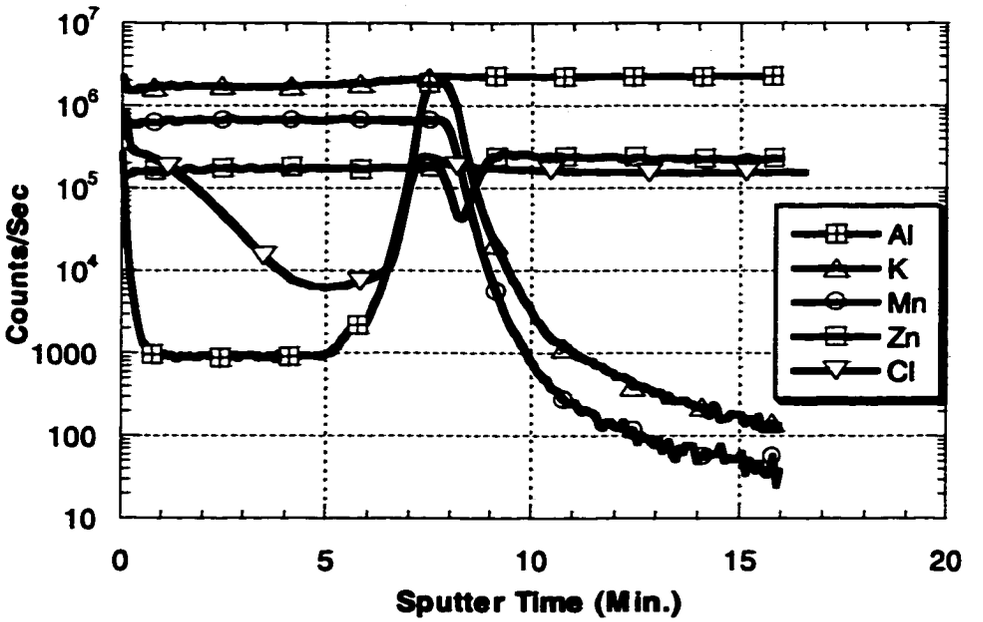

(b)

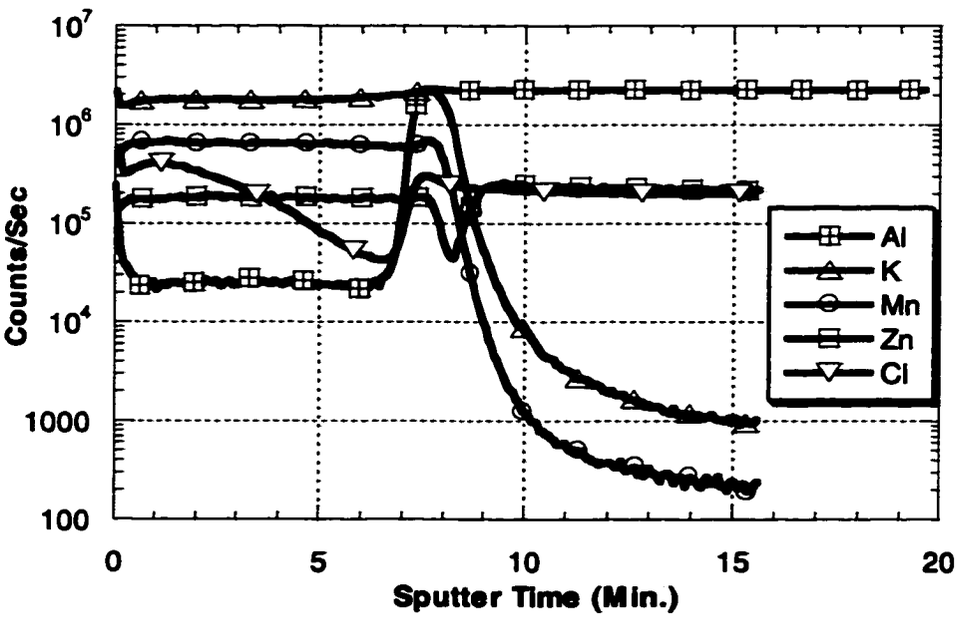

(c)

Reproduced with permission of the copyright owner. Further reproduction prohibited without permission.

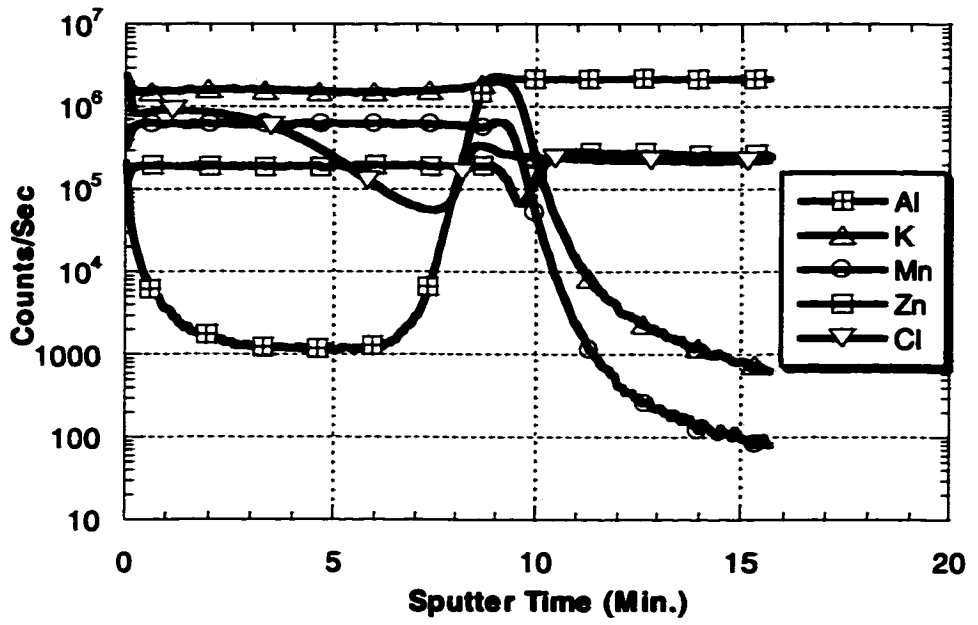

(d)

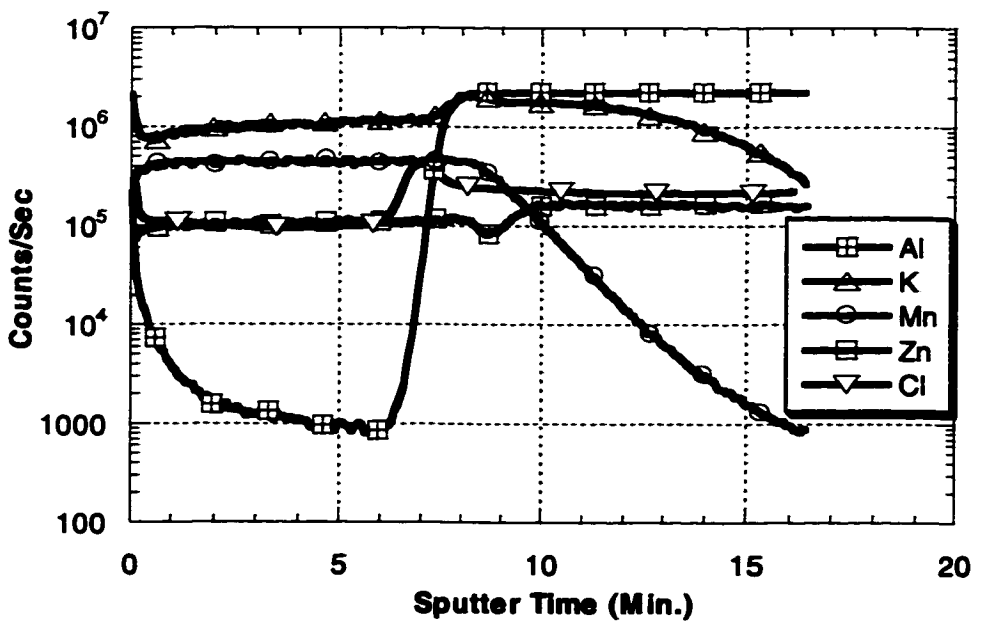

(e)

Reproduced with permission of the copyright owner. Further reproduction prohibited without permission.

In the as-deposited sample without KCl, Mn and S are uniformly distributed over the entire film. The insulator/phosphor interface is sharp. Five minutes of anneal at 700°C or 800°C does not change this situation. No diffusion of Mn^{2+} is detected.

Figure 4.2a is the profile from an as-deposited sample with a layer of evaporated KCl on top. Both K and Cl have much higher count rates in the first three minutes of sputter than in the rest of the film, while the count rates from all the other elements have the opposite trend. This clearly indicates the existence of a layer of KCl. In those annealed KCl doped samples, K has a uniform distribution in the phosphor layer and a sharp drop in the ATO layer in all cases, except after 5 minutes anneal at 800°C (Figure 4.2e), which shows extensive K diffusion into the ATO layer. The diffusion of Cl shows an increasing tendency with temperature. The higher the annealing temperature, the more completed is the Cl diffusion. The high Cl count rate in the ATO layer is from the ALE deposition precursors. As shown in Figures 4.2b, 4.2c, and 4.2d, the Cl profiles display a decreasing gradient in the phosphor layer with increasing temperature. In sample annealed at 800°C, the gradient becomes zero. A uniform Cl distribution in phosphor layer is detected. Also in this sample, Mn diffusion into the ATO layer is detected. It seems the diffusion rates of K and Cl are quite different in ZnS:Mn, with K being much faster than Cl. It is possible that the diffusion mechanisms of these two species are different, which will be further addressed in later sections. The insulator/phosphor interface is sharply defined in all the samples except the one annealed at 800°C.

Although K and Cl have comparable ionic radii (1.51Å for K^+ and 1.67Å for Cl^-), they seem to take different diffusion mechanisms. To investigate the diffusion of K, the K/Zn ratios from the as-deposited and the ones after anneal are plotted in Figure 4.3. It

Reproduced with permission of the copyright owner. Further reproduction prohibited without permission.

can be seen that there is little difference among the annealed samples. The temperature dependence is very small. This implies that the diffusion barrier for K into ZnS is low and thus the diffusivity of K in ZnS is very large. This is consistent with the observation that alkaline elements have large diffusivities in other systems. It is speculated that K takes either the grain boundaries or interstitials as its diffusion paths. Unlike the diffusion of K, Cl seems to have more temperature dependence, which suggests a different diffusion mechanism that associates with higher diffusion barrier. Further conclusions will be presented later with other results.

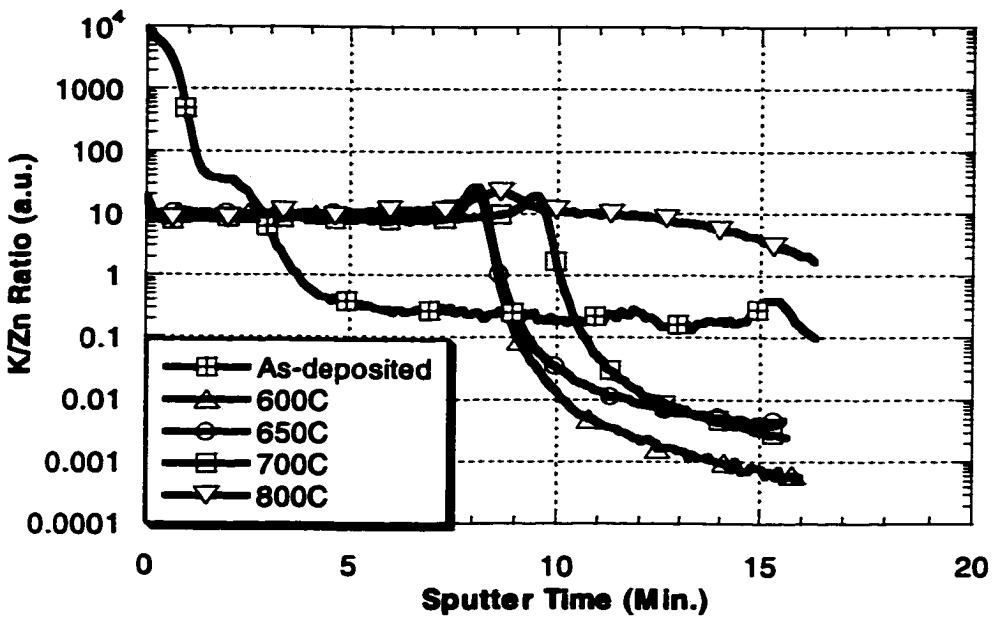

Figure 4.3 K/Zn ratios from as-deposited and annealed samples.

4.3.2 Transmission Electron Microscopy (TEM)

Both XTEM and PTEM samples were investigated to characterize the effect of annealing and KCl co-dopant on the microstructure of ZnS:Mn thin films. Based upon SIMS results, samples with and without KCl after annealing at 650°C and 700°C were

Reproduced with permission of the copyright owner. Further reproduction prohibited without permission.

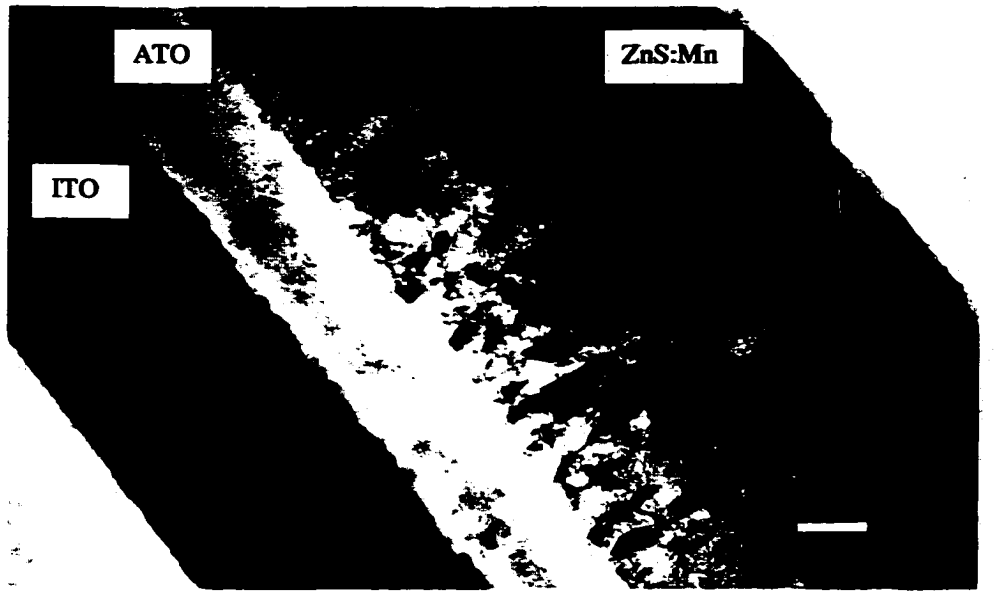

(a)

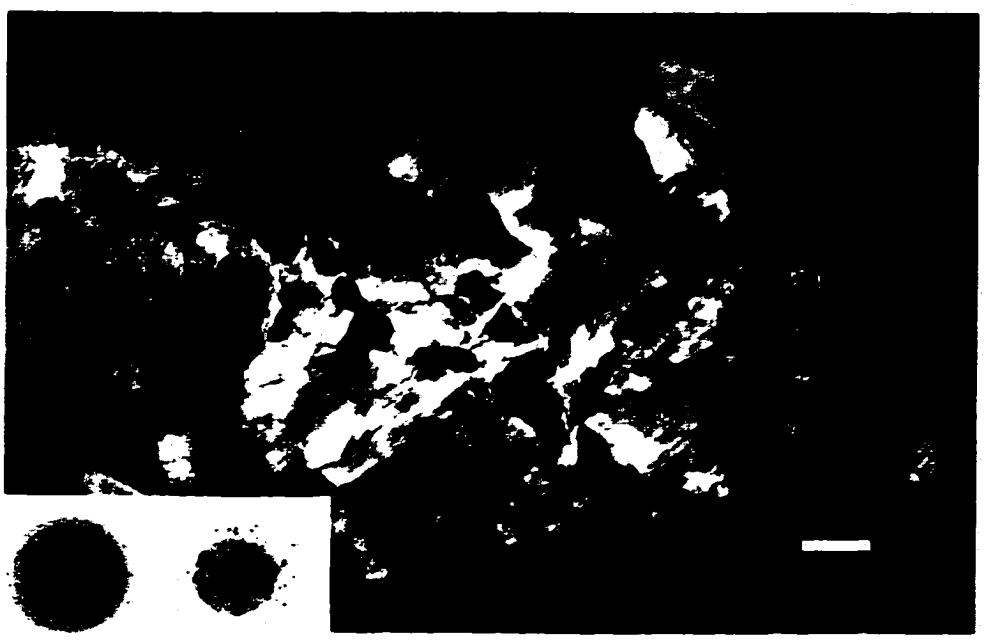

(b)

Figure 4.4 TEM micrographs taken from the ACTFEL device with as-deposited ZnS:Mn phosphor. (a) XTEM, (b) PTEM and diffraction patterns. (Bar = 100nm)

Reproduced with permission of the copyright owner. Further reproduction prohibited without permission.

chosen for this experiment. Figure 4.4a and 4.4b, are the XTEM and PTEM bright field images and diffraction patterns from the as-deposited ZnS:Mn phosphor, while Figures 4.5 and 4.6 are from samples without KCl after RTA at 650°C and 700°C, respectively. All the bars shown in the micrographs are 100nm in length.

From Figure 4.4a, there are two types of grain morphologies. Close to the insulator/phosphor interface is a layer of very fine equiaxed grains. It is impossible to quantify the grain size from the bright field image due to the transmission nature of TEM. An estimated grain size from a limited number of grains gives a diameter of around 10nm. The thickness of this layer is roughly 100nm. With the growth of the film, columnar grains with slightly increased diameters form. Consequently, some of the grains disappear during growth, suggesting limited but finite grain growth occurred during deposition. Most of the grain boundaries are hard to define in the bright field image. This microstructure is typical of films by sputtering deposition and other PVD methods. Diffraction patterns from this sample show the sample has polycrystalline nature. There are a large amount of contrast bands in the columnar grains, which are believed to be certain types of lattice defects. The nature of these defects is determined by high-resolution transmission electron microscopy (HRTEM), which will be presented in Chapter 5.

The average diameter of the columnar grains is measured from a PTEM sample near the top insulator/phosphor interface of the sample. Figure 4.4b shows one of the micrographs taken from this foil. It is much easier to see that many grain boundaries are poorly defined in this micrograph. The average grain size measured in term of mean linear intercept, λ [86], is 89nm in this sample. Due to the sample preparation technique

Reproduced with permission of the copyright owner. Further reproduction prohibited without permission.

used in this study, the electron transparent area is large, which allows measurement of a large population of grains. The inset in Figure 4.4b is a diffraction pattern taken from a PTEM foil, showing the polycrystalline nature of the as-sputtered film. In addition, the grains are not completely randomly oriented. The texture of the polycrystalline ZnS:Mn will be further discussed after XRD data are presented. A diffraction pattern taken from a smaller area also shown on the right of the inset in Figure 4.4b shows twin spots and striations on certain diffraction spots.

Comparing Figure 4.5a with Figure 4.4a, slight grain growth occurred in both equiaxed and columnar grains during annealing at 650°C. However, the equiaxed grain layer can still be observed, and the defect density is still high in the columnar grains, as evident from the contrast bands inside grains. Most of the grain boundaries are still barely definable, although they are better than in the as-deposited sample. The grain size distribution is very broad, with an average columnar grain diameter of 126nm determined by measuring about 100 grains from the PTEM image.

Annealing at 700°C does not give rise to a significant change to the microstructure of ZnS:mn phosphor film, as shown in Figure 4.6a, although the equiaxed grain layer has a larger grain size. The columnar grain diameter is about the same as the 650°C annealed sample. An average grain size of 132nm from counting about 150 grains is obtained. The diffraction pattern inset in Figure 4.6b indicates no remarkable difference in crystallinity. In both XTEM and PTEM images, the contrast bands with different spacing are much clearer to see inside grains. Notice that the bands in this sample are aligned with certain crystallographic directions/planes.

Reproduced with permission of the copyright owner. Further reproduction prohibited without permission.

(a)

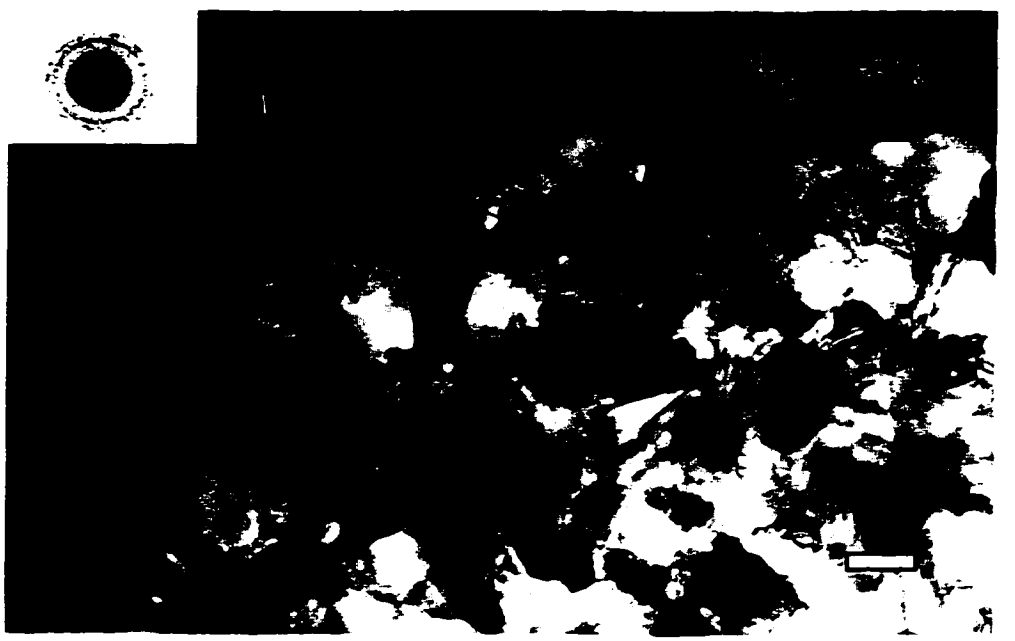

(b)

Figure 4.5 TEM Micrographs taken from ZnS:Mn films after 5 minutes of annealing at 650°C. (a) XTEM, (b) PTEM and diffraction pattern. (Bar = 100nm)

Reproduced with permission of the copyright owner. Further reproduction prohibited without permission.

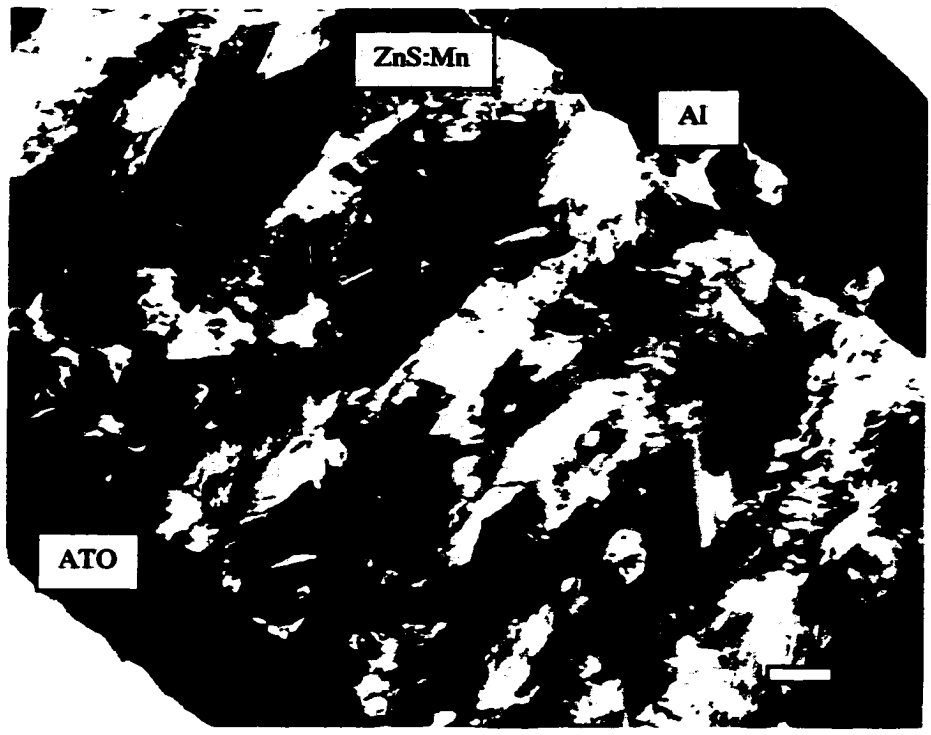

(a)

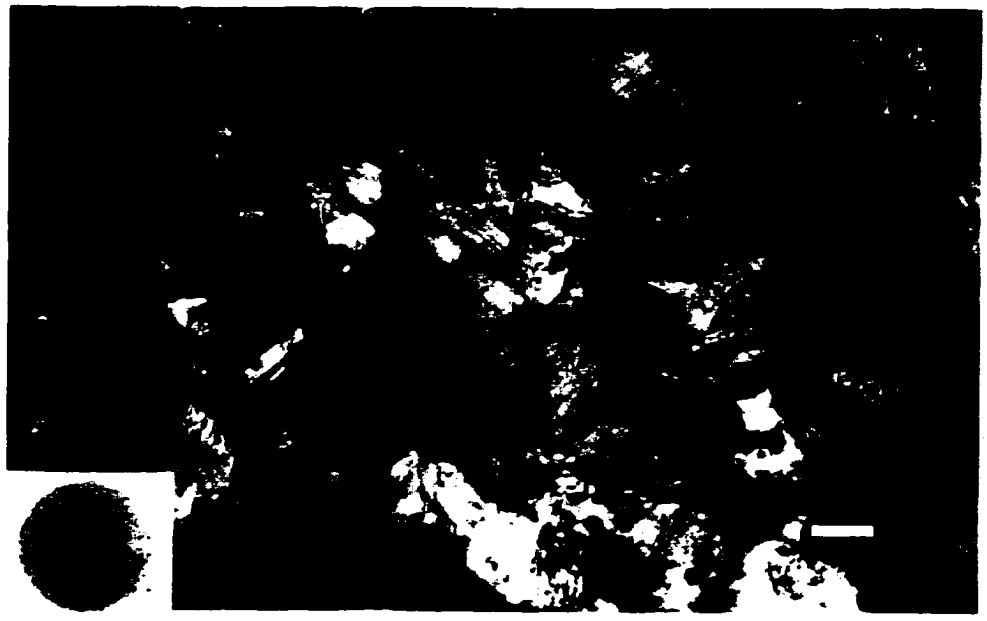

(b)

Figure 4.6 TEM micrographs and diffraction patterns from ZnS:Mn film after 5 minutes annealing at 700°C. (a) XTEM, (b) PTEM and diffraction pattern. (Bar = 100nm)

Reproduced with permission of the copyright owner. Further reproduction prohibited without permission.

Figures 4.7a and 4.7b are a bright field image at higher magnification and the diffraction pattern taken from the imaged area. The striations in the diffraction pattern correspond very well to the contrast bands in the bright field image. In Chapter 5, it will

(a)

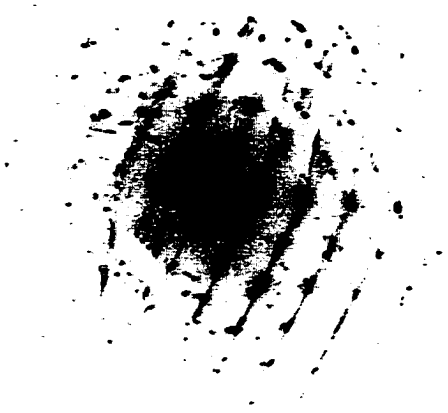

(b)

Figure 4.7 (a) TEM micrograph and (b) diffraction pattern taken from a ZnS:Mn sample after annealing at 700°C, illustrating that the contrast bands are aligned with certain crystallographic direction. (Bar = 100 nm)

Reproduced with permission of the copyright owner. Further reproduction prohibited without permission.

be further proved that these bands lie on {111} planes, which are the closest packed planes in ZnS of both hexagonal and cubic structures.

Figures 4.8 and 4.9 are micrographs taken from the samples with KCl doped ZnS:Mn annealed at 650°C and 700°C, respectively. The XTEM micrograph from the ZnS:Mn,KCl sample annealed at 650°C (Figure 4.8a) looks very similar to that from the ZnS:Mn sample after an RTA at 700°C without KCl (Figure 4.6a). The two kinds of grain morphologies still exist, despite grain growth having occurred during annealing. The bands inside grains can be clearly seen in both micrographs, and they are still in a large amount. However, the PTEM micrograph from this sample, as shown in Figure 4.8b, displays a different morphology from the previous PTEM images. Many grain boundaries are now sharply defined, and most are straight with little curvature. This suggests more grain growth occurred during RTA. The average grain size based upon 176 grains is 151nm, which is higher than its counterpart without KCl that has 126nm as the average grain size.

After an RTA at 700°C for 5 minutes, KCl co-doping of the ZnS:Mn phosphor leads to grain growth and removal of the equiaxed grain layer. The removal of the equiaxed grain layer is evident from comparison of the XTEM micrographs taken from the sample with KCl after RTA at 650°C and 700°C, respectively, as shown in Figures 4.8a and 4.9a. In the latter sample, columnar grains extend through the entire film, from the ATO/phosphor interface to the top. In other words, the microstructure in this sample becomes symmetrical, while in all the previously discussed samples, it is asymmetrical. Moreover, grooves on top surface of the film due to grain growth can be clearly seen from Figure 4.9a. The average grain size value is 187nm based upon a count of 86

Reproduced with permission of the copyright owner. Further reproduction prohibited without permission.

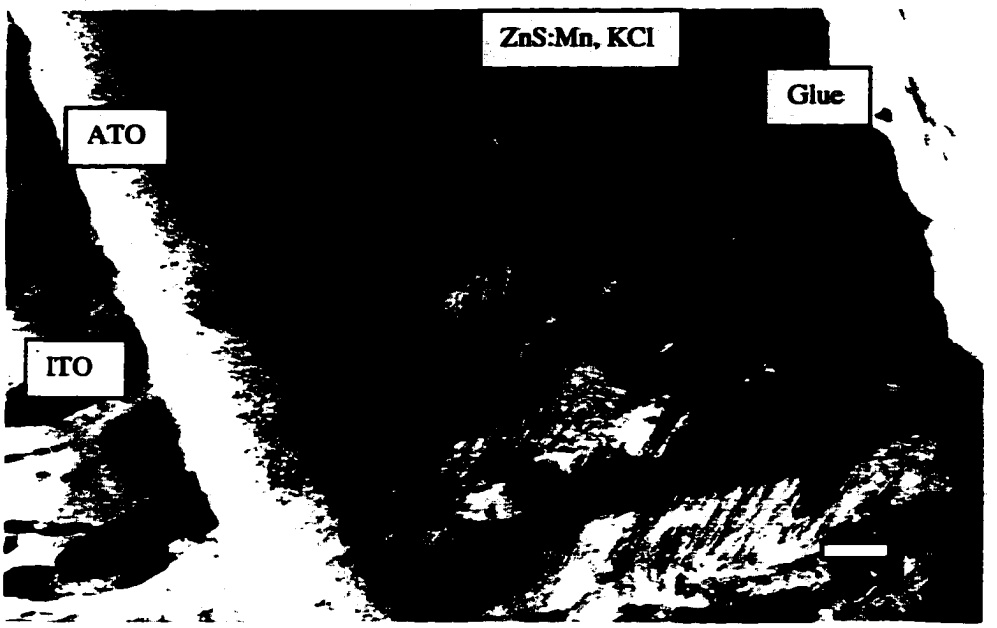

(a)

(b)

Figure 4.8 TEM micrographs from ZnS:Mn, KCl films after 5 minutes of annealing at 650°C. (a) XTEM, (b)PTEM and diffraction pattern. (Bar = 100nm)

Reproduced with permission of the copyright owner. Further reproduction prohibited without permission.

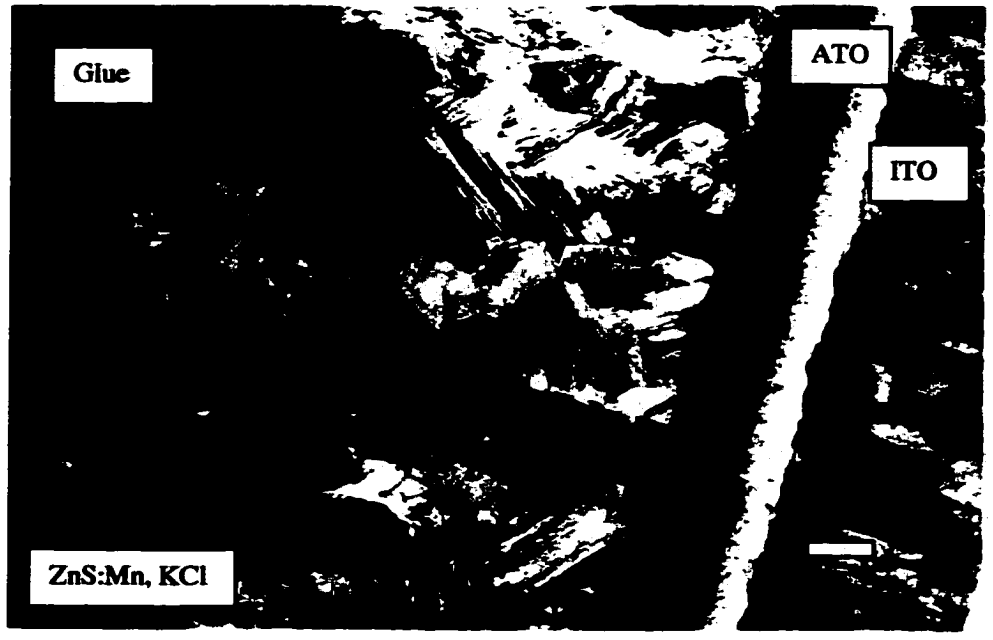

(a)

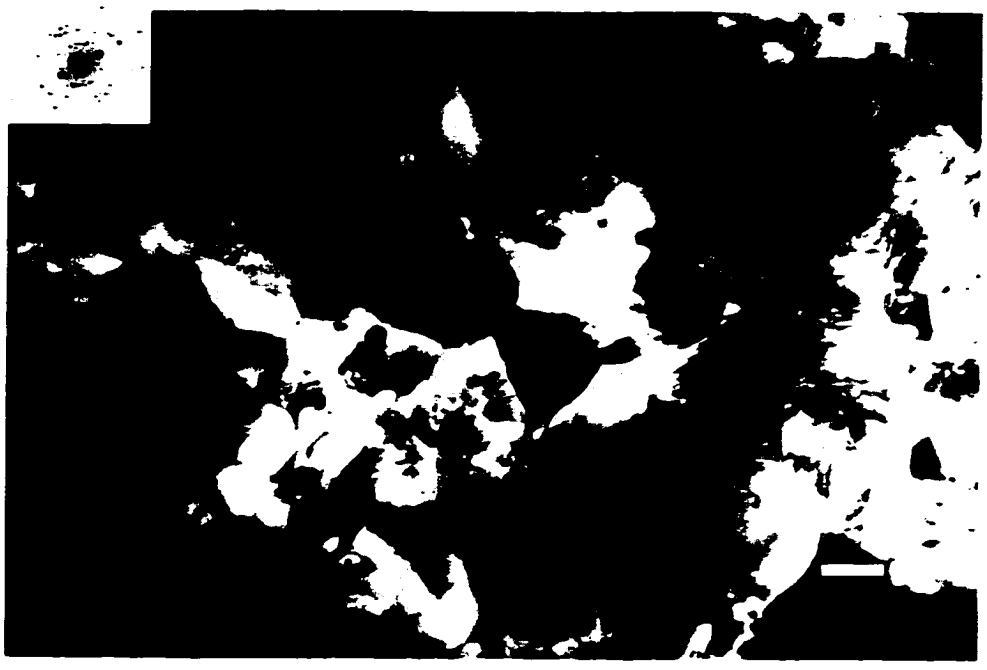

(b)

Figure 4.9 TEM micrographs from ZnS:Mn, KCl after 5 minutes of annealing at 700°C. (a) XTEM, (b) PTEM and diffraction pattern. (Bar = 100nm)

Reproduced with permission of the copyright owner. Further reproduction prohibited without permission.

grains. Introduction of KCl results in bigger grains, but fails to decrease the defect density inside grains. The diffraction patterns in both cases (Figure 4.8b and Figure 4.9b) indicate that texture develops in these samples. Further discussion will be delayed until after the XRD results section.

Since annealing and the introduction of KCl do not significantly reduce the density of the bands within the grains, their nature is intriguing. First, pure ZnS samples are investigated. Figure 4.10 shows the XTEM micrograph and the diffraction pattern of the as-sputtered ZnS film. The features are analogous to the as-sputtered ZnS:Mn film shown in Figure 4.4a. The two different grain morphologies, high density of bands in grains, barely definable grain boundaries, and slight grain growth during deposition are all evident. The diffraction pattern in Figure 4.10b indicates the film is textured as well. Some striations of the diffraction spots corresponding to the bands in the bright field image are also observed.

RTA at 700°C results in very slight grain growth, as seen from Figure 4.11a. But it improves the interface area and results in more clearly defined grain boundaries. Streaks in the diffraction spots are shown in Figure 4.11b, which corresponds to the huge amount of bands in bright field image. It is clear that these bands result from the low stacking fault energy of ZnS [87]. The bands can be stacking faults, microtwins or polytypism. It will be shown below that they are dominated by microtwins and stacking faults. Obviously, 1mol% of Mn does not make much difference in the ZnS microstructure. This is consistent with the fact that the ionic radii of Mn^{2+} and Zn^{2+} ions are similar (0.8Å vs. 0.74Å). Besides, they have the same valence.

Reproduced with permission of the copyright owner. Further reproduction prohibited without permission.

(a)

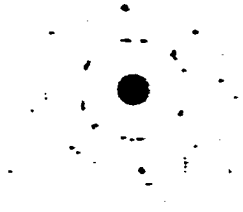

(b)

Figure 4.10 TEM micrographs taken from as-deposited pure ZnS. (a) XTEM, and (b) diffraction pattern. (Bar = 100nm)

Reproduced with permission of the copyright owner. Further reproduction prohibited without permission.

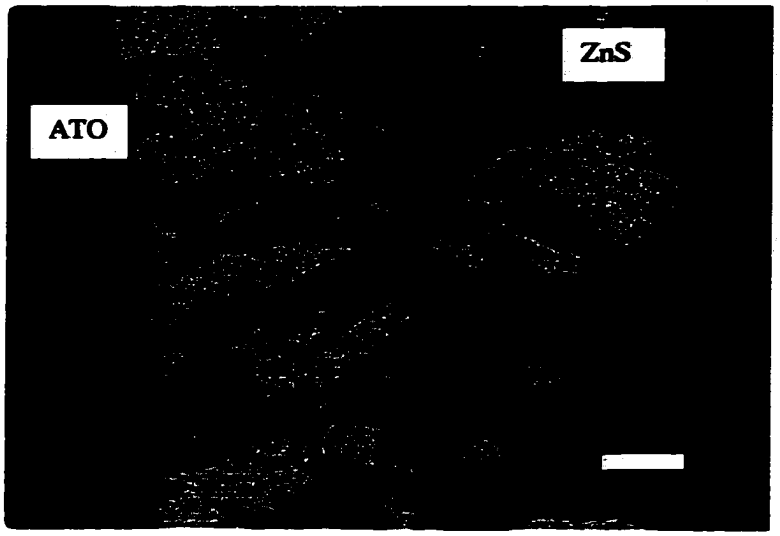

(a)

(b)

Figure 4.11 TEM micrographs taken from pure ZnS film after 5 minutes of annealing at 700°C. (a) XTEM, and (b) diffraction pattern. (Bar = 100nm)

4.3.3 Compositional Analysis by Energy Dispersive Spectrometry (EDS)

EDS was performed on a PTEM foil of the ZnS:Mn,KCl sample after RTA at 700°C for 5 minutes. An area with the grain boundaries "edge-on" to the detector is shown in Figure 4.12. Four grain boundaries and five spots inside different grains are detected, as numbered 1 to 9 in Figure 4.12. The composition line scans across the grain boundaries 1, 3, and 9 are shown in Figure 4.13. Grain boundary 7 is not detected by line

Reproduced with permission of the copyright owner. Further reproduction prohibited without permission.

scan. The line profiles show comparable concentration levels in all the adjacent grain pairs. A very slight drop in counts indicates the grain boundary position, as indicated in each plot, since grain boundaries have relatively open lattice structure. This will be more clearly illustrated by the stationary probe data presented later. Because of the low concentration of K^+, Mn^{2+} and Cl^- ions, signals from these species cannot be detected by line scans. Therefore, a stationary probe with longer sampling time is used at the numbered spots in Figure 4.12. Please note, boundary 9 is not detected by stationary probe. The data are summarized in Table 4.1. Chlorine is still not detectable in any sampling area due to its low atomic number and low concentration.

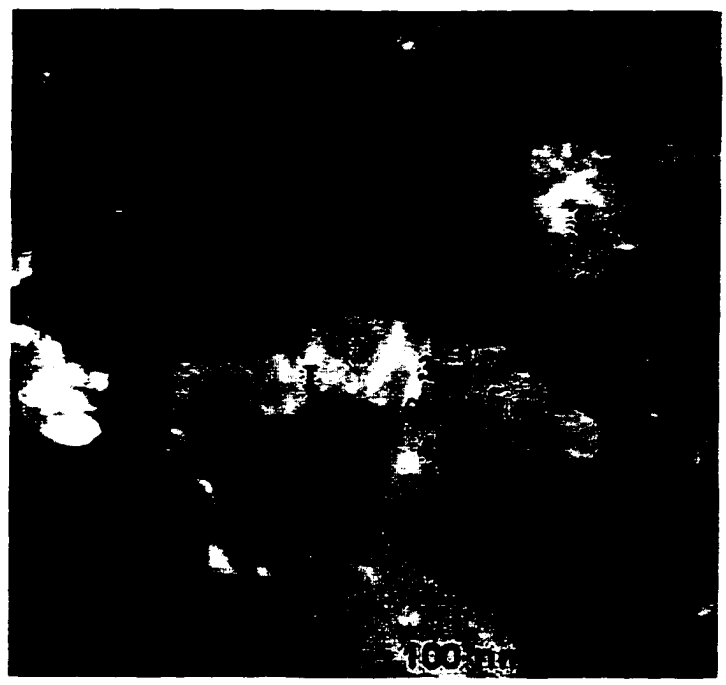

Figure 4.12 TEM micrograph showing the region where EDS was performed.

Reproduced with permission of the copyright owner. Further reproduction prohibited without permission.

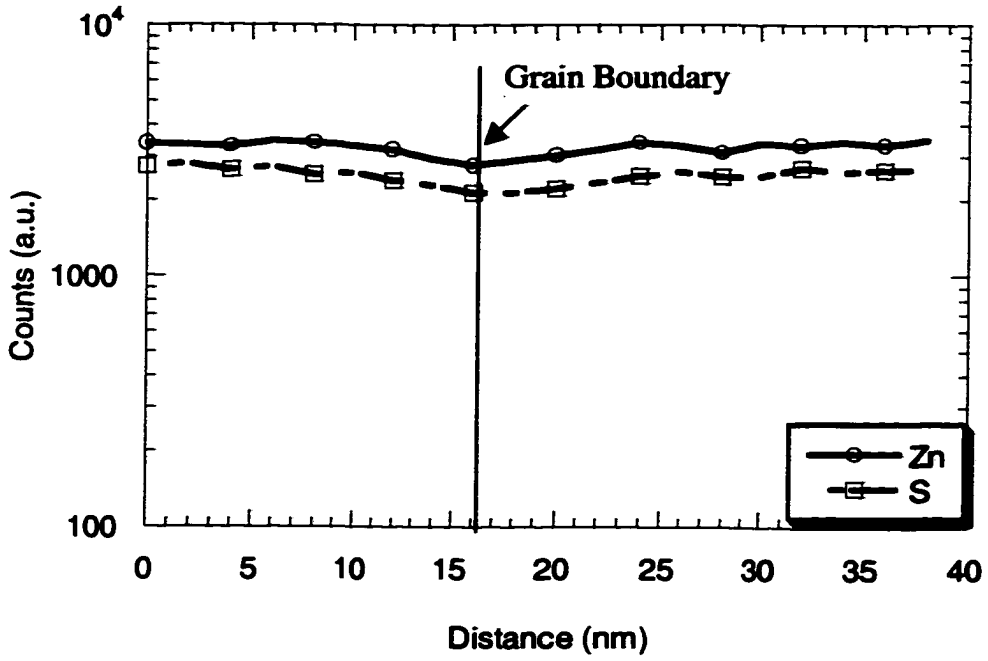

(a)

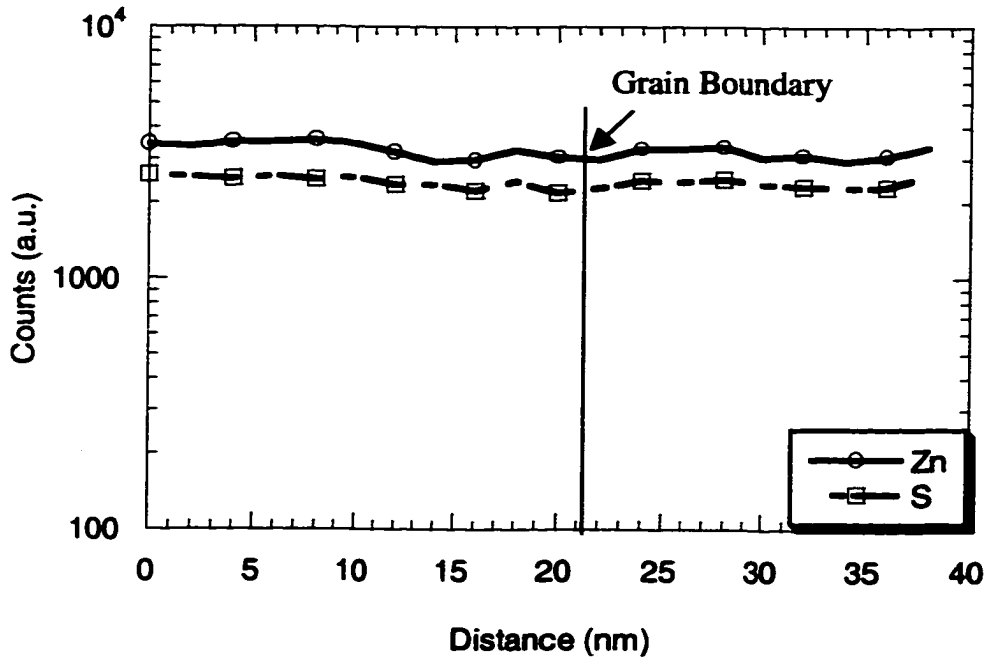

(b)

Figure 4.13 38nm line profiles of Zn and S elements across grain boundary (a)#1, (b)#3, and (c)#9.

Reproduced with permission of the copyright owner. Further reproduction prohibited without permission.

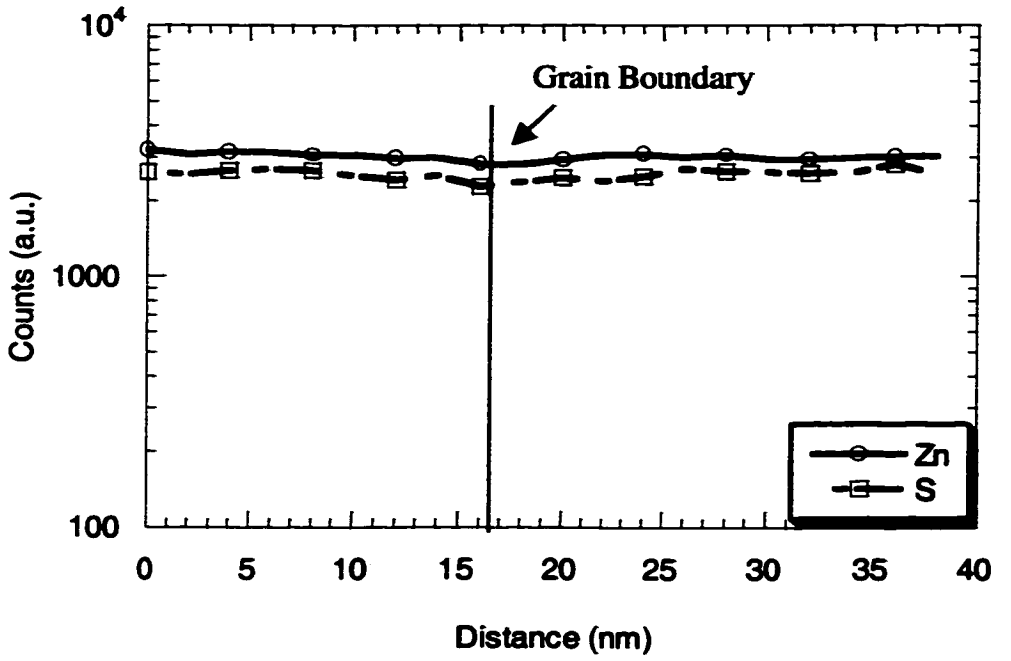

(c)

Table 4.1 Stationary Probe EDS Data from ZnS:Mn,KCl after RTA at 700°C.

Region	Counts (a.u.)			
	Zn	S	K	Mn
1 (GB)	31441	26883	296	170
2	48770	41754	418	423
3 (GB)	42650	34967	268	287
4	55041	46675	424	246
5	49860	42394	462	372
6	59395	51018	302	467
7 (GB)	55346	47452	299	295
8	65376	56214	303	427

From the stationary probe data, it is clear that the ratio of Zn to S is constant over all the detected areas. The lower counts at grain boundaries (points 1, 3 and 7) are obvious in all the detectable species, which is due to the open structure at the grain

Reproduced with permission of the copyright owner. Further reproduction prohibited without permission.

boundaries. The ratio of Mn to Zn counts is also nearly constant, suggesting Mn^{2+} is uniformly incorporated in the ZnS lattice.

As discussed in the SIMS results section, K diffusion has very little temperature dependence. It is postulated that K diffusion mechanisms be either grain boundary related or interstitial related. If the grain boundaries were the preferred diffusion paths for K, K segregation to the grain boundaries would be expected. However, EDS data show obviously lower counts of K^+ ions at grain boundaries versus inside grains, similar to the other species, which means grain boundary diffusion cannot be the operating mechanism. Considering its ease of diffusion at relatively low temperatures, and the difficulty to substitute either Zn^{2+} or Mn^{2+} due to its much larger ionic radius, it is believed that the K diffusion is associated with interstitials. Further conclusion is drawn in next section after the XRD results are presented.

4.3.4 X-Ray Diffractometry (XRD)

Texture is an important issue in ZnS:Mn phosphors, since it affects the electrical properties of the ZnS host lattice, as reported in reference [45]. Introduction of KCl and/or annealing may give rise to a texture different from the growth texture from sputter. XRD is used to evaluate the crystal structure and the texture after different processing. Please note that the 2θ scan only generates information from the crystal plane parallel to the film surface [80]. Table 4.2 summarizes the XRD data regarding the effect of annealing with and without KCl co-doping. The relative intensities from certain selected XRD peaks versus different processing parameters are shown as a bar chart in Figure 4.14.

Reproduced with permission of the copyright owner. Further reproduction prohibited without permission.

Table 4.2 XRD data of the effects of annealing and KCl co-doping.

				As-deposited		700°C	
Index	2θ	Inten. (a.u.)	Relative %	Counts (a.u.)	Relative %	Counts (a.u.)	Relative %
(01-10)	26.9	100	13.6	96	4.9	0	0.0
(0002)+(111)	28.5	184	25.0	961	49.4	1063	49.8
(10-11)*	30.5	87	11.8	458	23.6	497	23.3
(200)	33.1	10	1.4	71	3.7	123	5.8
(10-12)	39.6	28	3.8	17	0.9	0	0.0
(220)+(11-20)	47.5	132	18.0	85	4.4	98	4.6
(10-13)	51.8	54	7.3	0	0.0	0	0.0
(20-20)	55.5	11	1.5	0	0.0	0	0.0
(311)+(11-22)	56.3	77	10.5	202	10.4	303	14.2
(20-21)	57.6	12	1.6	0	0.0	0	0.0
(0004)+(222)	59.1	4	0.5	28	1.4	15	0.7
(20-22)	63.6	6	0.8	0	0.0	0	0.0
(400)	69.5	6	0.8	17	0.9	34	1.6
(20-23)	73.9	15	2.0	0	0.0	0	0.0
(331)	76.8	9	1.2	0	0.0	0	0.0
(420)	79.1	2	0.3	0	0.0	0	0.0
(10-15)	82.3	11	1.5	0	0.0	0	0.0
(422)	88.5	9	1.2	9	0.5	10	0.5
		735	100.0	1944	100.0	2133	100.0

Reproduced with permission of the copyright owner. Further reproduction prohibited without permission.

Table 4.2 continued.

800°C		600°C		650°C	
Counts (a.u.)	Relative %	Counts (a.u.)	Relative %	Counts (a.u.)	Relative %
161	7.8	0	0.0	0	0.0
912	43.9	745	47.6	876	47.1
506	24.4	449	28.7	515	27.7
119	5.7	79	5.0	106	5.7
18	0.9	0	0.0	0	0.0
50	2.4	66	4.2	92	5.0
0	0.0	0	0.0	0	0.0
0	0.0	0	0.0	0	0.0
256	12.3	177	11.3	216	11.6
0	0.0	0	0.0	0	0.0
23	1.1	20	1.3	20	1.1
0	0.0	10	0.6	0	0.0
32	1.5	20	1.3	24	1.3
0	0.0	0	0.0	0	0.0
0	0.0	0	0.0	9	0.5
0	0.0	0	0.0	0	0.0
0	0.0	0	0.0	0	0.0
16	0.8	0	0.0	0	0.0
2077	100.0	1566	100.0	1858	100.0

Reproduced with permission of the copyright owner. Further reproduction prohibited without permission.

Table 4.2 continued.

700°C, w/ KCl		750°C, w/ KCl		800°C, w/ KCl	
Counts (a.u.)	Relative %	Counts (a.u.)	Relative %	Counts (a.u.)	Relative %
0	0.0	0	0.0	0	0.0
1005	52.8	1018	43.3	686	34.7
445	23.4	595	25.3	529	26.8
102	5.4	204	8.7	296	15.0
0	0.0	0	0.0	27	1.4
77	4.0	62	2.6	36	1.8
0	0.0	0	0.0	0	0.0
0	0.0	0	0.0	0	0.0
240	12.6	372	15.8	313	15.8
0	0.0	0	0.0	0	0.0
0	0.0	21	0.9	18	0.9
0	0.0	0	0.0	0	0.0
35	1.8	59	2.5	71	3.6
0	0.0	0	0.0	0	0.0
0	0.0	0	0.0	0	0.0
0	0.0	0	0.0	0	0.0
0	0.0	0	0.0	0	0.0
0	0.0	22	0.9	18	0.9
1904	100.0	2353	100.0	1976	100.0

Reproduced with permission of the copyright owner. Further reproduction prohibited without permission.

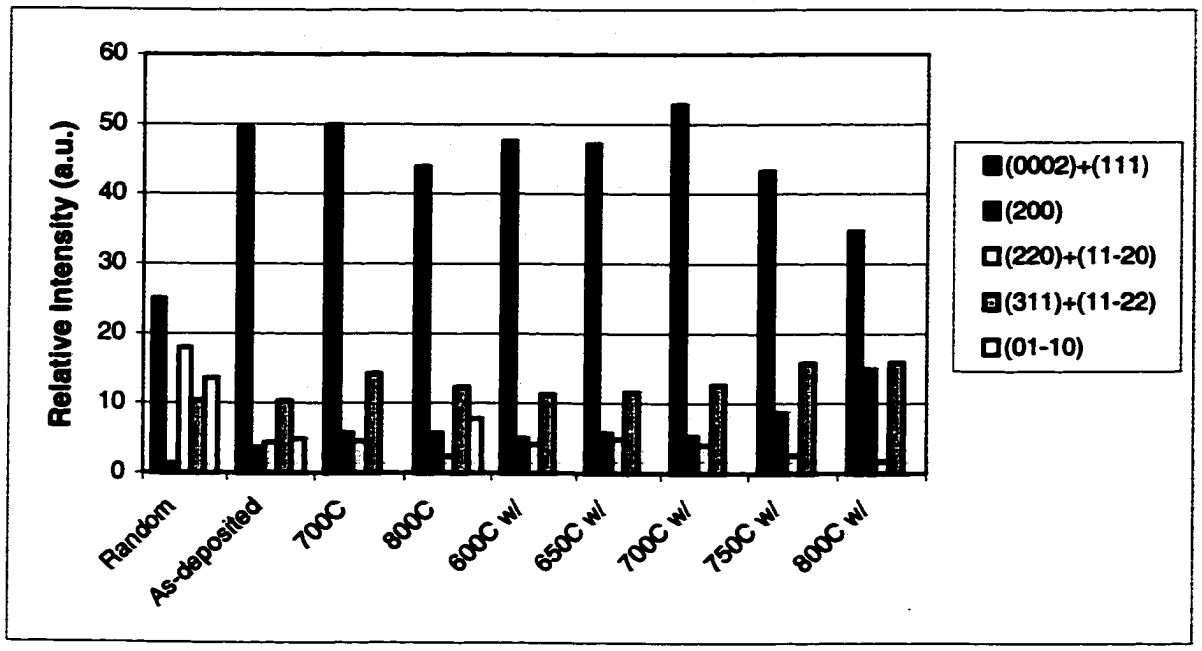

Figure 4.14 XRD results of certain orientations from samples with and without KCl upon annealing.

As introduced in Chapter 2, ZnS hexagonal structure is stable above 1024°C, while the cubic structure is stable below 1024°C, as shown in Figure 2.7. Due to its low stacking fault energy and the nature of magnetron sputtering, the as-deposited films have a mixture of both structures, in spite of the deposition temperature of 180°C being well below the phase transformation temperature. This can be seen from the XRD spectrum from the as-deposited film in Figure 4.15. Due to the low resolution of the X-ray diffractometer used in this study, some peaks from the cubic and haxagonal phases are not separable, such as c(111) and h(0002), and c(311) and h(11-22), as shown in Figure 4.15. Comparing with a random orientation sample, c(111) + h(0002), c(200) and c(222) + h(0004) show higher relative intensities in the as-deposited films, where "c" stands for cubic and "h" for hexagonal. On the other hand, h(10-12), c(422), c(311) + h(11-22) and c(220) + h(11-20) have lower relative intensities, suggesting that the growth texture of

Reproduced with permission of the copyright owner. Further reproduction prohibited without permission.

ZnS:Mn film is c(200) with slight c(111) + h(0002) combination. The peak at 2θ of 30.5° is a result of both diffraction from ZnS h(10-11) planes and polycrystalline ITO, thus this peak is not discussed.

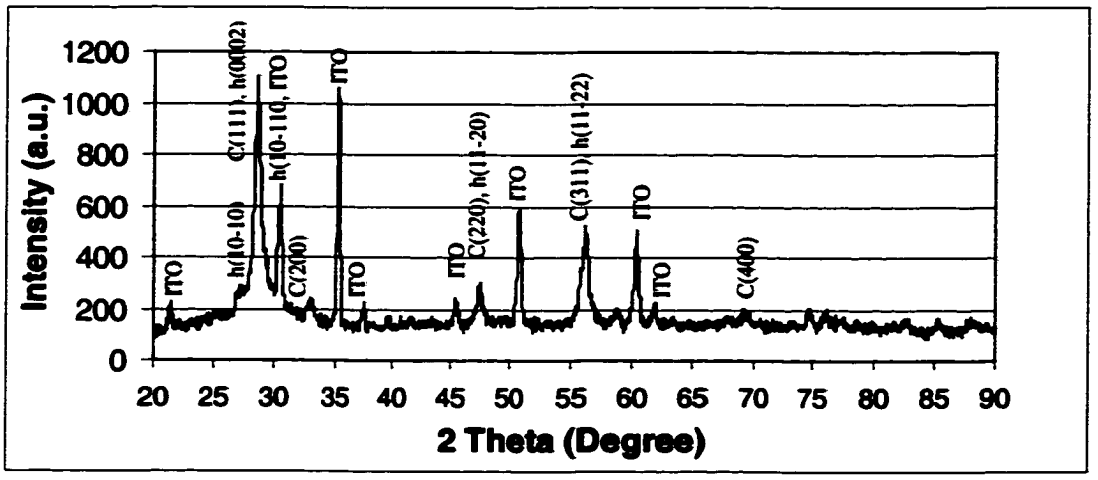

Figure 4.15 XRD spectrum taken from as-deposited ZnS:Mn film showing both hexagonal and cubic structures exist.

With annealing ZnS:Mn for 5 minutes at 700°C or 800°C, no significant changes occur, in terms of texture, except that the relative intensity of the peak from c(311) + h(11-22) is enhanced.

After the KCl is introduced, the annealing temperature dependence of texture is different. First, the disappearance of h(01-10) peak from the hexagonal structure and the increase of the relative intensities of the c(200), c(400), and c(422) cubic peaks show that KCl incorporation into the ZnS:Mn lattice helps to stabilize the cubic structure. This effect appears the strongest for an annealing temperature higher than 750°C. As shown in Figure 4.14, the relative intensities of the combination peak h(0002) + c(111) are comparable up to 700°C, and then show drops from 700°C, while c(200), c(400), and c(311) + h(11-22) show increases after 700°C. In addition, the c(422), which is not

Reproduced with permission of the copyright owner. Further reproduction prohibited without permission.

detectable in samples annealed at temperatures lower than 750°C, starts to show up after annealing at higher temperature. In other words, cubic peaks increase at the expense of the hexagonal peaks in samples annealed with KCl. The apparent texture change from c(111) + h(0002) to c(200) might result from the following two possibilities. One is a real texture change due to growth of c(200) orientated grains at the expense of c(111). The other is from a phase transformation because some of h(0002) is converted to c(200). Both mechanisms may operate simultaneously. In either case, the cubic structure of ZnS is stabilized, and c(200) texture is enhanced by the presence of KCl. This conclusion is consistent with the observation of the contrast bands in the TEM bright field image (Figure 4.9a) having an angle about 55° relative to the film surface.

Recalling the EDS results presented previously, no K segregation is detected at the grain boundaries. It is suspected that KCl must incorporate into the ZnS lattice uniformly. Combining with the information that cubic structure of ZnS is stabilized by KCl, it is found that there is a "big" interstitial site located at (0.5, 0.5, 0.5), as shown in Figure 4.16.

The lattice coefficient of cubic ZnS is 5.4060Å, and the ionic radius of S^{2-} is 1.84Å. The calculated size of this interstitial is sufficiently large for an interstitial ion with radius of less than 1.90Å, thus K^+ will fit. If this is the case, the K diffusion is believed to take interstitial mechanism. The little temperature dependence of K diffusion into ZnS:Mn, which is addressed earlier, is now explainable, since diffusions taking interstitials are always faster and less temperature dependent than other diffusion mechanisms. Considering Cl^- and S^{2-} have comparable ionic radii, (1.67Å for Cl^- and 1.84Å for S^{2-}), a Cl^- can substitute an S^{2-} site. In this way, the high diffusion barrier for

Reproduced with permission of the copyright owner. Further reproduction prohibited without permission.

Cl into ZnS:Mn, as shown by the SIMS results can be explained. To compensate the extra charge, a Zn^{2+} vacancy is expected to present in the lattice for every pair K^+ and Cl^-. In fact, the existence of Zn^{2+} vacancies is thermodynamically preferred in ZnS:Mn thin films, based upon the thermodynamics calculation from reference [88]. The interstitial K^+ and the substitutional Cl^- can both act as donors in ZnS:Mn,KCl [6], whose contribution to EL performance will be discussed later. However, it should be noticed that the interstitial site for K does not exist in ZnS with the hexagonal structure.

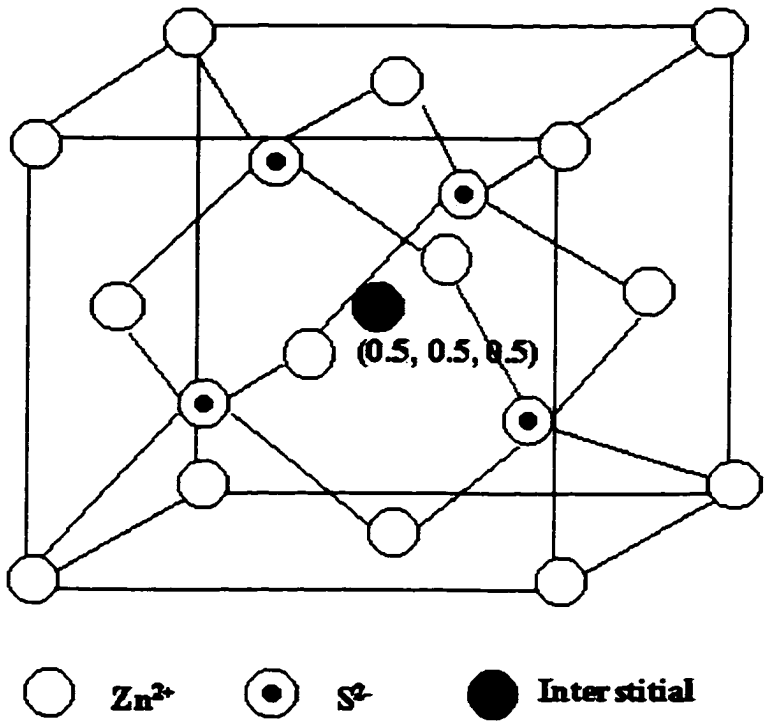

Figure 4.16 A unit cell of cubic ZnS compound showing the interstitial site.

The full width at half maximum (FWHM) can also be obtained from the XRD peaks. This is a measurement of the crystallite size of a polycrystalline sample. Note that the term of crystallite denotes a different feature from grain, and its size may be different from the grain size. A crystallite is generally defined by sub-grain boundaries, such as

Reproduced with permission of the copyright owner. Further reproduction prohibited without permission.

twin boundaries, dislocation cells, rather than by grain boundaries. But crystallite size can be used to characterize the crystallinity, in terms of grain structure and defect density. Figure 4.17 shows the FWHM of the ZnS h(0002)+c(111) peak as a function of the annealing temperature. It is evident that the KCl co-dopant increases the crystallite size much more than only annealing without KCl, particularly at annealing temperature higher than 700°C.

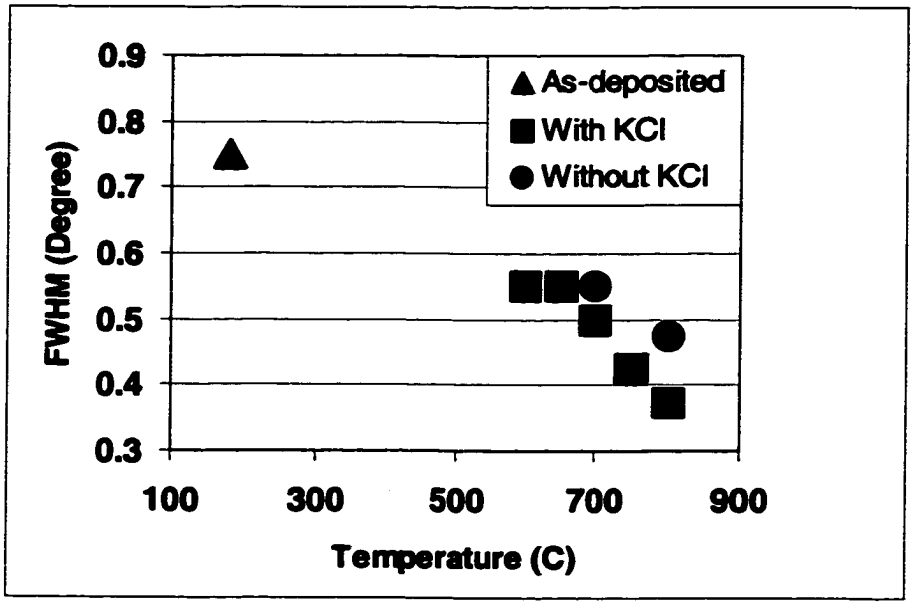

Figure 4.17 The FWHM data from sample with and without KCl upon annealing.

4.3.5 Electroluminescence (EL) Properties

Figure 4.18 shows the EL brightness vs. voltage curves of the samples with and without KCl co-dopant, and the threshold voltages V_{th}, brightness at 40V above the threshold voltage B_{40}, and luminous efficiency at 40V above the threshold voltage η_{40},

Reproduced with permission of the copyright owner. Further reproduction prohibited without permission.

are summarized in Table 4.3. Since all samples are from the same batch of deposition, the thickness is uniform and equal to 0.98μm.

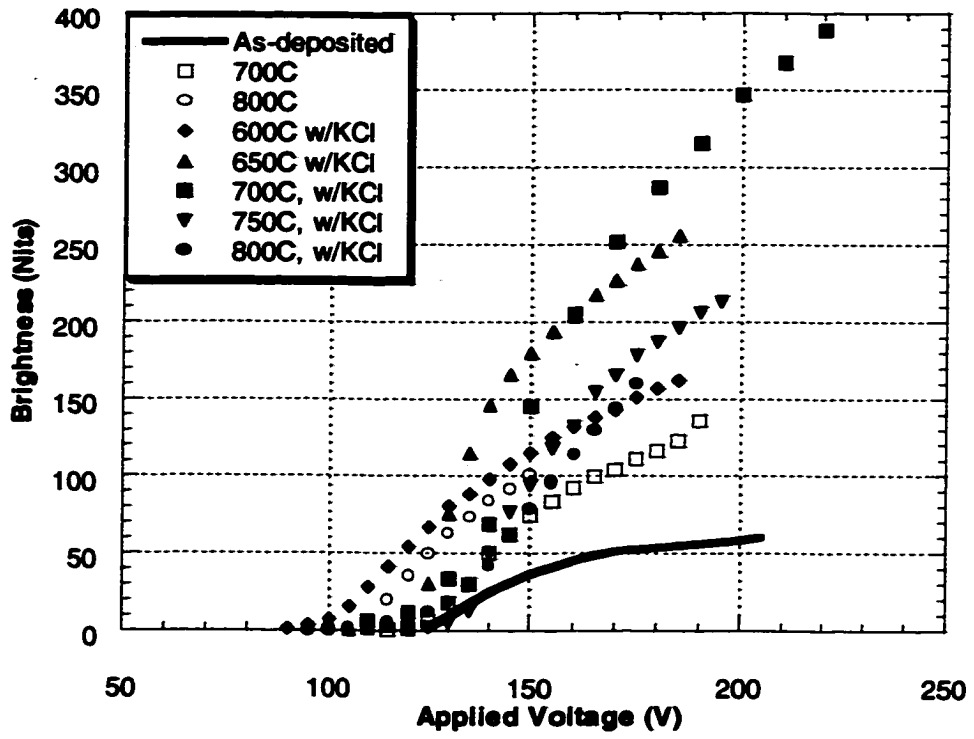

Figure 4.18 EL brightness as a function of applied voltage from samples with and without KCl after different RTA processes.

Table 4.3 A summary of EL properties from samples with and without KCl

		V_{th} (V)	B_{40} (Nits)	η at B_{40} (lm/W)
Without KCl	As-deposited	125	48.7	0.2275
	700°C	125	99.6	0.4463
	800°C	110	101	0.5428
With KCl	600°C	105	97.9	0.5073
	650°C	120	204	0.7843
	700°C	130	252	0.9879
	750°C	135	178	0.9324
	800°C	130	144	0.9464

Reproduced with permission of the copyright owner. Further reproduction prohibited without permission.

The as-deposited films have a high threshold voltage and low brightness, consistent with the heavily defected microstructure they have. First, the layer of the equiaxed grains in very small size can be a "dead layer" to hot electrons. When 100V of voltage is applied across the phosphor layer whose thickness is about 1μm, an electric field strength of 1MV/cm is generated. For electrons with energy of 2 to 3eV, the mean free path is about 10nm, based upon numerical Monte Carlo simulation. This is comparable to the estimated average grain size in this equiaxed layer. Therefore, the grain boundaries in this layer can be scatter centers to the injected electrons during their transportation in the phosphor film, causing them to lose energies. On the other hand, these grain boundaries can also act as trap sites to the injected electrons, limiting the number of electrons transported in the phosphor. Consequently, a high threshold voltage is requested to overcome any scattering and trapping. Besides, any kind of lattice defects can result in non-radiative combination of the luminescent centers, which causes phonon generation rather than photon generation for EL.

Five minutes of post-sputter annealing at 700°C or 800°C, results in slightly reduced threshold voltage. The brightness values are doubled to 100nits for both annealing temperatures. The observed grain growth in the phosphor can reduce the density of trap sites and scatter centers, resulting lower threshold voltages. The increased EL brightness is believed to be associated with the crystallinity improvement as well. Although no experimental observations are available on the annealing effects on the point defect concentration and the type, it is suspected that most of them are annealed out after 5 minutes at 800°C. This temperature is about $0.6T_m$ of ZnS when T_m is the melting pint in °K.

Reproduced with permission of the copyright owner. Further reproduction prohibited without permission.

In the samples with KCl co-dopant, remarkable improvement in the EL properties is measured after RTA at 650°C and 700°C. The B_{40} value is five times of that from the as-deposited sample, and more than two times of the ZnS:Mn sample without KCl. These changes are accompanied by a slight increase in the threshold voltage. As seen in Figure 4.18, the slopes of the B-V data are larger for ZnS:Mn,KCl samples annealed at 650°C and 700°C, comparing to their counterparts without KCl.

The increase in threshold voltage in these samples can be understood as follows. First, it is possible that a distribution of interfacial defect states locate close to the conduction band in the as-deposited sample. They act as donors, so that they can be ionized at relatively low voltages. This would cause a low threshold voltage and a leaky turn-on behavior, as observed in the as-deposited sample. The improvement of the crystallinity from KCl incorporation into the lattice during annealing helps to remove these energy states, resulting in higher threshold voltage. Secondly, according to SIMS results presented in section 4.3.1, a uniform distribution of K^+ ions in phosphor films is achieved even at 600°C, and little difference is observed with temperature, as illustrated in Figure 4.3. Thus, Cl^- ions must play a more important role to give rise to the improved EL properties in samples RTAed at 650°C and 700°C, respectively. A model to explain the increases threshold voltage can be found in work reported in reference [6]. Lastly, the slight change in texture of the phosphor with KCl may change the interface state characteristics, including the state density and the trap depth, which would accordingly change the turn-on properties.

The improvement on the microstructure of these KCl doped samples as addressed in section 4.3.2 evidently makes contributions to improve the EL brightness. The

Reproduced with permission of the copyright owner. Further reproduction prohibited without permission.

removal of the equiaxed fine grain layer allows electrons tunneled from the interface to be accelerated to sufficient high energies for impact excitation. Reduction of the grain boundary area and other lattice defects by grain growth will reduce the density of non-radiative recombination paths. In addition, the donor Cl^- ions in the lattice will displace the Fermi energy level towards the conduction band, which results in a higher electron density in the phosphor.

The decrease in both the threshold voltage and the EL brightness in 800°C annealed sample is suspected to be associated to the K^+ and Mn^{2+} diffusion into the ATO insulator layer (Figure 4.2e), with the former changing the dielectric coefficient of the insulator and the latter causing loss of luminescent centers. According to Equation (2-13), a lower dielectric coefficient of the insulator would cause less voltage drop across the phosphor layer, which means a smaller portion of the applied voltage is really applied across the phosphor. On the other hand, incorporation of K^+ and Mn^{2+} ions into the ATO insulator would also damage the insulator/phosphor interface and create defect states near the conduction band, which consequently causes a lower threshold voltage and a leaky turn-on.

Another important characteristics regarding the performance of ACTFEL devices is luminous efficiency. The efficiency and the EL brightness vs. the applied voltages are plotted in Figure 4.19, and the efficiency values at 40V above the threshold voltage are summarized in Table 4.3. In general, the efficiencies are much lower than the best reported value of 5lm/W for ZnS:Mn ACTFEL devices [3, 45]. The half stack devices used in this study is believed to be one of the reasons for this difference, since the interface state at the Al/phosphor interface is quite different from that of the

Reproduced with permission of the copyright owner. Further reproduction prohibited without permission.

ATO/phosphor interface, and is believed to be much less efficient. In addition, the field distribution is different for samples without the top dielectric layer.

In all the cases, the efficiency increases at first and then saturates with the applied voltage, although the brightness is still increasing. The efficiency of the as-deposited sample is extremely low, at about 0.2lm/W, indicating only a small fraction of the electrons that flow from cathode to anode have the capability to efficiently impact excite the luminescent centers, and/or the ratio of radiative vs. non-radiative recombination is low. Both effects can result from a heavily defected microstructure. Annealing doubles the efficiency, while KCl doping makes more than a four-fold improvement. Again the sample RTAed at 700°C gives the highest luminous efficiency. With the annealing temperatures above 750°C, the luminous efficiency shows a very slight decrease, which is consistent with the EL brightness results.

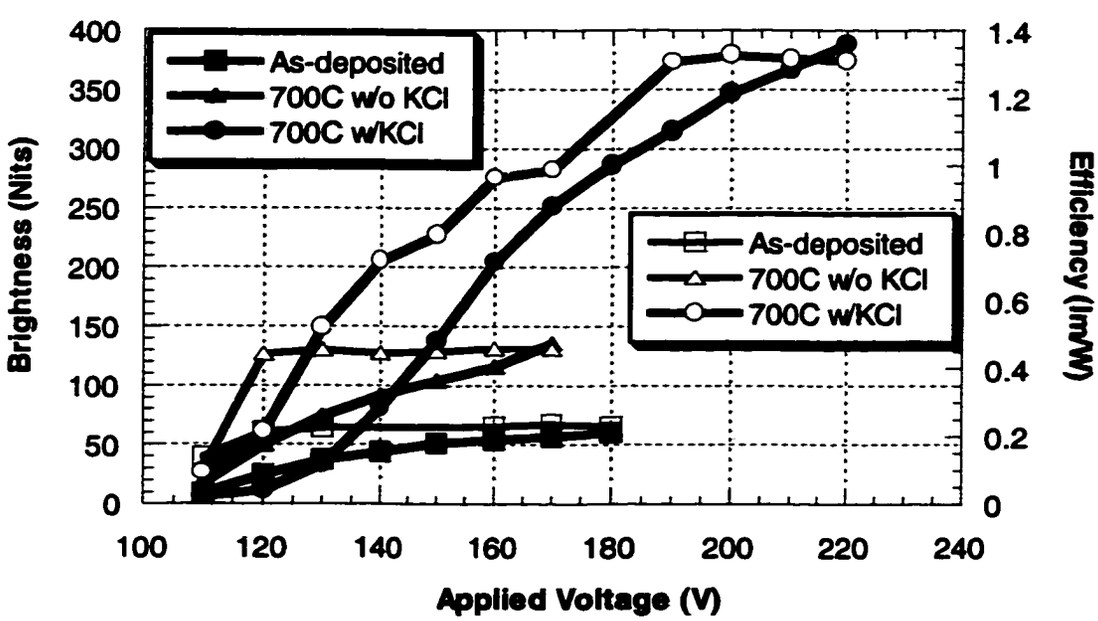

Figure 4.19 Effects of RTA and KCl co-doping on EL brightness (solid symbols) and luminous efficiency (open symbols).

Reproduced with permission of the copyright owner. Further reproduction prohibited without permission.

Luminous efficiency is defined as the brightness divided by the consumed power. At low voltages when the device is just turned on, the brightness is controlled by the number of hot electrons available to excite the luminescent centers. Two steps are involved in this excitation process; the injection of the electrons from the interface states and the acceleration of the electrons into high-energy states. Higher the threshold voltage, more electrons can tunnel into the phosphor and accelerated to higher energies, which results in increased EL brightness. During this period, an increased efficiency with the increasing voltage is observed due to the increased excitation efficiency for Mn^{2+} luminescent centers at higher electric fields. Above a certain voltage that is well above the threshold voltage, the brightness saturates with respect to the increased voltage. This is believed to be due to excitation saturation of the luminescence centers. In addition, when the external field is above the threshold field, the ACTFEL device is functioning as two back to back Zener diodes. With an increase in the external field, the electric field across the phosphor layer does not increase proportionally to increased voltage, as it does before reaching the threshold voltage. In fact, it is believed that the electric field of the phosphor film remains constant above the threshold voltage, which is called the clamp effect [15]. All the voltage above the threshold is transferred to the insulators. Experimental verification of this effect can be found in references [89, 90, 91]. In the case of luminous efficiency, with increase in voltage, more and more electrons are transferred from cathode to anode, resulting an increased current and accordingly an increased power input. Thus, saturation in luminous efficiency results.

The emission spectra at 40V above threshold voltage as a function of annealing temperature are plotted in Figure 4.20. All curves peak at 580nm to 584nm. The CIE

Reproduced with permission of the copyright owner. Further reproduction prohibited without permission.

coefficients from these samples at 40V above the threshold voltages are shown in Table 4.4. Neither anneal nor the incorporation of KCl changes the color of the EL emission.

Table 4.4 CIE Coefficients at (V_{th} + 40) from samples with and without KCl

		X	Y
Without KCl	As-deposited	0.5386	0.4591
	700°C	0.5325	0.4651
	800°C	0.5402	0.4576
With KCl	600°C	0.5393	0.4582
	650°C	0.534	0.4637
	700°C	0.5315	0.4662
	750°C	0.5316	0.4655
	800°C	0.5337	0.464

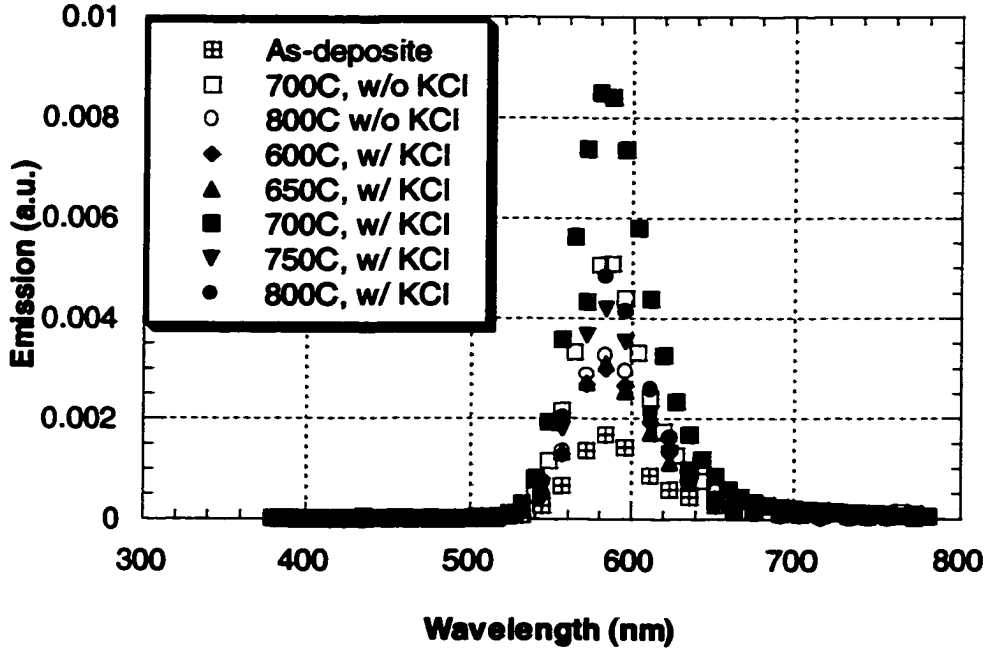

Figure 4.20 EL emission spectra at (V_{th} + 40) from samples with and without KCl.

Reproduced with permission of the copyright owner. Further reproduction prohibited without permission.

4.3.6 Photoluminescence (PL) Properties

Photoluminescence (PL) is widely used as a method to characterize the defects and luminescence center properties, especially the radiative relaxation properties. PL is carried out on the as-deposited sample and samples after 700°C or 800°C annealing with and without KCl. PL spectra from 500nm to 650nm are presented in Figure 4.21a. These peaks are from the Mn^{2+} luminescent centers. Without KCl, PL intensities from annealed samples are about twice that from the as-deposited sample. It is believed that the 5 minutes anneal helps to improve the radiative relaxation of the Mn^{2+} centers by annealing out some of the lattice defects that cause non-radiative de-excitation. In samples of ZnS:Mn,KCl, the PL intensity is about the same after 600°C and becomes lower after 800°C, comparing to the as-deposited ZnS:Mn. There must be other emissions present in these samples, resulting from the defects causing by KCl incorporation.

The PL spectra at shorter wavelengths are shown in Figure 4.21b, and two peaks at 452nm and 510nm are detected only for annealed samples of ZnS:Mn,KCl. These peaks become more evident after annealing at 800°C. Although it is not clear what relaxation causes these peaks, it is speculated that they are associated with certain defects introduced by KCl doping. It has been reported the self-activated (SA) relaxation of ZnS is detected by PL at 460nm [44], which is resulted from zinc vacancy and the co-activator situated at the nearest lattice point from the zinc vacancy. The incorporated K^+ and Cl^- and the resulted zinc vacancy in ZnS:Mn,KC phosphor may generate certain point defect complexes that are good for EL emission by providing additional electrons, but reduces

Reproduced with permission of the copyright owner. Further reproduction prohibited without permission.

PL emission from Mn^{2+} ions by absorbing incoming photons. Secondly, the emission from Mn^{2+} is forbidden. The forbidden rule is relaxed because of the lack of center

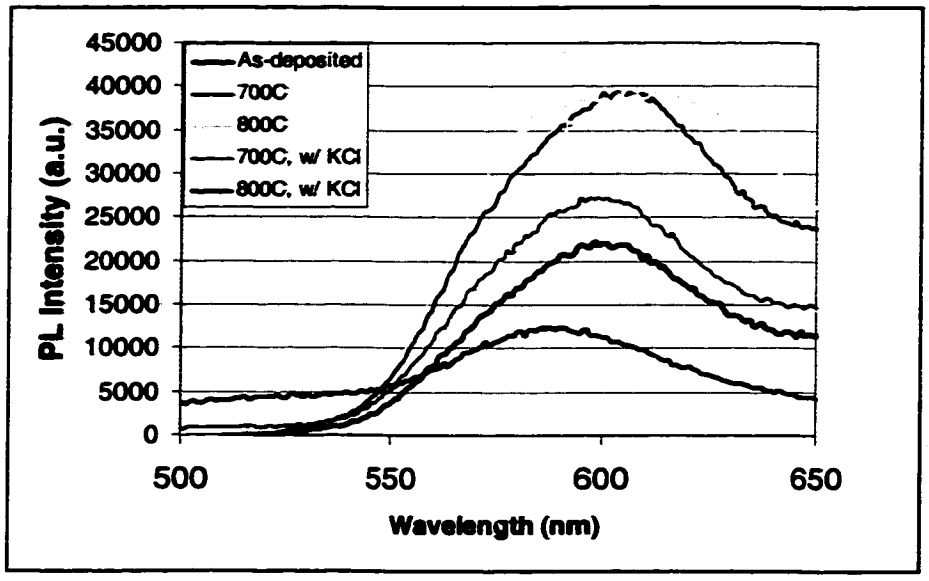

(a)

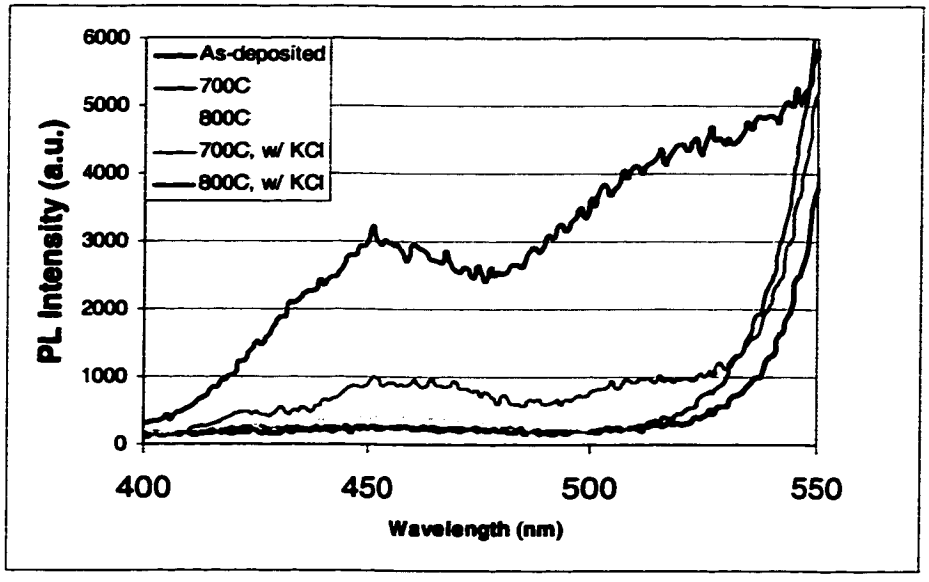

(b)

Figure 4.21 Effects of annealing and KCl doping on PL from (a) Mn^{2+} and (b) defects from KCl.

Reproduced with permission of the copyright owner. Further reproduction prohibited without permission.

symmetry of Mn^{2+} in ZnS lattice. It is speculated that the Mn^{2+} site symmetry becomes more ideally tetrahedral resulted from KCl incorporation with annealing, which decreases the probability of the allowable emission from Mn^{2+}, and thus lower PL intensities are observed.

With all the experimental results presented, it is believed that the significant improvement in EL with KCl doping is mainly resulted from the remarkably improved excitation process, since KCl doping deteriorates the radiative relaxation process of the Mn^{2+} centers.

4.4 Summary

The as-deposited ZnS:Mn phosphor thin films have a heavily defected microstructure and a combination of hexagonal and cubic phases, which result in a low EL brightness (48.7nits as B_{40}) and low luminous efficiency (0.2275lm/W at B_{40}). Anneal at 650°C or 700°C for 5 minutes induces limited grain growth in the columnar grain region, from 89nm as-deposited to 126nm at 650°C and 132nm at 700°C. The B_{40} values of ZnS:Mn are doubled from 48.7nits to 99.6nits and slightly lower threshold voltages from 125V to 110V are measured.

In samples with KCl, grain growth is enhanced and the equiaxed grain layer is removed by 5 minutes anneal at 700°C. Interstitial mechanism is believed to operate in K diffusion into ZnS:Mn. No segregation of K to the grain boundaries is detected. Cl diffusion is much less than K, and is speculated to be associated with substituting S sites

Reproduced with permission of the copyright owner. Further reproduction prohibited without permission.

in ZnS. The existence of KCl in ZnS:Mn lattice appears to stabilize the cubic phases and causes cubic (200) texture enhancement.

The significant improvement in B_{40}, sharp turn-on, increase in threshold voltage, and higher efficiency at B_{40} are believed to be resulted from the improvement of the Mn^{2+} excitation process. The better crystallinity and the creation of donor states by Cl^- substitution on the S^{2-} lattice and K^+ interstitials are the main contributions. The radiative relaxation of Mn^{2+} is degraded with the presence of KCl, as detected by PL. Two peaks at 452nm and 510nm are detected in PL spectra of annealed ZnS:Mn,KCl, which are speculated to be associated with K^+ and/or Cl^- related point defect complexes that benefit EL but detract from the PL emission. Besides, anneal at elevated temperatures at the presence of KCl makes the tetrahedral structure of the ZnS:Mn more ideal, so that the probability of the forbidden emission increases.

Annealing at 800°C causes the B_{40} and V_{th} to decrease and the threshold voltage slightly drop as well. These property changes are attributed to extensive diffusion of K^+ and Mn^{2+} into the ATO layer. The PL intensities from Mn^{2+} also show decreased intensities from samples after an 800°C anneal compared to a sample annealed at 700°C.

Reproduced with permission of the copyright owner. Further reproduction prohibited without permission.

CHAPTER 5
ZnS:Mn WITH Ga_2S_3 AS A CO-DOPANT

5.1 Introduction

Introduction of KCl during annealing of ZnS:Mn brings significant improvement in EL brightness, luminous efficiency, and a slight increase in threshold voltage. With respect to the microstructure, enhanced grain growth is observed and the so-called "dead layer" is removed after 5 minutes of RTA at 700°C. Previous studies showed that SrS:Ce co-doped with Ga_2S_3 experienced a significant reduction in threshold voltage and an increase in EL brightness due to remarkable grain growth after two minutes of anneal at 810°C [92]. Since gallium enrichment was detected at both grain boundaries and triple points of SrS by EDS in TEM, it was postulated that a liquid gallium phase existed at the grain boundaries and the triple points, acting as a flux agent. The grain boundary migration was accelerated with the presence of the gallium phase, and remarkable grain growth was resulted. Accordingly, improved EL properties were observed. It was expected that Ga_2S_3 would lead to grain growth and thus improve EL performance in ZnS:Mn phosphor as well.

Reproduced with permission of the copyright owner. Further reproduction prohibited without permission.

5.2 Results and Discussions

5.2.1 Secondary Ion Mass Spectrometry (SIMS)

The SIMS profiles from ZnS:Mn,Ga_2S_3 samples as-deposited and after annealing at 700°C, 800°C for 5 minutes, or 3.5 minutes at 835°C are shown in Figure 5.1. Due to the low glass transition temperature of the Corning 7059 glass substrates (598°C), a shorter RTA time is used at 835°C.

Ga has diffused throughout the entire phosphor film in all the annealed samples. The GaO^+ signal is high at the phosphor/ambient interface due to the excessive Ga_2S_3 that could not be removed during or after processing. In the sample RTAed at 700°C, no diffusion of any element is detected at the insulator/phosphor interface.

The diffusion paths of Ga^{3+} into ZnS are not clear, but grain boundaries are suspected to be the dominant ones. Ga^{3+} has a relatively small ionic radius of 0.62Å, more than 15% smaller than Zn^{2+} and Mn^{2+} ions, (0.74Å and 0.80Å, respectively). It would be hard for Ga^{3+} to incorporate into the ZnS lattice by substitution with such a large lattice mismatch, because a large strain field in the vicinity will be generated. In addition, the valence of Ga^{3+} is different from Zn^{2+} and Mn^{2+}, too. Therefore, the solubility Ga^{3+} in the lattice is limited and Ga_2S_3 segregation at the grain boundaries is expected. In this way, Ga_2S_3 still can work as a flux agent to increase the grain boundary mobility and allow grain growth.

Reproduced with permission of the copyright owner. Further reproduction prohibited without permission.

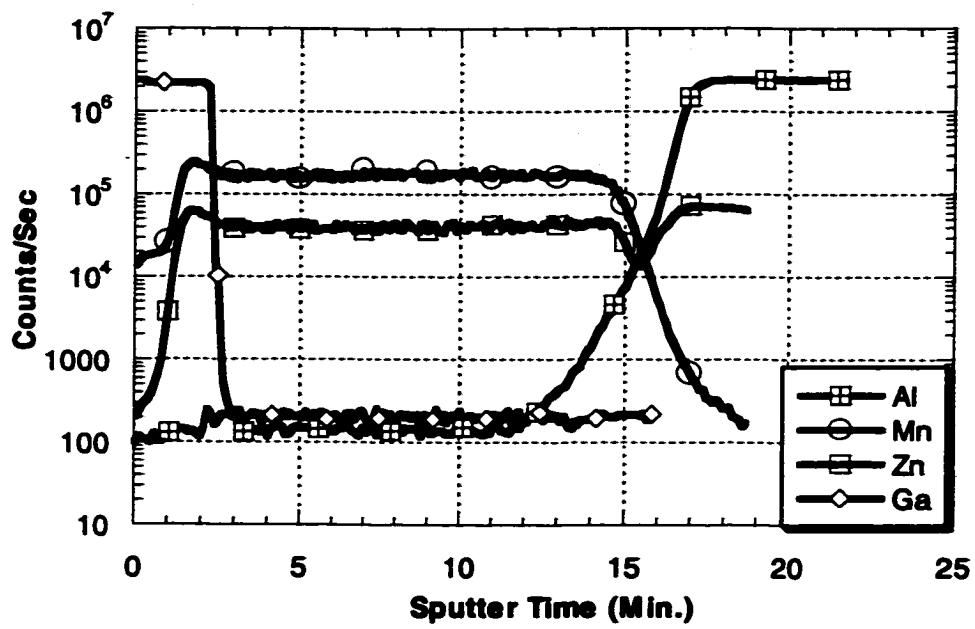

(a)

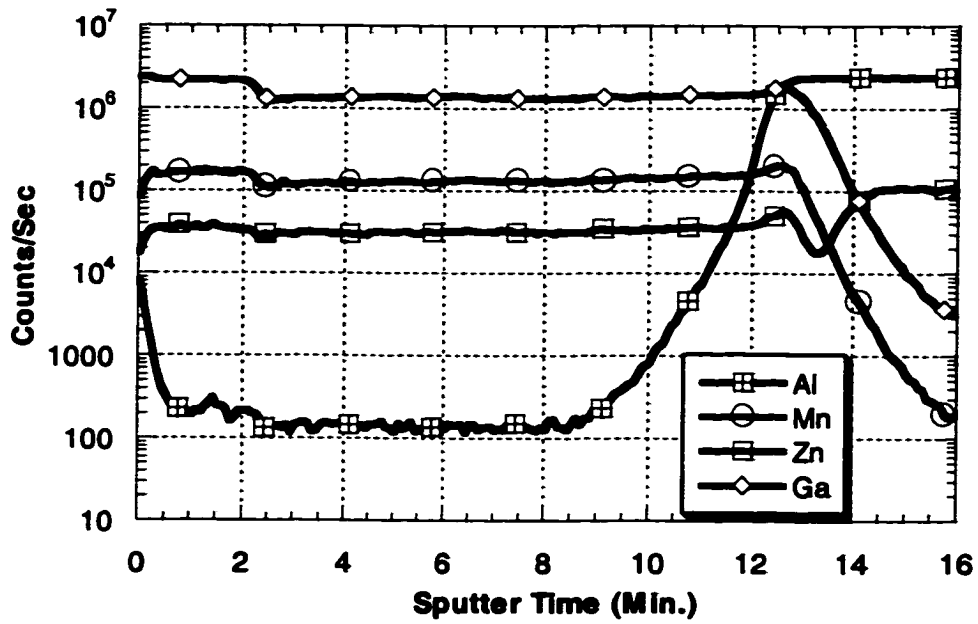

(b)

Figure 5.1 SIMS profiles from ZnS:Mn samples with Ga_2S_3 (a) as-deposited, after annealing at (b) 700°C, (c)800°C, and (d) 835°C.

Reproduced with permission of the copyright owner. Further reproduction prohibited without permission.

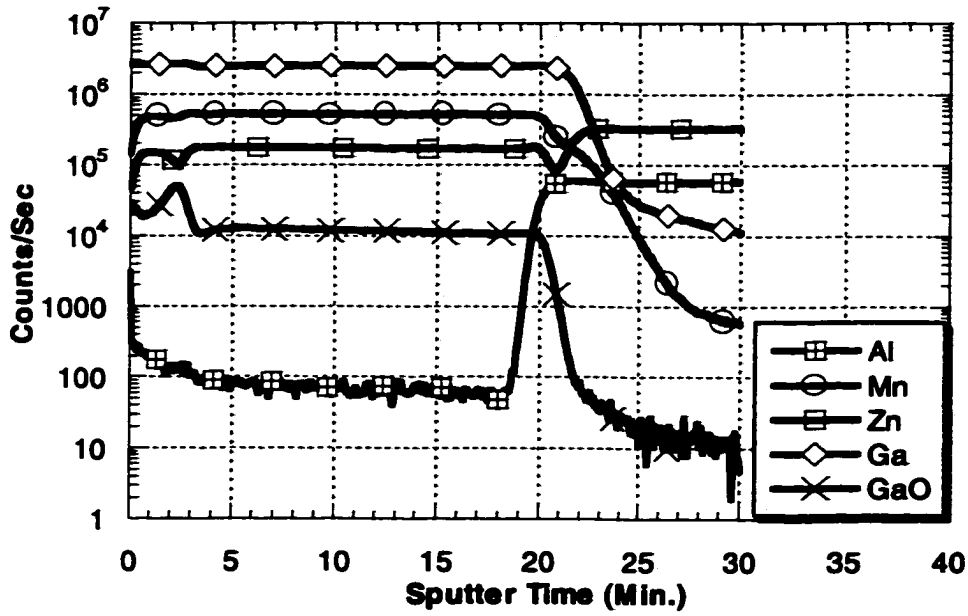

(c)

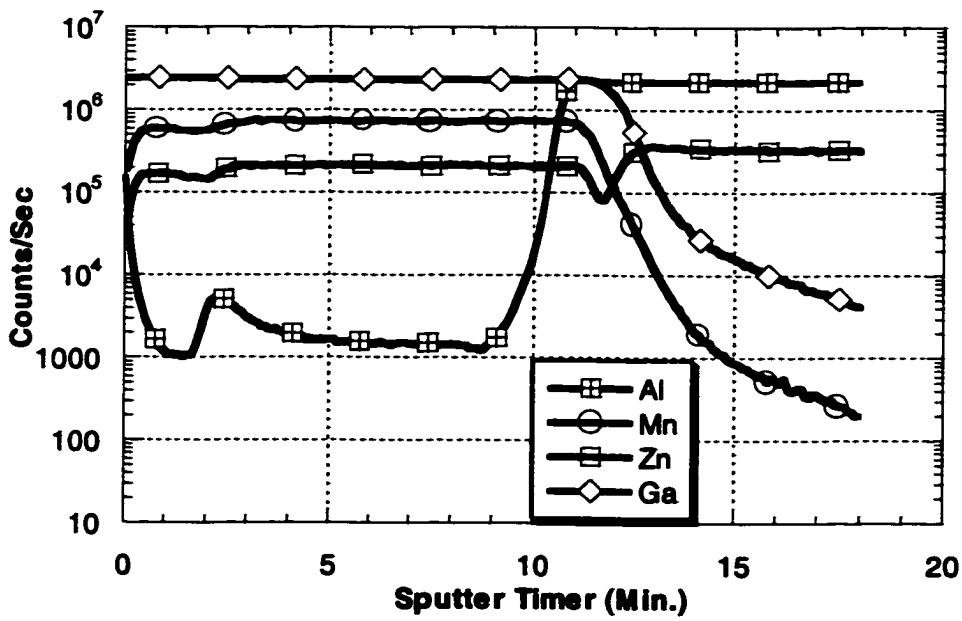

(d)

Reproduced with permission of the copyright owner. Further reproduction prohibited without permission.

5.2.2 X-ray Diffractometry (XRD)

Table 5.1 summarizes the XRD data from ZnS:Mn as-deposited, or 800°C annealed with and without Ga_2S_3. Figure 5.2 gives the two theta scan spectra from as-deposited and after anneal at 800°C for 5 minutes with and without Ga_2S_3 samples. The peaks are indexed as shown. The bar chart in Figure 5.3 shows the relative intensity of certain peaks.

In all the samples, a combination of both cubic and hexagonal structures is clearly seen. As discussed in the previous Chapter, the growth texture in the as-deposited sample is c(200) plus slight c(111) + h(0002) combination. Comparing the peak intensities of the samples with and without Ga_2S_3 after RTA at 800°C, no significant difference is observed. The only exception is that the h(10-11) peak, which increases at the expense of the c(200) peaks. But peak overlap between an ITO diffraction peak and the ZnS h(10-11) makes it difficult to reliably quantify this change.

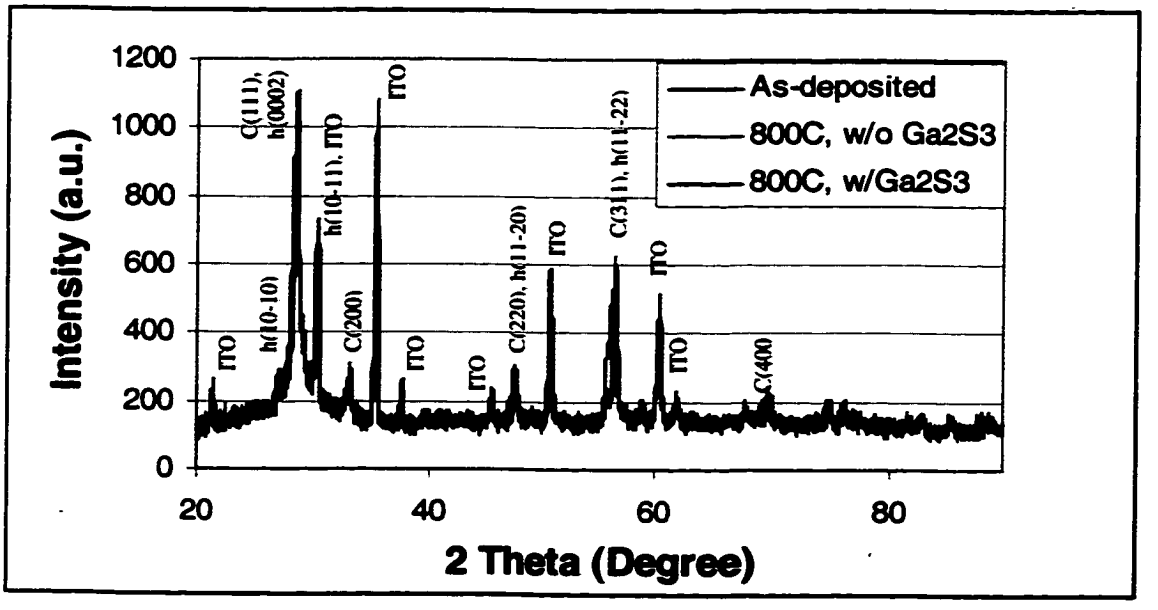

Figure 5.2 X-ray diffraction spectra from the as-deposited and after 5 minutes anneal at 800°C with Ga_2S_3 samples.

Reproduced with permission of the copyright owner. Further reproduction prohibited without permission.

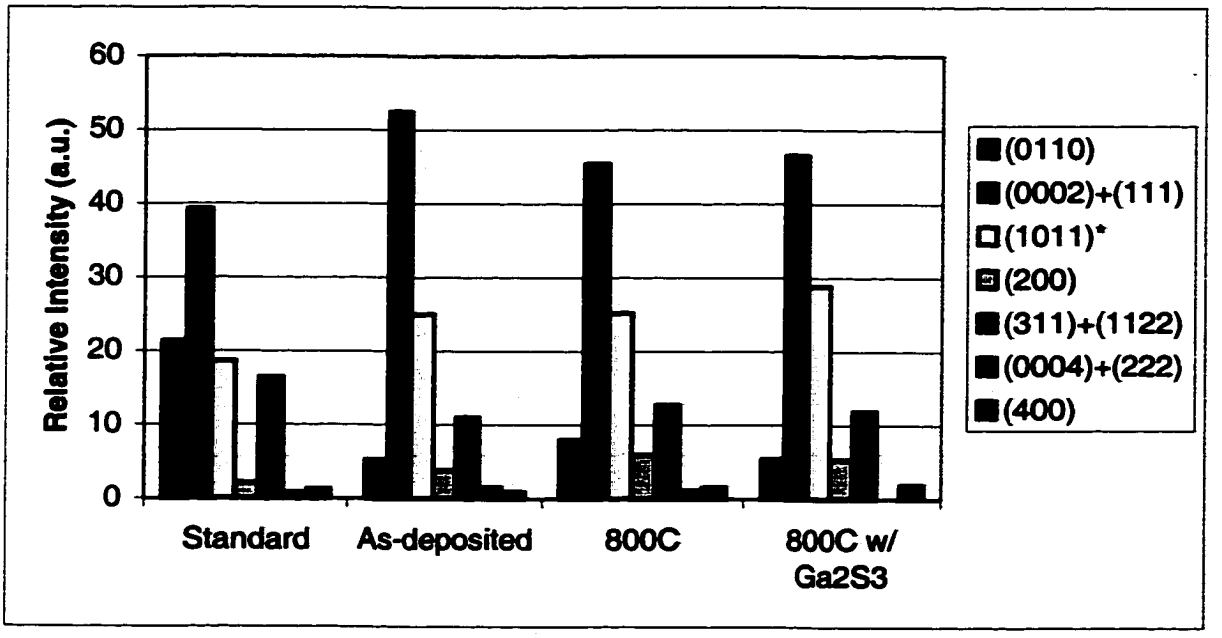

Figure 5.3 Effects of Ga_2S_3 co-doping on the texture of 800°C annealed ZnS:Mn samples.
(Note, h(10-11) overlaps one of the peaks from ITO sublayer.)

Table 5.1 XRD results from samples RTAed at 800°C, with and without Ga_2S_3.

				As-deposited		800°C		800°C w/ Ga_2S_3	
Index	2θ	Inten. (a.u.)	Rel. (%)	Counts (a.u.)	Rel. (%)	Counts (a.u.)	Rel. (%)	Counts (a.u.)	Rel. (%)
(0110)	26.9	100	13.6	96	4.9	161	7.8	106	5.2
(0002)+(111)	28.5	184	25.0	961	49.4	912	43.9	906	44.3
(1011)*	30.5	87	11.8	458	23.6	506	24.4	562	27.5
(200)	33.1	10	1.4	71	3.7	119	5.7	104	5.1
(1012)	39.6	28	3.8	17	0.9	18	0.9	0	0.0
(220)+(1120)	47.5	132	18.0	85	4.4	50	2.4	92	4.5
(1013)	51.8	54	7.3	0	0.0	0	0.0	0	0.0
(2020)	55.5	11	1.5	0	0.0	0	0.0	0	0.0
(311)+(1122)	56.3	77	10.5	202	10.4	256	12.3	231	11.3
(2021)	57.6	12	1.6	0	0.0	0	0.0	0	0.0
(0004)+(222)	59.1	4	0.5	28	1.4	23	1.1	0	0.0
(2022)	63.6	6	0.8	0	0.0	0	0.0	0	0.0
(400)	69.5	6	0.8	17	0.9	32	1.5	38	1.9
(2023)	73.9	15	2.0	0	0.0	0	0.0	8	0.4
(331)	76.8	9	1.2	0	0.0	0	0.0	0	0.0
(420)	79.1	2	0.3	0	0.0	0	0.0	0	0.0
(1015)	82.3	11	1.5	0	0.0	0	0.0	0	0.0
(422)	88.5	9	1.2	9	0.5	16	0.8	0	0.0
		735	100.0	1944	100.0	2077	100.0	2047	100.0

Reproduced with permission of the copyright owner. Further reproduction prohibited without permission.

5.2.3 Transmission Electron Microscopy (TEM)

Images and diffraction pattern were collected from XTEM samples with Ga_2S_3 after 5 minutes of anneal at 800°C or 835°C, as shown in Figures 5.4, and 5.5. For comparison, the XTEM image from the sample without Ga_2S_3 after 5 minutes of anneal at 800°C is shown in Figure 5.6.

In the samples with Ga_2S_3, the bands, poor grain boundary contrast and small grain size indicate that even after the high temperature anneal at 800°C or 835°C, only very limited grain growth occurs. Slightly groovy surfaces on both samples can also be seen. The equiaxed grain layer thickness is decreased and the columnar grains are much better developed. The diffraction patterns show that the films are textured, consistent with XRD data. Streaks from certain diffraction spots can be seen, which correspond to the contrast bands in the bright field images.

No difference in microstructure is observed after annealing at 800°C versus 835°C (compare Figures 5.4a and 5.5a). Contrary to SrS:Ce,Ga_2S_3 system, Ga_2S_3 does not cause grain growth in ZnS at temperature above 810°C. Comparing the microstructure of ZnS:Mn,KCl in Figure 4.8 to that of ZnS:Mn,Ga_2S_3 in Figure 5.4a and 5.5a, Ga_2S_3 does not help grain growth as KCl does. Instead, the grain sizes in ZnS:Mn,Ga_2S_3 annealed at 800°C and 835°C are smaller than that in the samples without Ga_2S_3 after 5 minutes anneal at 800°C, as shown in Figure 5.6a. This suggests that Ga_2S_3 pins the ZnS grain boundaries rather than increases their mobility.

The density of the bands is high in all these three samples, although they have different spacing. The bands in samples with Ga_2S_3 seem to be much finer in spacing than samples without Ga_2S_3. As introduced previously, these bands can be micro-twins,

Reproduced with permission of the copyright owner. Further reproduction prohibited without permission.

polytypes, or stacking faults in nature. In order to get a clear understanding of them, further characterization, high resolution TEM is conducted on Ga_2S_3 co-doped sample after 5 minutes anneal at 800°C. The results show that they are basically micro-twins and stacking faults.

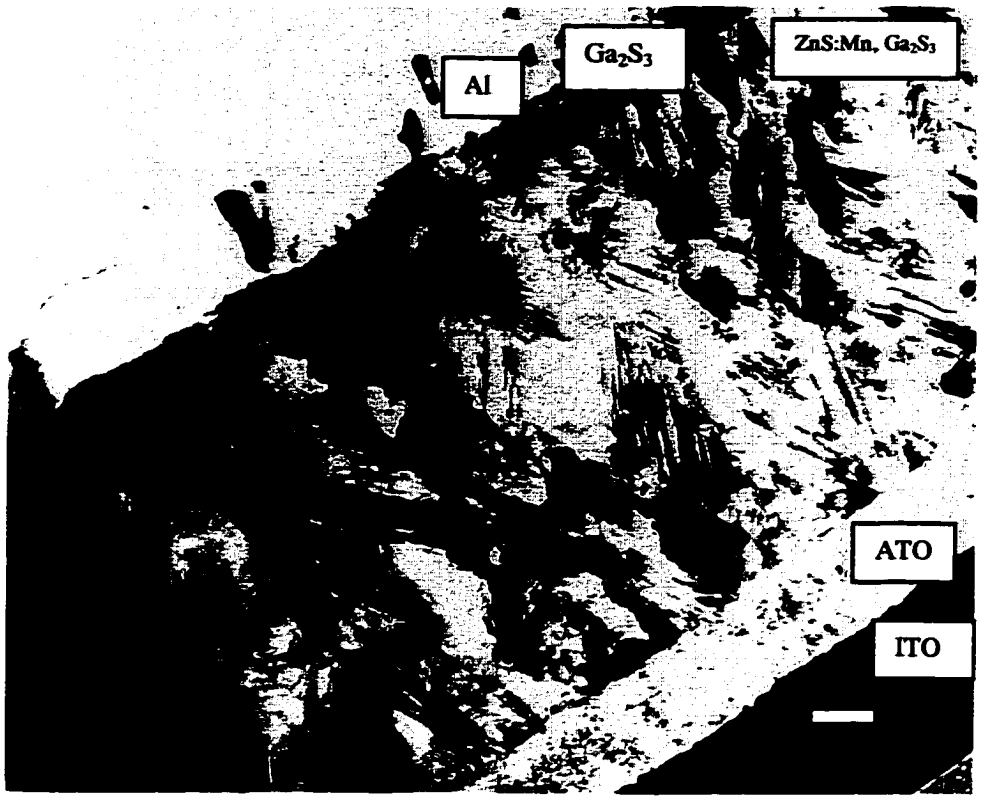

(a)

(b)

Figure 5.4 (a) XTEM micrograph and (b) diffraction pattern from sample with Ga_2S_3 after annealing at 800°C for 5 minutes. (Bar = 100nm)

Reproduced with permission of the copyright owner. Further reproduction prohibited without permission.

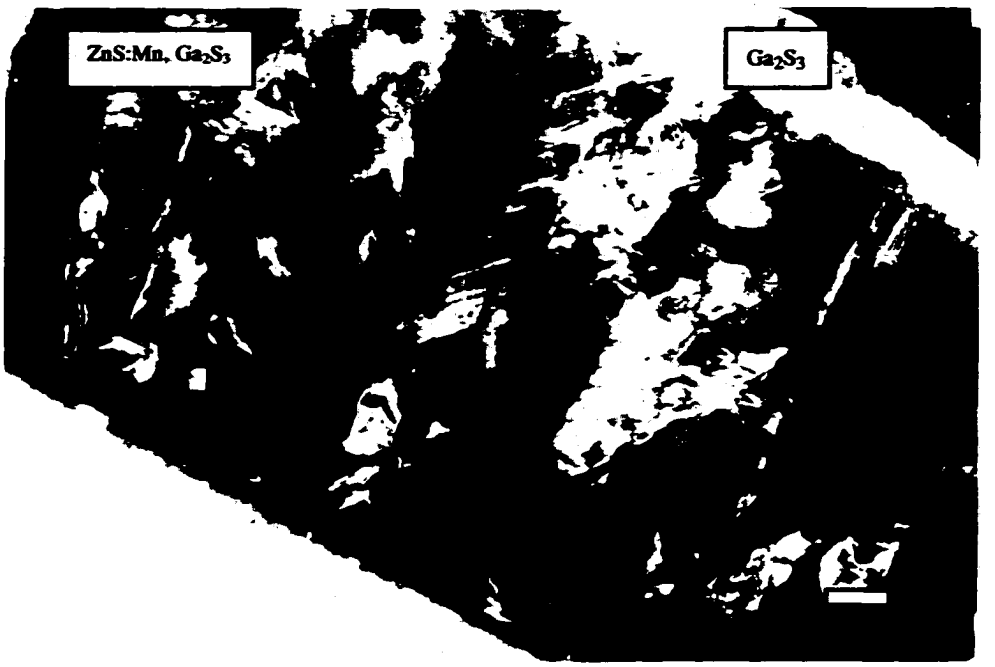

(a)

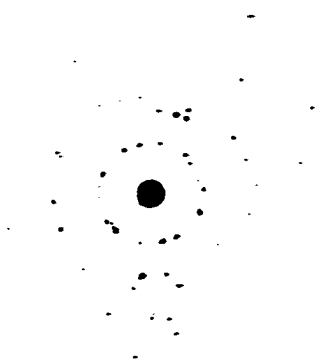

(b)

Figure 5.6 (a) XTEM micrograph and (b) from sample with Ga_2S_3 after annealing at 835°C for 3.5 minutes. (Bar = 100nm)

Reproduced with permission of the copyright owner. Further reproduction prohibited without permission.

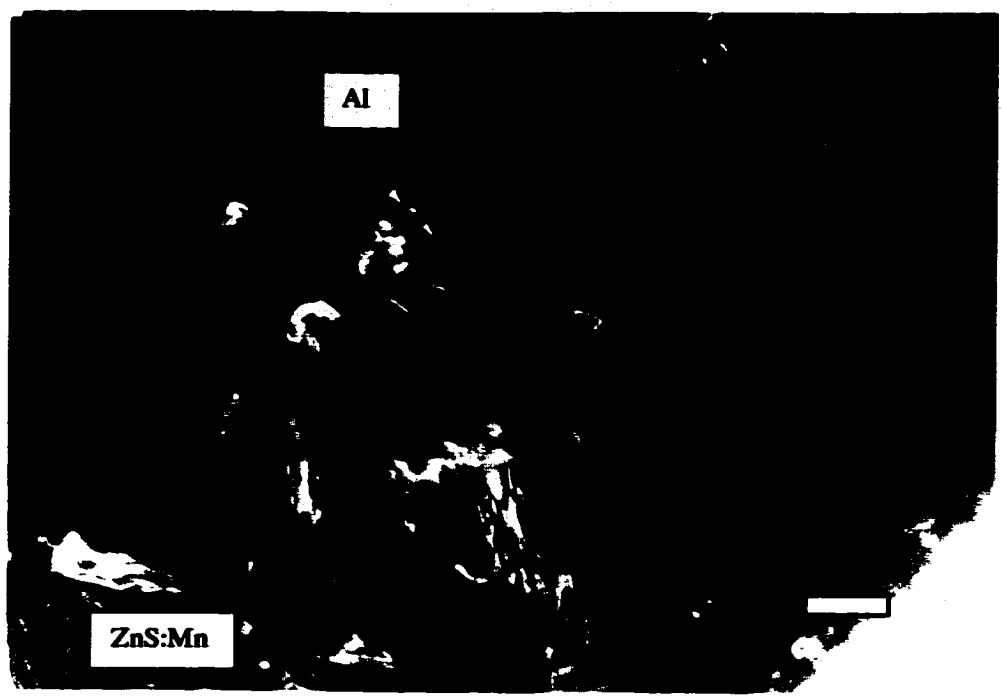

(a)

(b)

Figure 5.6 (a) XTEM micrograph and (b) diffraction pattern from ZnS:Mn sample RTAed at 800°C for 5 minutes. (Bar = 100nm)

An XTEM micrograph from ZnS:Mn,Ga_2S_3 sample annealed at 800°C for 5 minutes is shown in Figure 5.7. It is taken along a direction very close to the B = [011] zone axis. After rotating the diffraction pattern 63° relative to the bright field image in

Reproduced with permission of the copyright owner. Further reproduction prohibited without permission.

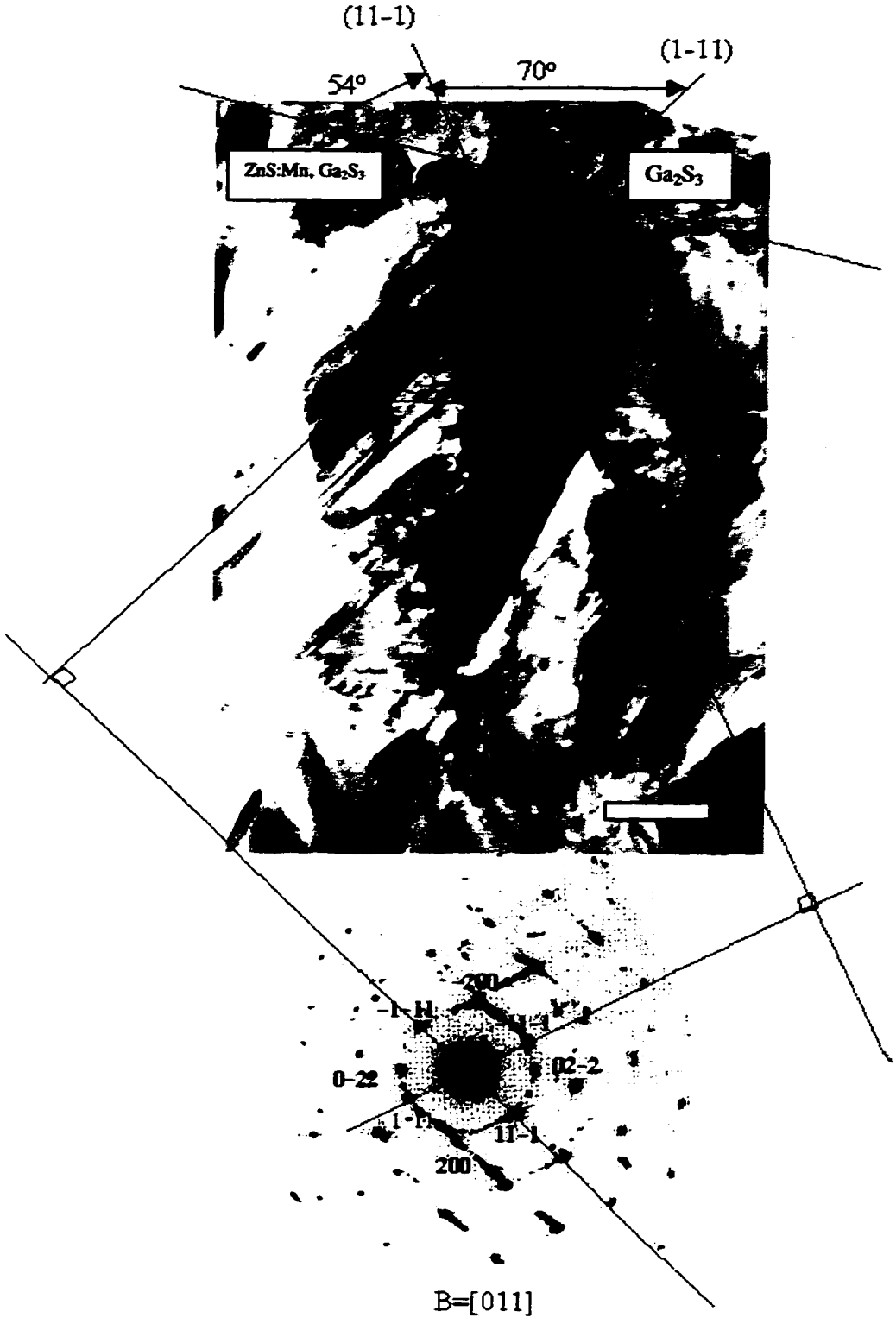

Figure 5.7 Bright field image and diffraction taken from sample with Ga_2S_3 after 5 minutes of annealing at 800°C. (Bar =100nm)

Reproduced with permission of the copyright owner. Further reproduction prohibited without permission.

150K, the pattern is indexed as shown. It is obvious that the striations only along <111> directions, parallel to {111} planes, which are the close packed planes in both cubic and hexagonal structures of ZnS. Also, the angle between the film surface and the (11-1) plane is 54°, which suggests that the film surface parallel to (200) planes. This observation is consistent with the XRD results, showing the texture in this sample is cubic (200) with slight c(111) + h(0002) combination.

Since this area is very parallel to the [011] zone axis, it is possible to perform high resolution TEM (HRTEM) to identify the nature of these bands. Figures 5.8 to 5.10 are HRTEM micrographs with the beam parallel to [011] zone axis. Every spot in the HRTEM micrograph consists of a pair of zinc and sulfur atoms, since their spacing is below the TEM resolution.

A native 60° dislocation is observed, as shown in Figure 5.8a. The term 60° dislocation comes from the fact that this kind of dislocation always lies at an angle about 60° relative to its Burgers vector. It lies on {111} planes with Burgers vector parallel to <110> directions. This kind of dislocation usually dissociates into 90° and 30° partials with Burgers vectors of the (a/6)<112> type. The 30° partial dislocation, which is very localized, is located at the left end and the 90° partial is at the right side. The 30° partial is much easier to recognize, since an additional plane is inserted at the core, as shown in the schematic in Figure 5.9. Between these two partial dislocation is an intrinsic stacking fault spread about 7.3nm.

In materials with low stacking fault energies, formation of either stacking faults or twins is fairly easy. In the case of ZnS, which has been reported to have a very low stacking fault energy [87], other low SFE features have been reported, such as

Reproduced with permission of the copyright owner. Further reproduction prohibited without permission.

polytypism and switching between cubic and hexagonal phases. However, no regular polytypes are observed in this study, but it should be noticed that the total volume of the material studied by HRTEM is very limited. In fact, because of the polycrystalline nature and the small grain size in the sample, it is hard to find a thinned area with certain zone axis. In addition, some of the polytypes have very long repeating cycles, which requires

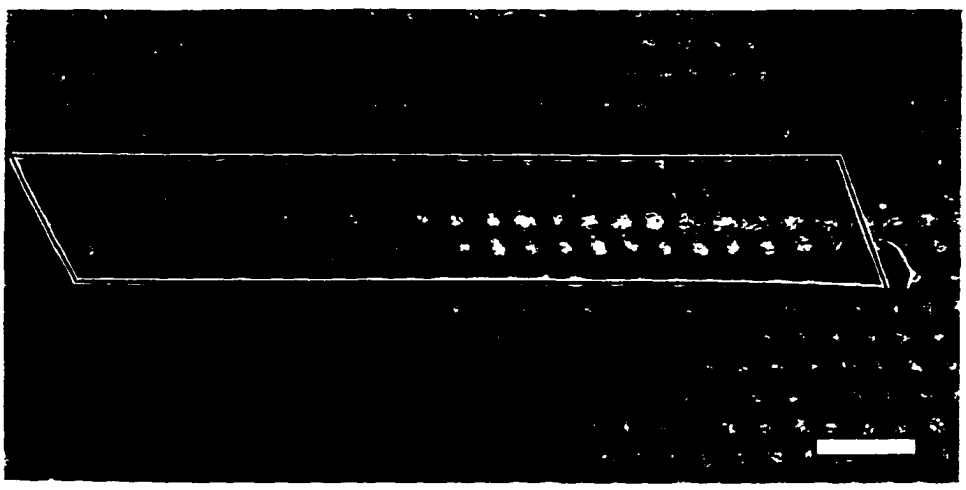

(a)

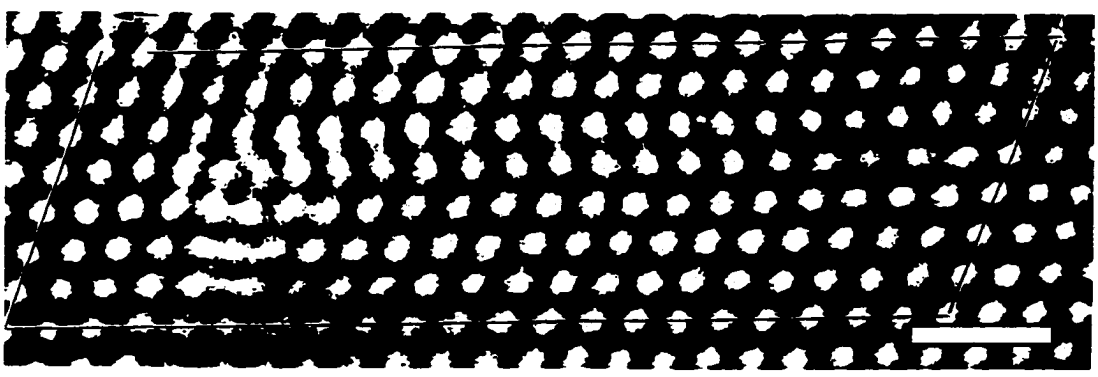

Figure 5.8 (a) A HRTEM image and (b) a simulated high resolution TEM image of a 60° dislocation. (Bar = 1nm).

Reproduced with permission of the copyright owner. Further reproduction prohibited without permission.

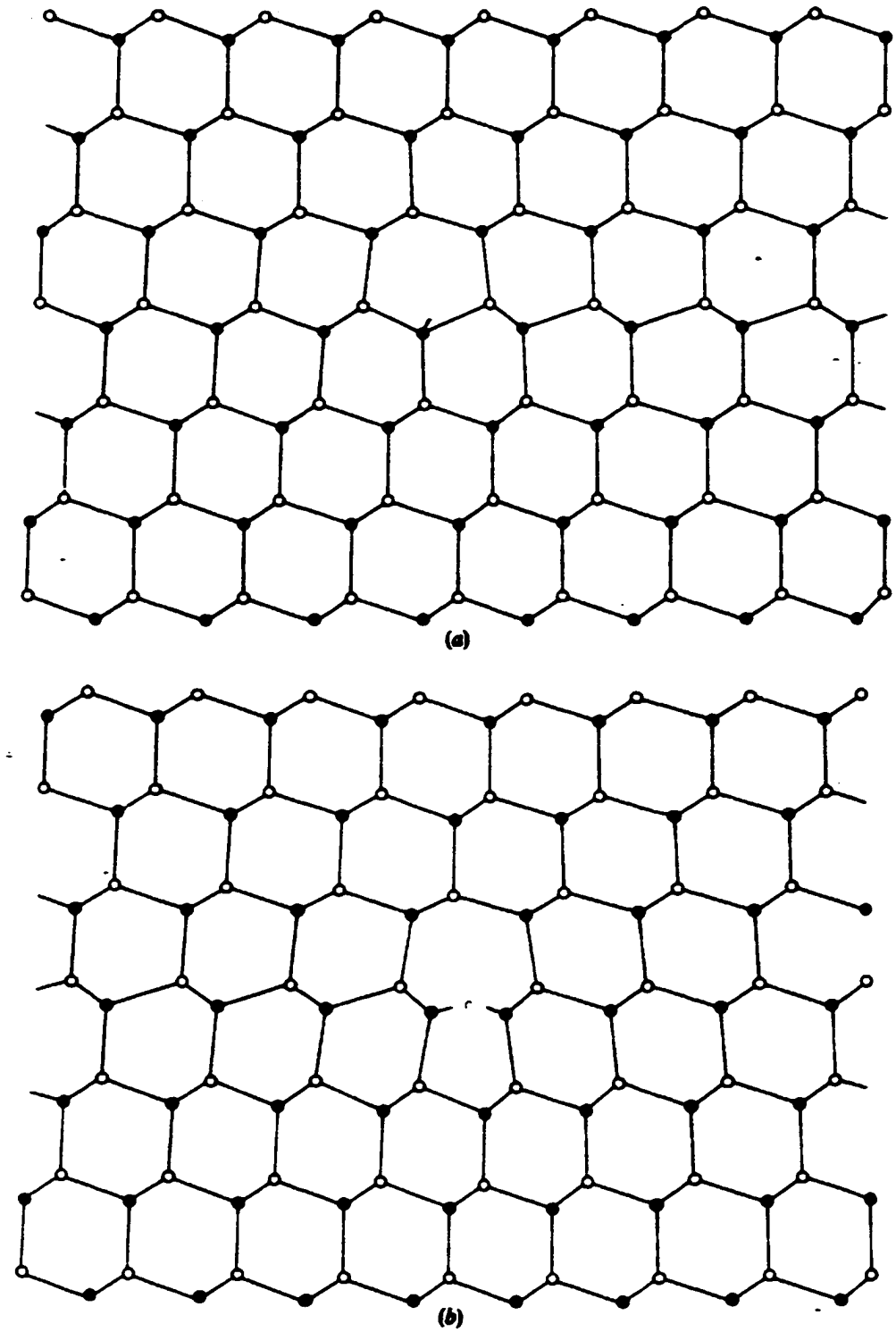

Figure 5.9 Model of (a) the 30° and (b) 90° partial dislocations for II-VI compound [28].

Reproduced with permission of the copyright owner. Further reproduction prohibited without permission.

a large thinned area for identification. Consequently, only regular switching between hexagonal and cubic is detected. Figure 5.10 is a HRTEM micrograph of such switching. Switching between hexagonal (2H) and cubic (3C) can be attributed to the low stacking fault energy of ZnS.

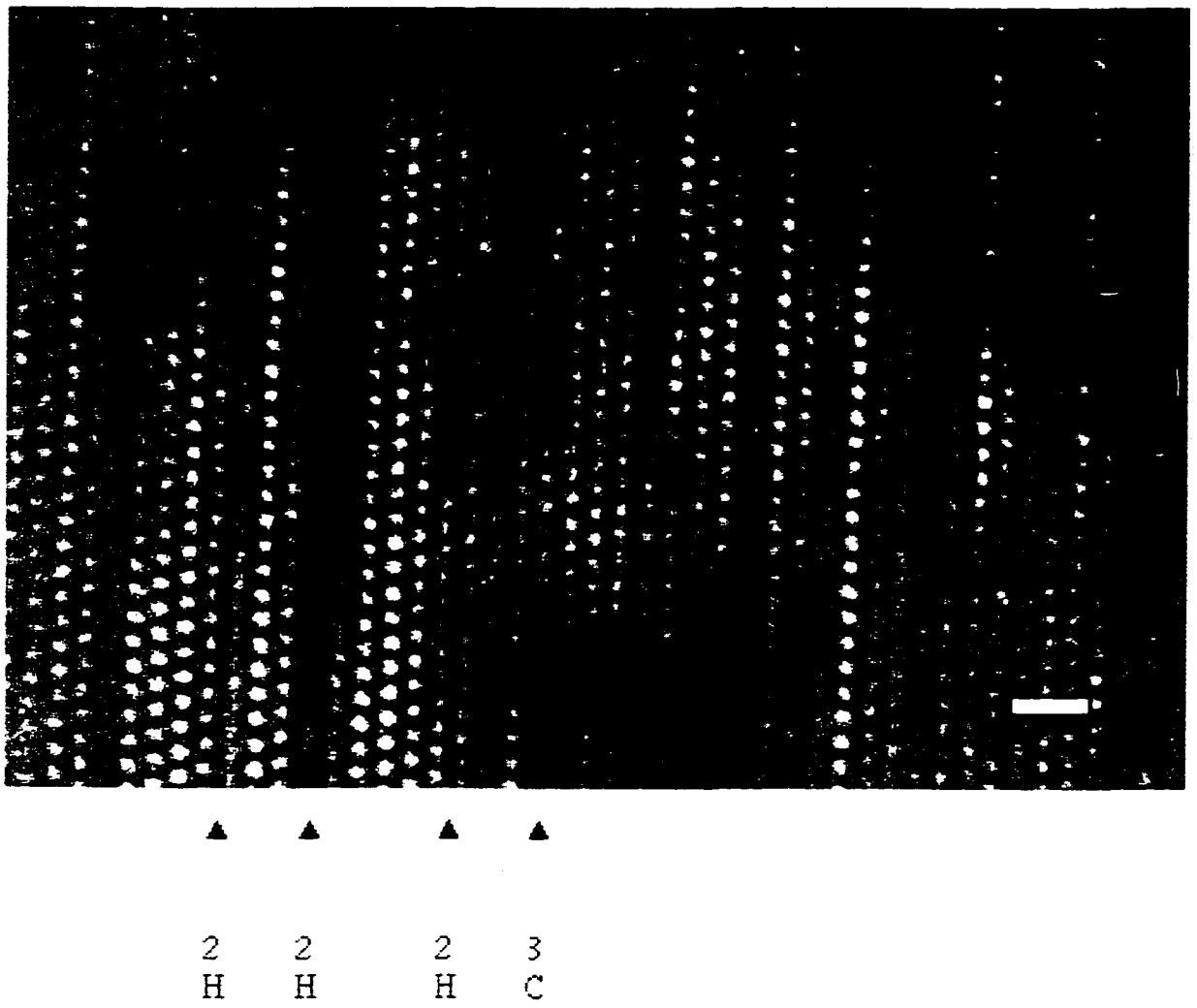

Figure 5.10 HRTEM micrograph showing switch from hexagonal to cubic. The inset bar is 1nm.

According to the phase diagram in Figure 2.7, the hexagonal phase is only stable at temperatures above 1024°C. However, a mixture of both crystallographic phases

Reproduced with permission of the copyright owner. Further reproduction prohibited without permission.

characterizes the microstructure of the as-deposited films. It can be explained by the following two reasons. First, the energetic ions from the magnetron sputtering lead to stacking errors in the lattice. Secondly, since ZnS has fairly low stacking fault energy, the existence of stacking faults does not affect the system free energy very much.

An intrinsic stacking fault and microtwins are shown in the HRTEM micrograph in Figure 5.11. A schematic for extrinsic and intrinsic stacking faults is shown in Figure 5.12. Due to the limited volume of material sampled by HRTEM, the actual characteristic

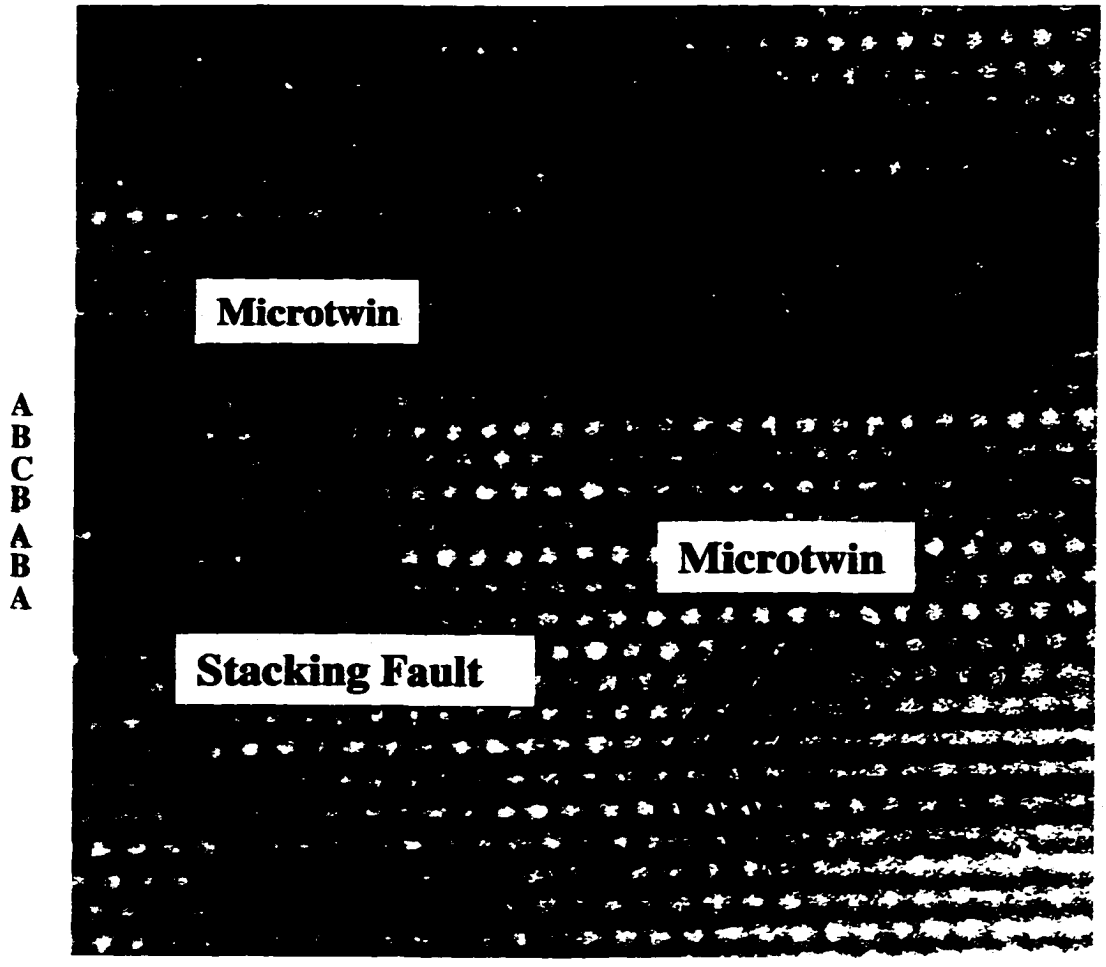

Figure 5.11 HRTEM image showing an intrinsic stacking fault and a micro-twin. (Bar = 1nm).

Reproduced with permission of the copyright owner. Further reproduction prohibited without permission.

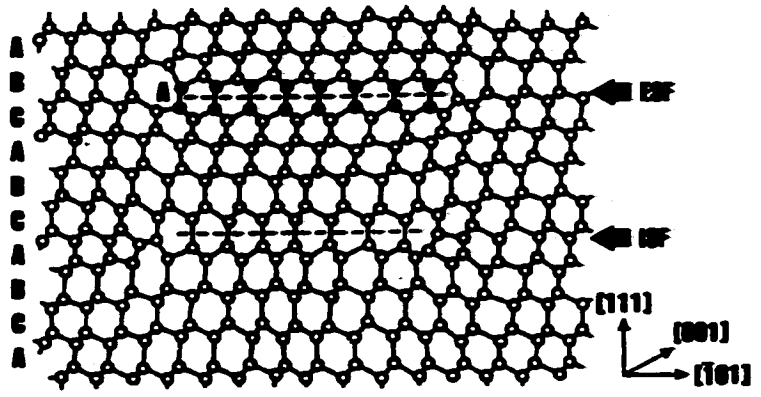

Figure 5.12 A schematic of extrinsic and intrinsic stacking faults [73].

of each band observed in bright field TEM micrographs cannot be identified with clarity. It is likely that they are dislocations, microtwins, large range polytypes, stacking faults or crystal structure switching. Among these defects, dislocations and stacking faults, plus point defects, are thought to be electrically active, since all of them have dangling bonds. Thus, they are considered to be more important to the EL performance of the phosphors than the other three.

5.2.4 Compositional Analysis by Energy Dispersive Spectrometry (EDS)

To verify the speculation that Ga_2S_3 hinders grain growth in ZnS:Mn by pinning the grain boundaries, it is important to know the distribution of it in the samples. EDS analysis was carried out on a PTEM ZnS:Mn,Ga_2S_3 sample annealed at 800°C for 5 minutes. Both line profiles and stationary probes were used. The stationary probe results are summarized in Table 5.2

Figure 5.13a shows a PTEM micrograph and the location of a line scan, while Figure 5.13b is the composition profile along the line. The counts for Mn^{2+} are low due

Reproduced with permission of the copyright owner. Further reproduction prohibited without permission.

to its low concentration. Higher concentration of Ga is detected at the grain boundary than in the grain matrix, indicating grain boundary segregation of gallium. Figure 5.14

(a)

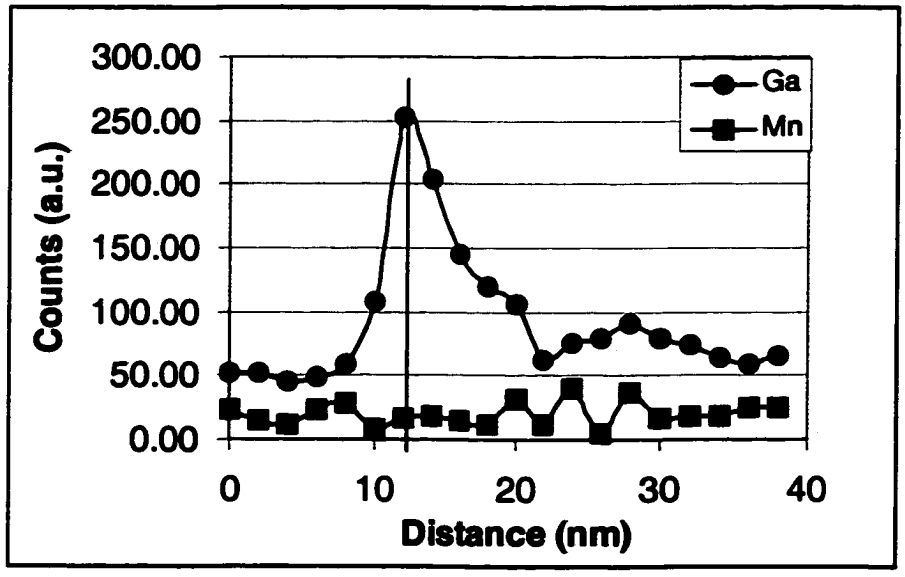

(b)

Figure 5.13 (a) A PTEM micrograph showing the region where EDS is done, and (b) the resulted distribution of Ga^{3+} and Mn^{2+} ions.

Reproduced with permission of the copyright owner. Further reproduction prohibited without permission.

(a)

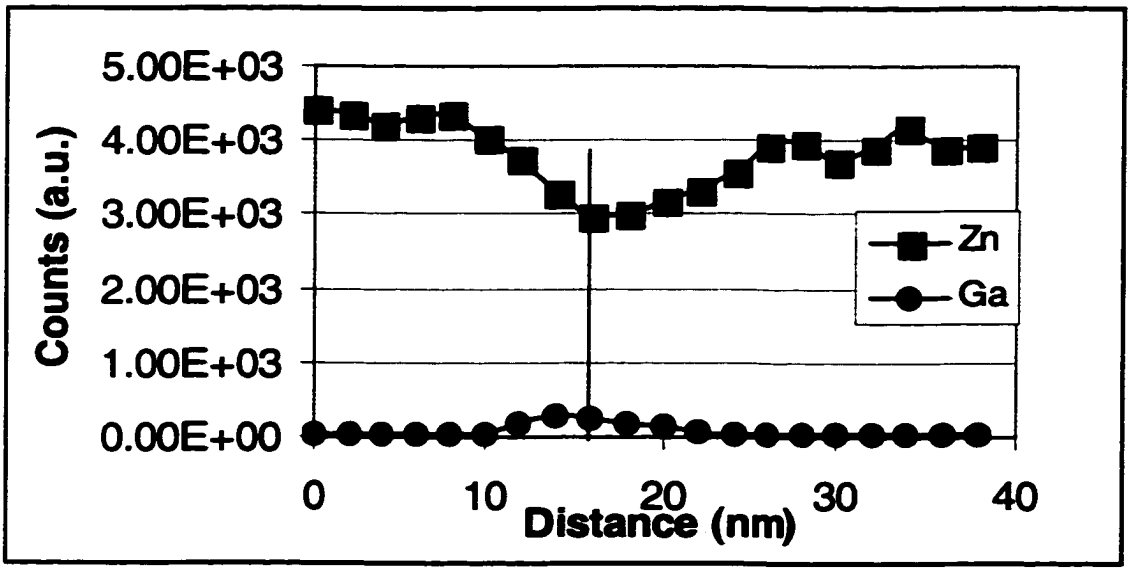

(b)

Figure 5.14 (a) A PTEM micrograph showing where the line scanning is done, (b) the resulted distribution of Zn and Ga, and (c) Ga counts plotted at an expanded range.

Reproduced with permission of the copyright owner. Further reproduction prohibited without permission.

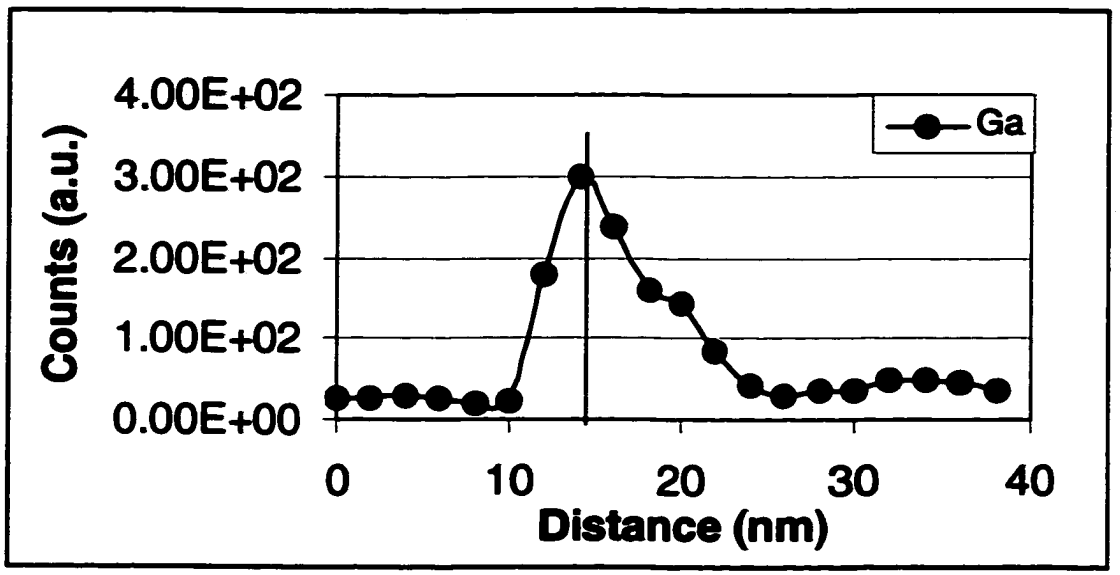

(c)

shows another area. The zinc counts are very high, as shown in Figure 5.14b, but again, grain boundary segregation of Ga is observed. Figure 5.14c shows the same Ga data with and expanded ordinates. Note that in both Figures 5.13b and 5.14b and 5.14c, the Ga count rate is high and Zn count rate is low at the grain boundaries. It is believed that the Ga rate increases due to grain boundary segregation, while the Zn count rate decreases due to the relative low atom density at the grain boundary.

Figure 5.15 is a typical EDS spectrum taken from a stationary probe at the matrix and grain boundary. The Zn peaks at 8.638 KeV, S peaks at 2.308 KeV and Ga peaks at 9.251 KeV are labled. Consistently, segregation of Ga at the grain boundary is obvious. Figure 5.16 shows the areas where the stationary probe data are collected. From the summary in Table 5.2, it is clear that Zn gives lower counts at the grain boundaries than in the grains, and Ga shows higher counts at the grain boundaries than in the grains,

Reproduced with permission of the copyright owner. Further reproduction prohibited without permission.

consistent with the line scanning data. Note that the S counts are higher at the grain boundaries than in the grain, presumably due to a concentration of S in Ga_2S_3 versus ZnS. Segregation of Ga_2S_3 to the grain boundaries would support the assumption that grain boundaries are the primary diffusion path for Ga_2S_3; moreover, the solubility of Ga_2S_3 in ZnS:Mn is low. Unfortunately, the segregated Ga_2S_3 fails to act as a flux agent for grain growth. More likely, it pins the grain boundaries and hinder the mobility of the grain boundaries.

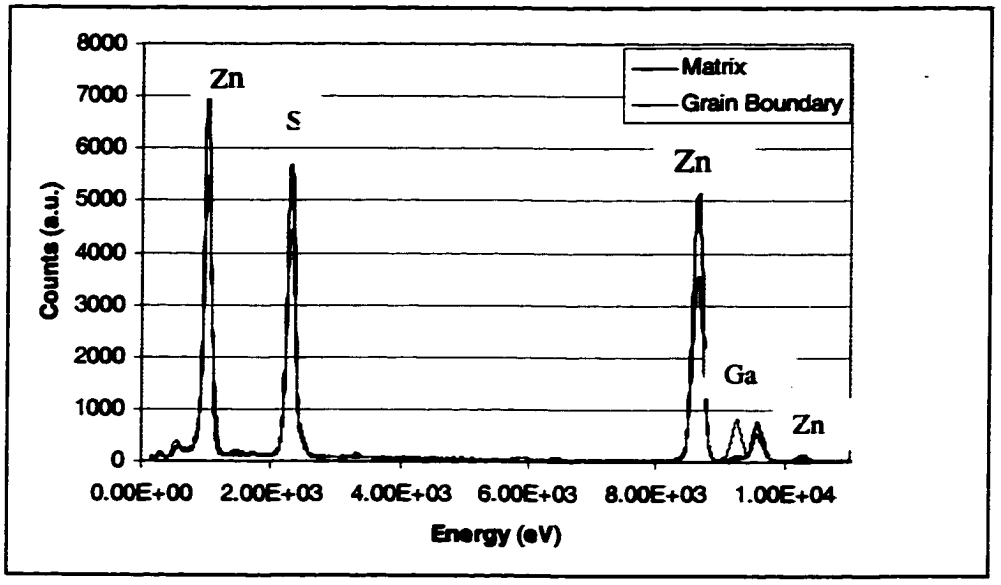

Figure 5.15 EDS spectra showing the chemistry at the grain boundary and at the matrix.

Table 5.2 Stationary probe data for Zn, S, and Ga from three sampling areas in Figure 5.16.

	Area (a)		Area (b)		Area (C)	
	Matrix	Grain Boundary	Matrix	Grain Boundary	Matrix	Grain Boundary
Zn	24186	23556	100511	69638	62004	55592
S	18681	20497	82223	62978	47962	53201
Ga	890	1339	1200	15280	8247	9045

Reproduced with permission of the copyright owner. Further reproduction prohibited without permission.

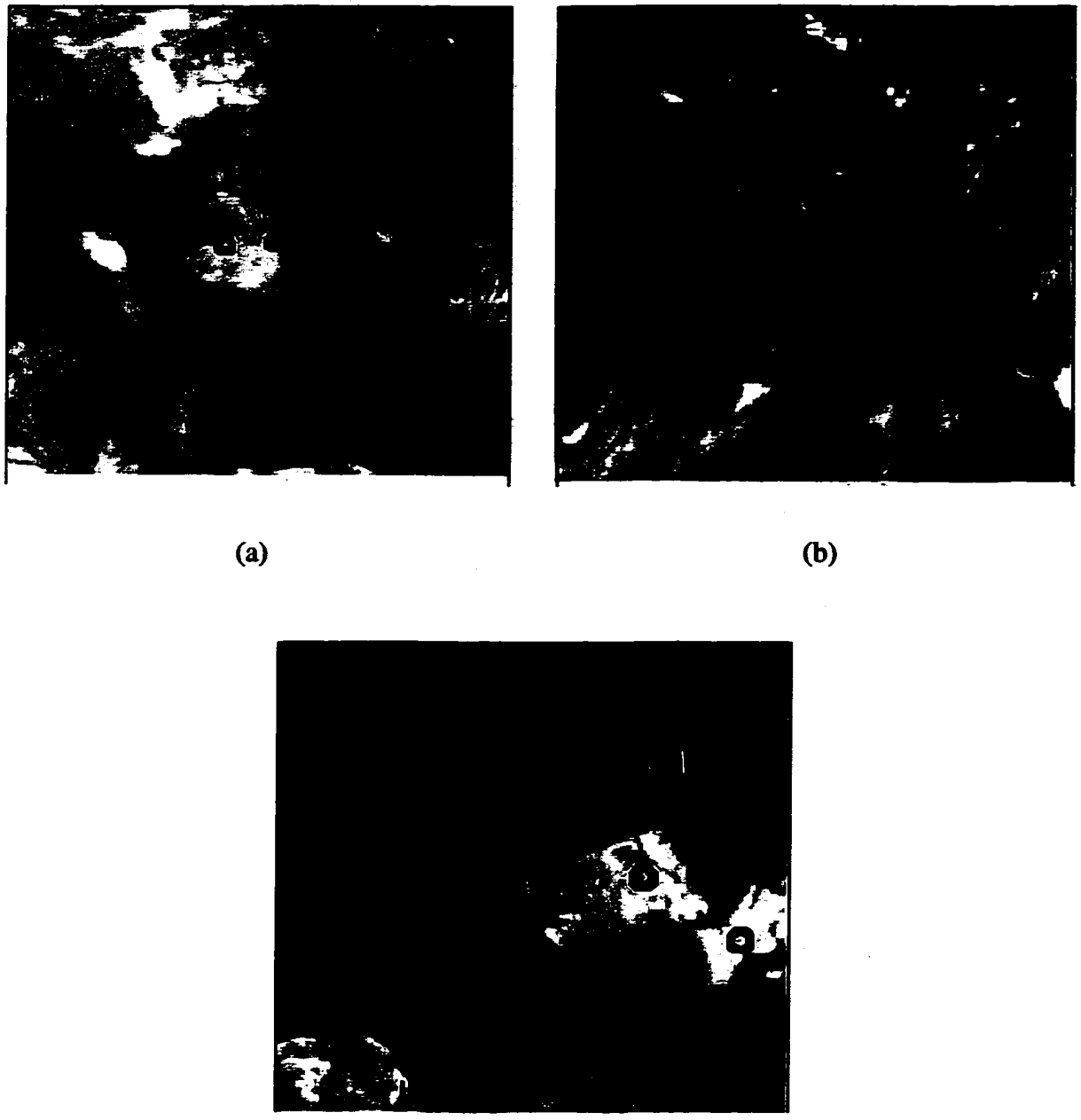

(a) (b)

(c)

Figure 5.16 PTEM mcirographs showing the areas where the EDS was conducted.

5.2.5 Electroluminescence (EL) Properties

The EL brightness as a function of the applied voltage (B-V) is shown in Figure 5.17. For comparison, the data from ZnS:Mn samples without Ga_2S_3 after RTA at 700°C

Reproduced with permission of the copyright owner. Further reproduction prohibited without permission.

or 800°C are also presented. Threshold voltage B_{40} values, CIE coefficients, and the luminous efficiency data are summarized in Table 5.3.

Table 5.3 Effects of Ga_2S_3 on EL properties

		V_{th} (V)	B_{40} (Nits)	CIE Coefficients X	CIE Coefficients Y	η at (V_{th} + 40V) (lm/W)
Without Ga_2S_3	As-deposited	125	48.7	0.5386	0.4591	0.2275
	700°C	125	99.6	0.5325	0.4651	0.4463
	800°C	110	101.0	0.5402	0.4576	0.5428
With Ga_2S_3	700°C	95	34.4	0.5396	0.4578	0.2432
	800°C	85	37.9	0.5431	0.4549	0.2596
	835°C	80	37.0	0.5410	0.4588	N/A

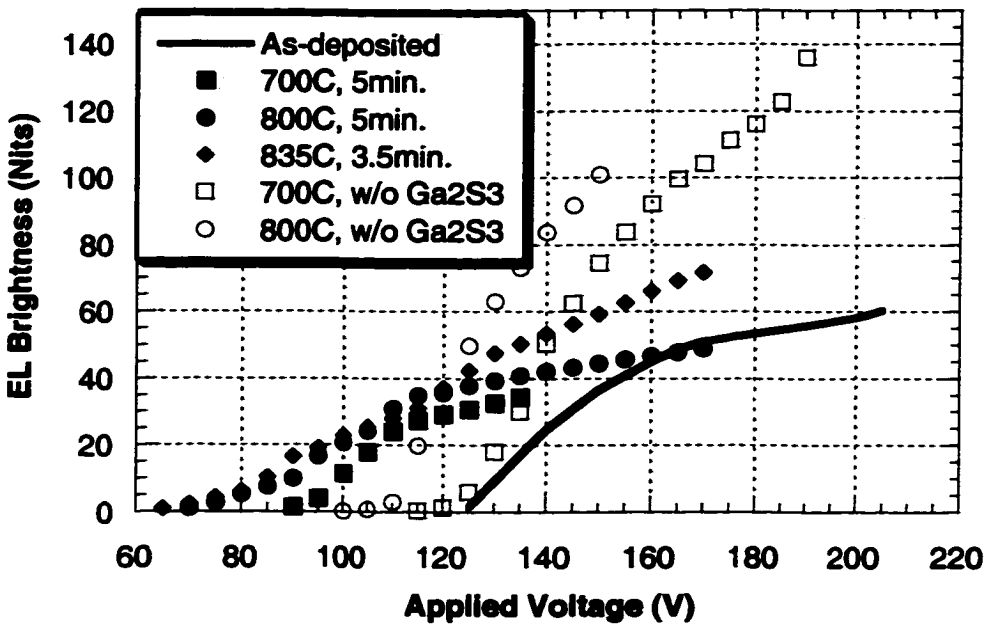

Figure 5.17 B-V curves from samples with and without Ga_2S_3 co-dopant after different annealing treatments.

Comparing the samples with and without Ga_2S_3 after same annealing treatment, it is observed that the addition of Ga_2S_3 causes a reduced threshold voltage and degraded brightness B_{40} and luminous efficiency η_{40}. They are at the level of the as-deposited

Reproduced with permission of the copyright owner. Further reproduction prohibited without permission.

sample. In addition, the ZnS:Mn,Ga_2S_3 samples have a "leaky" turn-on behavior, as shown by the shallow slopes of the B-V curves.

Normally, the turn-on properties are determined by the phosphor and the insulator/phosphor interface properties, such as interfacial defects, dopant(s), interface roughness, and phosphor texture. If there are shallow defect states at the interface close to the conduction band of the ZnS:Mn, which act as donor states, a "leaky" turn-on can be expected, because the electrons in these donor states can tunnel into the conduction band at a relatively low voltage. As discussed in the previous Chapter, once the electric field inside the phosphor reaches its threshold, it does not increase a lot with the increasing applied voltage. In other words, above the threshold voltage, most of the extra applied voltage goes to the insulators. Therefore, a low threshold voltage results in a low electric field in the phosphor, and it will be difficult to accelerate the electrons to high enough energy states to efficiently impact excite the luminescence centers. Poor EL brightness due to low hot electron population becomes inevitable. The microstructure of the ZnS:Mn,Ga_2S_3 samples shown in the TEM images in Figure 5.4a and 5.5a, indicates that the insulator/phosphor interface is not very much improved after annealing, comparing to the as-deposited sample. With the high defect density at the interface area, it is expected that some of the defects have their states close to the conduction band and ZnS:Mn, whose electrons can be ionized at a relatively low voltage. In addition, these defects are not well defined, instead, they have a distribution at the interface. Besides, Ga_2S_3 segregation to the grain boundaries and/or the diffusion of Ga into the ATO layer can be sources of such interfacial defect donor states as well.

Reproduced with permission of the copyright owner. Further reproduction prohibited without permission.

The low EL brightness from $ZnS:Mn,Ga_2S_3$ can be associated with several factors, including the heavily defected microstructure, insufficient density of energy at the interface, low population of hot electrons, low excitation probability, improper concentration of the luminescent centers, and unfavorable energy transfer among ions. It is known that little improvement in lattice structure occurs during annealing, according to the TEM analysis. The density of the contrast bands, which basically are stacking faults, microtwins and switches between cubic and hexagonal, can be bad to the EL properties, especially stacking faults. Generally, there are two partial dislocations at both ends of the stacking fault, which means it can be electrically active because of the dangling bonds. The concentration of luminescence centers should not be the problem, since these samples are from the same batch as the samples used for the KCl doping investigation, reported in Chapter 4. The rest of the factors will be discussed below.

There is a possibility that energy transfer from Mn^{2+} to Ga^{3+} occurs during the EL process, since EDS confirms the existence of a small amount of Ga inside the grains. Energy transfer occurs during relaxation process, i.e., after the electrons in the luminescent centers have been excited to a higher energy level by the hot electrons. For normal EL relaxation, electrons should return to the ground state by producing luminescence, i.e., by generating a photon. However, when energy transfer occurs, these excited electrons in Mn^{2+} may release all or part [3] of the energies they have to another ion, such as a Ga^{3+} ion that has lower energy state. This type of energy transfer is usually non-radiative, and thus makes no contribution to EL performance, causing low EL brightness. Non-radiative energy transfer from Mn^{2+} ions to other ions or lattice defects is common and important to EL in the phosphor [86]. However, energy transfer can be

Reproduced with permission of the copyright owner. Further reproduction prohibited without permission.

beneficial to EL process, if it happens by transferring energy from another species to the luminescent centers. In the case of Ga^{3+} in ZnS:Mn, it has been reported that the incorporation of Ga^{3+} modifies the crystal field. The observed EL emission shifts to longer wavelength (more reddish) [89]. Luminescence lifetime measurement is a good technique to verify the existence of energy transfer between Ga^{3+} and Mn^{2+}, since non-radiative relaxation from Mn^{2+} luminescent centers have much short life time than the radiative relaxation.

To understand whether Ga_2S_3 dopant has deteriorated the radiative relaxation of the Mn^{2+} luminescent centers, room temperature photoluminescence data are collected from ZnS:Mn,Ga_2S_3 and ZnS:Mn samples, as shown in Figure 5.18. For accuracy, all samples were placed on a single holder. By comparing the sample with Ga_2S_3 with those without, the former ones have higher PL brightness, which means the radiative relaxation of Mn^{2+} is improved by the incorporation of Ga_2S_3. The operating mechanism is suspected to be associated with the possible energy transition from Ga^{3+} to Mn^{2+} induced by photon.

It is clear that Ga_2S_3 improves PL brightness of ZnS:Mn, but deteriorates EL brightness. Since basically PL characterizes the radiative relaxation of the luminescence centers, it is believed that the low EL brightness is resulted from bad luminescence center excitation. Further, it can be either or both of the following causes: low hot electron population, and low excitation probability.

A low interface energy states density and the failure to accelerate the injected electrons to high energy states during their transportation in the phosphor can cause a low hot electron population. In current study, there is no experimental data that can

Reproduced with permission of the copyright owner. Further reproduction prohibited without permission.

characterize the interface states density. However, the transportation of the injected electrons and the acceleration during this process are considered to be bad, due to the high defect density in the phosphor and the low threshold voltage which results in low electric field in the phosphor above threshold. It is possible that the electric field is not high enough to accelerate the injected electrons to high energy states. The excitation probability is a function of the product of electron mean free path and the electric field in the phosphor. Again, because of the heavily defected lattice and the low electric field in the phosphor, the excitation probability is expected to be low. It is very likely that both mechanisms operate in this case simultaneously.

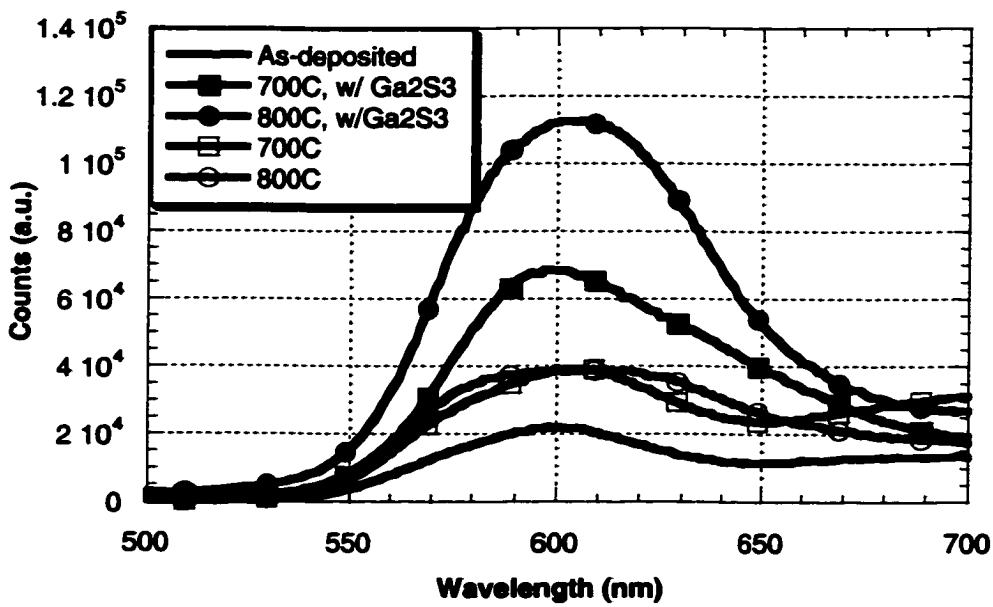

Figure 5.18 PL spectra from samples with and without Ga_2S_3 as-deposited or after 5 minutes of annealing at 700°C or 800°C.

Reproduced with permission of the copyright owner. Further reproduction prohibited without permission.

5.3 Summary

When Ga_2S_3 is introduced into the ZnS:Mn by diffusion at elevated temperatures, grain boundaries are the primary diffusion paths. Because of the low solubility in ZnS:Mn, most of it segregates to the grain boundaries. Instead of acting as a flux agent to enhance grain boundary mobility, Ga_2S_3 pins the grain boundaries and impedes the grain growth. In addition, Ga_2S_3 does not reduce the lattice defects in the ZnS:Mn phosphor, leading to degraded EL performance after annealing.

The half-stack EL devices from ZnS:Mn,Ga_2S_3 have lowered threshold voltage and comparable EL brightness and luminous efficiency as the as-deposited ZnS:Mn samples. The reduction in threshold voltage is postulated to be resulted from interfacial lattice defects from deposition and which remain after annealing (for example, pinned by Ga_2S_3). These defects may have a range of energy states near the conduction band so that they can be excited at relatively low voltages. The low brightness is suspected to be related to insufficient hot electrons and low excitation probability, since the improved PL brightness from ZnS:Mn,Ga_2S_3 indicates the radiative relaxation of these samples is good. The suspected mechanism for this improvement is the possible energy transfer from Ga^{3+} to Mn^{2+} induced by photon.

Reproduced with permission of the copyright owner. Further reproduction prohibited without permission.

CHAPTER 6
ZnS:Mn WITH KCl AND Ga_2S_3 AS CO-DOPANTS

6.1 Introduction

As addressed in Chapters 4 and 5, the introduction of KCl into the ZnS:Mn lattice causes enhanced grain growth, elimination of the equiaxed grain layer at the insulator/phosphor interface, increases in EL brightness and luminous efficiency, as well as a slightly increase in the threshold voltage. However, when Ga_2S_3 is incorporated into the ZnS:Mn phosphor, neither the microstructure nor the EL performance shows improvement. The threshold voltage decreases, and the EL turn-on is "leaky". In this Chapter, the effects of adding both KCl and Ga_2S_3 to ZnS:Mn will be discussed.

Addition of these two co-dopants is achieved by double annealing. In other words, co-dopant #1 is thermal evaporated and RTA #1 is performed, followed by thermal evaporation of co-dopant #2 and RTA #2. To determine which co-dopant dominates the EL properties and microstructure, double co-doping is carried out in the following two sequences, KCl first followed by Ga_2S_3, and Ga_2S_3 first followed by KCl. Since 5 minutes at 700°C gives the best improvement on EL properties on KCl co-doped ZnS:Mn thin films, and 800°C for 5 minutes does the same for Ga_2S_3 co-doped samples, annealing at these two conditions are conducted.

Reproduced with permission of the copyright owner. Further reproduction prohibited without permission.

6.2 Results and Discussions

6.2.1 Secondary Ion Mass Spectrometry (SIMS)

Figure 6.1 shows the SIMS profiles of samples after double annealing at 800°C with and without single co-dopant. Figure 6.2 is the SIMS profiles from double co-doping after annealing at either 700°C or 800°C. After double annealing at 800°C, the distributions of all the dopant species in phosphor layers are uniform. Diffusion of Mn, Ga, Cl and K into ATO layers is clearly seen, especially K, Cl and the Mn in KCl co-doped samples. As given in Figure 6.1c, K has comparable counts in the ATO layer and in the phosphor layer.

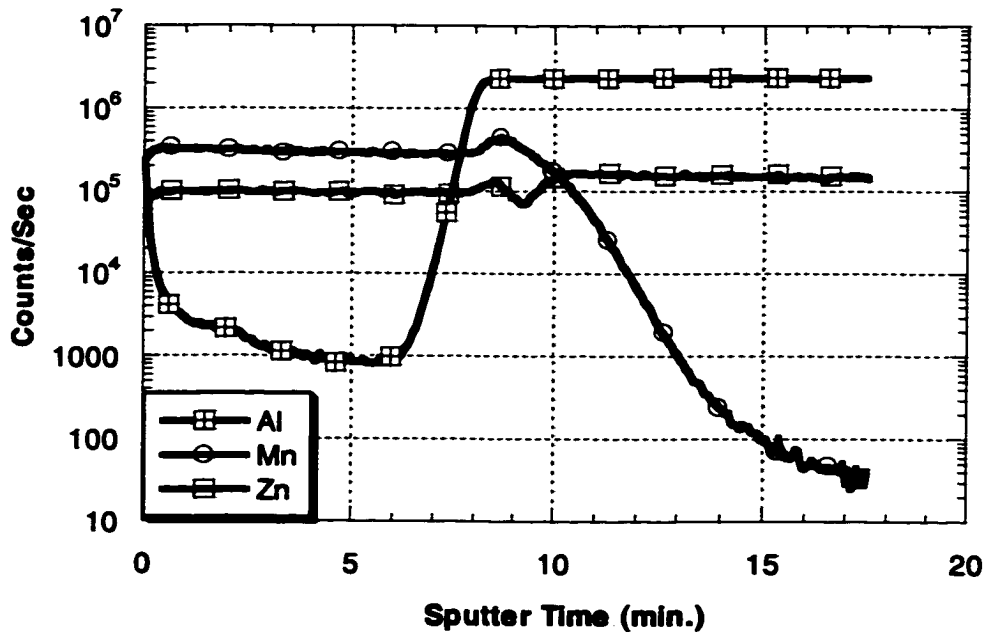

(a)

Figure 6.1 SIMS profile from ZnS:Mn sample after double annealing at (a) 800°C, (b) 800°C, 800°C with Ga_2S_3, (c) 800°C, 800°C with KCl.

Reproduced with permission of the copyright owner. Further reproduction prohibited without permission.

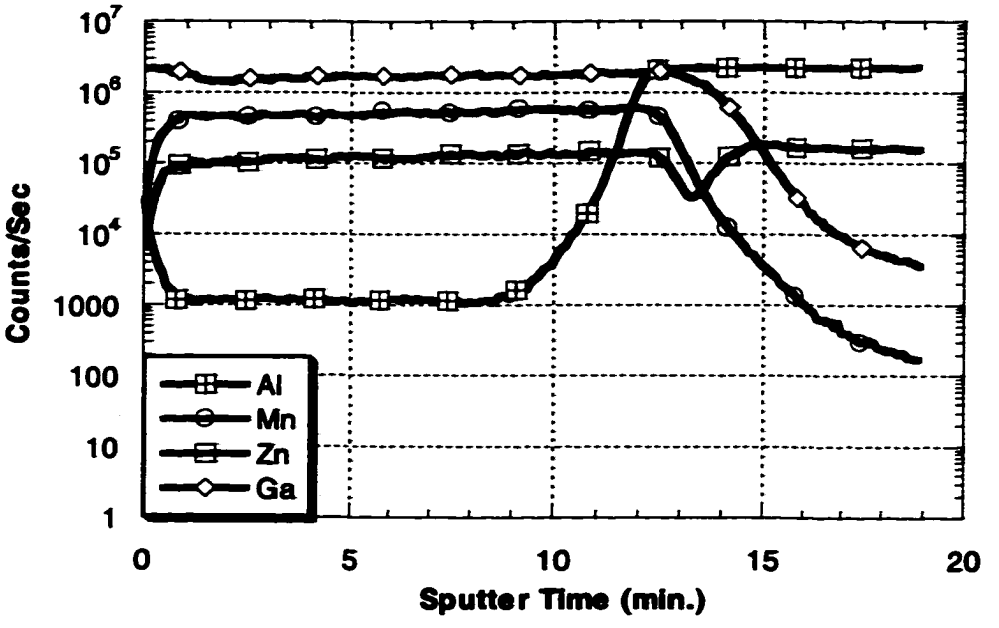

(b)

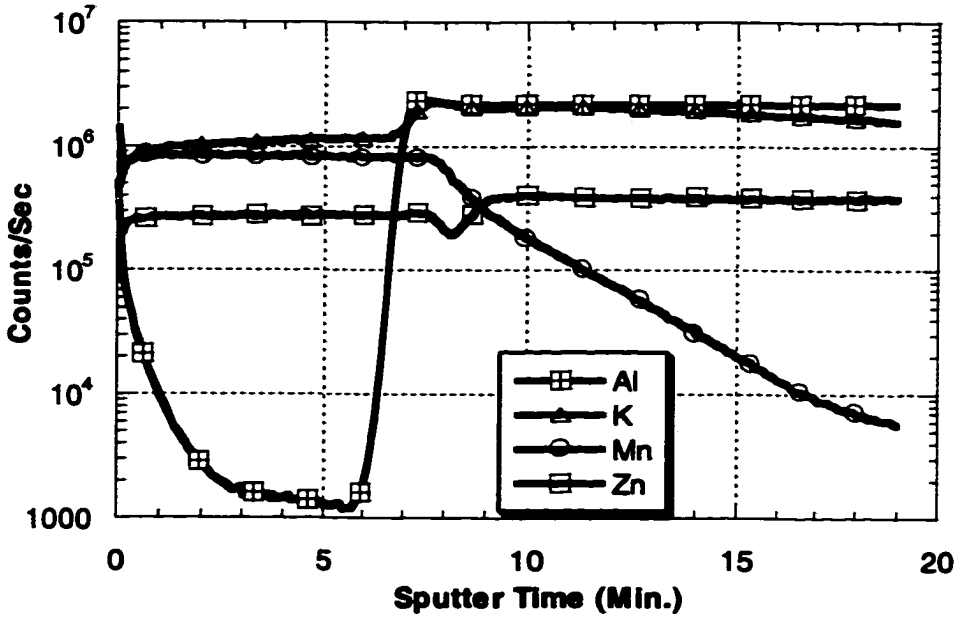

(c)

Reproduced with permission of the copyright owner. Further reproduction prohibited without permission.

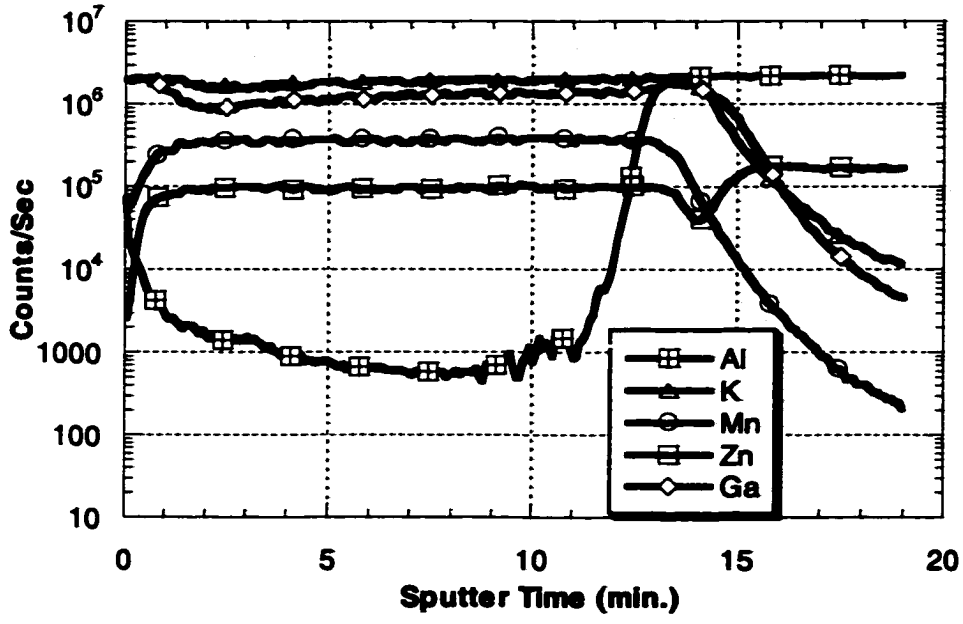

(a)

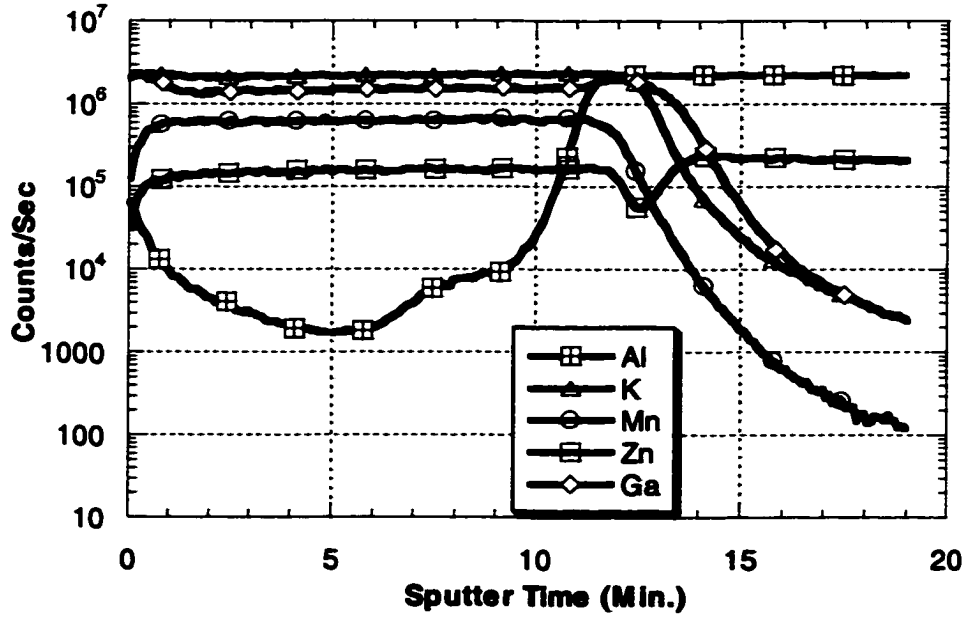

(b)

Figure 6.2 SIMS profiles from (a) 800°C with Ga_2S_3, 700°C with KCl, (b) 800°C with Ga_2S_3, 800°C with KCl, and (c) 700°C with KCl, 800°C with Ga_2S_3.

Reproduced with permission of the copyright owner. Further reproduction prohibited without permission.

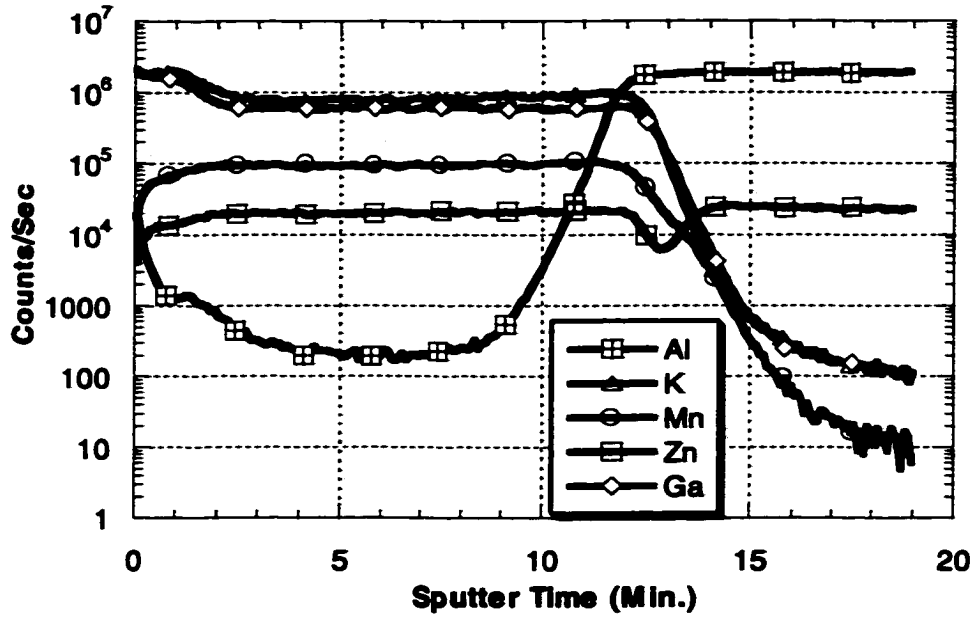

(c)

For samples with both dopants, diffusion of all species into the insulator near the insulator/phophor interface is indicated. However, the incorporation of K into ATO at 800°C is prevented by the first annealing with Ga_2S_3 (Figure 6.2b). The diffuse insulator/phosphor interface in all the samples with both co-dopants, as shown in Figure 6.2, suggests the possibility of forming $AlGa_2O_4$ phase.

6.2.2 X-ray Diffractometry (XRD)

XRD results from the double doped/double annealed samples and their comparisons are listed in Table 6.1. The relative intensities from certain peaks are presented in the bar chart in Figure 6.3.

Compared to the as-deposited sample, double annealing stabilizes the cubic structure, similar to the single anneals. This is based upon the disappearance of the h(01-

Reproduced with permission of the copyright owner. Further reproduction prohibited without permission.

10) and h(10-12) peak for samples annealed at high temperatures, and the increases in c(200), c(400) and c(422), as shown in Figure 6.3a and Table 6.1. The slight reduction of c(111) + h(0002) peaks and increase in c(200) and c(400) peaks can be resulted from either phase transformation and/or a change in texture, as discussed in Chapter 4.

Table 6.1 XRD results from samples after double annealing and double co-doping.

				As-deposited		700°C, 800°C	
Index	2θ	Inten. (a.u.)	Relative %	Counts (a.u.)	Relative %	Counts (a.u.)	Relative %
(0110)	26.9	100	13.6	96	4.9	0	0.0
(0002)+(111)	28.5	184	25.0	961	49.4	1232	47.3
(1011)*	30.5	87	11.8	458	23.6	571	21.9
(200)	33.1	10	1.4	71	3.7	204	7.8
(1012)	39.6	28	3.8	17	0.9	0	0.0
(220)+(1120)	47.5	132	18.0	85	4.4	76	2.9
(1013)	51.8	54	7.3	0	0.0	0	0.0
(2020)	55.5	11	1.5	0	0.0	41	1.6
(311)+(1122)	56.3	77	10.5	202	10.4	404	15.5
(2021)	57.6	12	1.6	0	0.0	0	0.0
(0004)+(222)	59.1	4	0.5	28	1.4	24	0.9
(2022)	63.6	6	0.8	0	0.0	0	0.0
(400)	69.5	6	0.8	17	0.9	52	2.0
(2023)	73.9	15	2.0	0	0.0	0	0.0
(331)	76.8	9	1.2	0	0.0	0	0.0
(420)	79.1	2	0.3	0	0.0	0	0.0
(1015)	82.3	11	1.5	0	0.0	0	0.0
(422)	88.5	9	1.2	9	0.5	19	0.7
		735	100.0	1944	100.0	2604	100.0

Reproduced with permission of the copyright owner. Further reproduction prohibited without permission.

Table 6.1 continued.

700°C, 800°C, w/ KCl		700°C, w/KCl, 800°C, w/ Ga_2S_3		800°C, 800°C		800°C, 800°C, w/ KCl	
Counts (a.u.)	Relative %	Counts (a.u.)	Relative %	Counts (a.u.)	Relative %	Counts (a.u.)	Relative %
72	2.9	0	0.0	0	0.0	0	0.0
961	38.1	784	42.7	949	44.7	538	36.2
635	25.2	543	29.6	610	28.7	424	28.6
306	12.1	106	5.8	193	9.1	164	11.0
0	0.0	0	0.0	0	0.0	0	0.0
59	2.3	61	3.3	46	2.2	31	2.1
0	0.0	0	0.0	0	0.0	0	0.0
0	0.0	0	0.0	0	0.0	0	0.0
396	15.7	216	11.8	266	12.5	256	17.2
0	0.0	0	0.0	0	0.0	0	0.0
21	0.8	24	1.3	0	0.0	0	0.0
0	0.0	34	1.9	0	0.0	0	0.0
71	2.8	50	2.7	46	2.2	72	4.8
0	0.0	0	0.0	0	0.0	0	0.0
0	0.0	0	0.0	0	0.0	0	0.0
0	0.0	0	0.0	0	0.0	0	0.0
0	0.0	0	0.0	0	0.0	0	0.0
0	0.0	16	0.9	15	0.7	0	0.0
2521	100.0	1834	100.0	2125	100.0	1485	100.0

Reproduced with permission of the copyright owner. Further reproduction prohibited without permission.

Table 6.1 continued.

800°C, w/ KCl, 800°C, w/ Ga_2S_3		800°C, 800°C, w/ Ga_2S_3		800°C, w/ Ga_2S_3, 800°C, w/ KCl	
Counts (a.u.)	Relative %	Counts (a.u.)	Relative %	Counts (a.u.)	Relative %
0	0.0	82	3.4	0	0.0
1018	41.3	1082	45.4	967	45.0
600	24.3	566	23.7	524	24.4
237	9.6	142	6.0	149	6.9
16	0.6	0	0.0	0	0.0
64	2.6	110	4.6	92	4.3
0	0.0	0	0.0	0	0.0
0	0.0	0	0.0	0	0.0
400	16.2	320	13.4	331	15.4
0	0.0	0	0.0	0	0.0
19	0.8	18	0.8	23	1.1
14	0.6	0	0.0	0	0.0
71	2.9	44	1.8	35	1.6
0	0.0	0	0.0	0	0.0
0	0.0	0	0.0	0	0.0
0	0.0	0	0.0	0	0.0
0	0.0	0	0.0	0	0.0
27	1.1	20	0.8	26	1.2
2466	100.0	2384	100.0	2147	100.0

Reproduced with permission of the copyright owner. Further reproduction prohibited without permission.

Table 6.1 continued.

800°C, 700°C		800°C, 700°C, w/ Ga_2S_3		800°C, w/ Ga_2S_3, 700°C, w/ KCl	
Counts (a.u.)	Relative %	Counts (a.u.)	Relative %	Counts (a.u.)	Relative %
0	0.0	71	3.0	108	4.6
992	46.7	1122	47.9	1076	45.4
471	22.2	590	25.2	562	23.7
172	8.1	110	4.7	139	5.9
0	0.0	0	0.0	0	0.0
59	2.8	110	4.7	112	4.7
0	0.0	0	0.0	0	0.0
0	0.0	0	0.0	0	0.0
346	16.3	292	12.5	310	13.1
0	0.0	0	0.0	0	0.0
14	0.7	18	0.8	18	0.8
0	0.0	0	0.0	0	0.0
45	2.1	30	1.3	29	1.2
0	0.0	0	0.0	0	0.0
0	0.0	0	0.0	0	0.0
0	0.0	0	0.0	0	0.0
0	0.0	0	0.0	0	0.0
23	1.1	0	0.0	18	0.8
2122	100.0	2343	100.0	2372	100.0

In general, the introduction of KCl in double annealing enhances the changes in XRD peaks from samples without KCl, as seen in Figure 6.3b. With KCl, the cubic phase increases significantly, based on the increase in the intensity ratios of cubic versus hexagonal peak intensities. The c(200) texture is more provident, since the c(200) peak intensity is about ten times of the random particle's, while that of c(111) + h(0002) is only 30% more than the random particle's.

Reproduced with permission of the copyright owner. Further reproduction prohibited without permission.

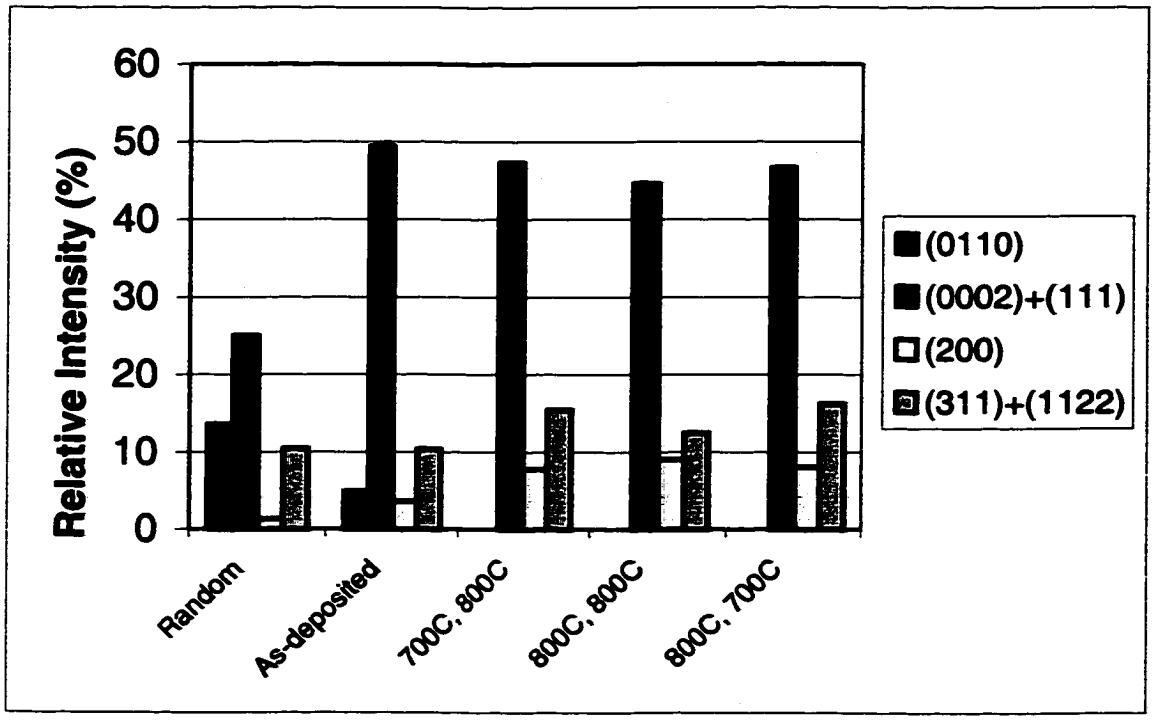

(a)

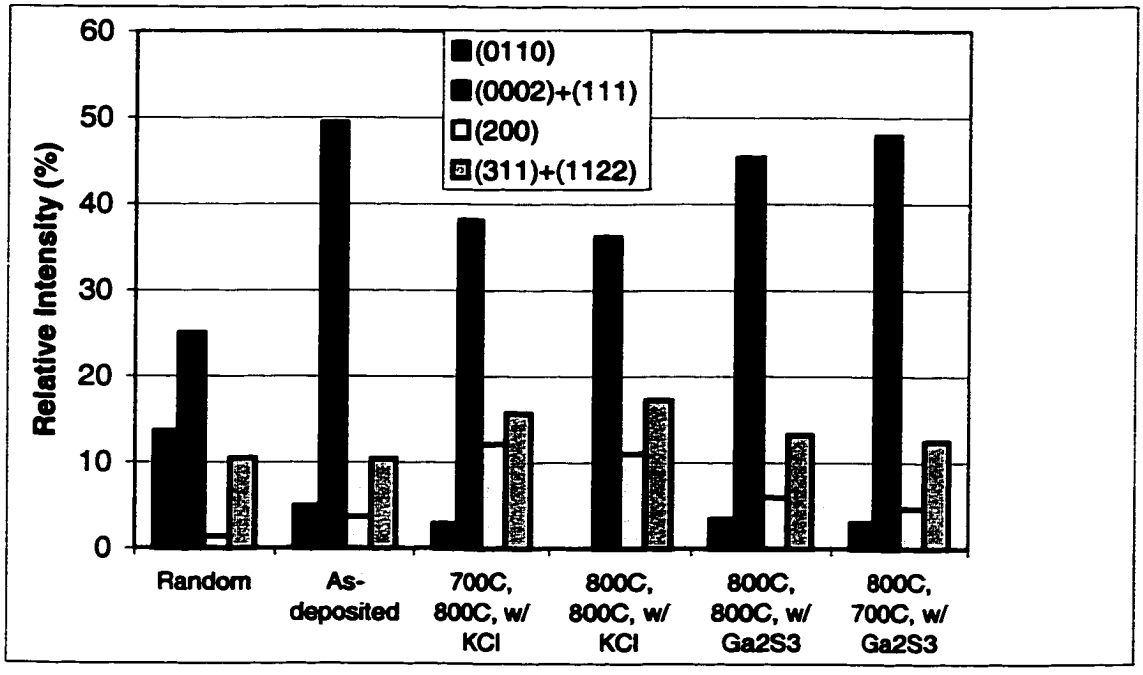

(b)

Figure 6.3 Effects of (a) double annealing, (b) double annealing with single codopant, and (c) double annealing with double co-dopants on the texture.

Reproduced with permission of the copyright owner. Further reproduction prohibited without permission.

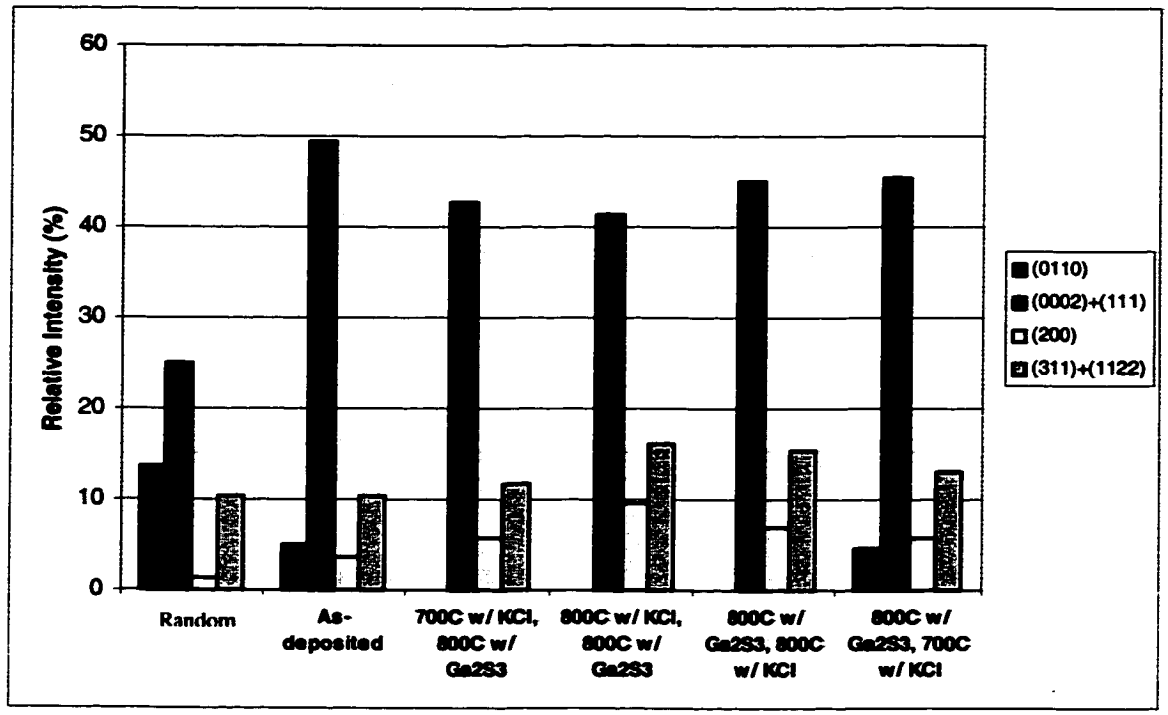

(c)

Contrary to the effects of KCl, Ga_2S_3 slightly enhances the c(111) + h(0002) orientations and stabilizes the hexagonal phase (see Table 6.1, Figures 6.3a, 6.3b and 6.3c). For example, the h(10-10) peak that can be annealed out by double annealing without co-dopants or with KCl alone, still exists in Ga_2S_3 co-doped samples, as illustrated in Figure 6.3b. Moreover, the intensities from c(200) and c(400) peaks are less than the corresponding samples without Ga_2S_3.

In the samples that are diffused with KCl first followed by Ga_2S_3, the XRD results indicate that the changes are a combination of those from KCl or Ga_2S_3 alone. On the other hand, when the samples are doped with Ga_2S_3 first followed by KCl, the XRD

Reproduced with permission of the copyright owner. Further reproduction prohibited without permission.

results look much similar to those from only Ga_2S_3. It seems that KCl cannot change the microstructure pinned by Ga_2S_3, in terms of texture.

6.2.3 Transmission Electron Microscopy (TEM)

In an effort to understand the effects of double annealing, double co-doping on the microstructure of ZnS:Mn, XTEM samples from selected samples are investigated. Figure 6.4 gives the TEM micrographs and the corresponding diffraction pattern taken from ZnS:Mn,KCl after double annealing at 800°C. The top layer is the reflective aluminum electrode. The white crack at the phosphor/ATO interface is caused either by sample preparation or the double annealing process.

Unlike the grain morphology observed before, huge grains extending the entire film thickness are developed in this sample, as evidently shown in Figure 6.4. Some of them have diameters of 500nm. The equiaxed fine grain layer has been completely removed. The grooves where grain boundaries emerge on the free surface are easily seen. All the grain boundaries are sharply defined, and the defect density inside the grains is largely reduced, although contrast bands can still be seen across the whole grain. The grain growth is not uniform, as illustrated in Figure 6.4b, which is taken from another area of the same sample as in Figure 6.4a. The diffraction pattern is shown as an inset in Figure 6.4b. Not surprisingly, no ring pattern is observed. Corresponding to the existence of the bands seen in the bright field image, twin spots are captured in the diffraction pattern, which indicates that most of the bands are microtwins. Unlike stacking faults who have partial dislocations at both ends, microtwins do not have dangling bonds and are expected to be less electrical active.

Reproduced with permission of the copyright owner. Further reproduction prohibited without permission.

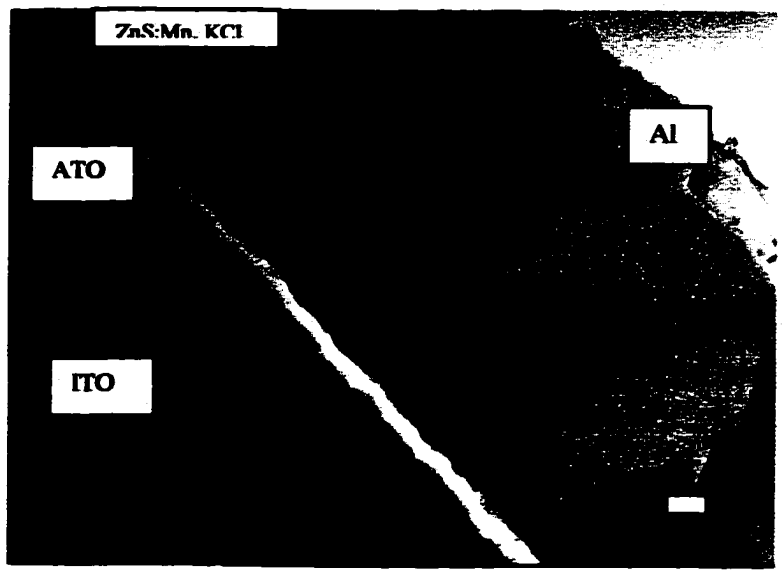

(a)

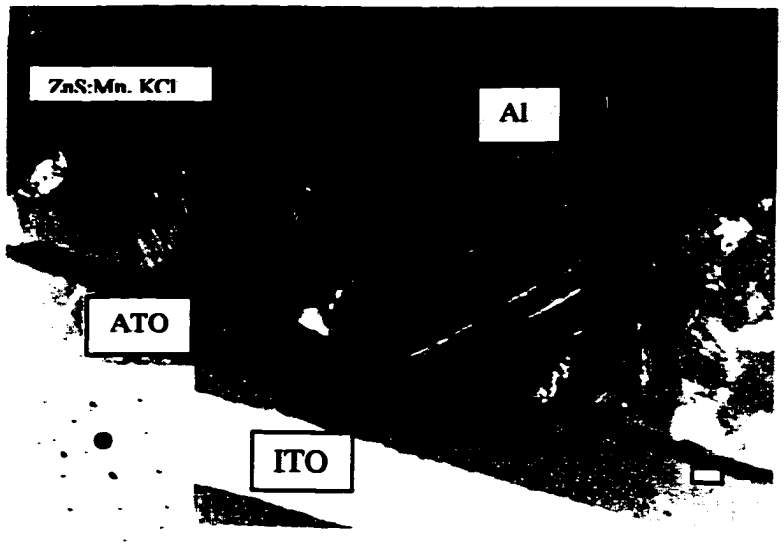

(b)

Figure 6.4 XTEM micrograph and diffraction pattern taken from the sample with KCl after double annealing at 800°C. (a) and (b) are from different areas. (Bar = 100nm)

Reproduced with permission of the copyright owner. Further reproduction prohibited without permission.

Since no evidence is found in any sample for recrystallinzation (i.e., no evidence of nucleation and growth of new grains), the growth mechanism is believed to be *in situ* growth. *In situ* grain growth means some of the grains grow at the expense of others. It can be achieved in the following ways. First, it happens when certain grains have more favorable crystal orientations than the others. The driving force for this kind of growth is the reduction of grain boundary and surface energies. The free energy associated with the grain boundary is reduced by reducing the grain boundary volume fraction. Changing the texture reduces the surface energy term, since the surface energy varies with crystal planes. Second, it is possible when diffusion induced grain boundary migration occurs. This mechanism is attributed to the diffused species changing the grain boundary energy and thus enhancing the mobility and/or the driving force for grain boundary migration. Third, it can also be achieved by enhanced dislocation motion that causes grain boundary motion. This is usually associated with the existence of point defects, such as a flux of vacancy to assist dislocation climb.

In KCl doped samples, the significant grain growth is believed to follow both diffusion induced grain boundary migration and enhanced dislocation motion mechanisms. Grain boundary motion is critical to grain growth, since the grain growth rate is proportional to both driving force and the mobility of grain boundary [69]. Grain boundaries can always be treated as an array of dislocations [86], with the low angle boundaries having edge dislocation spaced larger than the core dimension, and high angle boundaries having dislocation spacing smaller than the core dimension. Therefore, the motion of grain boundaries can be modeled in term of dislocation motion. Because the significant grain growth only occurs in the samples co-doped with KCl and annealed at

Reproduced with permission of the copyright owner. Further reproduction prohibited without permission.

high temperatures (800°C), it is speculated that KCl, together with the zinc vacancies, helps the glide and climb of the dislocations in ZnS:Mn lattice at elevated temperatures.

A specific situation is shown schematically in Figure 6.5. An α dislocation whose dislocation line coming out of the paper, is shown by an extra half plane in the lattice. A K interstitial is located at the end of this dislocation, since the dislocation core is known to have more space. Assuming there are zinc vacancies at position 1, as shown in Figure 6.5a, it is possible for the K interstitial to move one step left, as shown in Figure 6.5b,

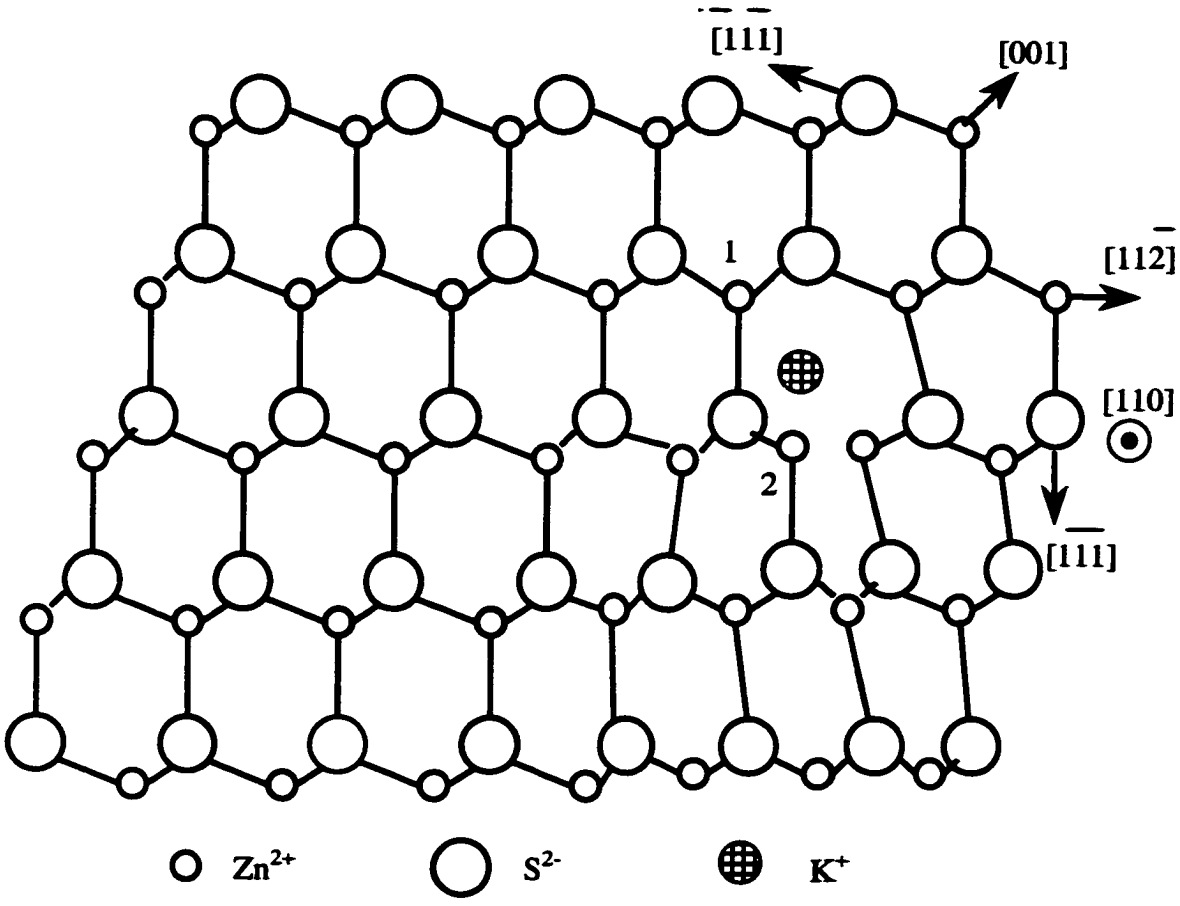

(a)

Figure 6.5 Schematics showing how KCl helps dislocations glide in ZnS:Mn. (a) original state,(b) after glide, and (c) after climb.

Reproduced with permission of the copyright owner. Further reproduction prohibited without permission.

especially at elevated temperatures when the mobility of zinc and sulfur vacancies are high. As discussed in Chapter 4, K has high mobility in ZnS even at relatively low temperature. In this way, the dislocation line has glided one atomic plane from its original position. With more zinc vacancies locating ahead, it can glide further. Considering another situation, if there are zinc vacancies locating at position 2 in Figure 6.5a, this dislocation can climb down one atomic plane at high temperature, as shown in Figure 6.5c. It is clear that both glide and climb require a flux of vacancies, which means at higher temperature, this dislocation motion is more significant.

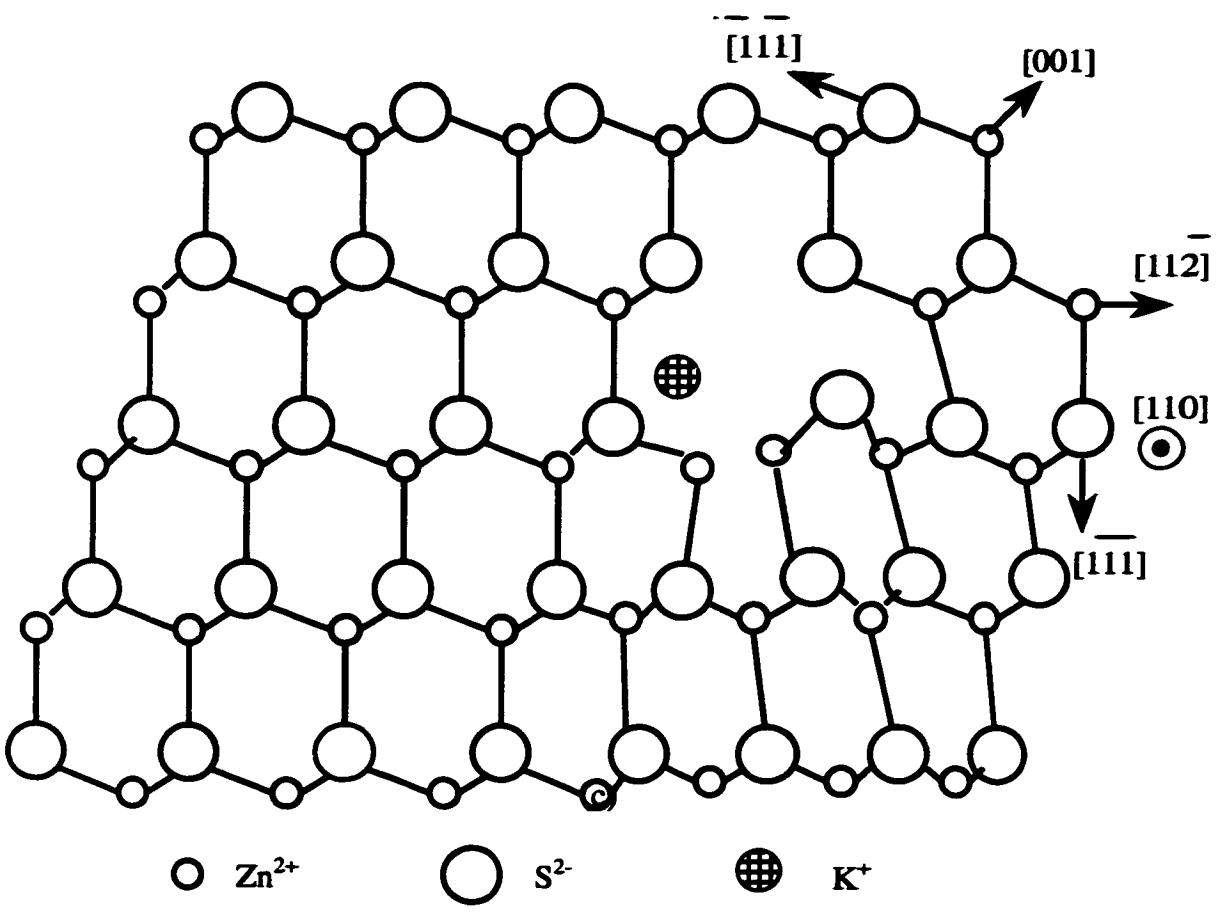

(b)

Reproduced with permission of the copyright owner. Further reproduction prohibited without permission.

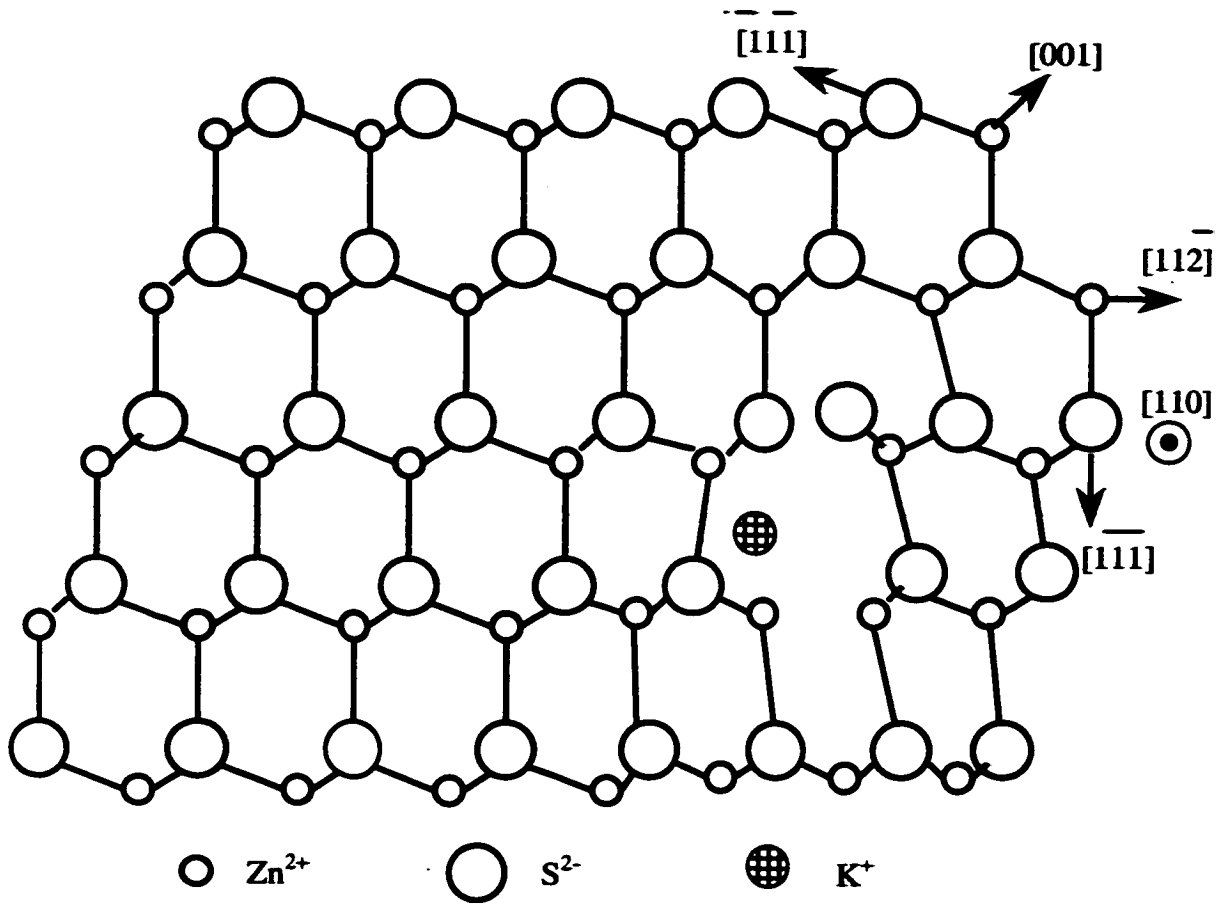

(c)

Figure 6.6 shows the XTEM micrograph and the diffraction pattern taken from the sample with Ga_2S_3 after double annealing at 800°C. The two layers on top of the phosphor film are the aluminum electrode and the extra Ga_2S_3 layers, as labeled. In this case, grain growth does not occur and the defect density is comparable to that in the as-deposited state. However, the columnar grain boundaries are very clearly defined. There is still a large amount of bands in the columnar grains. The equiaxed fine grain layer is still present at the phosphor/ATO interface, although the size of those grains in this sample is about 40nm. The inset diffraction pattern in Figure 6.6 shows a strongly

Reproduced with permission of the copyright owner. Further reproduction prohibited without permission.

textured microstructure. Obviously, double annealing with Ga_2S_3 does not improve the crystallinity.

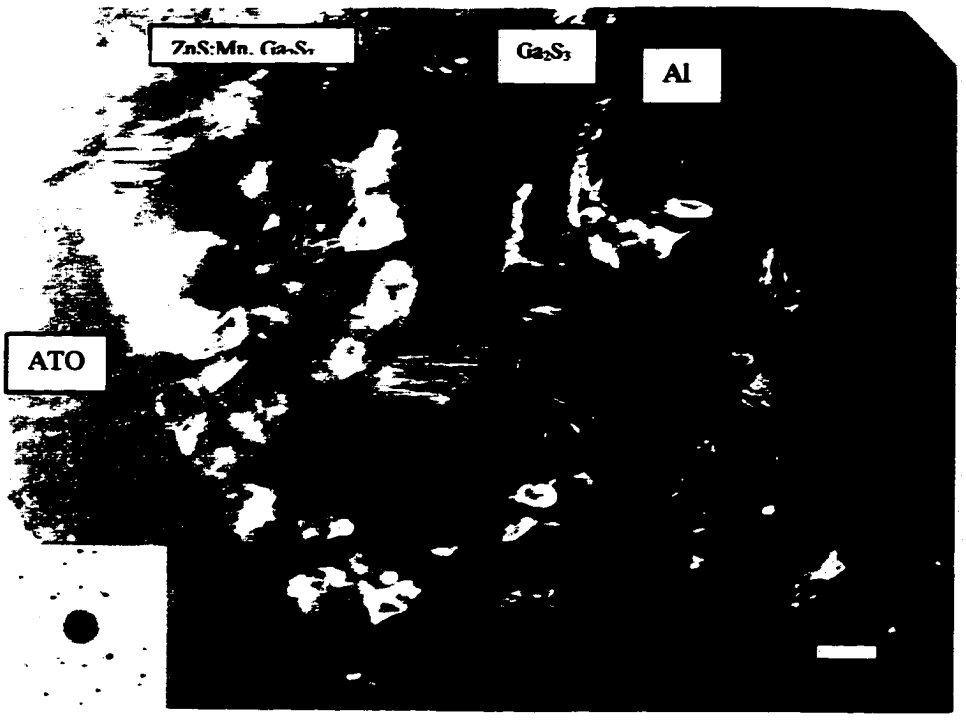

Figure 6.6 XTEM micrograph taken from sample with Ga_2S_3 after double annealing. (Bar = 100nm)

The micrograph and diffraction pattern taken from the sample doped with Ga_2S_3 followed by KCl at 800°C are shown in Figure 6.7. The microstructure is very similar to that shown in Figure 6.6. Therefore KCl doping as the second step does not lead to improved microstructure, even at an annealing temperature of 800°C. In some area, the grain morphology is not columnar, rather three-dimensional grains are seen. Normally, columnar grains in thin films becoming three-dimensional grains is a result of grain growth. In this case, the lateral dimension is still very small. It is suspected that the KCl does have the function to enhance grain growth to some extent in this sample. However,

Reproduced with permission of the copyright owner. Further reproduction prohibited without permission.

since the columnar grain boundaries have been pinned well by the Ga_2S_3 from the first doping process, the dislocation motion enhancement by KCl is not working. The inset diffraction pattern confirms the polycrystalline nature of the sample.

Figure 6.7 XTEM micrograph from sample doped with Ga_2S_3 followed by KCl at 800°C. (Bar = 100nm)

The bright field XTEM micrograph from the sample doped with KCl followed by Ga_2S_3 at 800°C is in Figure 6.8. Big grains with strain bands are observed. The aluminum electrode and a Ga_2S_3 layer are labeled. This imaged area has separated from the ATO layer, presumably during sample preparation. The diffraction contrast between these grains is quite weak, making it difficult to define the grain boundaries. Low diffraction contrast across the grain boundary implies they are low angle boundaries. This is consistent with the observation of strain bands, since grain boundaries are the strain relief sites in polycrystalline materials. The grain morphology is not uniform, and

Reproduced with permission of the copyright owner. Further reproduction prohibited without permission.

the defect density is variable. Generally, large diameter grains had low defect density and has strain bands, while the reverse is true for smaller grains. A single crystal diffraction pattern is achieved from this area, as the inset in the bright field image shown.

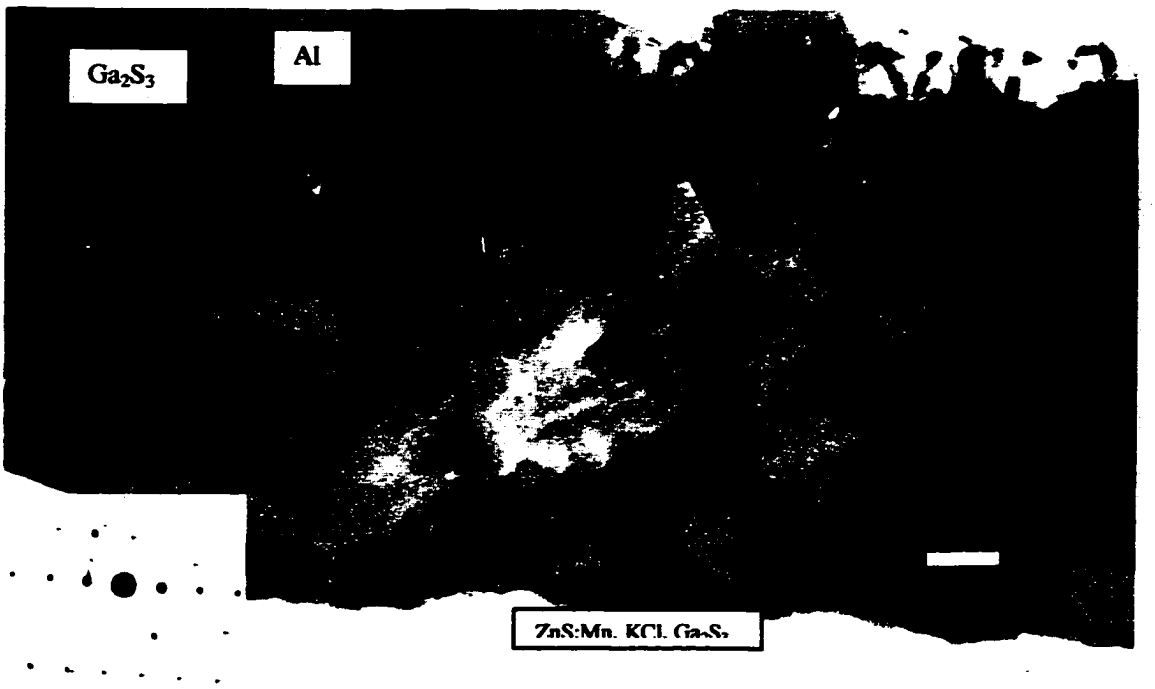

Figure 6.8 XTEM micrograph from sample doped with KCl first followed by Ga_2S_3 at 800°C. (Bar = 100nm)

As will be shown later, the sample co-doped with Ga_2S_3 at 800°C followed by KCl at 700°C has the best EL brightness. The XTEM micrograph and the diffraction pattern taken from this sample are shown in Figure 6.9. The bright field image looks very much like the one with Ga_2S_3 after double annealing at 800°C (Figure 6.6). The grains are still columnar, with very limited growth during annealing. The defect density is still very high, and the diffraction pattern shows texture and streaks.

Reproduced with permission of the copyright owner. Further reproduction prohibited without permission.

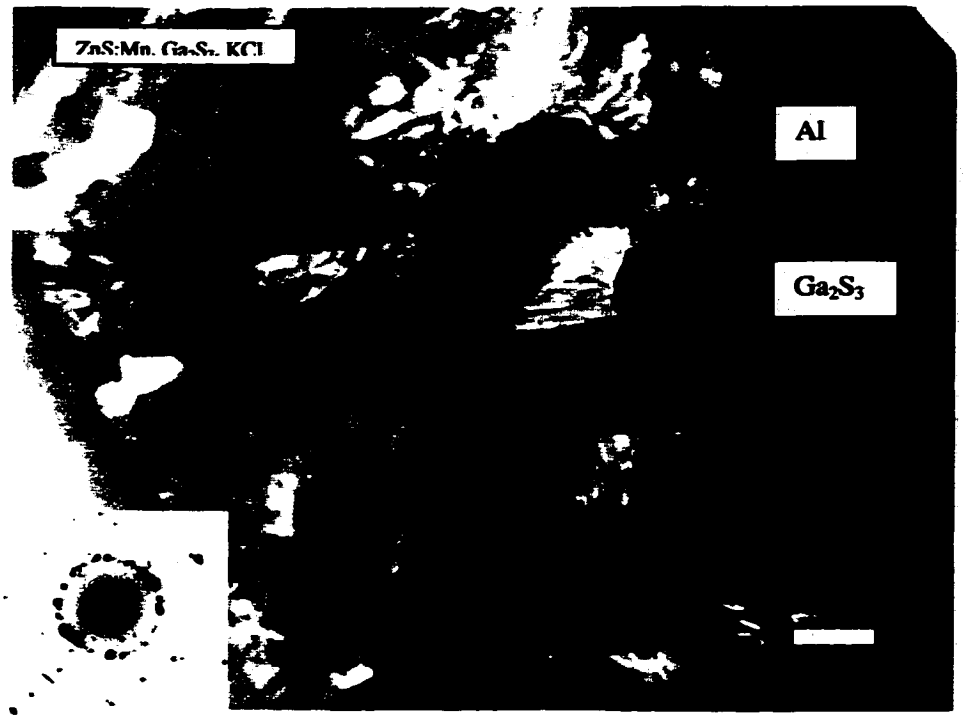

Figure 6.9 XTEM micrograph from sample doped with Ga_2S_3 at 800°C followed by KCl doping at 700°C. (Bar = 100nm)

In summary, KCl helps to reduce defects and enhances grain growth by assisting dislocation motion at high temperatures (800°C), while Ga_2S_3 hinders grain growth by pinning the grain boundaries and therefore does not help to reduce defects. If a sample is diffused with Ga_2S_3 first followed by KCl, the grain boundaries are pinned so strongly by Ga_2S_3 that the KCl has very little impact on the microstructure. As reported in Chapter 5, the Ga_2S_3 segregates at the grain boundaries with little solubility in the ZnS:Mn lattice. It is postulated that segregated Ga_2S_3 pins the dislocations at the grain boundaries, which prohibits KCl from enhancing dislocation motion. As a result, the microstructure consists of columnar grains with relatively small diameters. On the other hand, if a sample is

Reproduced with permission of the copyright owner. Further reproduction prohibited without permission.

diffused with KCl first followed by Ga_2S_3, KCl can be incorporated into the ZnS:Mn lattice and generate a microstructure with larger grains.

6.2.4 Compositional Analysis by Energy Dispersive Spectrometry (EDS)

A sample doped with Ga_2S_3 first at 800°C followed by KCl at 700°C is analyzed with EDS using both line profiles and stationary probes. Figure 6.10 is a PTEM micrograph of the investigated area. Figure 6.11 shows the composition line profiles for Zn, S, and Mn across the boundary marked #1 in Figure 6.10. Lower counts for both Zn and S are detected at the boundary versus the grain matrix, while Ga exhibits the opposite

Figure 6.10 PTEM micrograph from ZnS:Mn doped with Ga_2S_3 at 800°C followed by KCl doping at 700°C, showing the region where EDS is conducted.

Reproduced with permission of the copyright owner. Further reproduction prohibited without permission.

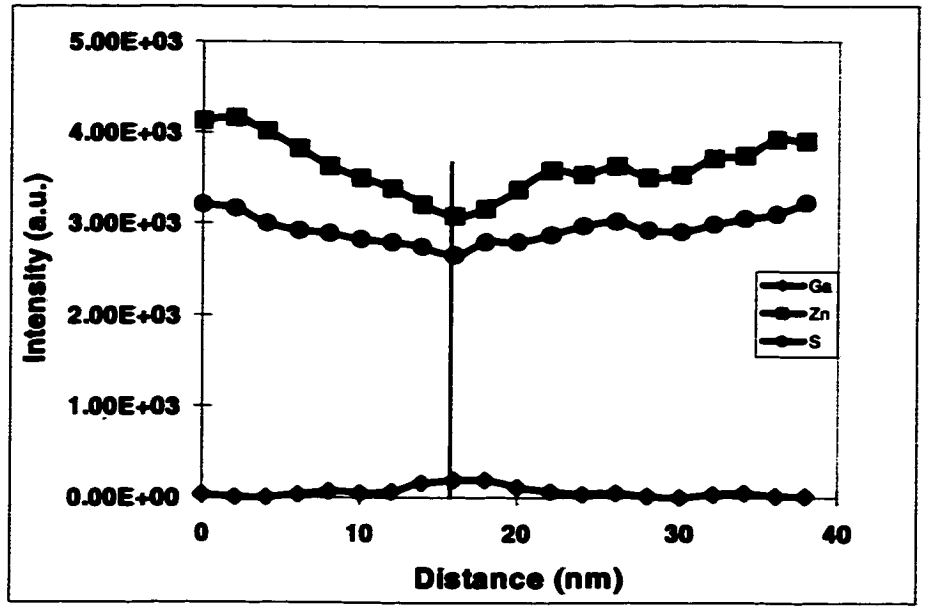

(a)

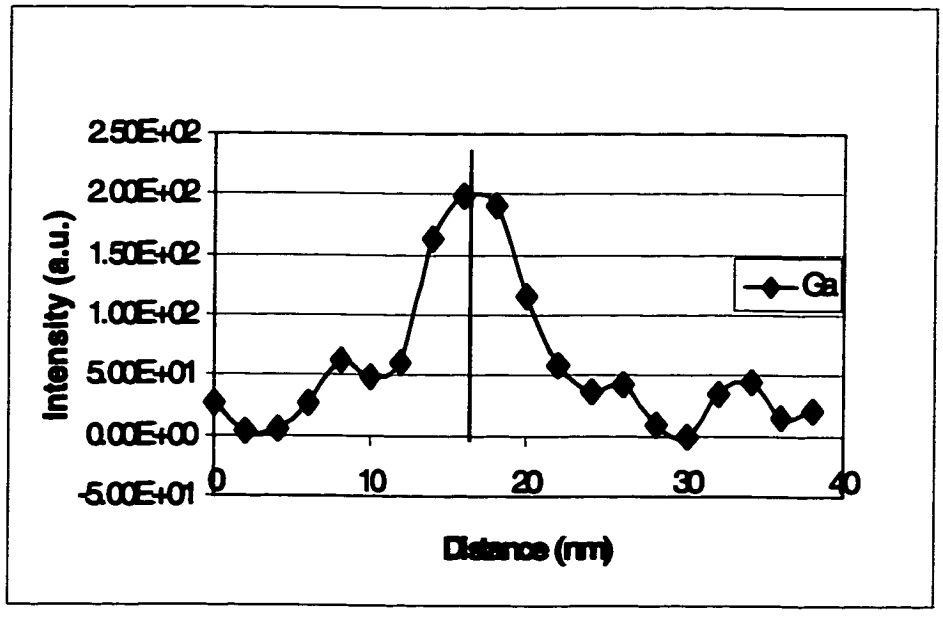

(b)

Figure 6.11 (a)Line profile data from line scanning across grain boundary #1. (b) Ga data plotted in an expanded vertical scale.

Reproduced with permission of the copyright owner. Further reproduction prohibited without permission.

trend. The Ga intensity versus distance is shown Figure 6.11b on an expanded vertical scale. This clearly shows gallium segregation to the grain boundary. Due to low concentration, signals from K and Cl are not detected in the line scans. Stationary probe with a longer sampling time is employed to get the information regarding K distribution. It is not possible to detect Cl due to its low atomic number and low concentration.

Table 6.2 summarizes the stationary probe data from the locations numbered in Figure 6.10. Similar to the single annealed samples with Ga_2S_3, Ga shows higher counts at grain boundaries and triple points, and S shows higher ratios to Zn at grain boundaries and triple points versus the grain matrix. Again, these data confirm that Ga_2S_3 segregates to grain boundaries and triple points. Unlike samples with only KCl, where K is uniform, K in the ZnS:Mn,Ga_2S_3,KCl shows higher concentrations at grain boundaries and triple points.

Table 6.2 Stationary probe data from locations numbered in Figure 6.10

Region	Zn	S	K	Mn	Ga
1 (GB)	57206	49169	762	571	4716
2 (GB)	35667	39109	1206	427	5358
3 (GB)	42541	41807	910	446	2622
4	73622	62931	454	541	N/A*
5	68597	60048	628	574	670
6	53982	47454	466	408	377
7 (TP)	18461	25509	1131	244	6285
8 (TP)	25585	31171	984	310	5399

6.2.5 Electroluminescence (EL) Properties

Figure 6.12 shows the EL brightness as a function of the applied voltage from samples with double co-dopants versus as-deposited or single co-doped samples. The

Reproduced with permission of the copyright owner. Further reproduction prohibited without permission.

corresponding threshold voltages B_{40} values, CIE coefficients at (V_{th} + 40), and luminous efficiency at (V_{th} + 40) are summarized in Table 6.3.

From Figure 6.12a, double annealing causes lower threshold voltages, increased B_{40}, and increased η_{40}, compared to the as-deposited and the single annealed samples. These improved EL properties result from improved crystallinity from annealing.

Table 6.3 EL properties of samples from samples with and without double co-dopants.

	V_{th} (V)	B_{40} (Nits)	CIE coefficients X	CIE coefficients Y	η at (V_{th} + 40) (lm/W)
As-deposited	125	48.7	0.539	0.4591	0.2275
700°C, 800°C	110	103.0	0.532	0.4658	
700°C, 800°C, w/ KCl	100	144.0	0.533	0.4647	
700°C w/ KCl, 800°C, w/ Ga_2S_3	85	64.2	0.546	0.4517	
800°C, 800°C	100	131.0	0.54	0.4579	0.650121
800°C, 800°C, w/ KCl	95	141.0	0.536	0.4615	0.615864
800°C w/ KCl, 800°C, w/ Ga_2S_3	70*	49.9*	0.546	0.4516	0.361441
800°C, 800°C, w/ Ga_2S_3	85	58.0	0.544	0.4537	0.21429
800°C w/ Ga_2S_3, 800°C, w/KCl	130	51.5	0.535	0.4625	
800°C, 700°C	115	135.0	0.53	0.4671	
800°C, 700°C, w/ Ga_2S_3	90	64.0	0.538	0.4596	
800°C w/ Ga_2S_3, 700°C, w/KCl	115	120.0	0.543	0.455	

Figure 6.12b shows the effects from double annealing on samples with only KCl. The B-V curves show lower threshold voltages, compared to as-deposited and single annealed samples. This is opposite to the increased V_{th} from KCl after a single anneal, presumably due to diffusion of K, Cl and Mn into the ATO layer.

Reproduced with permission of the copyright owner. Further reproduction prohibited without permission.

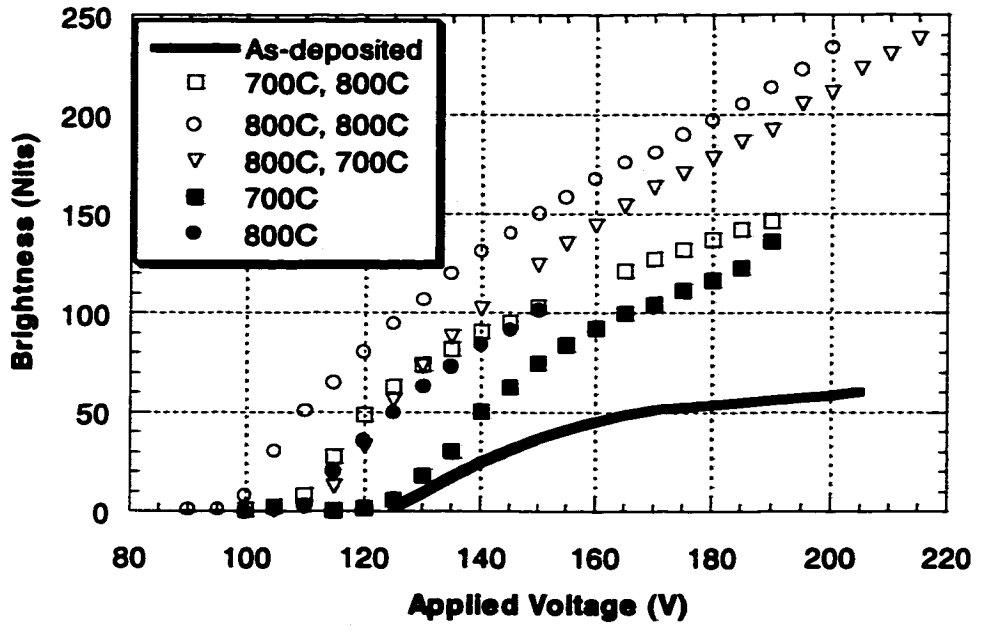

(a)

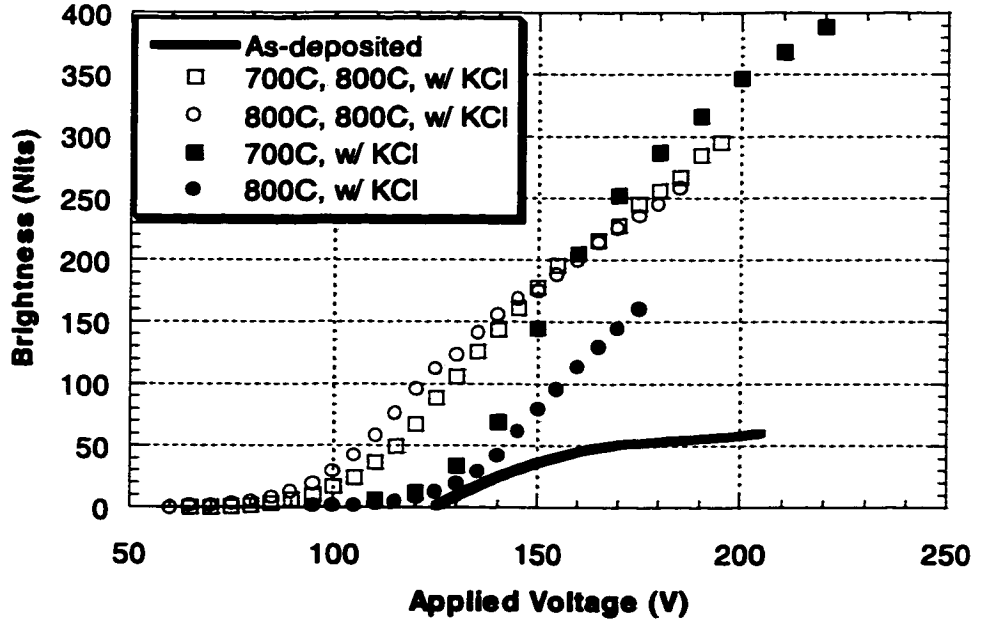

(b)

Figure 6.12 B-V curves from samples (a) without co-dopant after double annealing, (b) with KCl after double and single annealing, (c) with Ga_2S_3 after single and double annealing.

Reproduced with permission of the copyright owner. Further reproduction prohibited without permission.

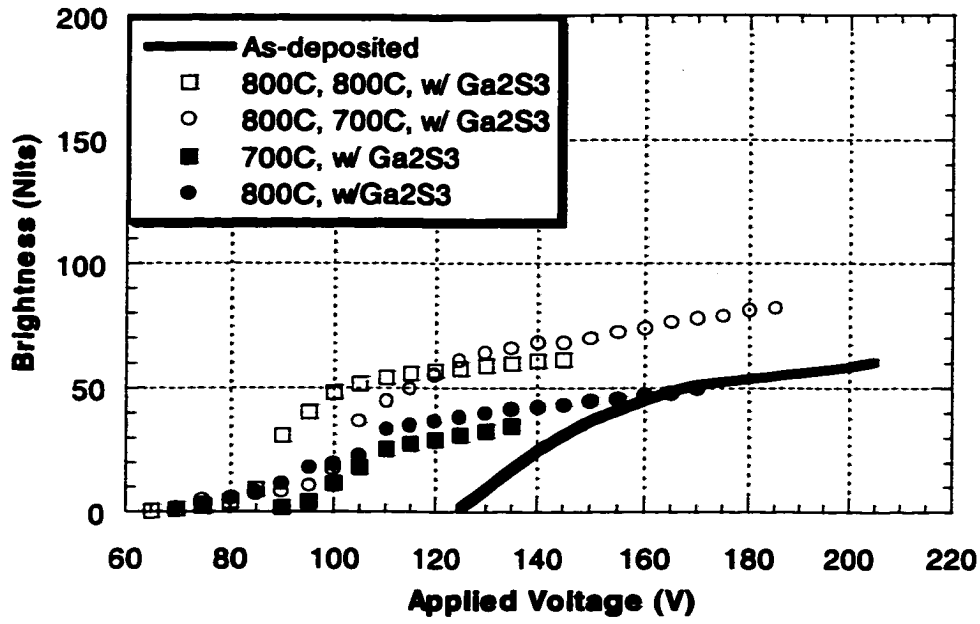

(c)

The effects of Ga_2S_3 after double annealing are shown in Figure 6.12c. Comparing to the single annealed samples, no changes of threshold voltage and a very slight increase in EL brightness is observed. All of the samples have "leaky" turn-on behavior, and they saturated at fairly low voltages.

The effects of double annealing at 800°C on the luminous efficiency of the samples with only one co-dopant are illustrated in Figure 6.13. Two groups of behavior are observed. The samples with KCl and those without after annealing have comparable brightness and luminous efficiency values, along with a sharp turn-on and saturation at higher voltages. The sample with Ga_2S_3 has similar EL brightness and efficiency levels as the as-deposited sample.

Reproduced with permission of the copyright owner. Further reproduction prohibited without permission.

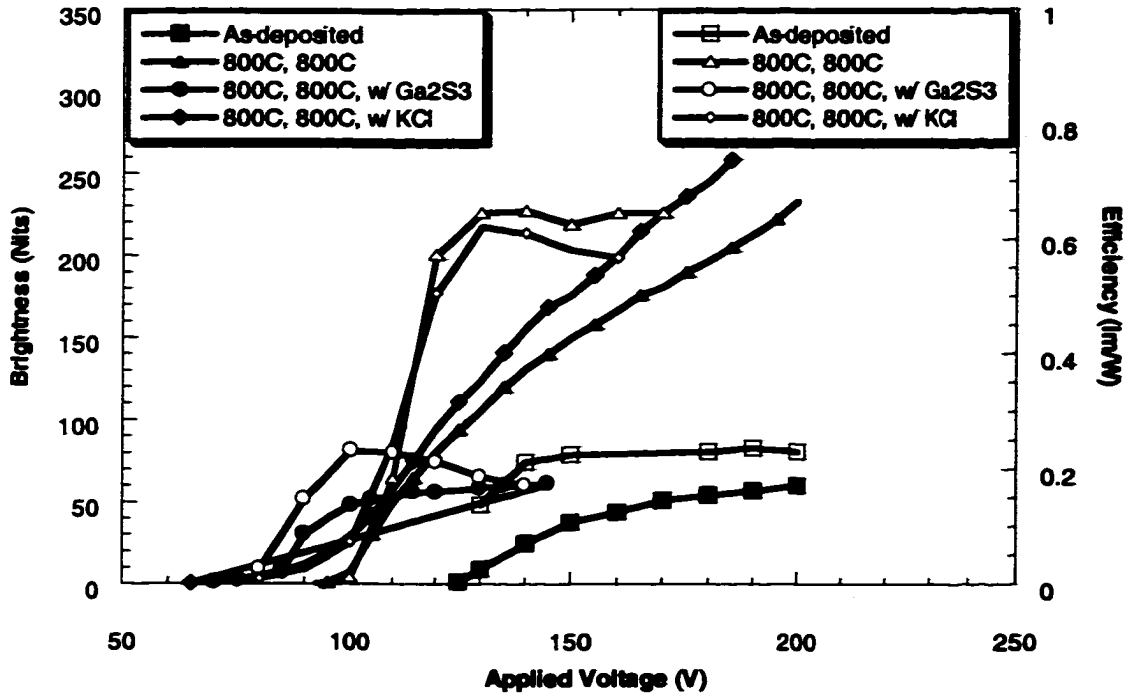

Figure 6.13 Brightness (solid symbols) and efficiency (open symbols) vs. applied voltage from samples with both KCl and Ga_2S_3.

B-V data from samples with both KCl and Ga_2S_3 dopants after double annealing are plotted in Figure 6.14. In samples doped and annealed with KCl first, the B-V curves are similar to each other. However, in samples doped with Ga_2S_3 first followed by KCl, the 100°C difference between 700°C and 800°C for the KCl diffusion temperature is really important. In fact, the sample doped with KCl at 800°C burns out before it is fully turned on. Consistent results are achieved from several devices made from the same phosphor film. Therefore, it is postulated that higher V_{th} and higher B_{40} would be achieved, if it were not burned out.

Reproduced with permission of the copyright owner. Further reproduction prohibited without permission.

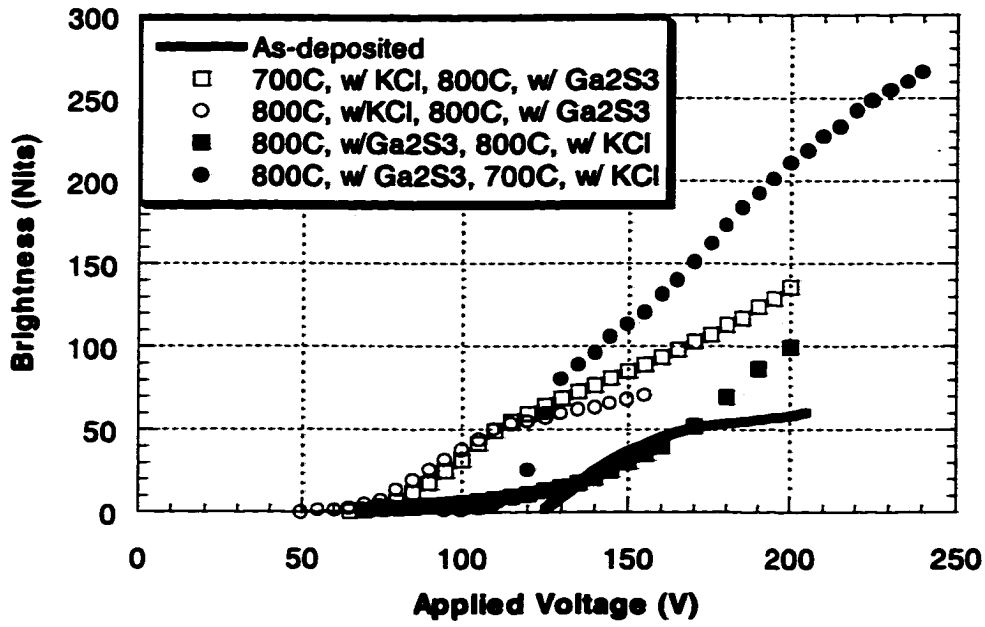

Figure 6.14 B-V plots from samples with both KCl and Ga_2S_3.

As shown by the TEM results, the sample co-doped with KCl first followed by Ga_2S_3 shows abnormal grain growth and significant removal of microstructural defects, while samples doped with Ga_2S_3 first followed by KCl have very limited grain growth and little improvement to the microstructure. However, the EL properties from the Ga_2S_3 first group are much better than the KCl first group. Therefore some unobservable features are controlling the EL properties, such as the point defects.

As discussed earlier for single dopant, Ga_2S_3 appears to introduce defects that cause early turn-on and low radiative vs. non-radiative recombination ratio. The data in Figure 6.14 are consistent with the fact that these defects are introduced when Ga_2S_3 diffusion is the second step, in spite of the general improvement in microstructure. As a result, low threshold voltages and low EL brightness values are observed. When Ga_2S_3 diffusion is followed by KCl diffusion, defects from Ga_2S_3 are annealed out by the

Reproduced with permission of the copyright owner. Further reproduction prohibited without permission.

second anneal in the presence of KCl. Increased threshold voltages and higher B_{40} values are resulted. Thus the last anneal appears to dominate the EL properties.

The B-V data from samples doped with Ga_2S_3 followed by KCl both show two stages in the B-V behavior. The device turns on at a fairly low voltage with a very low EL brightness about 10nits. This low brightness level is maintained in the next 40 volts in both cases. Turn-on at such a low voltage suggests that the electrons be injected from defect states instead of from interface states. With such a low turn-on voltage, the electrons do not have high enough energy to efficiently excite the Mn^{2+} luminous centers. When the device experiences another turn-on, the brightness increases rapidly. It is believed that this second turn-on is associated with the KCl dopant. The reported Cl^- donor level in ZnS is 0.264eV below the conduction band. It is possible that the electrons in this state are ionized at the second turn-on voltage, so that additional electrons are generated throughout the phosphor to impact excite the luminescent centers.

Samples doped with KCl first followed by Ga_2S_3 do not have high EL brightness, but they show the highest brightness in the voltage range between 75V to 110V. This probably results from improvement of the microstructure. Recall that the XRD data showed changes in the texture of these samples. The electrical properties vary with the texture of crystalline solids [46]. It is suspected that this texture change modifies the insulator/phosphor interface, and thus, results in the current specific turn-on properties. The clean interface and less defect density inside grains make fewer traps for hot electrons. However, with the voltage increasing, it is speculated that defects resulted from Ga_2S_3 become dominant, and thus low EL brightness is resulted.

Reproduced with permission of the copyright owner. Further reproduction prohibited without permission.

6.3 Summary

The introduction of both KCl and Ga_2S_3 by double annealing gives rise to complicated modifications of the ZnS:Mn thin film phosphors, in term of both microstructure and EL properties. Double annealing gives slight increases in B_{40} and decreases in threshold voltage. With KCl, samples show phase transformation and texture change after double annealing, especially when the annealing temperature is 800°C. Cubic structure with c(200) texture becomes more stable. Large grain growth resulting in grains with diameter of 500nm and much lower defect density are observed in TEM micrographs. The incorporated KCl is postulated to enhance dislocation motion and consequent grain growth, and thus improved EL brightness. In double annealed samples with Ga_2S_3, neither the microstructure nor the EL brightness is improved because Ga_2S_3 pins the grain boundaries and triple points by segregation and introduces point defects that are bad to EL.

When both KCl and Ga_2S_3 are doped into samples, significant grain growth only occurs in samples that are doped with KCl first. However, the EL brightness from these samples is low due to defects introduced by the Ga_2S_3 from the second step. On the other hand, the microstructure is poor in samples doped with Ga_2S_3 first, but the KCl heals the point defects in the second step of annealing and results in fairly good EL brightness. The B-V curves from these samples have two stages, a very leaky turn-on at voltage below 100V, and a sharp turn on at higher voltages. The first one is believed to be associated with the defects the have a range of energy states close to the conduction band,

Reproduced with permission of the copyright owner. Further reproduction prohibited without permission.

while the second one is associated with the ionization of electrons from Cl^- donors whose state is 0.264eV below the conduction band.

Reproduced with permission of the copyright owner. Further reproduction prohibited without permission.

CHAPTER 7
CONCLUSIONS AND FUTURE WORK

The ZnS:Mn thin films deposited by RF magnetron sputter system have a combination of hexagonal and cubic phases and c(200) with slight h(0002) + c(111) mixture are the preferred growth orientations. The microstructure is heavily defected. There are two types of grain morphologies through the thickness of the ZnS:Mn films. At the insulator/phosphor interface, is a 100nm thick layer of equiaxed grains with an average grain size of 10nm. At distance >100nm from the insulator/ZnS:Mn interface, columnar grains develop with an average diameter of 89nm. There is a large amount of contrast bands inside grains as observed by transmission electron microscopy (TEM). These bands are dominantly microtwins, stacking faults or switching between hexagonal and cubic structures. The as-deposited EL properties are poor, with a V_{th} of 125V, B_{40} of 48.7nits, and η_{40} of 0.2275lm/W for the half stack devices, (i.e., top dielectric film is not deposited). Poor EL properties are attributed to the heavily defected microstructure.

When KCl is diffused into the ZnS:Mn thin film at 700°C, the columnar grain growth is enhanced (average columnar diameter of 187nm versus 132nm from sample without KCl). In addition, the equiaxed grain layer is removed completely. A mechanism is postulated by which KCl helps dislocation motion in ZnS:Mn, which presumably lead to grain growth. EL properties are improved significantly. The B_{40} is 252nits, five times that of an as-deposited sample (48.7nits) and 2.5 times that of a

Reproduced with permission of the copyright owner. Further reproduction prohibited without permission.

sample annealed without KCl (99.6nits). A slight increase in V_{th} is detected. It is postulated that incorporated Cl^- ions act as donors, which supply additional electrons to the phosphor conduction band. The improvement in crystallinity also decreases the number of scatter centers for hot electrons and reduces non-radiative relaxation sites as well. All of these effects contribute to improved EL properties.

After Ga_2S_3 is diffused into the phosphor layer by 5minute anneal at 800°C, a uniform distribution of Ga versus film thickness is measured with SIMS. Grain growth in columnar grains is less than in ZnS:Mn without Ga_2S_3. The defect density inside grains is still high. Energy dispersive spectrometry (EDS) of fluorescent X-ray in the transmission electron microscope (TEM) showed that Ga segregated to grain boundaries and triple points. It is postulated that Ga_2S_3 diffuses primarily along grain boundaries, but does not incorporate into the ZnS lattice. The Ga_2S_3 in ZnS:Mn fails to act as a flux agent to increase grain growth as expected. Instead, it pins the grain boundaries and prevents them from moving, even at elevated temperatures. ZnS:Mn,Ga_2S_3 shows lower EL brightness than the as-deposited ZnS:Mn film (37.9nits versus 48.7nits). The B-V turn-on in ZnS:Mn,Ga_2S_3 samples is "leaky", which is attributed to shallow donor levels from Ga_2S_3 induced defects. Electrons in these levels can tunnel into the conduction band of the phosphor at relatively low voltages, resulting a low threshold voltage and a "leaky" turn-on. Electrons injected into the phosphor experience low fields and cannot be accelerated to sufficiently high energy states to impact excite Mn^{2+}. High PL brightness from ZnS:Mn,Ga_2S_3 films indicates that there are sufficient luminous centers in the phosphor which relax radiatively, consistent with the postulation that there are insufficient hot electrons for EL due to the heavily defected microstructure.

Reproduced with permission of the copyright owner. Further reproduction prohibited without permission.

In ZnS:Mn samples diffused by KCl first followed by Ga_2S_3 showed poor EL properties, despite significant grain growth (grain size at 500nm). For sample doped with Ga_2S_3 first followed by KCl, the EL brightness is much better. It is postulated that those Ga_2S_3 induced defects which are harmful to EL are annealed in the presence of KCl. In addition, EDS results show K segregation to the grain boundaries in this sample.

In future work, the follow aspects should be investigated:

(1) The effects of the equiaxed grain layer. To investigate the effects of this equiaxed layer at the insulator/phosphor interface, samples with 100nm of ZnS:Mn buffer layers should be investigated. By co-doping this buffer layer with KCl at 700°C, grains with diameter much larger than or at the same level of the thickness should be achieved. Then continue to deposit to get a total thickness of 1μm. By comparing samples with and without buffer layers, the effects of the equiaxed fine grain layer can be determined.

(2) The correlation between PL and EL in ZnS:Mn,KCl should be studied. In the present study, ZnS:Mn,KCl samples showed significantly improved EL, but very poor PL. The poor PL brightness is attributed to incorporation of KCl leading to increased symmetry of Mn^{2+} in ZnS lattice. To verify this argument, calculation and experiment should be done.

(3) Luminescence life time measurement of ZnS:Mn, Ga_2S_3 samples should be measured. The results will indicate whether there are energy transfer from Mn^{2+} to Ga^{3+} or other lattice defects in ZnS lattice. These data are necessary to determine the reasons for low EL brightness in ZnS:Mn,Ga_2S_3 samples.

(4) The electrical properties of the defects. It is still a puzzle that in the double co-doped samples, the sample doped with KCl first followed by Ga_2S_3 shows lower EL

Reproduced with permission of the copyright owner. Further reproduction prohibited without permission.

brightness, although it has significant grain growth and low defect density. While the sample doped with Ga_2S_3 first followed by KCl shows better EL brightness, despite a defected microstructure. By conducting cathodoluminescence (CL) in TEM, it is possible to characterize the electrical properties of those contrast bands, which will be helpful to explain this intriguing phenomenon.

Reproduced with permission of the copyright owner. Further reproduction prohibited without permission.

REFERENCES

1. P. H. Hollway, S. Jones, P. Rack, J. Sebastian, T. Trottier, 10th Internatioanl Symposium on the Applications of Ferroelectrics, in A. Safari, B. Kulwicki (Eds.). IEEE, Piscataway, NJ, 1997, p. 127.

2. P. D. Rack, A. Naman, P. H. Holloway, S-S. Sun, R. T. Tuenge, MRS Bulletin, Vol. 21, 1996, p.49.

3. P. D. Rack, P. H. Holloway, Materials Science & Engineering R, Vol. R21, No. 4, 1996, p. 171.

4. K. Miyashita, M. Shibata, Digest of Japan Display, 1993, p. 100.

5. S. Kobayashi, J. F. Wager, A. Abu-Dayah, EL 92, 1992, p. 234.

6. K. Waldrip, J. Lewis, M. Davidson, Q. Zhai, P. Holloway, submitted to Applied Physics Letter B.

7. R. E. Hummel, Electronic Properties of Materials, 2nd edition, Springer-Verlag, 1993, p. 25.

8. K, Bhattacharyya, S. M. Goodnick, J. F. Wager, Journal of Applied Physics Vol. 73, 1993, p. 3390.

9. K. Brennan, Journal of Applied Physics, Vol. 64, 1988, p. 4024.

10. R. March, Go. O. Muller, Journal of Crystal Growth, Vol. 101, 1990, p. 967.

11. K. Bhattacharyya, S. M. Goodnick, J. F. Wager, unpublished work. For further information, please check PTCOE quarterly reports.

12. E. Bringuier, Journal of Applied Physics, Vol. 70, 1991, p. 4505.

13. E. Bringuier, Journal of Applied Physics, Vol. 67, 1990, p. 7040.

14. S. Sze, Physics of Semiconductor Devices, Wiley, New York, 1981, p. 149.

15. Y. A. Ono, Electroluminescent Displays, World Scientific Publishing Co., 1995, p. 21.

Reproduced with permission of the copyright owner. Further reproduction prohibited without permission.

16. R. Mach, G. O. Muller, Semiconductor Science and Technology, Vol. 6, 1991, p. 305.

17. P. A. Keller, Information Display Vol. 1, 1996, p.36.

18. Y. A. Ono, Electroluminescent Displays, H. L. Ong Ed., Series on Information Display, World Scientific, Singapore, 1995, Vol. 1, p. 68.

19. H. Ohnishi, N. Sakuma, K. Ieyasu, Y. Hamakawa, Journal of Electrochemistry Society, Vol. 130, 1983, p. 2115.

20. T. Mitsui, N. Yamamoto, J. Yoshino, T. Tadokoro, S. Ohta, K. Yanashima, K. Inoue, Applied Surface Science 100/101, 1996, p. 625.

21. C. B. Thomas, D. Sands, K. M. Brunson, H. S. Reehal, Journal of Electrochemistry Society, Vol. 136, 1989, p. 1235.

22. R. C. Sharma, Y. A. Chang, Journal of Phase Equilibria, Vol. 17, No. 3, 1996, p.261.

23. L. L. Chang, L. Esaki, R. Tsu. Applied Physics Letters, Vol. 19, 1971, p. 143.

24. P. Pirouz, X. J. Ning, Institute of Physics Conference Service, Vol. 146, 1976, p. 69.

25. P. Haasen, Acta Met., Vol. 5, 1957, p. 598.

26. G. Lu, D. J. H. Cockayne, Philosophical Magazine A, Vol. 53, 1986, p. 297.

27. P. B. Hirsch, Defects in Semiconductors, edited by J. Narayan, T. Y. Tan, MRS Symposium, Proceedings, Vol. 2, 1981, p. 257.

28. Y. Y. loginov, P. D. Brown, C. J. Humphreys, Institute of Physics Conference Service, Vol. 146, 1994, p. 431.

29. D. Gwinner, R. Labusch, Journal of Physics Paris, Vol. 40, 1979, p. 117.

30. A. Zozime, W. Schroeter, Philosophical Magazine A, Vol. 56, 1989, p. 565.

31. R. Jones, S. Oberg, S. Marklund, Philosophical Magazine B, Vol. 43, 1981, p. 839.

32. A. R. Verma, P. Krishna, Polymorphism and Polytypism in Crystals, 1966, p.63.

33. Y. Nakanishi, Y. Fukuda, Y. Hatanaka, G. Shimaoka, Applied Surface Science Vol.48/49, 1991, p. 297.

Reproduced with permission of the copyright owner. Further reproduction prohibited without permission.

34. J. M. Hurd, C. N. King, J. Electron. Mater. Vol. 8, 1979, p. 897.

35. D. Petre, I. Pintilie, M. L. Ciurea, T. Botila, Thin Solid Film, Vol. 260, 1995, p. 54.

36. J. M. Blackmore, G. W. Blackmore, D. C. Rodway, M. J. Slater, Thin Solid Film, Vol. 192, 1990, p. 309.

37. C. Frey, D. Serafin, R. Boudreau, Dig. 1988 SID International Symposium, Anaheim, 1988, p. 16.

38. J. M. Blackmore, A. G. Cullis, Thin Solid Films, Vol. 199, 1991, p. 321.

39. T. Suntla, J. Antson, A. Pakkala, S. Lindfors, Dig. 1980 SID International Symposium, San Diego, 1980, p. 108.

40. J. Ihanus, M. Ritala, M. Leskela, T. Prohaska, R. Resch, G. Friedbacher, M. Grasserbauer, Applied Surface Science Vol. 120, 1997, p. 43.

41. K. Hirabayashi, H. Kozawaguchi, Jpn. J. Appl. Phys. Vol. 25, 1986, p. 711.

42. T. Takahara, M. Endo, K. Chiba, A. Kondo, Dig. 1991 SID International Symposium, Anaheim, 1991, p. 66.

43. M. Shiiki, O. Kanehisa, Journal of Crystal Growth, Vol. 117, 1992, p. 1035.

44. H. Kina, Y. Yamada, Y. Maruta, Y. Tamura, Journal of Crystal Growth, Vol. 169, 1996, p. 33.

45. T. Nire, A. Matsuno, A. Miyakoshi, K. Ohmi, Japanese Journal of Applied Physics, Vol. 33, 1994, p. 2605.

46. C. Chen, S. Husurisnto, X. Lu, M. D. Koretsky, Journal of Electrochemistry Society, Vol. 145, 1998, p. 226.

47. S. Schoen, M. Chaichimansour, W. Park, T. Yang, B. K. Wagner, C. J. Summers, Journal of Crystal Growth, Vol. 175/176, 1997, p. 598.

48. A. Hunter, A. H. Kitai, Journal of Luminescence, Vol. 4046, 1990, p. 227.

49. W. Tong, T. K. Tran, W. Park, S. Schoen, B. K. Wagner, C. J. Summers, Proceedings of the First International Conference on the Science and Technology of Display Phosphors, San Diego, USA, 1995, p.25.

50. H. T. Lin, D. H. Rich, D. B. Witty, Journal of Applied Physics, Vol. 75, 1994, p. 8080.

Reproduced with permission of the copyright owner. Further reproduction prohibited without permission.

51. P. M. Petroff, R. A. Logan, A. Savage, Physics Review Letters, Vol. 44, 1980, p. 287.

52. J. Wang, J. W. Steeds, M. Henini, Journal of Physics IV, Vol. 1, 1991, p. C6-125.

53. R. Mach, G. U. Reinsperger, G. O. Mueller, B. Selle, G. Matzkeit, Journal of Crystal Growth, Vol. 117, 1992, p. 1002.

54. C. W. Wang, T. J. Sheu, Y. K. Su, M. Yokoyama, Applied Surface Science, Vol. 113/114, 1997, p. 709.

55. Y. Tanaka, H. Morishita, J. T. Ryu, I. Katayama, K. Oura, Surface Science, Vol. 363, 1996, p. 161.

56. B. A. Movchan, A. V. Demchishin, Fiz. Metal. Metalloved Vol. 28, 1969, p. 83.

57. J. A. Thornton, Journal of Vacuum Science Technology, Vol. 11, 1974, p. 666.

58. J. A. Thornton, Annual Review of Materials Science, Vol. 7, 1977, p. 239.

59. H. J. Frost, Materials Characterization, Vol. 32, 1994, p. 257.

60. L. J. Friedrich, S. K. Dew, M. Brett, T. Smy, Thin Solid Films, Vol. 266, 1995, p. 83.

61. B. K. Chakraverty, Journal of Physics and Chemistry of Solids, Vol. 28, 1967, p. 2401.

62. B. K. Chakraverty, Journal of Physics and Chemistry of Solids, Vol. 28, 1967, p. 2413

63. C. S. Nichols, C. M. Mansuri, S. J. Townsend, D. A. Smith, Acta, Metall. Mater. Vol. 41, 1993, p. 1861.

64. C. V. Thompson, Scripta Metallurgica et Materialia, Vol. 28, 1993, p. 167.

65. C. S. Smith, Metal Interface, 1952, p. 65.

66. D. Weaire, N. Rivier, Contemporary Physics, Vol. 25, 1984, p. 59.

67. W. W. Mullines, Journal of Applied Physics, Vol. 27, 1956, p. 861.

68. H. J. Frost, Scripta Metall, Vol. 22, 1987, p.65.

69. H. J. Frost, C. V. Thompson, Journal of Electronic Materials, Vol. 17, 1988, p. 447.

Reproduced with permission of the copyright owner. Further reproduction prohibited without permission.

70. P. A. Beck, M. L. Holtzworth, P. R. Sperry, Trans. AIME, Vol. 180, 1949, p. 163.

71. J. E. Palmer, C. V. Thompson, H. I. Smith, Journal of Applied Physics, Vol. 62, 1987, p. 2492.

72. W. W. Mullines, Acta Metall., Vol. 6, 1958, p. 414.

73. M. Hiller, G. R. Purdy, Met. Trans., Vol. 3, 1972, p. 2757.

74. J. W. Cahn, J. D., Pan, R. W. Balluffi, Scripta Metall., Vol. 13, 1979, p. 503.

75. S. C. Han, D. Y. Yoon, and M. K. Vrun, Acta Metall. Mater, Vol. 43, 1995. P. 977.

76. B. N. Singh, T. Leffers, Scripta Metall., Vol. 8, 1975, p.549.

77. J. P. Benedict, R. M. Anderson, S. J. Klepeis, Materials Research Society Symposium Proceedings, Vol. 523, 1998, p. 19.

78. L. A. Giannuzzi, J. L. Drown, S. R. Brown, R. B. Irwin, F. A. Stevie, Materials Research Society Symposium Proceedings, Vol. 480, 1997, p. 19.

79. S. Mahajan, K. Harsha, Principles of Growth and Processing of Semiconductors, WCB, McGraw –Hill, 1998, p. 104.

80. J. P. Guillemet, B. De Mauduit, B. Pieraggi, E. Campo, E. Scheid, Journal of Materials Science Letters, Vol. 12, 1993, p. 910.

81. D. B. Williams, C. B. Carter, Transmission Electron Microscopy, 1996, p. 141, 143.

82. D. H.-I, Su, H. T. Shisido, F. Tsai, L. Liang, F. C. Mercado, Materials Research Society Symposium Proceedings, Vol. 480, 1997, p. 105.

83. F. Shaapur, T. Stark, T. Woodward, R. J. Graham, Materials Research Society Symposium Proceedings, Vol. 480, 1997, p. 173.

84. J. S. Lee, H. H. Kim, Y. W. Jeong, Graham, Materials Research Society Symposium Proceedings, Vol. 480, 1997, p.29.

85. E. Bugiel, Materials Science Research Symposium Proceedings, Vol. 480, 1997, p. 89.

86. R. DeHoff, Microstructure Notes.

87. A. Cerma, P. Krishna, Polymorphism and Polytypism in Crystals, John Wiley & Sons, Inc., 1966, p.40.

Reproduced with permission of the copyright owner. Further reproduction prohibited without permission.

88. S. Shih, P. Keir, J. Viljanen, and J. Wager, Journal of Applied Physics, Vol.78, 1995, p. 5775.

89. D. H. Smith, J. Luminescence Vol. 23, 1981, p. 209.

90. Y. A. Ono, h. Kawakamin, M. Fuyama, and K. Onisawa, Japanese Journal of Applied Physics, Vol. 26, 1987, p.1482.

91. Y. S. Chen and D. C. Krupka, J. Applied Physics, Vol. 43, 1972, p. 4089.

92. A. Naman, Ph.D Dissertation, 1997.

Reproduced with permission of the copyright owner. Further reproduction prohibited without permission.

BIOGRAPHICAL SKETCH

The author was born in Beijing, China. Her education started from spring 1976. After her high school graduation from the 54th Middle School in Beijing in 1986, she attended the Department of metal physics and chemistry in the University of Science and Technology, Beijing, China. In 1990 she received her B.S. and immediately started graduate school in the same department. After receiving her M.S. degree in materials science, she was employed by China International Trust and Investment Corporation (CITIC) as a project engineer in Nonferrous Metals Division. In 1996, she enrolled in the University of Florida to pursue her Ph.D.

Reproduced with permission of the copyright owner. Further reproduction prohibited without permission.

I certify that I have read this study and that in my opinion it conforms to acceptable standards of scholarly presentation and is fully adequate, in scope and quality, as a dissertation for the degree of Doctor of Philosophy.

Paul H. Holloway, Chairman
Professor of Materials Science and Engineering

I certify that I have read this study and that in my opinion it conforms to acceptable standards of scholarly presentation and is fully adequate, in scope and quality, as a dissertation for the degree of Doctor of Philosophy.

Kevin S. Jones, Cochairman
Professor of Materials Science and Engineering

I certify that I have read this study and that in my opinion it conforms to acceptable standards of scholarly presentation and is fully adequate, in scope and quality, as a dissertation for the degree of Doctor of Philosophy.

Robert T. DeHoff
Professor of Materials Science and Engineering

I certify that I have read this study and that in my opinion it conforms to acceptable standards of scholarly presentation and is fully adequate, in scope and quality, as a dissertation for the degree of Doctor of Philosophy.

Michael J. Kaufman
Professor of Materials Science and Engineering

Reproduced with permission of the copyright owner. Further reproduction prohibited without permission.

I certify that I have read this study and that in my opinion it conforms to acceptable standards of scholarly presentation and is fully adequate, in scope and quality, as a dissertation for the degree of Doctor of Philosophy.

Timothy J Anderson
Professor of Chemical Engineering

This dissertation was submitted to the Graduate Faculty of the College of Engineering and to the Graduate School and was accepted as partial fulfillment of the requirements for the degree of Doctor of Philosophy.

December 1999

M. Jack Ohanian
Interim Dean, College of Engineering

Winfred M. Phillips
Dean, Graduate School

Reproduced with permission of the copyright owner. Further reproduction prohibited without permission.